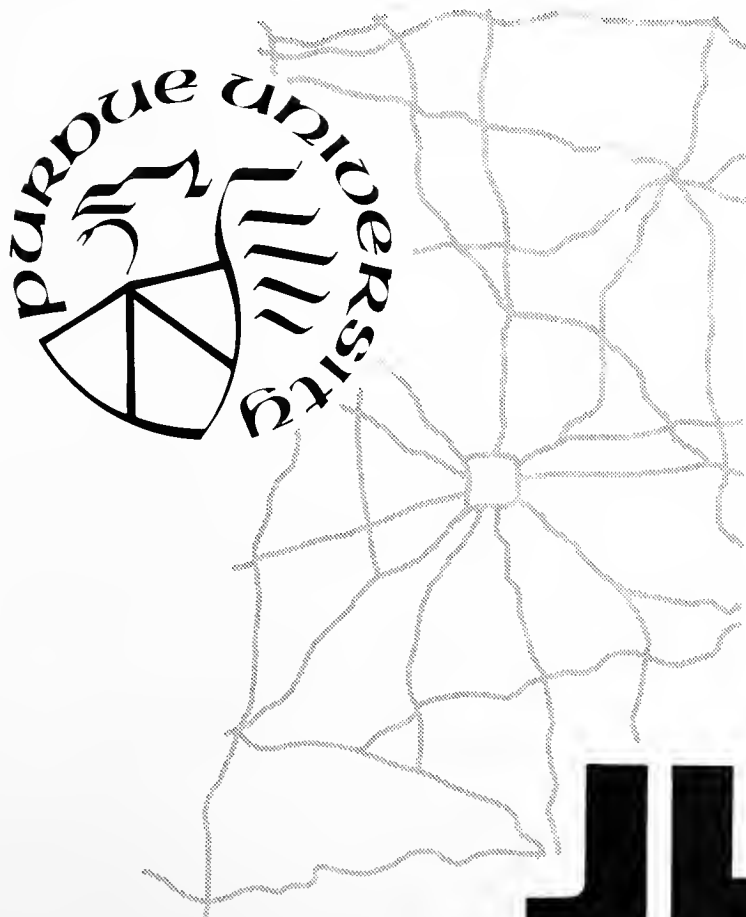


MECHANISM FOR THE COMPACTION AND RESPONSE OF KAOLINITE

NOVEMBER 1972 – NUMBER 36



BY

RALPH J. HODEK

JHRP

JOINT HIGHWAY RESEARCH PROJECT
PURDUE UNIVERSITY AND
INDIANA STATE HIGHWAY COMMISSION



Final Report

MECHANISM FOR THE COMPACTION AND RESPONSE OF KAOLINITE

TO: J. F. McLaughlin, Director November 9, 1972
Joint Highway Research Project
FROM: H. L. Michael, Associate Director Project: C-36-5G
Joint Highway Research Project File: 6-6-7

Attached is a Final Report entitled "Mechanism for the Compaction and Response of Kaolinite", by Mr. Ralph J. Hodek. This work was conducted under the supervision of Professor C. W. Lovell, Jr. of our staff.

The purpose of this study was to extend existing soil compaction models to better fit the observed soil conditions during and after compaction. This extension took into account the fact that the soil is made up of macroscopic aggregations of clay particles prior to compaction.

The results indicated that, for Kaolinite compacted in the laboratory by static pressures under conditions of no lateral strain, the deformable aggregate soil model is appropriate to explain the achievement of compaction. It was also confirmed that the soil aggregate characteristics influence some of the engineering properties, notably swelling pressure, and that simple relations which are amenable to quantification exist between net input energy and compacted unit weight.

It was suggested that this model be validated for other soils and other types of compaction including field compaction. Further, it was suggested that general quantification of the prediction of the achievement of compacted unit weight should lead to a more widespread use of procedural type compaction specifications.

The report is submitted for acceptance as fulfillment of the objectives of this study.

Respectfully submitted,

Harold L. Michael

Harold L. Michael
Associate Director

HLM:ms

cc: W. L. Dolch	M. L. Hayes	C. F. Scholer
R. L. Eskew	C. W. Lovell	N. B. Scott
W. H. Goetz	G. W. Marks	J. A. Spooner
M. J. Gutzwiller	R. D. Miles	N. W. Steinkamp
G. K. Hallock	J. W. Miller	H. R. J. Walsh
R. H. Harrell	G. T. Satterly	E. J. Yoder

Digitized by the Internet Archive
in 2011 with funding from
LYRASIS members and Sloan Foundation; Indiana Department of Transportation

Final Report
MECHANISM FOR THE COMPACTION
AND RESPONSE OF KAOLINITE

by

Ralph J. Hodek
Graduate Instructor in Research

Joint Highway Research Project

Project No.: C-36-5G

File No.: 6-6-7

Conducted By
Joint Highway Research Project
Engineering Experiment Station
Purdue University
In Cooperation With
Indiana State Highway Commission

Purdue University
West Lafayette, Indiana
November 9, 1972

ACKNOWLEDGMENTS

The writer expresses his thanks to Dr. Israela Ravina for her assistance with the particle orientation studies and to Mr. James Houston who labored from dusk to dawn on many occasions while deforming aggregates.

The guidance and counsel of Professor Sidney Diamond is acknowledged and appreciated as is the financial support of the Joint Highway Research Project of Purdue University.

The understanding and patience of the writer's major professor, Professor C. W. Lovell, Jr., has been in the true spirit of a professional and an educator and simple thanks cannot express this writer's appreciation.

TABLE OF CONTENTS

	Page
LIST OF TABLES	vi
LIST OF FIGURES	viii
LIST OF SYMBOLS	xv
ABSTRACT	xix
INTRODUCTION	1
REVIEW OF LITERATURE	3
Electrical Forces Among the Particles	4
Ionic Bonding	4
Hydrogen Bonding	5
Van der Waals' Bonding	5
Force of Repulsion	8
Hamaker Equation	8
Gouy-Chapman Double-Layer Concept	9
Summary of Forces Among Particles	12
Structure and Properties of Kaolinite	12
Structural Makeup	12
Ion Exchange Properties	14
Flocculation	15
Present Theories of Compaction	16
Lambe's Theory of Compaction	17
Olson's Theory of Compaction	18
Hogentogler's Theory	21
Role of Individual Clay Particles	22
Mechanical Properties of Compacted Soil	24
Types of Laboratory Compaction	24
Volumetric Swell	32
Swelling Pressure	51
COMPACTION MECHANISM HYPOTHESIS	56
Initial Soil Structure	56
Effect of Curing Time	61
Compaction Mechanism	62

TABLE OF CONTENTS, cont.

	Page
DESCRIPTION OF EXPERIMENTAL PROGRAM	67
Soil	67
Soil Preparation	68
Intra-aggregate Relations	71
Description of Mercury Intrusion Technique for the Determination of Aggregate Volume	73
Photographic Measuring Technique for the Determination of Aggregate Volume	85
Aggregate Weights and Weight-Volume Ratios	93
Description of Aggregate Deformation Test	95
FABRIC STUDIES	97
Sample Preparation for Diffraction Study	97
Determination of Particle Orientation	99
Direct Examination of Fabric	101
Sample Compaction	102
Swelling Pressure Measurements on Compacted Samples	110
RESULTS	114
Particle Orientation	114
Dry Unit Weights of Aggregates	116
Achievement of Compacted Unit Weight	121
End Results of Compaction and Saturation	126
Swelling Pressure	133
Aggregate Deformation	141
DISCUSSION OF RESULTS	146
Particle Orientation	146
Dry Unit Weights of Aggregates	152
Achievement of Compacted Unit Weight	158
End Results of Compaction and Saturation	179
Swelling Pressure Tests	188
Aggregate Deformation	208
Model Used by Other Investigators	211
SUMMARY AND CONCLUSIONS	212
Summary	212
Aggregate Studies	213
Achievement of Compacted Unit Weight	213
End Results of Compaction	214
Swelling Pressure	214
Conclusions	215

TABLE OF CONTENTS, cont.

	Page
RECOMMENDATIONS	216
LIST OF REFERENCES	218
APPENDICES	224
Appendix A: Aggregate Size Distribution Curves	224
Appendix B: X-Ray Diffractometer Settings	229
Appendix C: Peak Height Ratios	230
Appendix D: Additional Results of Achievement of Compacted Unit Weight	233
Appendix E: Explanation of Wald-Wolfowitz Run Test	252
Appendix F: Additional Moisture Content-Unit Weight Relations	256
Appendix G: Equations for Achievement of Compacted Unit Weight	263
Appendix H: Dimensions and Details of Compaction Mold	264
VITA	269

LIST OF TABLES

Table	Page
1. Classification Properties of EPK Airfloated Kaolin	67
2. Comparative Values of Defined Ratios of Interest Between Intra-aggregate and Total Soil Values .	75
3. Reproducibility Check on Photo Measurements . .	91
4. Sample Results of Aggregate Weight Distributions	93
5. Sample Results of Aggregate Dry Unit Weight Determinations	94
6. Particle Orientation by Peak Height Ratio . . .	115
7. Dry Unit Weights of Aggregates	120
8. End Results of Compaction and Saturation	129
9. Results of Wald-Wolfowitz Run Test	147
10. Measured and Calculated Aggregate Characteristics	153
11. Energy Required to Achieve a Given Unit Weight .	174
12. Slopes of the γ_m -w Relationships	176
13. Correlation by Quadratic Equation	180
14. Increase in Dry Unit Weight at Constant Load . .	181
15. Decrease in Dry Unit Weight Upon Release of Load	186
16. Tabulated Results of Swelling Pressure Tests . .	195
17. Elastic Properties of Aggregates	209

LIST OF TABLES, cont.

Table	Page
Appendix Tables	
C1. Particle Orientation by Peak Height Ratios . . .	231
E1. Detailed Results of Wald-Wolfowitz Run Test . .	254
G1. Equations of γ_m - E net Relationship for Samples Compacted at the 1,500 lb. Level	263

LIST OF FIGURES

Figure	Page
1. Net Interaction Energy, V , as a Function of Particle Separation, R	11
2. Kneading Compaction Curves for Edgar Plastic Kaolin	29
3. Impact Compaction Curves for Edgar Plastic Kaolin	30
4. Comparison of Strengths of Silty Clay Samples Prepared by Kneading and Static Compaction . . .	33
5. Swelling Pressure vs. Compaction Pressure . . .	35
6. Effects of Soaking in a Salt Solution	37
7. Swell and Shrinkage for Samples of Sandy Clay Prepared by Kneading and Static Compaction . . .	39
8. Effect of Temporary Restraint on Sample Swell .	43
9. Effect of Load on the Increase in Sample Thickness	44
10. Effect of Stress History on Swell of Compacted Samples of Sandy Clay	45
11. Effect of Salt Concentration on Swelling Behavior	48
12. Idealized Representation of Domains and Formation of Aggregate	58
13. Formation of Apparent Aggregate	60
14. Idealized Representation of Aggregate Compaction	64
15. Patterson-Kelley Blender	69
16. Gross Volume-Weight Relationships	72

LIST OF FIGURES, cont.

Figure	Page
17. Intra-Aggregate Volume-Weight Relationships . .	72
18. Intra-Aggregate Volume-Weight Relationships for an Assemblage of Aggregates	74
19. Total System Volume-Weight Relationships for an Assemblage of Aggregates	74
20. Penetrometers: Disassembled, Assembled with Sample, and Filled with Mercury	76
21. Filling Device	77
22. Representattion of Aggregate-Mercury System with- in Penetrometer at Insufficient Mercury Pressure to Completely Fill Inter-Aggregate and Surface Voids	81
23. Determination of Inter-Aggregate Voids ($V_V - \Sigma V_{VA}$) For a Loose Assemblage of Aggregates	83
24. Sample Enlargement Prints of Aggregates K-1, P4-R6	87
25. Sample Enlargement Print of Aggregates K-3, P6-R8	88
26. Aggregate Diameter Frequency Distribution . . .	90
27. Equipment Used for Sample Compaction	103
28. Compaction Mold and Related Accessories	104
29. Cell, Compactor Foot and Load Cell	105
30. Swelling Pressure Test Cell and Water Reservoir	111
31. Relationships Among Peak Height Ratio, Aggregate Size and Compactive Effort	117
32. Dependence of Peak Height Ratio on Molding Water Content	118
33. Dependence of Peak Height Ratio on Compactive Effort	119
34. Effect of Moisture Content on γ_d vs. Energy (P6-R8 Kaolinite; 1000 lb. Level).	122

LIST OF FIGURES, cont.

Figure	Page
35. Effect of Moisture Content on γ_d vs. Energy (P6-R8 Kaolinite; 1500 lb. Level)	123
36. Effect of Moisture Content on γ_m vs. Energy (P6-R8 Kaolinite; 1000 lb. Level)	124
37. Effect of Moisture Content on γ_m vs. Energy (P6-R8 Kaolinite; 1500 lb. Level)	125
38. Schematic Output from Compaction Test	127
39. Results of Swelling Pressure Tests (K-1 at 1000 Pound Levels)	135
40. Results of Swelling Pressure Tests (K-2 at 1000 Pound Level)	136
41. Results of Swelling Pressure Tests (K-3 at 1000 Pound Level)	137
42. Results of Swelling Pressure Tests (K-1 at 1500 Pound Level)	138
43. Results of Swelling Pressure Tests (K-2 at 1500 Pound Level)	139
44. Results of Swelling Pressure Tests (K-3 at 1500 Pound Level)	140
45. Single Aggregate Load vs. Deformation Results, Batch K-1	142
46. Single Aggregate Load vs. Deformation Results, Batch K-2	143
47. Single Aggregate Load vs. Deformation Results, Batch K-3	144
48. Degree of Saturation - Water Content Relation for Aggregates	155
49. Impact Compaction Curves for Grundite	161
50. Conventional and Equal Net Input Energy Moisture- Total Unit Weight Relations (P4-R6; 1000 lb Level)	162

LIST OF FIGURES, cont.

Figure	Page
51. Conventional and Equal Net Input Energy Moisture- Total Unit Weight Relations (P6-R8; 1000 lb Level)	163
52. Conventional and Equal Net Input Energy Moisture- Total Unit Weight Relations (P8-R10; 1000 lb Level)	164
53. Conventional and Equal Net Input Energy Moisture- Total Unit Weight Relations (P10-R12; 1000 lb Level)	165
54. Conventional and Equal Net Input Energy Moisture- Total Unit Weight Relations (P12-R20; 1000 lb Level)	166
55. Conventional and Equal Net Input Energy Moisture- Total Unit Weight Relations (P20-R40; 1000 lb Level)	167
56. Conventional and Equal Net Input Energy Moisture- Total Unit Weight Relations (P6-R8; 1500 lb Level)	168
57. Conventional and Equal Net Input Energy Moisture- Total Unit Weight Relations (P8-R10; 1500 lb Level)	169
58. Conventional and Equal Net Input Energy Moisture- Total Unit Weight Relations (P10-R12; 1500 lb Level)	170
59. Conventional and Equal Net Input Energy Moisture- Total Unit Weight Relations (P12-R20; 1500 lb Level)	171
60. Conventional and Equal Net Input Energy Moisture- Total Unit Weight Relations (P20-R40; 1500 lb Level)	172
61. Samples Compacted of K-2, P6-R8 Aggregates . . .	184
62. Samples Compacted of K-1, P12-R20 Aggregates . .	185
63. Idealized Representation of the Effects of Swelling on the Aggregate Skeleton	191

LIST OF FIGURES, cont.

Figure	Page
64. Idealized Results of a Swelling Pressure Test .	193
65. Stress vs Deformation Relationships for Samples of Silty Clay Prepared Dry and Wet of Optimum by Kneading and Static Compaction . .	200
66. Compacted Samples of K-1, P6-R8 Aggregates . . .	201
67. Swelling-Time Curves, Kneading and Static Compaction, Soil B2	203
68. Swelling-Time Curves, Undisturbed and Compacted States, Soil B1	203
69. Skeletal Strength as a Function of Effort and Moisture Content	206
Appendix Figures	
A1. Aggregate Size Distribution Curve for Batch K-1	224
A2. Aggregate Size Distribution Curve for Batch K-2	225
A3. Aggregate Size Distribution Curve for Batch K-3	226
A4. Aggregate Size Distribution Curve for Batch K-4	227
A5. Aggregate Size Distribution Curves for Batches K-1 through K-4	228
D1. Effect of Moisture Content on γ_d vs. Energy (P4-R6 Kaolinite; 1000 lb Level)	234
D2. Effect of Moisture Content on γ_d vs. Energy (P8-R10 Kaolinite; 1000 lb Level)	235
D3. Effect of Moisture Content on γ_d vs. Energy (P10-R12 Kaolinite; 1000 lb Level)	236
D4. Effect of Moisture Content on γ_d vs. Energy (P12-R20 Kaolinite; 1000 lb Level)	237
D5. Effect of Moisture Content on γ_d vs. Energy (P20-R40 Kaolinite; 1000 lb Level)	238

LIST OF FIGURES, cont.

Figure	Page
D6. Effect of Moisture Content on γ_d vs. Energy (P8-R10 Kaolinite; 1500 lb Level)	239
D7. Effect of Moisture Content on γ_d vs Energy (P10-R12 Kaolinite; 1500 lb Level)	240
D8. Effect of Moisture Content on γ_d vs Energy (P12-R20 Kaolinite; 1500 lb Level)	241
D9. Effect of Moisture Content on γ_d vs Energy (P20-R40 Kaolinite; 1500 lb Level)	242
D10. Effect of Moisture Content on γ_m vs Energy (P4-R6 Kaolinite;; 1000 lb Level)	243
D11. Effect of Moisture Content on γ_m vs Energy (P8-K10 Kaolinite; 1000 lb Level)	244
D12. Effect of Moisture Content on γ_m vs Energy (P10-R12 Kaolinite; 1000 lb Level)	245
D13. Effect of Moisture Content on γ_m vs Energy (P12-R20 Kaolinite; 1000 lb Level)	246
D14. Effect of Moisture Content on γ_m vs Energy (P20-R40 Kaolinite; 1000 lb Level)	247
D15. Effect of Moisture Content on γ_m vs Energy (P8-R10 Kaolinite; 1500 lb Level)	248
D16. Effect of Moisture Content on γ_m vs Energy (P10-R12 Kaolinite; 1500 lb Level)	249
D17. Effect of Moisture Content on γ_m vs Energy (P12-R20 Kaolinite; 1500 lb Level)	250
D18. Effect of Moisture Content on γ_m vs Energy (P20-R40 Kaolinite; 1500 lb Level)	251
F1. Conventional and Equal Net Input Moisture- Unit Weight Relations (P4-R6; 1000 lb Level) . .	257
F2. Conventional and Equal Net Input Moisture- Unit Weight Relations (P6-R8; 1000 lb Level) . .	258

LIST OF FIGURES, cont.

Figure	Page
F3. Conventional and Equal Net Input Moisture- Unit Weight Relations (P8-R10; 1000 lb Level) .	259
F4. Conventional and Equal Net Input Moisture- Unit Weight Relations (P10-R12; 1000 lb Level) .	260
F5. Conventional and Equal Net Input Moisture- Unit Weight Relations (P12-R20; 1000 lb Level) .	261
F6. Conventional and Equal Net Input Moisture- Unit Weight Relations (P20-R40; 1000 lb Level) .	262
H1. Plan and Side View of Compaction Mold	264
H2. Plan and Side View of Lucite Base	265
H3. Plan and Side View of Sample Confining Ring . .	266
H4. View of Section through Sample Confining Ring .	267
H5. Plan and Side View of Lucite Top Cap	268

LIST OF SYMBOLS

A	a constant
\AA	angstrom
B	Skempton's pore pressure parameter
B_a	pore air pressure parameter
B_w	pore water pressure parameter
C_1	a parameter
C_2	a parameter
$C.V.$	coefficient of variation
D	diameter of a circular pore
E	net energy; modulus of elasticity
F	force
G_s	specific gravity of solids
KV	kilovolts
P	load
R	radius of soil aggregates
S_r	degree of saturation
V	volume; volts
V_A	volume of an aggregate
V_a	volume of air
V_{aA}	volume of intra-aggregate air
V_{sA}	volume of solids for an aggregate

LIST OF SYMBOLS, cont.

V_{vA}	volume of intra-aggregate voids
V_v	volume of voids
V_w	volume of water
V_{wA}	volume of intra-aggregate water
W	weight
W_A	weight of aggregate
W_s	weight of solids
W_{sA}	weight of intra-aggregate solids
W_w	weight of water
W_{wA}	weight of intra-aggregate water
\bar{X}	arithmetic mean
Z	valence of ion; valence of electron
Z_1	valence of cation
Z_2	valence of anion
a	air
b	an empirical constant
dV/V	volumetric strain
e	void ratio
e_1	charge on electron
e_2	charge of proton
h	Planck's constant
$h\nu$	ionization energy of a molecule
n	an empirical constant; concentration of electrolyte
omc	optimum moisture content

LIST OF SYMBOLS, cont.

p	swelling pressure, pressure difference
pcf	pounds per cubic foot
psi	pounds per square inch
q_0	maximum normal stress
r	distance between cation and anion; distance between plates
rpm	revolutions per minute
s	solids
u_a	pore air pressure
u_w	pore water pressure
v_a	volume of air
w	water; moisture content
z	valence of cation
χ	Bishop's empirical factor, between 0 and 1
ψ_d	potential
α	polarizability of a molecule; linear compression
γ	surface tension
γ_d	dry unit weight
γ_m	total unit weight
γ_w	unit weight of water
ϵ'	dielectric constant
θ	contact angle; angle of orientation

LIST OF SYMBOLS, cont.

μ	dipole moment
π	pi, 3.14159+
σ	total normal stress; standard deviation

ABSTRACT

Hodek, Ralph Jerome. Ph.D., Purdue University, December 1972.
Mechanism for the Compaction and Response of Kaolinite.
Major Professor: C. W. Lovell, Jr.

Prediction of the characteristics and properties of compacted fine-grained soils is much aided by a physical soil mechanism or model. This model should fit as nearly as possible the observed soil conditions during and after compaction. This thesis reports an extension to existing soil compaction models, and applies it to explain the behavior of kaolinite compacted in the laboratory by static pressures under conditions of no lateral strain.

The experimental investigation included an examination, with appropriate strength and particle orientation determinations, of kaolinite aggregations at the compaction moisture content but prior to compaction. This was followed by experimental determination of the net energy input vs. compacted unit weight relations during compaction. In addition, the final unit weights, the response at constant compactive load, and the rebound after removal of the compactive effort, as well as particle orientation, were experimentally determined for the compacted samples.

Prior to compaction, the soil was separated into aggregate-sized fractions by sieving, and each compacted

sample was prepared using soil aggregates of one general size. The independent variables investigated were compactive effort, compaction moisture content, and soil aggregate size.

To further validate the model of compacted clay, constant volume swelling pressure determinations were made on selected compacted samples. The swelling pressures were monitored continuously after giving the samples access to water and the results are presented as swelling pressure vs. time relations.

The experimental findings confirmed the appropriateness of a deformable aggregate soil model to explain the achievement of compaction for kaolinite as prepared in the laboratory and then compacted statically. It was further confirmed that the soil aggregate characteristics, in particular deformability and size, influence both the compacted unit weight achieved and some of the engineering properties, notably swelling pressure. It was also established that the relations between net input energy and compacted unit weight are simple ones which are amenable to quantification in the case of static compaction under confined conditions.

It was concluded that the expanded soil particle-soil aggregate model proposed in this thesis explains a broader spectrum of observed phenomena than was previously possible, and use of the new model was recommended for future studies.

INTRODUCTION

During the author's studies at Purdue University he gradually took exception to the completeness of the existing explanations for the compaction of fine-grained soils. This led to the development of a somewhat different model and mechanism and finally in 1967 to a research proposal to the Indiana State Highway Commission through Purdue's Joint Highway Research Project. The proposal was subsequently funded, and the experimental program was completed in September, 1969.

The immediate objectives of this research are to determine a model and a mechanism which will adequately explain the achievement of compacted unit weight for kaolinite statically compacted in the laboratory. The explanation must be complete enough to explain the soil's condition before compaction, the interactions within the soil mass during compaction, and the observed behavior of the compacted soil.

The model hypothesized for this study is one in which the soil is made up of macroscopic aggregations of clay particles. During compaction, it is the interactions of these aggregates, their deformation characteristics, and

their ability to fit together in a compact mass which determine the end result unit weight for a given type of compaction and amount of effort. It is this same compacted macrostructure, an assemblage of aggregates, which determines to some extent the engineering behavior of the compacted soil.

As previously stated, this investigation was limited to one soil, kaolinite, statically compacted in the laboratory. The experimental approach was to study certain of the properties of the soil aggregates before compaction, to monitor the achievement of compaction, and to subject the compacted samples to a test significant to engineering practice. The achievement of compaction was examined by computing the energy required to densify the soil continuously from a low unit weight to the final unit weight achieved for each sample. The correctness of the model was determined by analysis of existing results, especially stress-strain and volumetric swelling, and from the results of constant volume swelling pressure determinations on the compacted samples.

In subsequent sections of this thesis will be found a review of the pertinent literature, a detailed description of the experimental program, the results of the experimental investigation, and the interpretation leading to a conclusion concerning the correctness of the author's hypothesis.

REVIEW OF LITERATURE

The systematic study of soil compaction, and the inter-related factors which are involved, was first reported by Proctor (46, 47, 48, 49)¹ in 1933 in a series of articles outlining a rational procedure for the selection of a desirable soil density and compaction water content, and a practical procedure for checking the compacted densities in the field. His ideas are still very much with us today in the form of the various standard compaction tests (59) and the penetration resistance needle.

The colloidal nature of clay particles and their arrangement within the soil mass has also been considered in some detail. Early explanations by Terzaghi (60) and Casagrande (10) concerning the particulate arrangement, or microstructure, of sedimentary clay deposits have helped to explain the seeming anomalies of the consolidation characteristics of these deposits under various conditions.

More recently single and double level microstructures, or fabrics, were used by Lambe (27, 28), Terzaghi (61), and others (54, 55) to explain the compaction process for fine-grained soils, as well as the post-compactive response of these materials.

1. Items in parentheses refer to alphabetically listed entries in the List of References, page 218.

The literature pertaining to these, and other related topics, will now be critically reviewed to form the framework of knowledge upon which this thesis rests.

Electrical Forces Among the Particles

As opposed to the usual body and boundary forces which predominately influence most engineering activities, the colloidal nature of clay particles (the kaolin used in this investigation has an approximate surface area of $18 \text{ m}^2/\text{gm.}$) makes the surface and distance-related electrically generated forces much more important. The following forces are among those which cause colloidal particles to be attracted to, or repelled by, each other.

Ionic Bonding

Although the ionic bond is thought of as a primary valence bond, the attractive force is entirely electrostatic, and therefore oppositely charged parts of two different particles will be held together in this manner. The expression for the ionic bonding force between a cation and an anion is:

$$F = - \frac{z_1 z_2 e_1^2}{\epsilon' r^2}$$

where: z_1 and z_2 are the valences of the cation and anion
 e_1 is the charge on an electron
 r is the distance separating the cation and anion

ϵ' is the dielectric constant of the separating medium

By convention, the negative sign (-) indicates attraction.

Hydrogen Bonding

Hydrogen bonding occurs as a result of two strongly electronegative oxygen atoms competing for the single electron of hydrogen. The unit layers of kaolinite, stacked one on top of the other, are bound together by hydrogen bonds between the oxygen and hydroxyl planes in adjacent units (12).

It has been suggested (26) that kaolin particles may also be bonded together in this manner when the silica tetrahedral sheet of one particle comes into contact with the alumina octahedral sheet of another particle.

Van der Waals' Bonding

Van der Waals' forces include those which result from interactions involving dipoles or temporary (induced) dipoles, as well as the London dispersion forces which come about by the nonsymmetric nature of the electron cloud on even the nonpolar molecules. These forces, as a group, are attractive between soil particles, and increase in strength as the particles approach one another. Each category of force is discussed below.

Orientation or Dipole-Dipole Interactions. Considering the model of two parallel permanent dipoles, the interacting force may be repulsive (+) or attractive (-), depending on the relative positions of the opposing poles. The expression for this force is:

$$F = \pm \frac{\mu_a \mu_b}{\epsilon' r^4}$$

where: μ_a and μ_b are the respective dipole moments as defined by the product of the charge and the distance between opposite charges.

For the case of two dipoles free to seek any possible rotation, there is a net attractive force shown by Keesom to be:

$$F \text{ average} = - \frac{2}{3} \frac{\mu_a^2 \mu_b^2}{r^7} \frac{1}{kT}$$

where: k is the Boltzmann constant, 1.38×10^{-16} ergs/degree
 T is the absolute temperature.

Induction Effects. Most molecules, even though they may not be permanent dipoles, under the effect of an electric field such as exists near an adjacent ion or permanent dipole become temporary dipoles as their centers of positive and negative charge move apart. The extent to which a molecule may become a temporary dipole is termed its polarizability. For the case of ion-induced dipole interaction, the expression is given by:

$$F = - \frac{1}{2} \frac{\alpha z^2 e^2}{\epsilon' r^5}$$

where: α is the polarizability of the molecule

z is the valence of the ion.

In the event that the field is being caused by a permanent dipole, the expression becomes, for the gaseous state:

$$F = - \frac{(\alpha_1 \mu_2^2 + \alpha_2 \mu_1^2)}{r^7}$$

where: μ is the dipole moment

Ion-Dipole Interaction. For the system involving an ion and a permanent dipole, the force generated is given by:

$$F = - \frac{z e \mu \cos \theta}{\epsilon' r^3}$$

where: z is the valence of the electron

θ is the angle of orientation of the dipole in the electrical field.

London Dispersion Forces. The electron cloud of a non-polar molecule at any time may not be spherical, and it may therefore affect another molecule so that a dipole-induced dipole type force acts between them. The expression for a pair of interacting non-polar molecules is:

$$F = - \frac{3}{2} \frac{h}{r^7} \left(\frac{V_1 V_2}{V_1 + V_2} \right) \alpha_1 \alpha_2$$

where: h is Planck's constant

V_1 and V_2 are the frequencies of vibration of the molecules.

This force is always attractive, and the net force when more than one pair is considered is vectorially additive.

Force of Repulsion

In addition to the above forces which are, on the whole, attractive in action, a definite repulsive force is present due to the reaction between their electron clouds when two atoms move closely together. Commonly an empirical relationship is used as an expression of this repulsive tendency. It is:

$$F = + \frac{b}{r^{n+1}}$$

where b and n have been adjusted to fit experimental results.

Hamaker Equation

Using a model consisting of two parallel plates, Hamaker describes the force between the plates as:

$$F = \frac{A}{b \pi r^3}$$

where: A is a constant taking into account the London-Van der Waals' forces

r is the distance between the plates.

Experiments carried out by Norrish (37) failed to confirm this equation for Na^+ montmorillonite plates, using

the value of 10^{-12} for A. In his work Norrish considered that at the equilibrium positions, the Van der Waals' attractive forces were balanced by double-layer repulsion, and at all interparticle spacings investigated the calculated repulsive force was far greater than the calculated attractive force.

Gouy-Chapman Double-Layer Concept

Gouy and Chapman, in 1910 and 1913 respectively, independently developed mathematical expressions describing the ion distribution and electric potential, as a function of distance from the plate, for the model of a charged plate in contact with an electrolytic solution. The so-called double layer consists of the charged plate as one layer, and a diffuse layer within the solution as the other.

As can be visualized, the ions in solution which have a charge opposite to that of the plate, are attracted to it, while the ions with the same charge as the plate are repelled by it. The concentration of counter ions decreases with increasing distance from the plate, and at some distance the solution can be considered "bulk."

Since each colloidal particle in a solution carries its own double layer, an interaction can be expected when two of the particles are brought together so that their double layers overlap. This interaction causes the ion distributions in the overlapping double layers to change,

i.e., work is being done on the system, and the result is a repulsion between the particles. A comprehensive discussion of double-layer theory is given by Overbeek (41).

Experimental verification of the double-layer theory has been attempted by Bolt (8). For a Na-montmorillonite subjected to one-dimensional compression and rebound where the void ratio varied between 25 and 3, the experimental data and the theoretical prediction based on double-layer theory showed good agreement. However, a Na-illite subjected to the same procedure, with the void ratio varying between 8 and 1, showed considerably less agreement with its theoretical prediction. In a discussion of Bolt's paper, Terzaghi (61) described natural clay soils as being "composed of inert soil particles and of clusters of clay-mineral particles forming minute osmotic cells." He went on to explain that this "cluster concept" reconciles many of the discrepancies between osmotic theory predictions and the known behavior of clays.

For the simplified case of two particles, Van Olphen (64) has shown the repulsive and attractive energies due to double-layer repulsion and Van der Waals' attraction, as well as the net effect of both of them, as a function of the spacing between the particles. His figure is reproduced as Figure 1 for three different electrolyte concentrations. The net interaction energy is shown as a dashed line, and the dashed line near zero particle spacing is the Born effect caused by the intimate contact of the crystal lattices of the two particles.

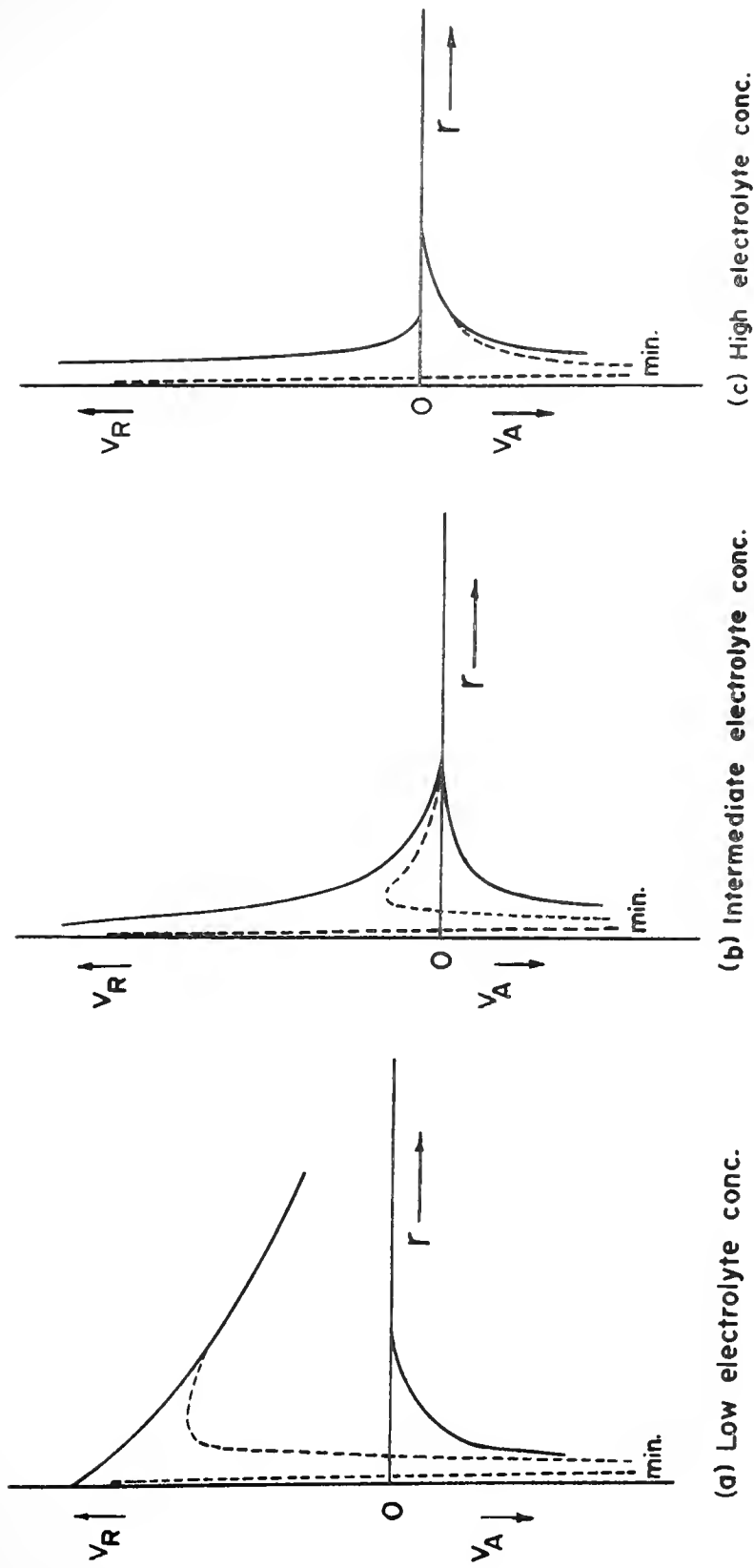


FIGURE 1 . NET INTERACTION ENERGY, V , AS A FUNCTION OF PARTICLE SEPARATION, r ; AFTER VAN OLPHEN (64)

Summary of Forces Among Particles

Consideration of the above mentioned sources of attractive and repulsive forces and their simplifying assumptions, among them the semi-infinite plate with its uniformly distributed charge, the free movement assumed, parallel plates, the dilute system, and the problem of vectorially summing the many effects, do not readily allow for the quantification of bond strength for the common, relatively low water content, soil-water systems encountered in this study.

Structure and Properties of Kaolinite

Included in this section are a discussion of the structural makeup of kaolinite, cation exchange sites, and other general properties. Unless otherwise referenced, the source of this material is Grim (12).

Structural Makeup

Most clay minerals, including kaolinite, are composed of two similar building blocks arranged differently and in different proportions. The two blocks are the octahedral unit repeating itself as a sheet, and the silica tetrahedral unit also repeating itself as a sheet in two dimensions.

The silica unit is comprised of four oxygen atoms arranged as the corners of a tetrahedron, with a silicon atom within the tetrahedron equidistant from the corners. This unit repeats itself, with all of the unit bases in the same plane, as an open hexagonal network with all of the tetrahedron tips pointing in the same direction.

The octahedral unit consists of six oxygen and/or hydroxyls in octahedral coordination with a centrally located aluminum, magnesium, or iron cation. This unit also repeats itself to form a sheet in two dimensions parallel to the plane formed by three of the octahedral oxygens or hydroxyls.

For the case of kaolinite, aluminum is the cation present within the octahedral sheet, and only two-thirds of the possible sites are filled. The kaolinite unit consists of one silica sheet and one alumina octahedral sheet combined, with the tetrahedral tips and the base layer of the octahedral sheet forming a common layer. The charges within this ideal structural unit are balanced, and the formula is $(\text{OH})_8\text{Si}_4\text{Al}_4\text{O}_{10}$. Although many clays show varying degrees of substitution within the lattice (for example Mg^{++} replacing Al^{+3}), kaolinite shows only a negligible amount of substitution, leading to a very small net negative charge, on the average.

This, then, is the repeating unit. Kaolinite is made up of many of these units stacked one on top of the other and held together by hydrogen bonds acting over very small separations of oxygen and hydroxyl planes in adjacent units. The strong bond between units is conducive to the building up of relatively thick particles. Typical particle dimensions for kaolinite are a diameter of 0.3 to 3 microns and a thickness of $1/3$ to $1/10$ of the diameter (29).

Ion Exchange Properties

Ion exchange is the ability of an ion within a solution to exchange positions with another ion originally sorbed to the surface of the clay particle or as a part of the lattice structure. The exchange itself is of little importance to this discussion. The importance is the presence of the sorbed ions in that they will, as the moisture content of the soil mass increases, dissociate themselves from the surface and become part of the diffuse double layer.

There are three causes for exchangeable ions to be available on clay particles. They are: unsatisfied charges around the edges of the particles due to broken bonds, substitutions within the lattice structure giving rise to charge deficiency, and the replacement of the hydrogen of exposed sheet hydroxyls by an exchangeable cation. Of these three, only broken bonds and replaced hydrogens of the hydroxyls are applicable to kaolinite, since a negligible amounts of lattice substitution occurs. This is borne out by the low cation-exchange capacity of kaolinite when compared with the other common clay minerals.

Experimental work by Thiessen (62) as interpreted by Van Olphen (64) indicates the existence of a positive edge charge on large kaolinite particles. The experiment consisted of mixing a kaolinite sol together with a negative gold sol and making electron micrographs of the result.

The micrographs showed the negatively charged gold particles attached almost exclusively to the edges of the much larger kaolinite particles.

For kaolinite, Schofield and Samson (53) found that under acid conditions and extending into the basic range for varying amounts (depending on the particular kaolinite), the particle edges are indeed positively charged as indicated by their adsorption of chloride anions.

Flocculation

Of utmost importance to subsequent behavior of the clay particles as a group is their initial state or arrangement among themselves. In general, we use the terms "flocculated" and "dispersed" as descriptors of the particulate arrangement within the mass. A dispersed structure is one in which the particles are not in intimate contact, being held apart in more or less parallel alignment by repulsive forces. In this orientation the mass properties are quite easily influenced by boundary loadings, change in ion concentration of the interparticle liquid, temperature, etc. (29). A flocculated structure is one in which the particles are in contact, so to speak. These "contacts" may be edge-to-face, face-to-face, or most likely a combination of the two.

Schofield and Samson (53) also detected two types of flocculated structures: an edge-to-face flocculation in a salt-free suspension caused by electrostatic attraction between the oppositely charged double layers, and a face-to-face flocculation when the double layers were depressed in a high-salt suspension.

Van Olphen (64) has identified the changes in flocculation for a dilute suspension of Na-montmorillonite with increasing salt concentration, with the aid of apparent viscosity measurements. To summarize Van Olphen's findings: for the electrolyte-free system, both double layers of each particle are well developed and thus are far enough apart that Van der Waals attraction is unimportant. Edge-to-face flocculation occurs due to attraction of the oppositely-charged double layers. As a small amount of NaCl is added, the double layers shrink. Repulsion dominates as the edge-to-face bonds break. A further increase in salt concentration further depresses the double layer, and edge-to-face contacts, with Van der Waals being dominant, occur. Finally, at very high salt concentrations, face-to-face flocculation occurs.

Present Theories of Compaction

Up to the present time, two reasonably quantitative explanations of the compaction process have appeared in the

soil mechanics literature. Lambe's theory (27) utilizes a clay microstructure approach, while Olson's (38) builds on a framework of partially-saturated effective stress concepts.

Lambe's Theory of Compaction

After presenting an explanation of soil microstructure (26), Lambe (27) used it to explain the characteristic shape of the molding water content vs. compacted dry unit weight plot as obtained by conventional laboratory methods. Lambe considered that water deficiency, the difference between the water necessary to fully develop the double layer of a given soil particle at a given stress state and the available water, is of fundamental importance.

Using the common terminology, his explanation holds that on the dry side of the compaction curve, the small amount of water present gives a very high electrolyte concentration which depresses the double layers, thus reducing the interparticle repulsion and causing a tendency toward flocculation of the colloids. Lambe has interpreted this as meaning a low degree of particle orientation and low density.

Near the optimum moisture content, the double layers have been expanded somewhat and the electrolyte concentration decreased, resulting in a less flocculated, more orderly structure, and a higher density. At this point,

the term "lubrication" is introduced as a descriptor for the increased interparticle repulsion which allows the particles to slide into the denser and more oriented state.

An increase in moisture content to a position wet of optimum, according to Lambe, further expands the double layer and further reduces the net attractive forces between particles. The soil is more oriented at this point, but the dry unit weight has decreased due to the large volume of water present, which now "interferes" with close packing.

In his explanation, Lambe considers a one-order system, that is, particulate microstructure. The initial state of the soil, other than its moisture content, is not considered. It seems that the change in microstructure, which is adequately proven experimentally (42), is due, in the main part, to the double-layer volume changes caused by water content changes. However in the closure to his paper related to the engineering properties of compacted clay, Lambe (28) explains the difference in the magnitudes of the vertical and horizontal permeabilities by invoking a second order of microstructure. In his words, "This fact...indicates that a high degree of particle alinement can occur in zones, with different alinements between zones, that is, random oriented packets of parallel particles."

Olson's Theory of Compaction

In a more recent paper, Olson (38) explained the achievement of increased dry density for some average clay soil subjected to laboratory kneading compaction, in terms of changes

in effective stress. His explanation is two-fold; he has developed a qualitative theoretical explanation for material up to its optimum moisture content, and a much briefer, and somewhat different, mechanism at water contents above the compaction optimum.

At a low moisture content, and with the soil in a loose condition prior to the start of compaction, the effective stresses in the soil are quite low due to the low confining pressure, low B -coefficients, and a low χ -coefficient. (χ is Bishop's empirical factor (5), varying from 1 for saturated soil to 0 for dry soil, and B is Skempton's empirical pore pressure parameter (57), later modified by Bishop (6) as B_w and B_a for the water and air phases, respectively, in a partly saturated soil.) For the first applications of the compactor, the soil is poorly confined and considerable deformation may occur before sufficient lateral resistance is developed. The horizontal shear resistance at some point provides the necessary confinement, and the effective stresses increase sufficiently to resist the applied stress. This process reoccurs with each additional compactor application, except that the increasing lateral confinement allows a smaller change in dry unit weight for each successive application. Finally, only transient elastic deformations occur with compactor applications.

For a higher moisture content, still below the optimum, the mechanism is similar except that B_w and χ have larger values, and the positive pore-water pressures induced by the application of the load allows the particles to slide

past one another more easily, into a denser state. As the number of applications increases, the residual effective stresses increase, the A factor decreases due to decreased deformation, and finally no further increase in unit weight can be achieved.

At the optimum moisture content, the air voids have become effectively discontinuous for transient loadings (16, 38). Since compaction is a process of removing air, the unit weight sensibly peaks. Therefore, a further increase in moisture above the optimum results in a lower dry unit weight, since air cannot be expelled and air which might have been expelled has been replaced by water.

In answer to the question of how the soil develops sufficient strength to carry compactor loads when above the optimum moisture content, Olson points out that the soil should be acting much as a saturated over-consolidated sediment, i.e., specifically at the larger strains, the pore pressure will decrease and so will the A factor. The increasing strength finally stops further penetration. Another possible explanation, according to Olson, is with the compactor contact area acting as a foundation footing, the bearing capacity increases with increasing penetration until an equilibrium is reached.

Olson offered no experimental verification for his theory. His physical soil model is rather vague, although he seems to be considering clay particles with a rather

high degree of autonomy with respect to fabric condition and alterations.

In a discussion of Olson's paper, McRae and Turnbull (34) advance a mechanism for density increase involving the rearrangement of colloidal particles into a denser packing, with the maximum density being limited by the saturated condition. According to McRae and Turnbull, "increasing the water content on the dry side of the curve 'lubricates' the particles and thus causes more movement of the particles with respect to each other; this movement increases the number of soil grains that are brought to a more intimate spacing, and the interparticle forces of attraction tend to maintain the more intimate spacing."

Hogentogler's Theory

Shortly after the appearance of Proctor's (46) compaction study, Hogentogler (17) presented his thoughts on the compaction of fine-grained soils. His explanation was that moisture increases up to the optimum moisture content cause lubrication of the particles, thus allowing them to slip into closer association with one another. Above the optimum moisture content, the soil mass "swells", and lower and lower unit weights are achieved.

It is interesting to note that Hogentogler used rather small (0.0025 mm. diameter is mentioned) particles as his interacting units, and that he differentiated between

solidified water, cohesive water, and capillary water, as related to moisture content and dry unit weight achieved after compaction.

Role of Individual Clay Particles

All of these hypotheses state or imply that individual clay particles or small collections of these plates in parallel array are the units which exert the pre-dominant influence on the compaction characteristics of the mass. It is this author's contention that much larger units, each being made up of many clay particles, have a more important effect on the compaction and post-compaction characteristics of the mass than has been previously realized.

It has been stated previously that at very high salt concentrations face-to-face flocculation occurs. It is not necessary to picture this situation as a few grams of clay in a liter of high-normality salt solution. A high salt concentration is also present when there is a deficiency of water to fully develop the double layers or even to hydrate the cations present on the particles' surfaces.

Quirk (51) put forth the model of "... the soil as a porous medium and in between the pores we have a clay matrix in which the clay particles or crystals are

oriented on a microscale." He considered each group of oriented clay particles (face-to-face flocculation) to be a domain. Quirk (52) also offered the opinion, without conclusive evidence, that for the same clay at the same moisture content differences in engineering behavior could be explained by having different proportions of intra-domain water and interdomain water.

In a discussion of a paper by Seed and Chan, McRae (33) showed results, in the form of photos, indicating the visible structural differences among as-compacted dry-side, as-compacted wet-side, soaked dry-side, and soaked wet-side samples of a silty clay prepared by kneading compaction. In his words,

"The exposed faces of these chunks of soil were obtained by breaking the soil open, as cutting would not demonstrate the texture of the exposed soil. ... It is evident from visual observation that there are marked differences between the soil chunks representing the dry side and the soil chunks representing the wet side. Note that on the dry side of optimum ... there is a somewhat smoother texture and as appearance of disintegration on an individual grain basis. This seems to be in harmony with Lambe's flocculated arrangement concept.

On the wet side, however, there is a definite layered or laminated texture. This laminated texture is more evident to the naked eye than these photographs of the unsoaked specimens would indicate. However, it is quite evident in the soaked chunks where the thin flakes and layers are readily seen from the disintegration in the soaking process. Lambe's dispersed wet-side concept may be essentially correct for the structure within the laminations or layers, but some further explanation appears needed to describe the over-all structure."

Although he advanced no extension or modification to the existing explanation of compaction, McRae did recognize that the soil system involved is more complex than the simple particle-particle picture presented.

Mechanical Properties of Compacted Soil

After laboratory compaction, the soil specimens are often subjected to a variety of mechanical tests to determine their response to conditions and loads which hopefully simulate field situations. In addition, micro-structure differences have been inferred from the responses of samples compacted by different methods, at different energy levels, and at different compaction water contents.

Three main types of laboratory compaction are generally employed; static compaction, impact compaction, and kneading compaction. The usual soil properties measured are the as-compacted unconfined strength (U), isotropically consolidated undrained strength (CIU), as-compacted and soaked CBR's, unconfined or axially unconfined swell, and swelling pressure for the condition of zero volume change.

Types of Laboratory Compaction

The most widely used compaction test for field control is the impact type. It has been standardized, and appears in the literature as ASTM D698-66T and D1557-66T (7). Briefly for D-698-66T, the procedure is to compact the soil in three layers in a 4-inch i.d., 1/30 ft.³ mold

with 25 blows/layer of a 5.5 lb. rammer of 2 inches diameter, falling 12 inches. The energy exerted is 148,500 inch lbs. per ft.³ of soil. The D1557-66T method differs in that the soil is compacted in five layers by a 10 lb. rammer falling 18 inches, with 25 blows/layer. The energy exerted by this method is 675,000 inch lbs. per ft.³ of soil, or about 4.5 times the energy exerted in D-698-66T. Both of these tests employ the aid of a collar above the mold. At the end of compaction, the collar is removed and the soil above the mold trimmed away. The amount of compacted soil which must be trimmed away is a function of the operator's skill and care. However, part of the compaction energy was "wasted" on this material.

It should also be mentioned that not all of the applied energy is used to densify the soil. Since the rammerhead is smaller than the inside diameter of the mold, an indeterminate amount of the energy is used to shove the unconfined portion of the soil horizontally and vertically upward. In all probability, some portions of the sample are actually loosened by the action of the rammer. As the density increases, the confined soil acts more and more elastically in its response to the rammer, and much of the applied energy is lost as the sample rebounds almost instantaneously. To illustrate the effect of a particular combination of soil surface area to tamper area, the

impact compaction results of Proctor (50) and Holtz and Lowitz (19) are cited.

Proctor compacted a clayey soil (liquid limit = 45 and plasticity index = 15) in two different size molds, 1/30 ft.³ and 1/20 ft.³, and applied the same compactive energy per cubic foot to each size. A 5-1/2 lb. tamper with a foot area of 3.14 in.² was used, and the drop height was varied to achieve the same input energy for both tests. The results using the 1/30 ft.³ mold with a ratio of $\frac{\text{tamper area}}{\text{mold area}} = 24.9\%$ gave a maximum dry unit weight of 98.0 pcf at 21% optimum moisture content. Using the 1/20 ft.³ mold with a ratio of $\frac{\text{tamper area}}{\text{mold area}} = 22.1\%$, the result was a maximum dry unit weight of 92.5 pcf at 25% optimum moisture content.

Holtz and Lowitz ran a similar type experiment on three different soils. They used a 1/20 ft.³ mold with a 5.5 lb., 3.14 in.² rammer, and a 1.5 ft.³ mold with a 187.5 lb., 70.9 in.² mechanical tamper. The ratios of $\frac{\text{tamper area}}{\text{mold area}}$ for these two sets of equipment were 21.8% and 24.4% respectively. Their results are shown below.

Soil -No. 4 Size	1/20 Ft. ³ Mold		1.5 Ft. ³ Mold	
	Max. Dry Unit Wt. pcf	omc, %	Max. Dry Unit Wt. pcf	omc, %
Sandy	116.1	10.1	117.5	9.4
Silty	120.0	11.7	120.0	11.7
Clayey	105.9	18.5	108.5	16.8

The results of both of these investigations demonstrate that as the percentage of the surface area covered by the compactor increases, for a constant input energy, the resulting unit weight increases and the omc decreases. More of the energy is thus used to increase unit weight and less is wasted in unnecessary soil displacements. It should be pointed out though that Proctor's experiment contained another variable, the height of hammer fall. This gave a variable impact velocity and may account for the large unit weight difference compared to the Holtz and Lowitz results which were obtained with a constant height of hammer fall.

When comparing the moisture-unit weight curves for a soil subjected to different energy levels of a given compaction type, only qualitative decisions can be reached concerning an energy-unit weight relationship based on the gross applied energy.

Two somewhat different methods are commonly used to achieve a unit weight increase by kneading action. They are the Harvard miniature compactor, and a larger, mechanical device operated in accordance with AASHTO Method T173 (59).

The suggested method of use for the Harvard miniature apparatus is described by ASTM (45). The apparatus consists of a 1/454 ft.³, 1-5/16 inch i.d. mold with collar, and a spring-loaded, 0.5 inch diameter, cylindrical tamper. The spring-loaded tamper is adjustable so that the spring starts to compress at some preset force on the tamper base. It is suggested that the soil be tamped in five layers, using

twenty-five 40 lb. tamps per layer. However, the suggested method has no official status, and there is a wide range of loads and number of tamps employed by various investigators.

A mechanical kneading-type compaction procedure has been standardized as AASHTO T173-60 (59). The primary purpose of this particular specification is to outline the method of preparation of samples for stabilometer and expansive pressure testing. The mechanical device, developed by the California Division of Highways, forms a compacted sample 4 inches in diameter and 2.5 inches high. Compaction involves 120 tamps from a circular segment foot of approximately 2.8 in.², using a 350 psi foot pressure. The kneading action is limited by the requirement that the foot pressure may be lowered so that the foot penetrates no more than 1/4 inch into the surface, after the first twenty tamps.

The comments concerning gross applied energy, discussed with respect to impact compaction, also apply to kneading-type compaction.

The effect of increasing the energy for a given type of compaction is shown in Figure 2 for Harvard miniature kneading compaction and in Figure 3 for impact compaction using a non-standard mold and rammer. These compaction curves, generated by Perloff (44), are for the same soil as was used in this study.

Static compaction has not been employed in any large degree for the development of moisture-unit weight relationships per se, and no widely accepted standard method exists

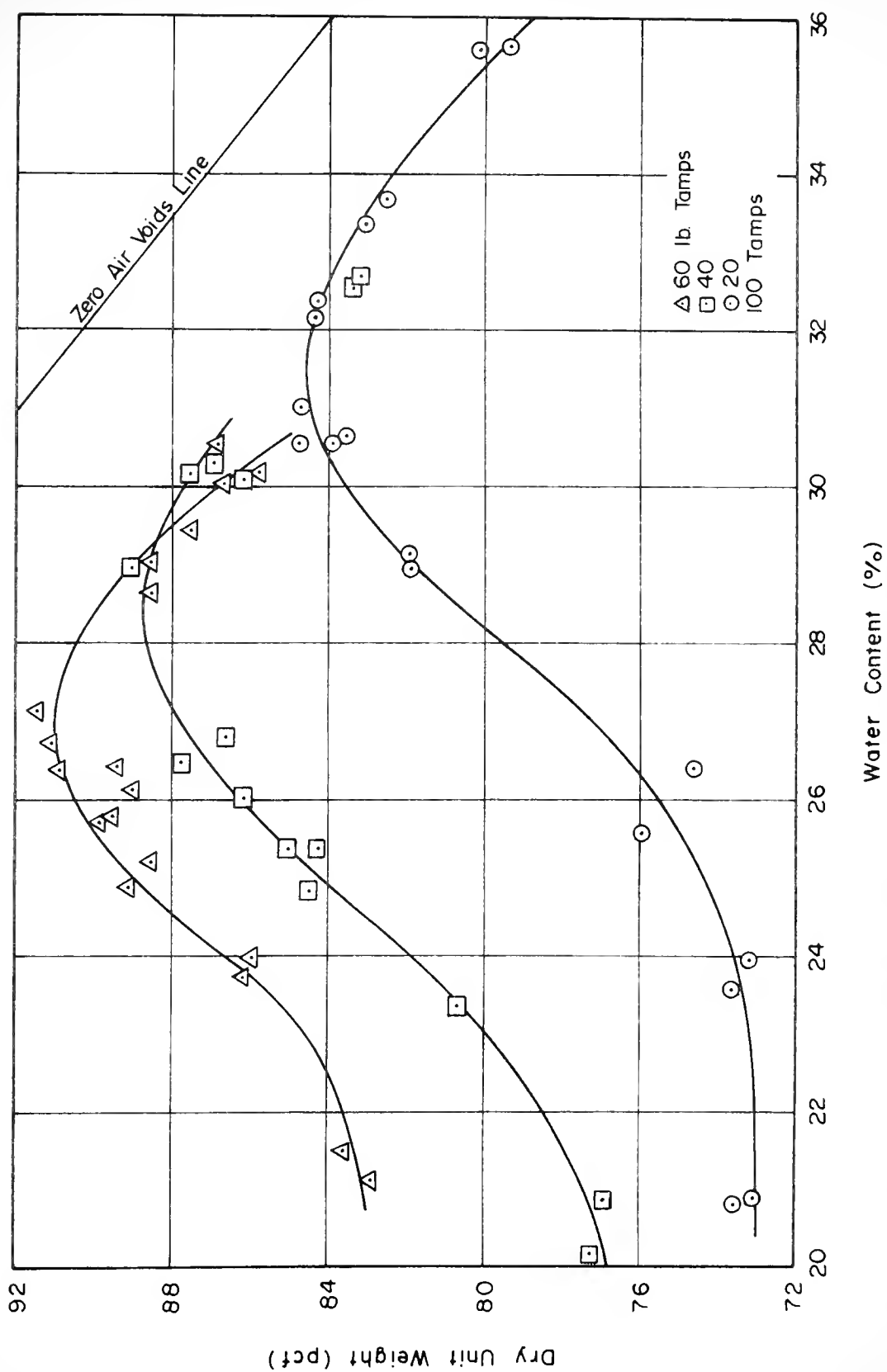


FIGURE 2. KNEADING COMPACTION CURVES FOR EDGAR PLASTIC KAOLIN; AFTER PERLOFF (44)

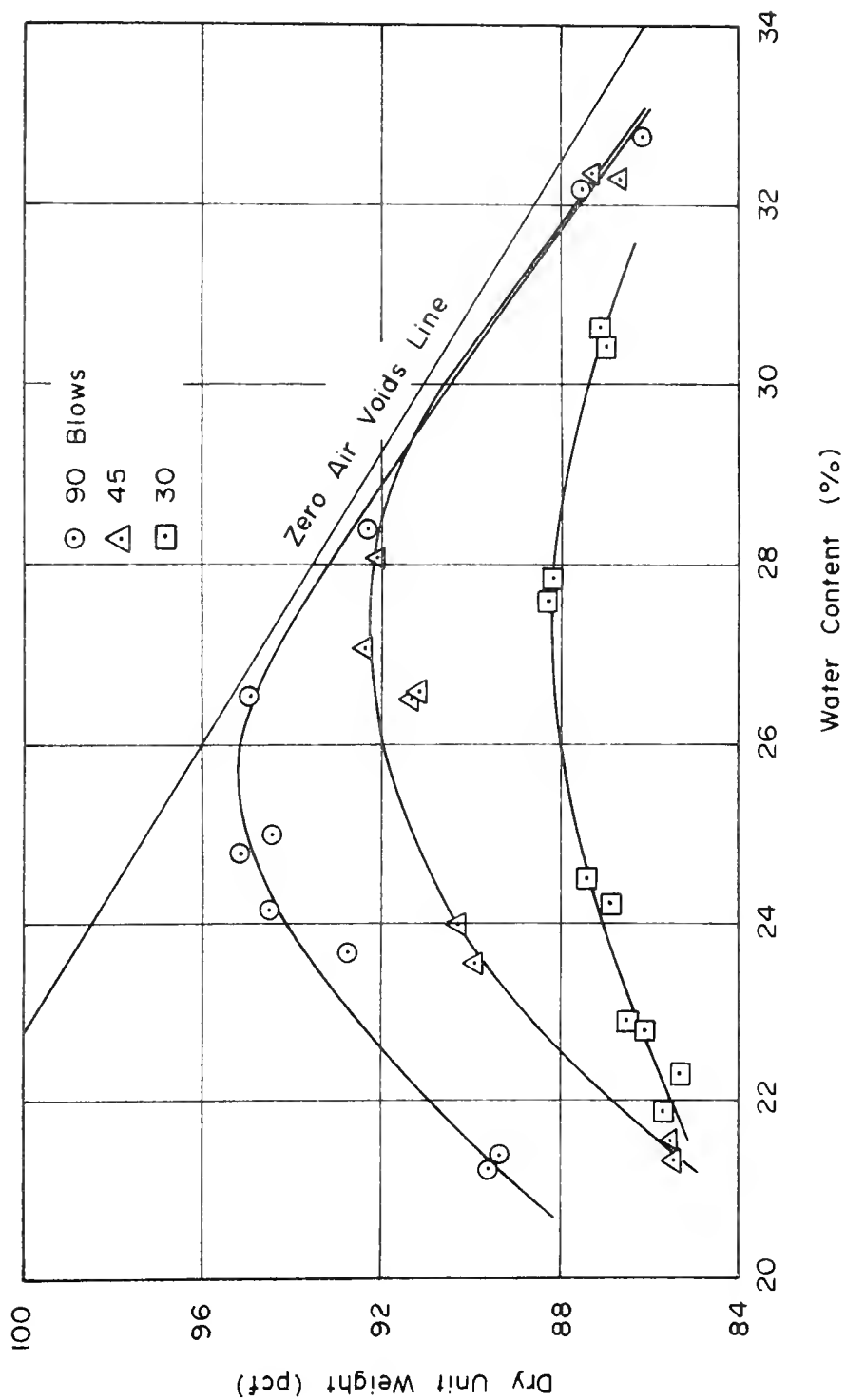


FIGURE 3. IMPACT COMPACTION CURVES FOR EDGAR PLASTIC KAOLIN; AFTER PERLOFF (44)

to the writer's knowledge. However, static compaction is often used for the preparation of laboratory samples for triaxial, permeability, and swelling pressure tests. Procedures vary, but they can conveniently be separated into two categories.

One procedure, where an end result is desired, employs a pressure increase until a predetermined sample height, corresponding to some dry unit weight or degree of saturation, is reached. At this point, the load is held constant for a few minutes and then removed.

The second method, procedural in nature, specifies a rate of loading, a maximum load, the length of time the maximum load will be maintained, and a rate of unloading. By this method, the soil response can be measured as dry unit weight, and the conventional moisture-unit weight relationship be found. However, since static compaction involves usually one repetition of a full coverage loading foot, there is a tendency for the soil to flow plastically between the foot and the mold at moisture contents appreciably above optimum.

The beauty of static-type compaction for laboratory investigations is that, with the aid of a load cell, the load-displacement relationship can be measured during the densification process. As previously pointed out, this cannot be conveniently monitored for impact or kneading compaction, since the compactors used are not full coverage.

Using and extending the general concepts advanced by Lambe (27, 28), Seed and Chan (55) concluded that for static, impact, and Harvard miniature kneading compaction, all samples prepared dry of optimum had similar, relatively flocculated structures, with minimal shearing deformations occurring during compaction.¹ For samples prepared wet of optimum, kneading compaction, with its larger shear strains¹, gave the most dispersed microstructure, while impact compaction produced a somewhat dispersed structure, and static compaction resulted in the least dispersed structure. The conclusions were based on strength, stress-strain, and shrinkage characteristics of a silty clay. An example of their results is shown in Figure 4. However, Seed and Chan also point out that different clays will react differently to compaction, some dispersing at water contents below their optimums, and others retaining their flocculated structures even under large shear strains at moisture contents above the optimum.

Volumetric Swell

A primary concern for compacted soil when under low surcharge and with free water available, is the tendency for the soil to imbibe water and increase in volume. Not only is the swell a function of the mineralogy of the soil, but it is also a function of the compaction type, the

1. The same conclusion with respect to particle-particle movement obtains in the author's aggregation hypothesis.

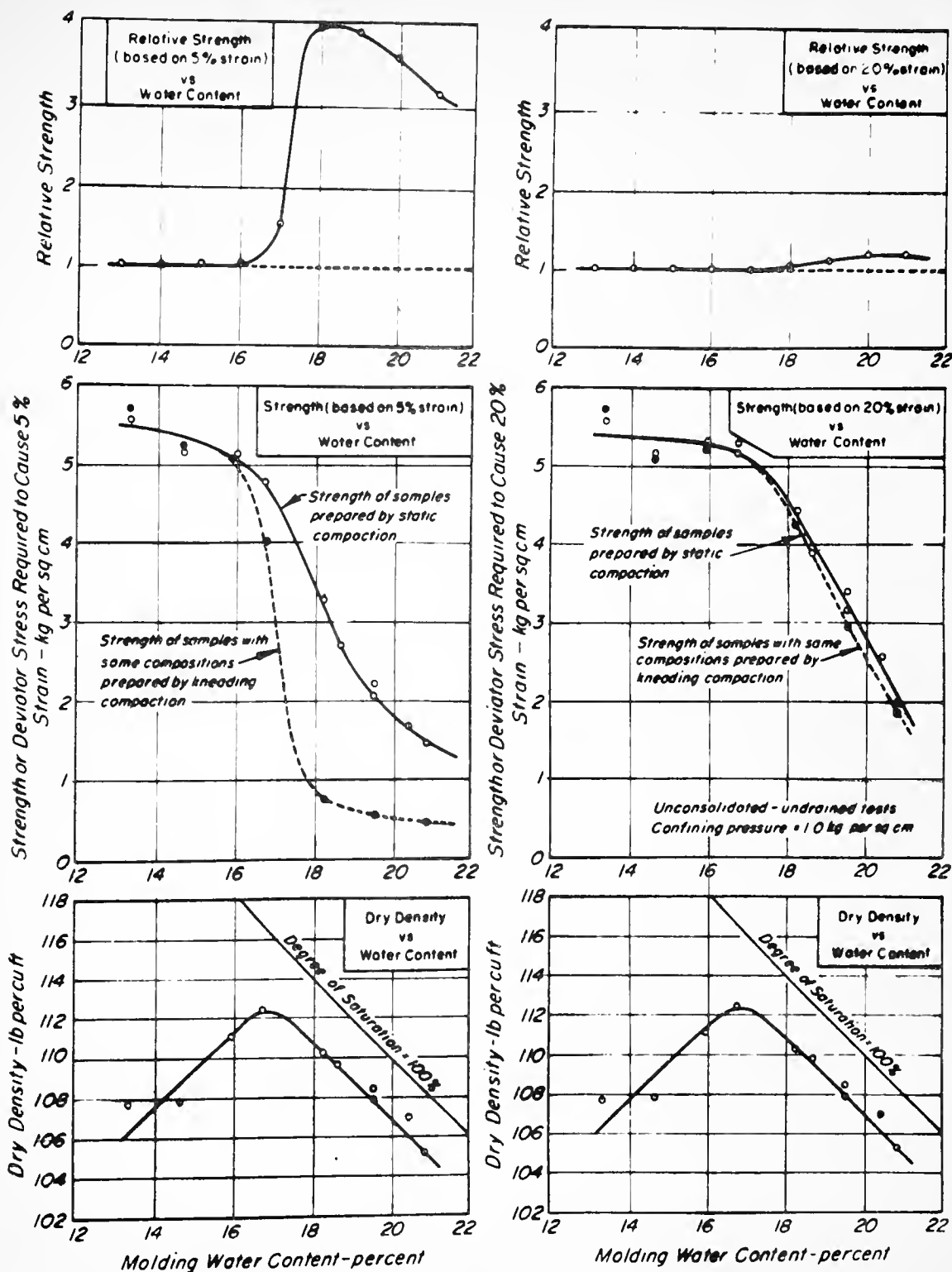


FIGURE 4. COMPARISON OF STRENGTHS OF SILTY CLAY SAMPLES PREPARED BY KNEADING AND STATIC COMPACTION; AFTER SEED AND CHAN (55)

compaction moisture content, the chemical character of the available water, as well as the effective surcharge against which the soil must do work if it is to increase in volume.

In an early investigation initiated in an attempt to cope with damaging volume changes in hydraulic structures, Holtz and Gibbs (18) concluded that volume increase was a function of the as-compacted dry density and water content, i.e., volume increase was inversely proportional to the water content and directly proportional to the dry density. Their tests were performed by measuring the volume increase of a sample compacted in, and laterally restrained by, a consolidometer ring, with free water available to the sample. Unfortunately, their sample compaction procedure was not specified.

Using a highly plastic clay with a liquid limit of 70 and a plastic limit of 26, Leonards (30) reported that for statically compacted samples, all at the same molding water content, a linear relationship exists between the compaction pressure and the swelling pressure. His results are shown in Figure 5.

Research conducted by Ladd (24) also demonstrated that volume change is inversely proportional to the molding water content on the dry side of the optimum moisture content. In addition, Ladd showed that volume change can be explained by double-layer concepts when he reported an inverse relationship between salt content of the imbibed

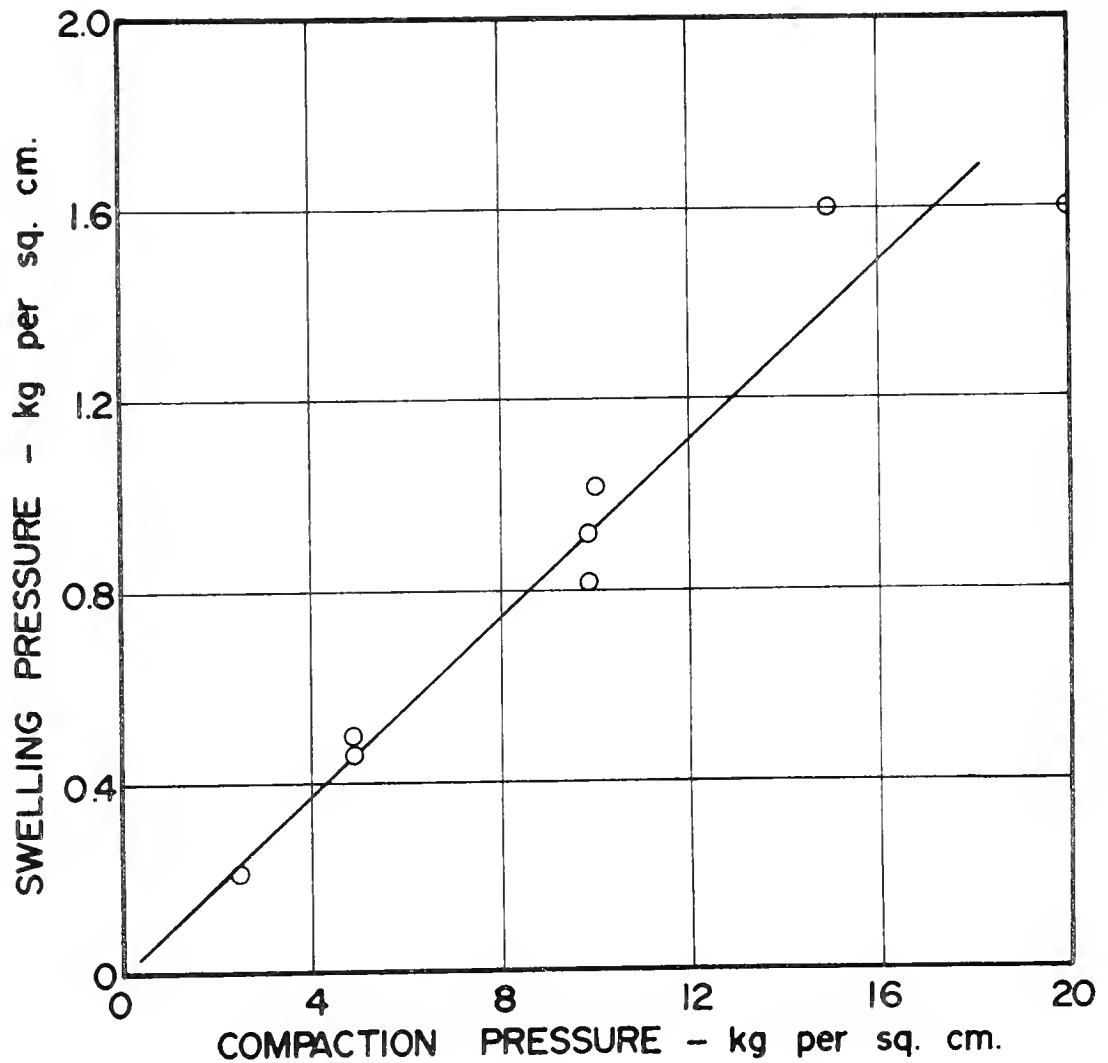


FIGURE 5. SWELLING PRESSURE VS.
COMPACTION PRESSURE; AFTER
LEONARDS (30)

pore fluid and the equilibrium volume change. These relationships are shown in Figure 6. He considered that adsorption and volume increase was a function of cation hydration, osmotic pressure, and capillarity. For Vicksburg Buckshot clay statically compacted in a Harvard miniature mold at minus 4% to plus 2% of the optimum moisture content he concluded that swell was due only to osmotic pressure and capillarity.

Lambe (28) also concluded that volume change properties could adequately be explained by double-layer considerations. His experimental verification consisted of changing the temperature of a consolidated sample of Boston blue clay with the sample loaded under a constant surcharge. The sample was consolidated at 20° C., the temperature was raised to 41° C., and finally the temperature was returned to 20° C. Under the constant surcharge, the clay compressed with the temperature increase, and expanded with the temperature decrease.

According to double-layer theory, a temperature increase and the resulting decrease of the dielectric constant depresses the double layer, and conversely, a temperature decrease expands the double layer. Starting from an equilibrium condition (20° C.) and then depressing the double layer (increasing the temperature to 41° C.) would result in a decrease in the osmotic pressure and a volume

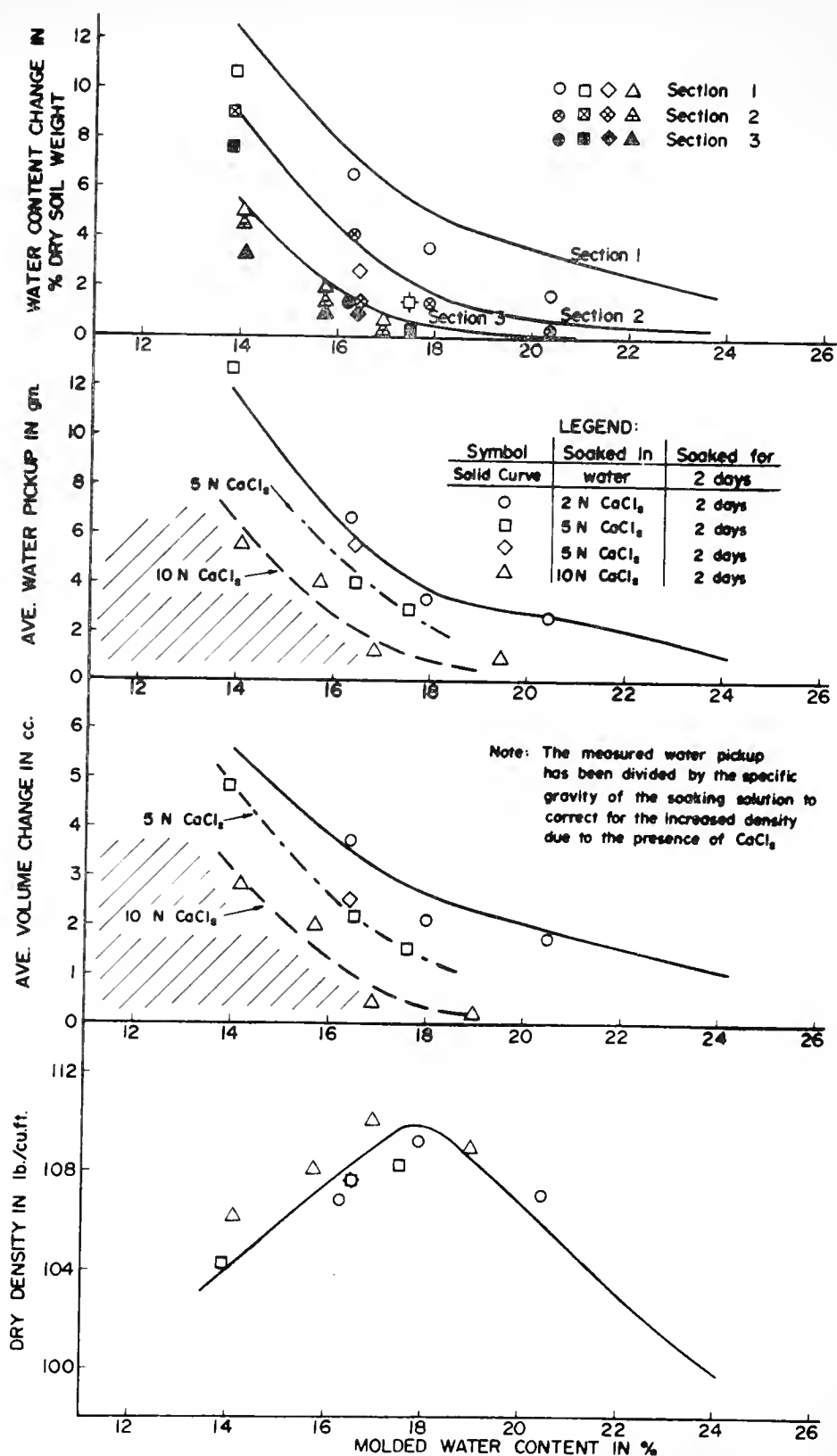


FIGURE 6. EFFECTS OF SOAKING IN A SALT SOLUTION; LADD (24)

decrease until the double layers and bulk water were again at equilibrium.

While confirming other reports that swelling tendency is inversely proportional to the molding water content, Seed and Chan (55) also investigated the effect of compactive type on the volume change characteristics. Using a sandy clay with a maximum dry density of 116.7 pcf at an optimum moisture content of 15.1% for a given input, and Harvard miniature-type compaction, they compacted kneading and static type samples at 113 pcf and 12.3% moisture content, and kneading and static type samples at 113.4 pcf and 17.0% moisture content.

The dry-side samples acted quite similarly in that the static sample showed 10% swell, and the kneading sample about 9.5%. Axial shrinkage upon drying from the as-compacted state also gave similar results, i.e., about 0.8% for both samples. The wet-side samples demonstrated a considerable dependence on compactive type. The static sample swelled 5.5%, and the kneading sample only swelled 3.1%. The axial shrinkage measurements gave 1.3% for the static sample and 4.0% for the kneading sample. Their results are shown in Figure 7. The authors point out that this is the expected result, that dry of optimum, neither compaction method imparts large shear strains to the sample, and a random, or well flocculated, structure is maintained. Wet of optimum, the kneading-type compaction imparts more

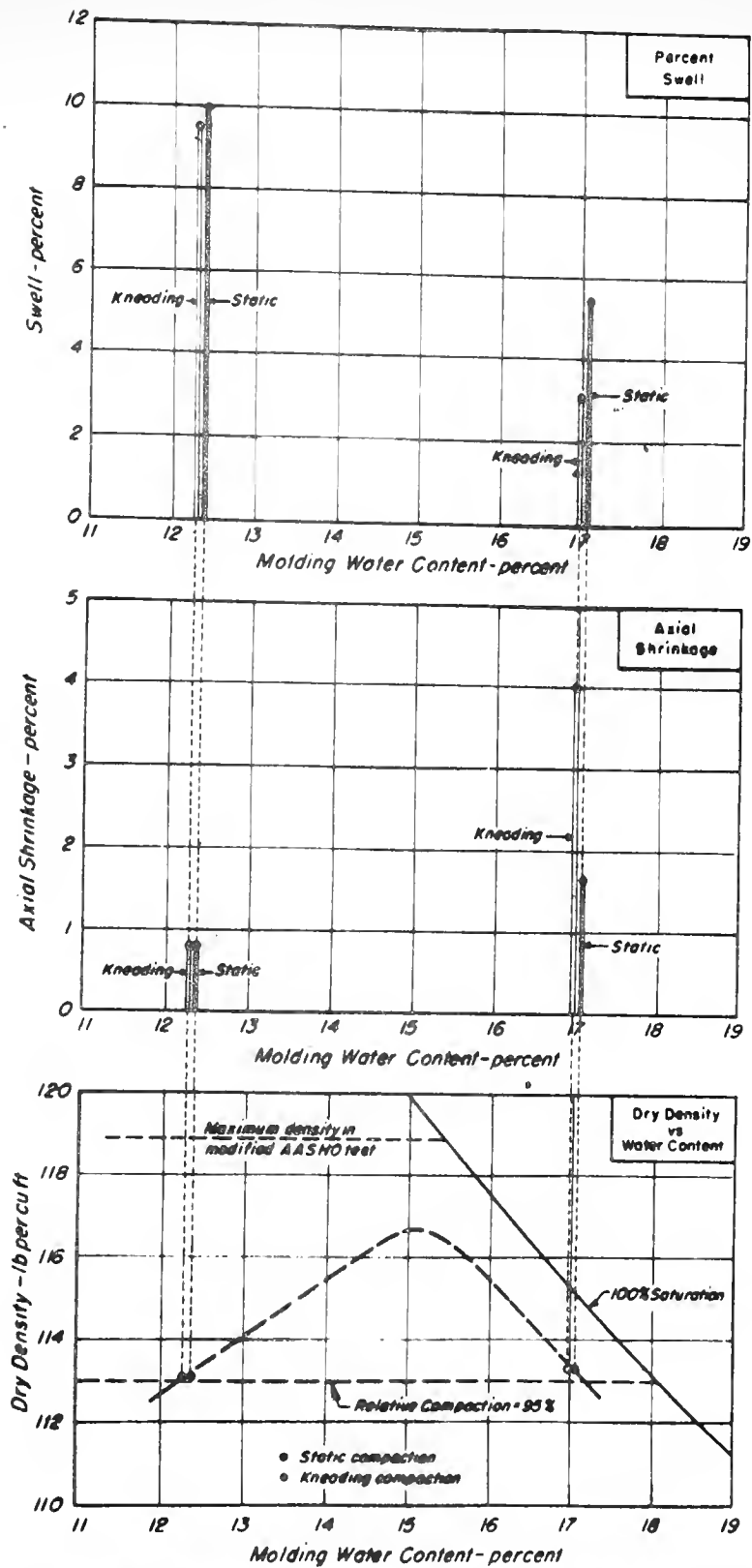


FIGURE 7. SWELL AND SHRINKAGE FOR SAMPLES OF SANDY CLAY PREPARED BY KNEADING AND STATIC COMPACTION; AFTER SEED AND CHAN (55)

shearing energy to the sample than does static compaction. Therefore, the wet-side structure for kneading compaction is significantly more oriented than the static type which, in turn, is slightly more oriented than the dry-side statically compacted sample.

From this we conclude that, at least for the conditions of Seed and Chan's testing program, as the degree of orientation increases, the swelling tendency decreases in the presence of free water, and shrinkage increases as the water is removed from the specimen.

In a slightly different demonstration, Seed and Chan (55) again showed that axial shrinkage is a function of the shearing induced in the specimen during compaction. Using the sandy clay soil, they compacted two samples to the same dry density, at the same water content, by kneading compaction. However, one sample was compacted using a tamping pressure of 80 psi which resulted in a foot penetration of 0.05 inches, while the other sample was subjected to a tamping pressure of 320 psi which resulted in a foot penetration of 0.43 inches. Both samples attained a dry density of 108 pcf, at a moisture content of 19.5%.

Both samples were dried from the as-compacted state. The axial shrinkage for the 0.05 inch foot penetration sample was 2.5%, and the shrinkage for the 0.43 inch foot penetration sample was 4.8%. Interpreted in terms of microstructure, the results indicate that increased shear strains, i.e.,

larger foot penetration, at constant density results in an increasingly dispersed structure.

In a discussion of Seed and Chan's (55) paper, Olson and Scott (40) introduced the concepts that were to become Olson's theory of compaction for fine-grained soils (38). In their discussion, Olson and Scott explained Seed and Chan's axial shrinkage results with the notion that at a water content far on the dry side of optimum, the volume is maintained by a very high negative pore pressure. Drying will result in an increase in negative pore pressure and a slight volume reduction, since the soil is highly incompressible. As the soil moisture becomes discontinuous, an elastic volume increase will occur. The net volume change will depend on the initial as-compacted moisture content and negative pore water pressure; the higher moisture content and larger density samples, starting from a much less negative as-compacted pore pressure and subjected to the same physical action during drying, will exhibit larger volume changes.

It is felt that Olson's explanation better fits the observed results, viz., that dry-side swell is larger than wet side due to the higher negative pore pressures; and extending his ideas, that kneading compaction on the wet side of optimum moisture content effectively lessens the remaining negative pore water pressure as witnessed by increased swell and decreased shrinkage of the statically compacted soil, when compared with the kneading results.

The importance of the effect of stress history on swelling has been clearly demonstrated by Barber (2) and Seed, Mitchell, and Chan (56).

Some of Barber's data have been plotted as Figures 8 and 9. Figure 8 shows the effect of volumetric restraint, for a period of 24 hours during water uptake, on the final height change of the sample after removing the confinement, as a function of molding water content for Tuxedo clay. Figure 9 shows the same trend for two soils which were statically compacted air-dry, and then unloaded step-wise after volumetric equilibrium was achieved at each step. The final increase in thickness at 0.02 kips per square foot for each soil unloaded in this manner is seen to be much less than that for duplicates allowed to achieve equilibrium under an initial surcharge of 0.02 kips per square foot. Barber considers these results to indicate particle rearrangements under the various restraints.

The same type of results were reported by Seed, Mitchell, and Chan (56) and are reproduced as Figure 10. Their data show that, qualitatively, the swelling of a compacted sample as a function of time resembles the unloading response of a saturated clay. It appears from their results that a surcharge-dependent collapse or internal structural rearrangement is occurring. The largest initial pressure, which presumably would cause the greatest particle rearrangement upon wetting, yields the least swell after all samples achieve final equilibrium under the same low surcharge pressure.

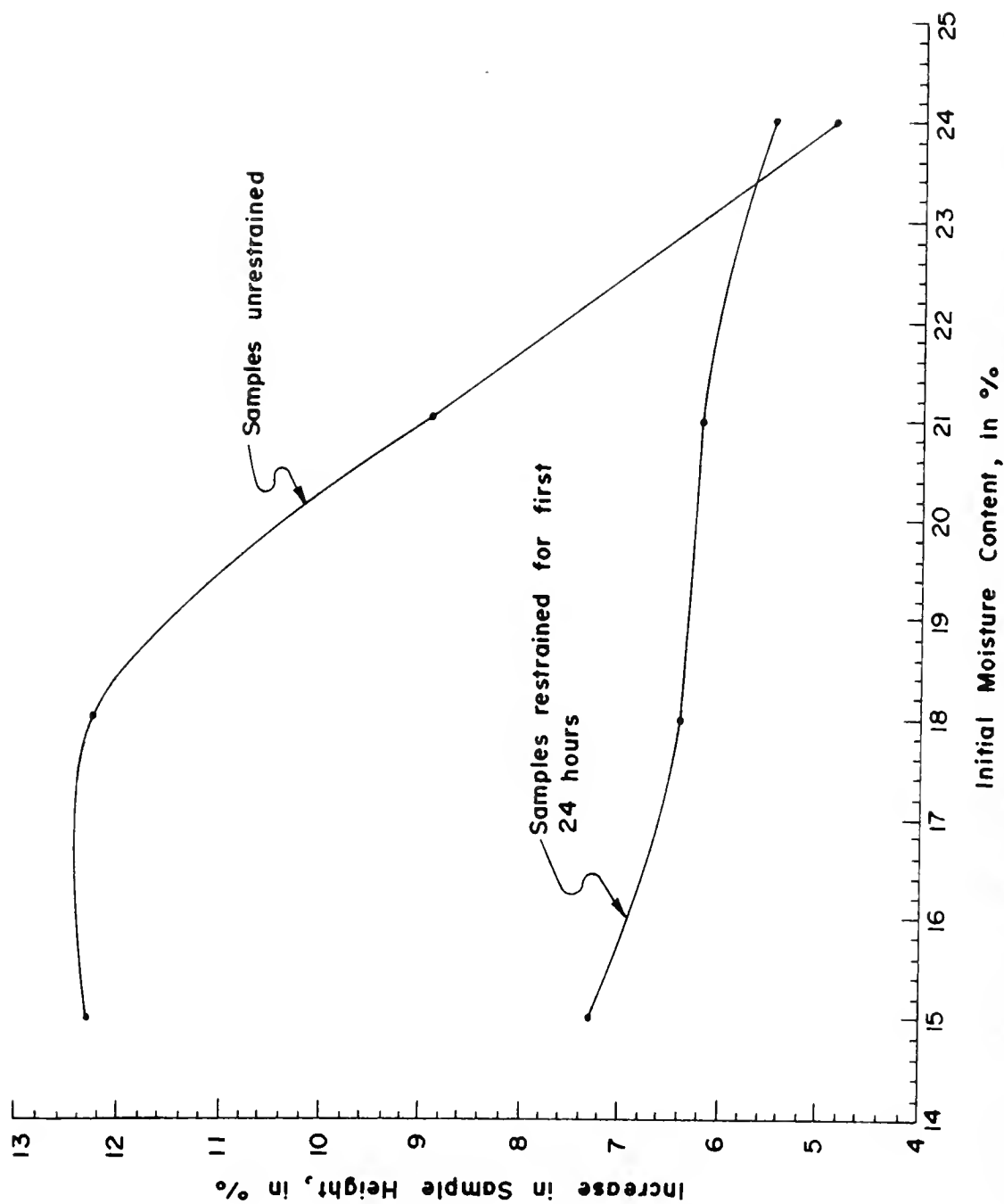


FIGURE 8. EFFECT OF TEMPORARY RESTRAINT ON SAMPLE SWELL; ADAPTED FROM BARBER (2)

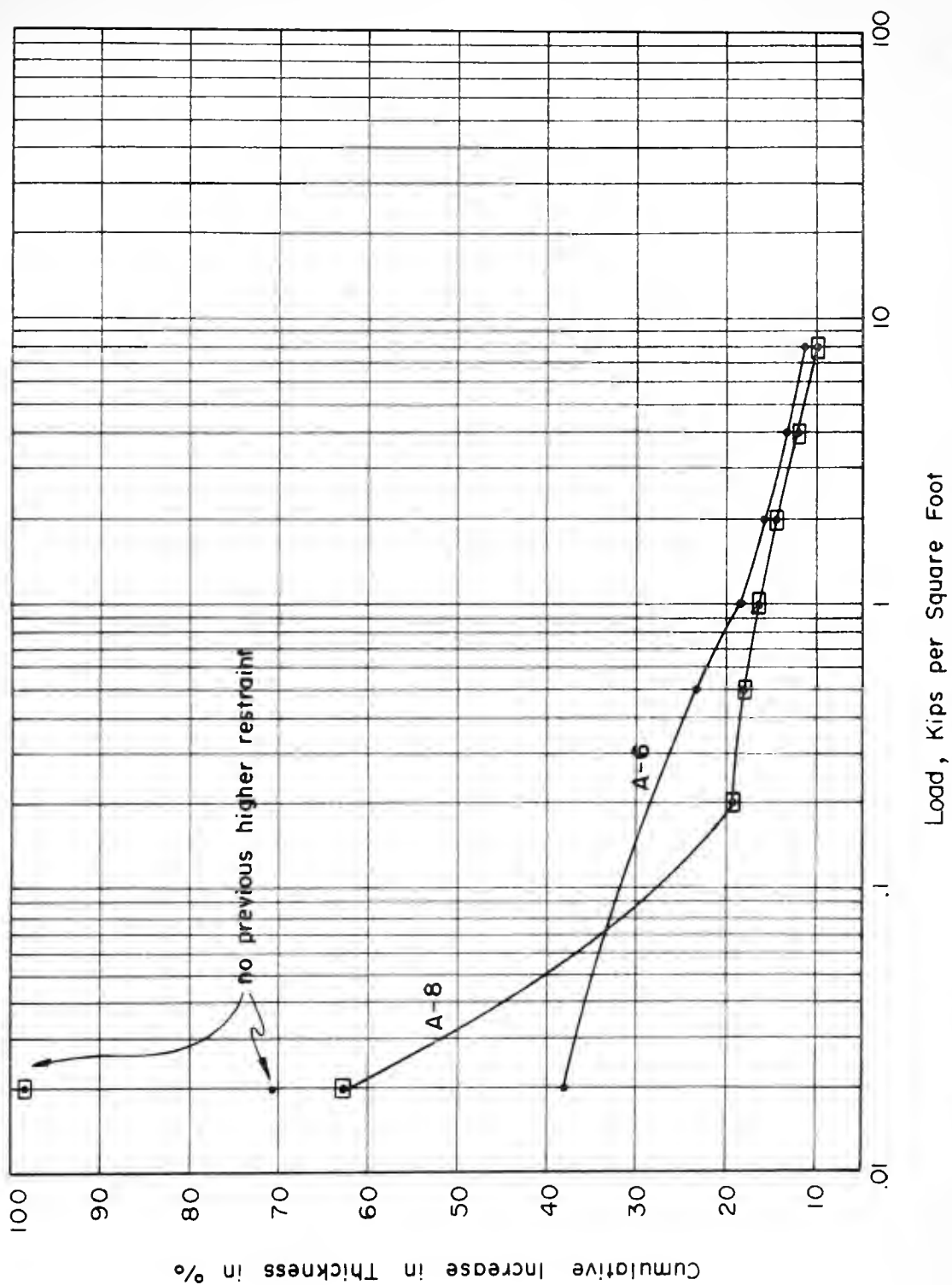


FIGURE 9. EFFECT OF LOAD ON THE INCREASE IN SAMPLE THICKNESS; ADAPTED FROM BARBER (2)

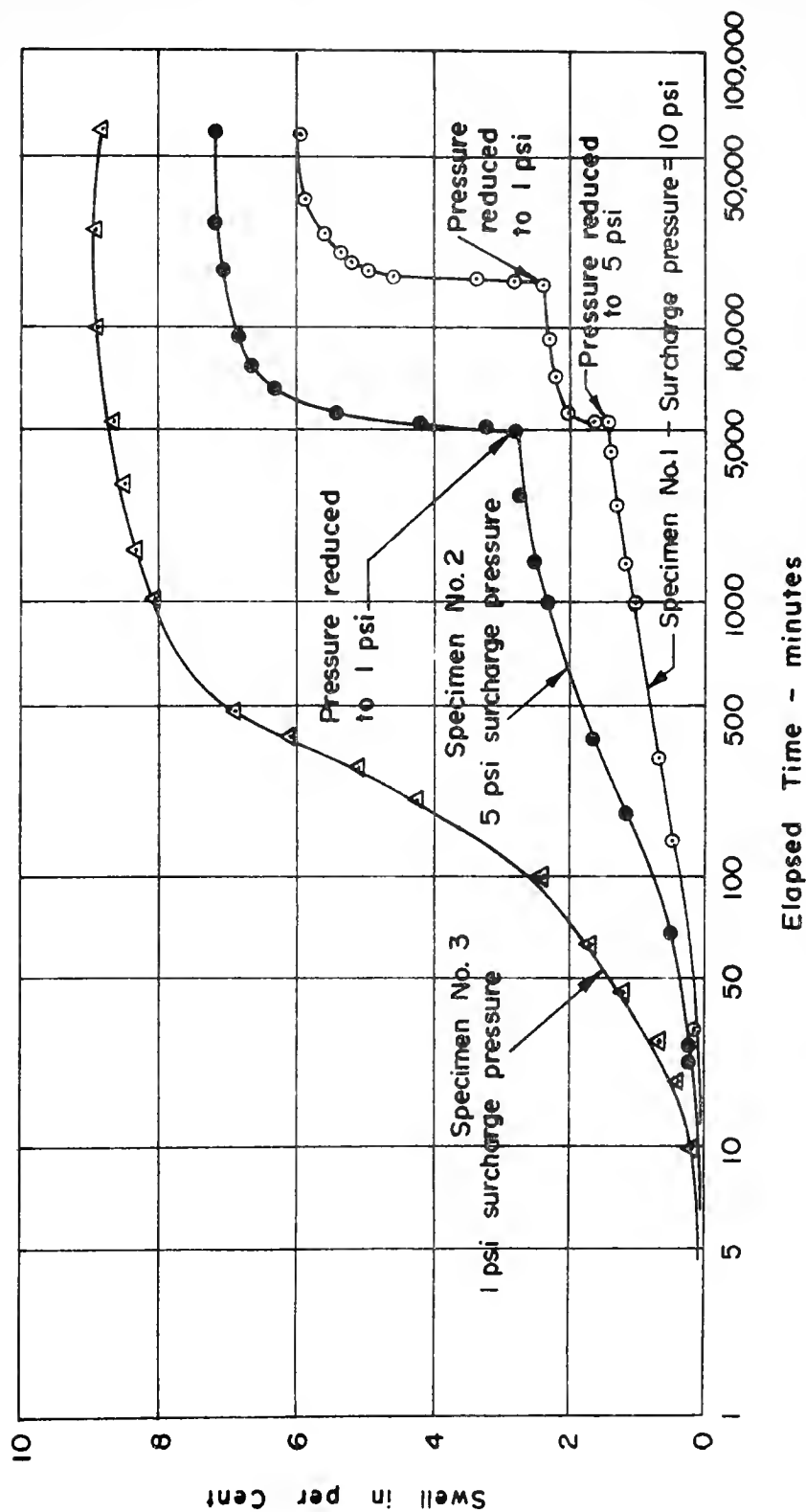


FIGURE 10. EFFECT OF STRESS HISTORY ON SWELL OF COMPACTED SAMPLES OF SANDY CLAY; AFTER SEED, MITCHELL, AND CHAN (56)

The composition of the liquid which the soil imbibes also affects the magnitude of the equilibrium volume change.

Seed, Mitchell, and Chan (56) varied the calcium acetate concentration in the water available to sandy clay samples compacted by static and kneading methods to a dry density of 111.3 pcf at 17.3% water content (wet of optimum). Their results showed, for the statically compacted sample, from 5.2% swell for a zero moles per liter calcium acetate solution, to 3.4% swell for a 2.0 moles per liter solution. For the kneading type sample, the swells were 3.6% and 1.1% at zero and 2.0 moles per liter solutions, respectively. All samples were allowed to swell under a 0.1 kg/cm^2 surcharge.

For both samples, the shapes of the curves of per cent swell vs. calcium acetate concentration indicate that further increases in calcium acetate content of the solutions would not further decrease the per cent swell significantly. Assuming that no further change in per cent swell can be achieved by an increase in calcium acetate concentration, its total effect on the static sample was to reduce the swell 1.8% or 35% of the zero concentration swell, and for the kneading sample, to reduce the swell 2.5% or 69% of the zero concentration swell.

The high sensitivity of the dispersed structure (kneading type) compared to the flocculated seems reasonable from the double layer viewpoint, yet it does not explain the high swell exhibited by the flocculated sample at very high calcium

acetate concentrations. This anomaly may be understandable in terms of effective stress differences for the two compactive types. Higher effective negative pore pressures in the static sample would easily explain its larger per cent swell.

Ladd (25) also investigated the effect of varying the cation concentration on the resulting swell of compacted clay. He used Vicksburg buckshot clay, a clay high in calcium montmorillonite, and dynamically compacted it into consolidometer rings. The liquid, either distilled water, a 0.5 molar CaCl_2 solution, or a 5 molar CaCl_2 solution, was made available to both sides of the soil sample simultaneously, and swelling was allowed to occur under a 200 pounds per square foot surcharge. Ladd's results are reproduced as Figure 11.

At all molding water contents, the per cent heave decreases as the molarity of the soaking solution increases. Ladd has estimated that the total ion concentration in the 5 molar CaCl_2 solution far exceeds the exchangeable cation concentration in the soil for all water contents. And, therefore, double layer expansion should not occur upon contact with the 5 molar solution.

Recognizing this, Ladd offered as explanations, for the volume changes observed at moisture contents below 21.5%, negative electric and London Van der Waals' force fields on water, cation hydration and the attraction of the particle surface for water, elastic rebound and a flocculated orientation, and the buildup of positive pressure in entrapped air

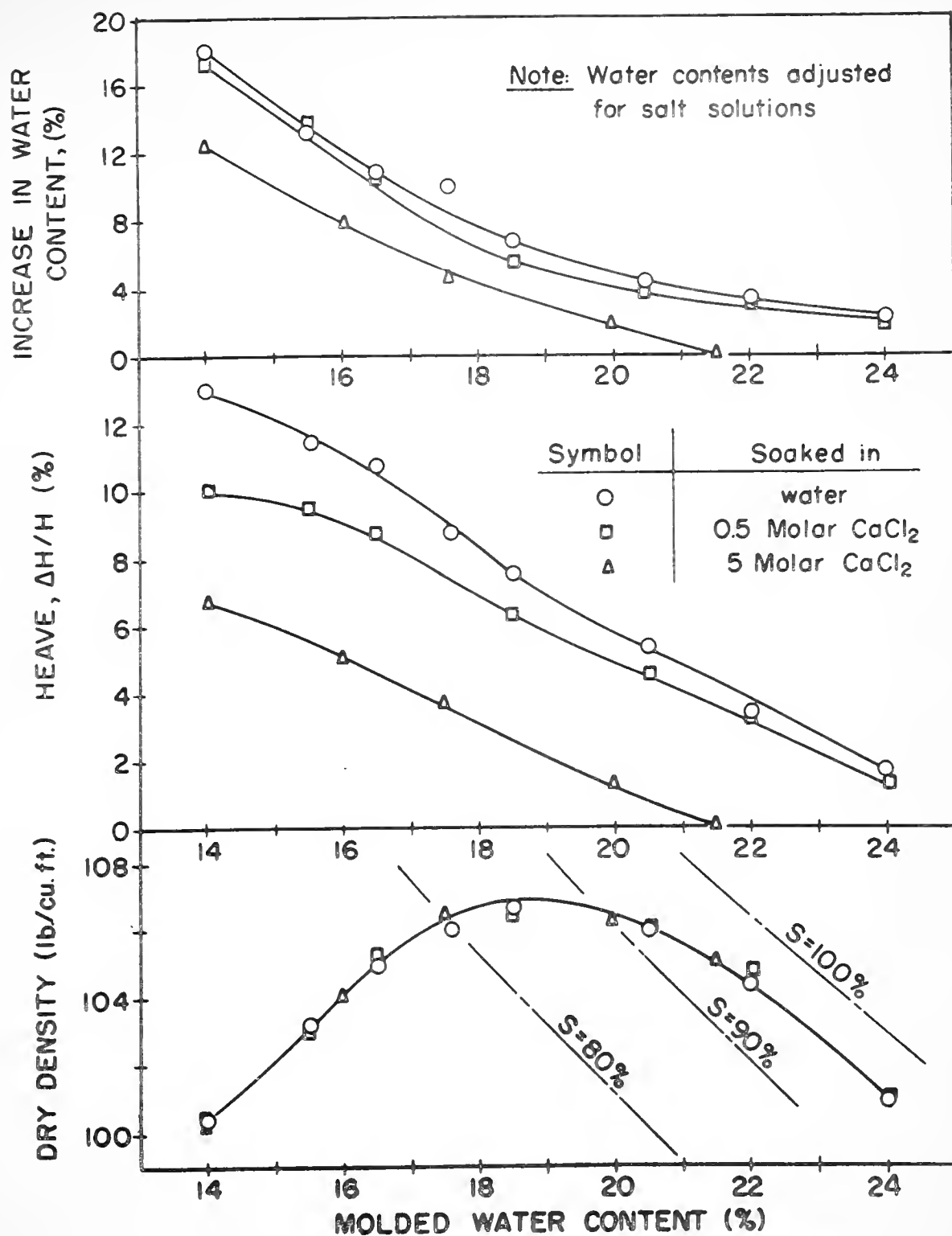


FIGURE II EFFECT OF SALT CONCENTRATION ON SWELLING BEHAVIOR; AFTER LADD (25)

during saturation. The first two factors would seem to be of minor importance, while elastic rebound would seem quite important, since the restraining forces - the negative pore water pressures - would be cancelled by the available water. Air pressure buildup could also explain some of the swell for Ladd's tests, since water was allowed to enter the sample from both sides rather than leaving one face of the sample open to the atmosphere, with air able to leave the sample as the wetting front advanced.

Temperature effects on the volume of a compacted sample can be extrapolated from theoretical and experimental studies on saturated soils. Lambe (27) has indicated that an increase in temperature will decrease the double layer thickness. This change takes into account the effect of temperature change on the dielectric constant of the water. Theoretical relationships developed by Campanella and Mitchell (9) take into account the volumetric change of water and mineral matter with temperature change. Their theory was confirmed by experimental results, and they found that during a temperature increase, water drains out of an isotropically consolidated sample, or if drainage is prevented, positive pore water pressures develop. They also confirmed that the opposite results occur if the sample is subjected to a temperature decrease.

For the partially saturated compacted soil, with negative pore water pressure restraining the sample somewhat,

a decrease in double layer thickness at constant water content will lessen the osmotic effect, causing the pore water pressure to become less negative, and allowing the soil to increase in volume until a new equilibrium is reached.

Similarly, an increase in available water, at constant stress, will decrease the negative pore water pressure and allow the soil to expand. Both of these phenomena occur due to a temperature increase; therefore, we may conclude that when negative pore water pressure is present, a temperature increase will cause the soil volume to increase.

In a recent investigation Barden, Madedor, and Sides (3) also investigated the volume change characteristics of compacted clay. Their method of approach was to subject compacted samples of naturally occurring clay to one-dimensional compression. Their objective was to determine the factors which influence parameters C_1 and C_2 in the equation

$$dV/V = C_1 d(\sigma - u_a) + C_2 d(u_a - u_w)$$

where: dV/V is volumetric strain,

σ is the total applied stress,

u_a is the pore air pressure, and

u_w is the pore water pressure.

Their results included the findings that

"Collapse occurred in all cases of samples compacted appreciably dry of optimum, on wetting to a zero suction pressure under a large applied stress... The higher the clay content the smaller the collapse, presumably because of the simultaneous swelling that must occur. Samples compacted close to optimum showed no collapse."

The authors alluded to the collapse mechanism being a sudden reduction in the rigidity of the skeleton caused by a flocculated structure which is inherently sensitive to negative capillary water pressure. They offered no substantiating experimental evidence.

In a discussion of a paper by Dudley (13), Leonards and Altschaeffl (31) pointed out that upon wetting, compacted clays may exhibit considerable volume decrease. They presented as evidence the results of one-dimensional compression tests on a limestone residual clay prepared by standard Proctor compaction. The results showed volume change as a function of the pressure on the sample for the as-compacted case as well as the relation generated when samples were allowed to imbibe water after reaching equilibrium with various pressures at the compaction moisture content. They concluded in part that volume change depends on the compaction water content and the applied pressure at which water is added.

Swelling Pressure

An important indicator of potentially troublesome volume changes is the swelling pressure generated by changes in the many variables inherent to the solid-water-air soil system. It is the pressure change that causes volume change in most cases, and a knowledge of swell pressure behavior will allow a better model of the compacted soil to be developed.

For the simplified model of a saturated system at constant volume, the Langmuir equation from double-layer theory predicts the swelling pressure to be (23):

$$p = 2nkT (\cosh ze_2 \psi_d/kT - 1)$$

where: p is the swelling pressure
 n is the concentration of electrolyte
 k is the Boltzmann's constant
 T is the absolute temperature
 z is the valence of the cation
 e_2 is the charge of a proton
 ψ_d is the potential midway between two parallel plates.

Unfortunately, the very factors which allow this relationship to be simply developed, i.e., parallel plates, a dilute saturated system, and zero volume change as the pressure is developed, make this equation unusable as a quantitative predictor for compacted soil. A critical examination of double layer theory, in particular the swelling pressure, has been made by Low (32) in which he concluded that "... it cannot be depended on for an accurate description of ionic exchange, clay swelling and other allied phenomena."

Seed, Mitchell, and Chan (56) have studied the effects of time, sample shape, soil structure, and the relationship between swell pressure and the amount of swell for compacted specimens.

Concerning time effects, their observations indicated that the increase in swell pressure may continue for a considerable period of time at an ever-decreasing rate, even for a high initial degree of saturation. Their data do not indicate any decrease in swell pressure after the sample is given access to water.

They explained that in some tests, the swell pressure did drop for a short time after water was introduced to the sample, and investigations indicated that after compaction and prior to confinement (a period of 30 minutes), the unrestrained upper surface of the sample developed a convex shape. As a result of this sample shape, the equilibrium swell pressure was less than for an identical sample trimmed planar before testing, and, as previously stated, there were initial decreases in swell pressure which were not observed for the trimmed samples.

The influence of slight volume change on the observed swell pressure was confirmed by the results of tests on identical samples, where proving bars of different stiffness were used to measure the developed pressure. As expected, the measured pressure increased with increasing stiffness of the proving bar.

The effect of soil structure on swelling pressure was demonstrated by the fact that for two soils, a sandy clay and a silty clay, higher swell pressures developed for the statically compacted samples than for kneading-type samples,

over the entire range of unit weight considered. Reasoning that kneading compaction results in a more dispersed structure than static compaction, they concluded that the more flocculated structure by static compaction was the reason for the larger swell pressures developed.

The effects of unit weight and moisture content on swelling pressure were found to be similar to the volume change results. That is, swelling pressure increased with increasing density and decreasing water content.

The procedure used by Seed, Mitchell, and Chan to measure both swelling pressure and per cent swell was such that water was introduced to the top of the sample through a perforated disc. Provisions for allowing air to escape at the bottom of the sample were not indicated. Therefore, the possible effects due to entrapped air, at high pressure within the sample, are not known.

A different conclusion concerning the effect of moisture content on swell pressure can be drawn from results reported by Olson (40). Illitic clay specimens were compacted by kneading compaction, placed in a consolidation press, the bottom of each sample was given access to water in small increments, and axial total stresses were adjusted so that no volume changes occurred. The result was that the swelling pressure vs. molding moisture content curves were quite similar in shape to the dry density vs. molding moisture content compaction relationships. That

is, swell pressure increased as the level of compaction increased, and for a given level of compaction the maximum swelling pressure occurred at the optimum moisture content.

According to Kassiff and Baker (22) the swelling pressure generated by a compacted clay which is given access to water is influenced by aging. This influence is due to two opposing factors, the increasingly negative pore water pressure developed during aging, and the formation with time of electrochemical bonds between the clay plates. Their results indicate that "the swell pressure of a compacted clay, particularly at high initial densities, tends to increase with aging and then gradually to decrease to approximately the final value after about 20 days."

COMPACTION MECHANISM HYPOTHESIS

The goal of this research is an explanation of the achievement of compaction of fine-grained soils in terms of soil structure and changes thereof. The explanation is based in part on findings of previous investigators, principally Lambe and Olson, and upon tests on a single commercial clay (Edgar Plastic Kaolin) in a single compaction mode (static). The hypothesis states the necessity of (a) recognizing a greater number of fabric levels than is common and (b) recognizing that the stress history prior to compaction can strongly influence the compaction result. The following is the postulated explanation for laboratory static compaction of kaolinite, from dry soil to the as-compacted state.

Initial Soil Structure

Before the addition of water to the kaolinite, no more than a few molecular layers of adsorbed water are present on the particles. In this state many of the particles, each being many unit layers thick, are flocculated in face-to-face fashion due to Van der Waals' forces, and probably hydrogen bonds which developed as the Van der Waals'

forces brought the particles closer together. Each group of face-to-face particles can be thought of as a domain. Depending on the amount of hydrogen bonding, much of the adsorbed water will be found on the domain surface rather than uniformly distributed around each flocculated particle in the packet. Figure 12 (a) is an idealized representation of three air-dry domains. The relative spacing between the domains is quite variable and for the mixing technique used in this research is constantly changing, but the orientation and spacing of particles within each domain is much more constant. Each particle within the domain is many units thick (not shown) and these repeating units are permanently fixed with respect to each other in the particle.

The usual procedure is to add water to the air-dry soil, either in increments or continuously, and to agitate or mix the soil so that the moisture is, in a gross sense, evenly distributed throughout the soil. This can be done manually or as was done in this research by means of a mechanical blender.

As the soil domains come into contact with the water mist during agitation in the mixer, the external double layers begin to form, and depending on the degree of bonding within the domain, water is adsorbed between the face-to-face particles and a slight swelling of the domain may occur. This is shown in Figure 12 (b).

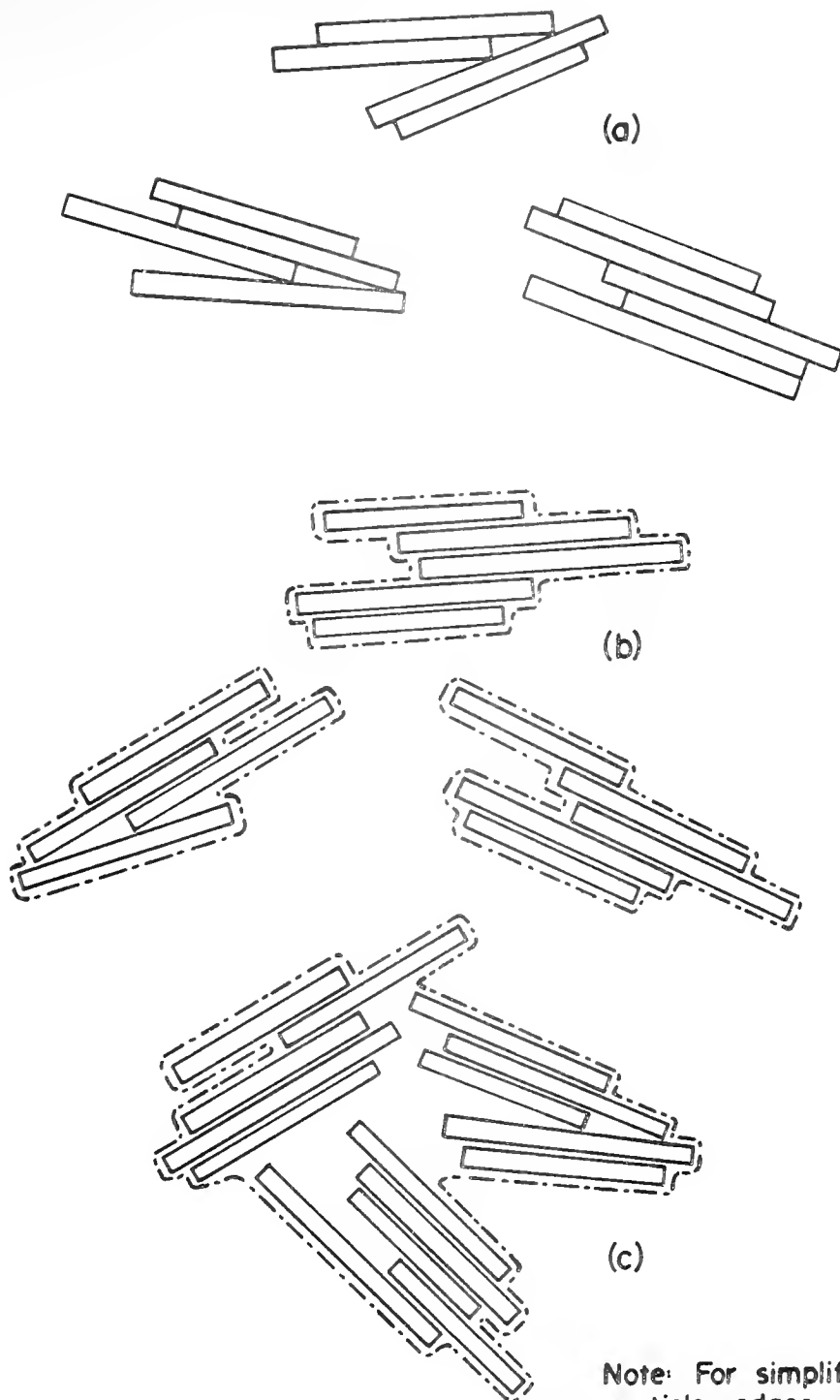


FIGURE 12. IDEALIZED REPRESENTATION OF DOMAINS AND FORMATION OF AGGREGATE

Figure 12 (c) shows the condition as more water is added. The external double layers continue to develop, and domains are held to one another in edge-to-face arrangement forming aggregates as they collide due to agitation by the mixer. This attraction is principally Van der Waals, and to some extent mutual desire for the water on the surfaces of the domains, since there is a large net water deficiency in the system. Continued agitation causes the flocculated groups of domains to grow in size and decrease in number. As water continues to be added, the water inevitably will be unevenly distributed among the many aggregates and domains. Hence domain-aggregate growth continues to occur since the water-poor domains are held at the water-rich sites on the surfaces of the aggregates.

At some point during the mixing operation the quantity of water on the surface of an aggregate may be large enough so that this water exhibits, at least temporarily, bulk water properties. Collisions and contacts among aggregates in this state will cause the aggregates to fuse due to capillary pressures caused by the menisci developed near their points of contact. These fused aggregates will be called apparent aggregates. This situation is shown in Figure 13 (a).

By this process the apparent aggregates will continue to grow with increasing water content. However, the shear strains developed within these quite large apparent

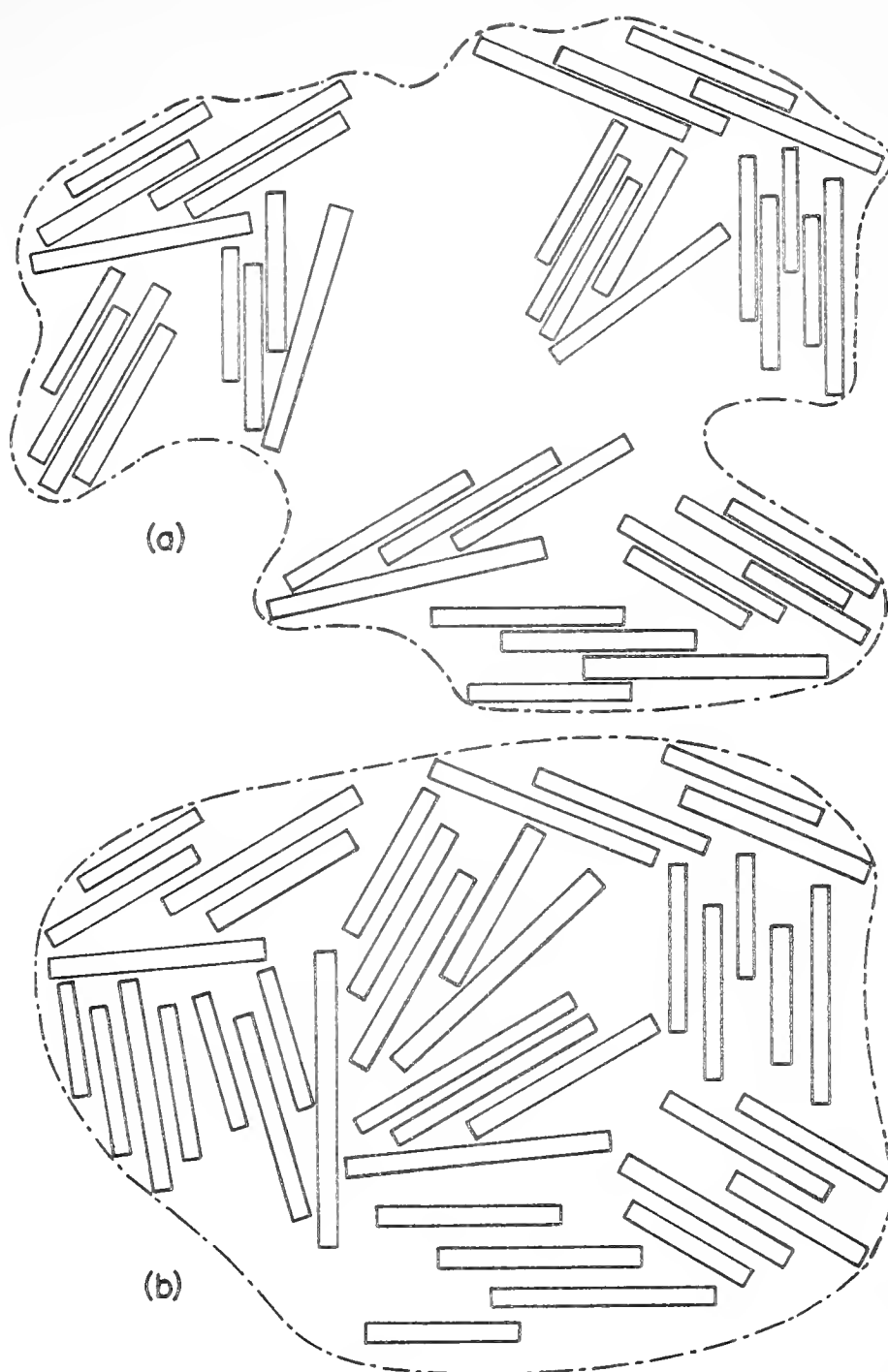


FIGURE 13. FORMATION OF APPARENT AGGREGATE

aggregates caused as they collide with the mixing apparatus will in time cause the aggregates within each mass to lose their individual identity. The shear strains and their accompanying moisture redistribution cause a more dispersed structure to occur within and among the domains. This is depicted in Figure 13 (b).

In summary, at the end of the mixing operation the soil batch consists of aggregates and apparent aggregates over a large size range, with a considerable range of water content, and with the state of the water varying from almost bulk to tightly held in a thickness of only a few molecular layers. The water distribution within each aggregate (we will no longer differentiate between aggregates and apparent aggregates) is not at equilibrium and can be expected to change with time, the pore water pressure is negative, yet the degree of saturation of the aggregate is quite high.

Effect of Curing Time

Upon completion of the mixing procedure it is quite probable that the moisture is unequally distributed among the aggregates. Since the water content is increased by spraying water onto the aggregates' surfaces and the mixing time is relatively short (typically about 30 minutes) neither the inter-aggregate nor the intra-aggregate moisture distribution has yet reached equilibrium.

Moisture can be redistributed among the aggregates by liquid flow and vapor flow. Liquid flow requires "points of contact" among the aggregates and the path length between aggregates having appreciably different moisture contents could be quite long. It is doubtful whether any significant moisture redistribution occurs in this manner. Moisture movement by vaporization and condensation probably does occur, and given a sufficient period of time the aggregates will achieve equilibrium with the ambient relative humidity.

Intra-aggregate moisture migration will occur as fluid flow more or less freely depending on the thickness of the water layer and the magnitude of the driving force. This driving force is actually the osmotic pressure developed due to the differences in cation concentration at various points in the liquid. Slight particle rearrangements and particle spacing changes will occur. The rearrangement will be essentially complete after all surface menisci have the same radius. The size of the radius depends on the amount as well as the cation concentration of the water and the properties of the clay mineral involved.

Compaction Mechanism

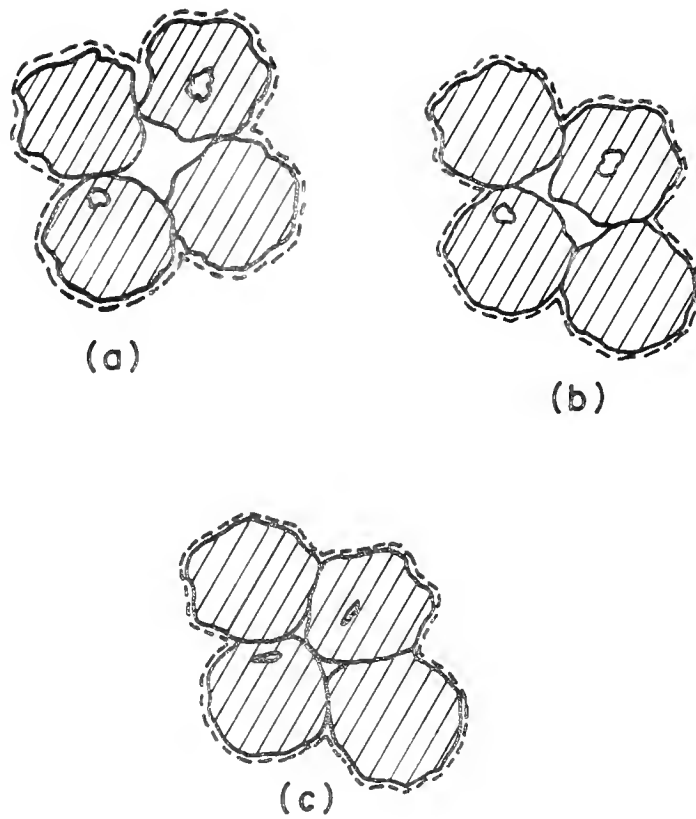
It has been postulated that prior to compaction the preparation of the clay soil causes the appearance of macroscopic balls or aggregates whose intra-aggregate moisture is at less than atmospheric pressure but with a relatively high degree of saturation, and one which is

significantly higher than that of the uncompacted mass as a whole.

Compaction is accomplished by the reduction of void space at a constant moisture content. That is, no water leaves the system. The density increase is due to the reduction of air voids only.

During compaction it is of secondary importance that the aggregates are made up of clay particles, since very little total aggregate volume change will occur (the volume of air within the aggregates is small). Densification can occur by rearrangement of aggregates into a denser packing even if they are individually rigid. However, at most compaction water contents, the aggregates act in a viscoelastic manner and can deform under the compactive load to conform to the available inter-aggregate void space.

Schematically this densification is illustrated in Figure 14. Parts (a) and (b) show the decrease in inter-aggregate void ratio (densification) which can occur with only translation and rotation. The aggregates have not changed shape or volume, they have merely been rearranged so that (b) is a denser packing than (a). Figure 14 (c) shows the further decrease in inter-aggregate void space which can occur if the aggregates deform to flatten at points of contact and to conform to the shapes of available voids. Figure 14 (c) shows as well the reduction of



Note: The volumes are considered to be those areas bounded by the dashed lines

FIGURE 14. IDEALIZED REPRESENTATION OF AGGREGATE COMPACTION.

intra-aggregate voids as two of the aggregates experienced unit weight increases due to aggregate volume decreases. For this figure volume (a) > volume (b) > volume (c).

Laboratory compaction may be achieved, as previously stated, by a number of different procedures including impact, kneading, and static type loadings and partial to full coverage of the surface of the soil. The procedure used in this investigation is a non-impact, rapid rise-time, controlled loading rate type of loading with full coverage of the soil surface. To better understand the explanation, it is stressed that at no time during compaction is the external compressive load released. It builds up rapidly to some predetermined peak, is maintained at this value for a time considerably longer than was required to reach the peak, and is finally released concluding densification of the soil.

The densification occurs, at an ever decreasing rate from the outset of loading, due to (1) aggregate rearrangements not requiring deformation, (2) aggregate rearrangements initiated by slight squashing or yielding, (3) void space filling as aggregates are deformed and literally flow into the necessary shape, and finally (4) the reduction of possible intra-aggregate air voids.

As the density increases, discrete aggregates become less and less apparent until finally they lose their individuality almost completely.

The microstructure or fabric of an individual aggregate also may change. If the change does occur it will be toward a more directional arrangement of particles, parallel to the plane of major stress increase. The particle reorientation occurs as a result of intra-aggregate straining and surface smearing. Fabric reorientation increases as density increases and as the aggregate water content increases.

DESCRIPTION OF EXPERIMENTAL PROGRAM

The experimental program designed for this investigation consists of two general parts. The first part is concerned with various properties and characteristics of the individual aggregates and is described in this section. The second part of the program investigates properties and characteristics of the soil mass during and after compaction. These tests are described in the following section entitled FABRIC STUDIES.

Soil

The single raw material used for this study was a naturally occurring Florida Kaolin mined commercially by the Edgar Plastic Kaolin Company and known as EPK Airfloated Kaolin. Its mineralogical composition is approximately 99.5% kaolinite with the remainder as quartz and mica.

The classification properties of this soil are given in Table 1.

Table 1. Classification Properties of EPK Airfloated Kaolin

Liquid Limit	58.5%
Plastic Limit	36.5%
Specific Gravity of Solids	2.60
Clay Fraction (< .002 mm)	81.0%

This particular soil was used because it is readily available in large batches which do not differ significantly from one another; a considerable amount of complimentary experimental information has been gathered for this soil at Purdue and elsewhere; and finally because its lack of impurities makes it amenable to the X-ray diffraction technique for measuring relative particle orientation. In addition to these reasons the lack of a significant quantity of inert filler, i.e., silt and sand, enhances resolution of the experimental results.

Soil Preparation

The initially air-dry soil was brought to the desired moisture content with the use of a Patterson-Kelley Twin Shell Liquid-Solids Blender, shown in Figure 15. In this machine the soil within the slowly rotating shell is continually dropping onto, and being agitated by, rotating high-speed beaters. The shell rotates at 20 rpm, while the beaters rotate at 2,800 rpm. The water is introduced through a flexible line into the hollow axle of the rotating beaters whereupon it enters the shell as a mist, due to the motion of the beaters. Figure 15 shows the blender equipped with a lucite shell, however a stainless steel shell was used for this soil preparation.

Detailed operational procedures were developed by trial, with the objective of producing a distribution of discrete soil aggregations. Test batches K-1 and K-2 each consisted

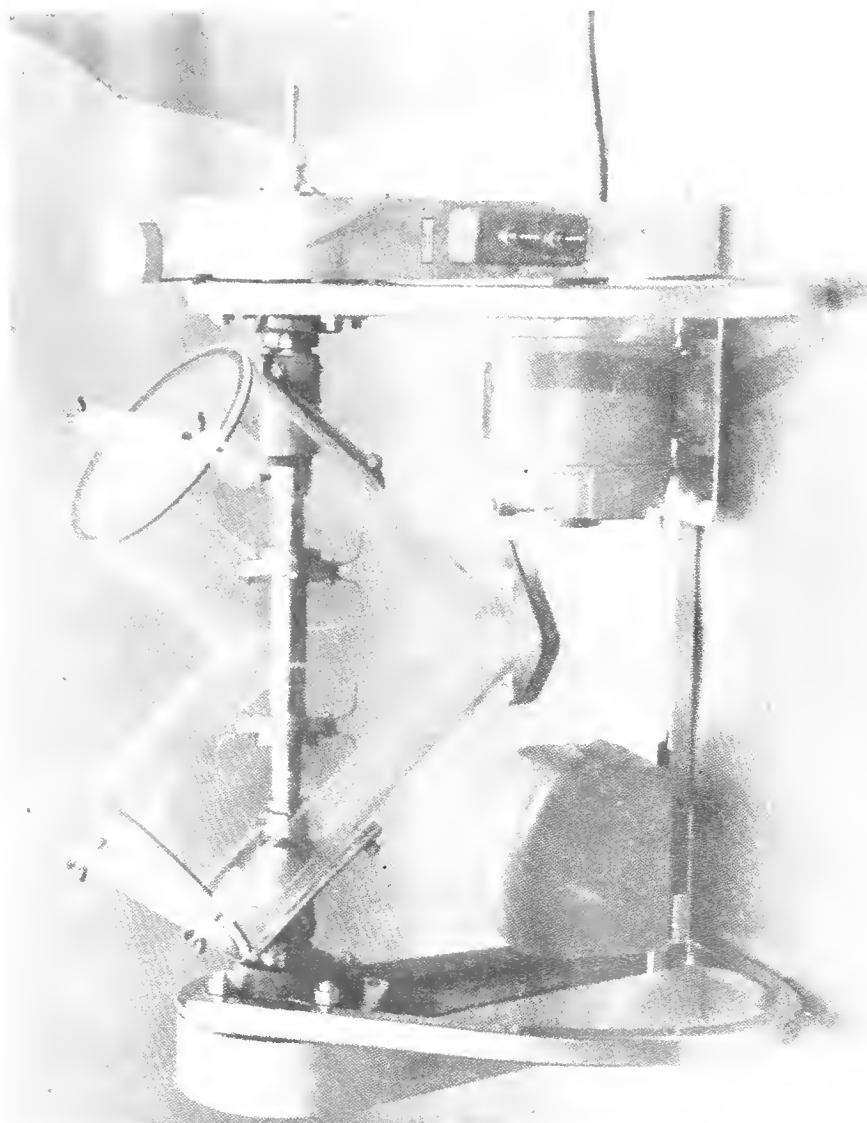


FIGURE 15. PATTERSON - KELLEY BLENDER

of approximately 10,000 grams of dry soil (the air-dry water content was between 1% and 2%) plus enough water for the desired moisture content. They were mixed in four parts each. The mixing procedure was to charge the shell with 2,500 gm. of soil, start the shell rotating, engage the high-speed beaters, add 100 ml. of water over a period of one minute, allow the rotation and agitation to continue for another four minutes, add another 100 ml. of water, etc., until the necessary amount of water has been added to the soil.

Several times during mixing, the beating and rotation were suspended while the shell was opened and soil clinging to the beaters and inside walls of the shell were scraped away. This procedure was also followed for the other three portions, and finally all four portions were combined and mixed gently by hand in a triple polyethylene bag. All layers of the bag were then sealed individually and the soil stored at room temperature for a minimum of 48 hours before further processing.

Batch K-3 was prepared in the same manner except that it contained 7,000 gm. of soil by dry weight and was mixed in two 3,500 gm. portions.

After the storage period, the soil was sieved gently by hand, in order to obtain variously sized fractions of the soil aggregations. The nest of U.S. standard sieves consisted of the #4, #6, #8, #10, #12, #20, #40, and the pan. The material retained on each sieve was stored in air-tight glass bottles at room temperature. The designation used

for the material includes the batch number, the smallest sieve size opening through which the aggregates passed, and the size sieve on which the aggregates were retained. For example, K-2, P8-R10 indicates that these aggregates are a part of batch K-2, they passed through the #8 U.S. standard sieve, and they were retained on the #10 sieve. Aggregate size distribution curves based on the sieve size openings are given for these batches in Appendix A.

The aggregate size distributions are recognized to be dependent upon the details of the mixing procedure. However, holding this procedure constant permitted a focus upon and an assessment of the water content variable in the production of aggregates.

Intra-aggregate Relations

It is conventionally convenient to separate schematically the three phases in a soil system. Where $s \equiv$ solids, $w \equiv$ water, $a \equiv$ air, $V \equiv$ volume, $W \equiv$ weight, and $V_v = V_w + V_a$. See Figure 16.

In this study, we require the additional subdivision of the void space into those portions within the aggregates (intra-aggregate) and those between the aggregates (inter-aggregate). Figure 17 illustrates the intra-aggregate volume, using the subscript "A" to denote intra-aggregate quantities.

A portion of the aggregate voids are surface ones, which introduces some uncertainty into the measure of

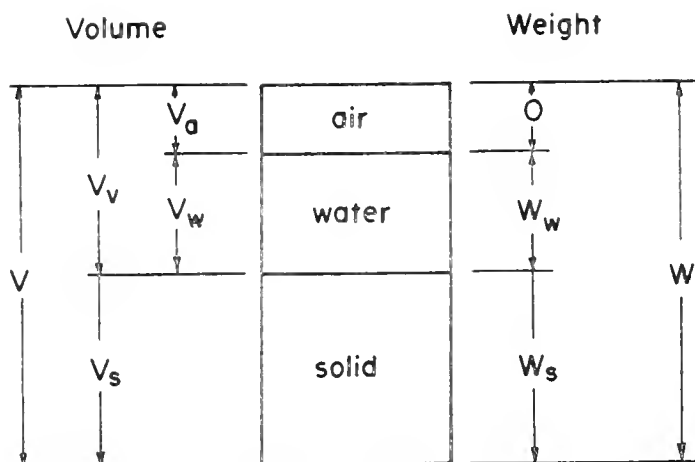


FIGURE 16. GROSS VOLUME-WEIGHT RELATIONSHIPS

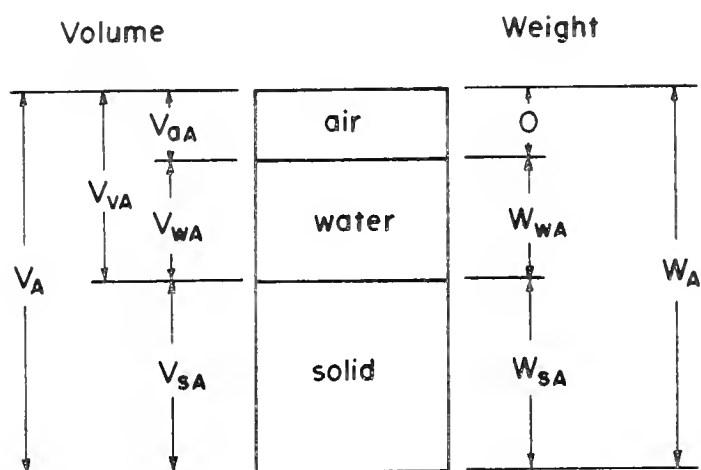


FIGURE 17. INTRA-AGGREGATE VOLUME-WEIGHT RELATIONSHIPS

aggregate volume. The bulk specific gravity interpretations useful for "permanent" mineral aggregations may also be applied here.

If a collection of aggregations is characterized by intra-aggregate measures, these measures are averages for the collection. To show that a collection of aggregates is involved, introduce the symbol " Σ ", as in Figure 18.

In a compacted soil mass, we have defined inter-aggregate void space as well. The total phase diagram could be drawn as shown in Figure 19.

Table 2 shows the comparative values of defined ratios of interest between intra-aggregate and total soil values.

With respect to the intra-aggregate quantities, $\Sigma V_{vA} + V_s = \Sigma V_A$ appears in the denominator of three tabled ratios. Further, V_s can be determined from W_s and an experimental determination of the apparent specific gravity, G_s , viz.,

$$V_s = \frac{W_s}{G_s \gamma_w}$$

and $\Sigma V_{vA} = \Sigma V_A - V_s$

Accordingly, to characterize the condition of the aggregates, volume measurements on them are required.

Description of Mercury Intrusion Technique for the Determination of Aggregate Volume

The intrusion equipment used consists of a penetrometer, Figure 20, and a mercury filling device, Figure 21.

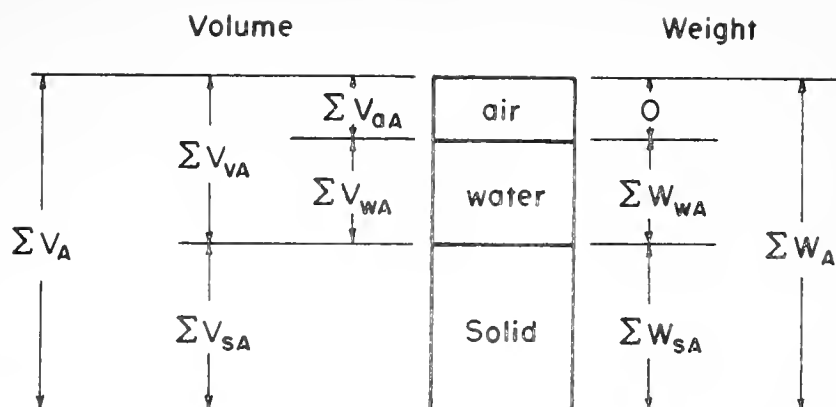


FIGURE 18. INTRA-AGGREGATE VOLUME-WEIGHT RELATIONSHIPS FOR AN ASSEMBLAGE OF AGGREGATES

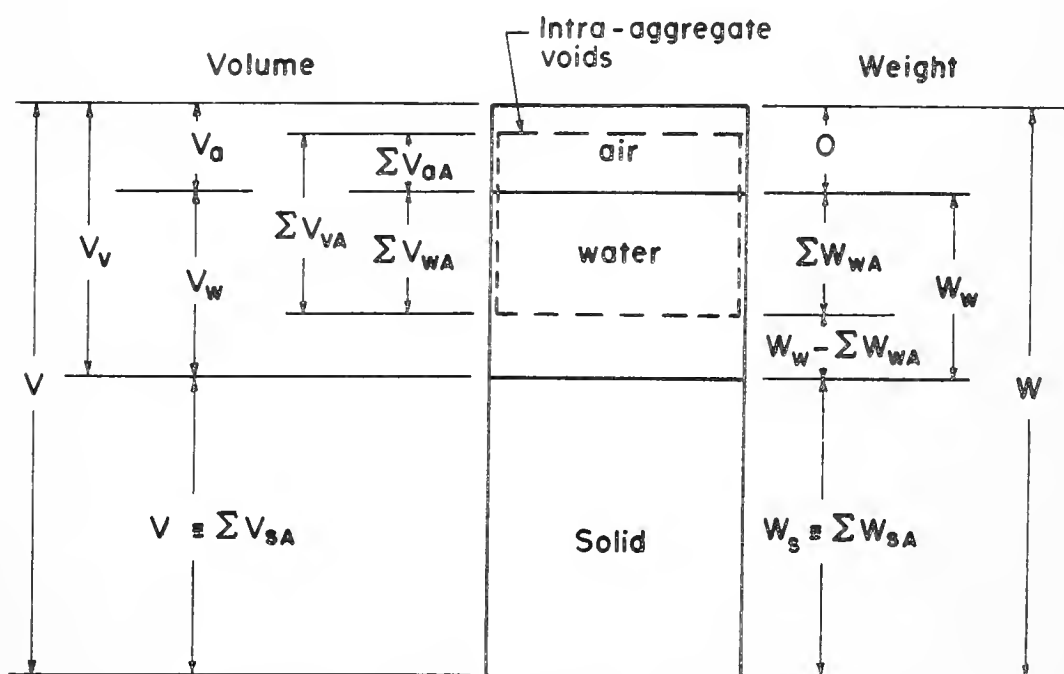


FIGURE 19. TOTAL SYSTEM VOLUME-WEIGHT RELATIONSHIPS FOR AN ASSEMBLAGE OF AGGREGATES.

Table 2. Comparative Values of Defined Ratios of Interest Between Intra-aggregate and Total Soil Values.

<u>Ratio</u>	<u>Total</u>		<u>Intra-aggregate</u>
water content	$\frac{W_w}{W_s}$	\geq	$\frac{\sum W_{wA}}{W_s}$
degree of saturation	$\frac{V_w}{V_v}$		$\frac{\sum V_{wA}}{\sum V_{vA}}$
void ratio	$\frac{V_v}{V_s}$	$>$	$\frac{\sum V_{vA}}{V_s}$
porosity	$\frac{V_v}{V_v + V_s}$		$\frac{\sum V_{vA}}{\sum V_{vA} + V_s}$
dry unit weight	$\frac{W_s}{V_v + V_s}$	$<$	$\frac{W_s}{\sum V_{vA} + V_s}$
wet unit weight	$\frac{W}{V_v + V_s}$		$\frac{W_s + \sum W_{wA}}{\sum V_{vA} + V_s}$

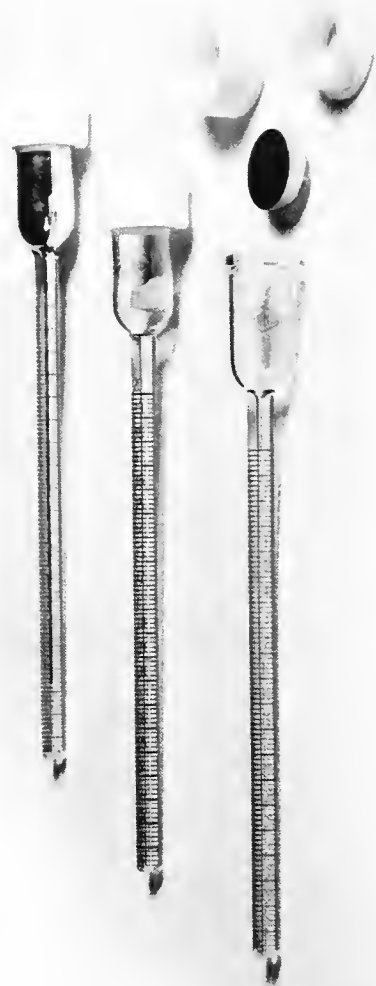


FIGURE. 20. PENETROMETERS: DISASSEMBLED, ASSEMBLED WITH SAMPLE, AND FILLED WITH MERCURY; AFTER WINSLOW (66)

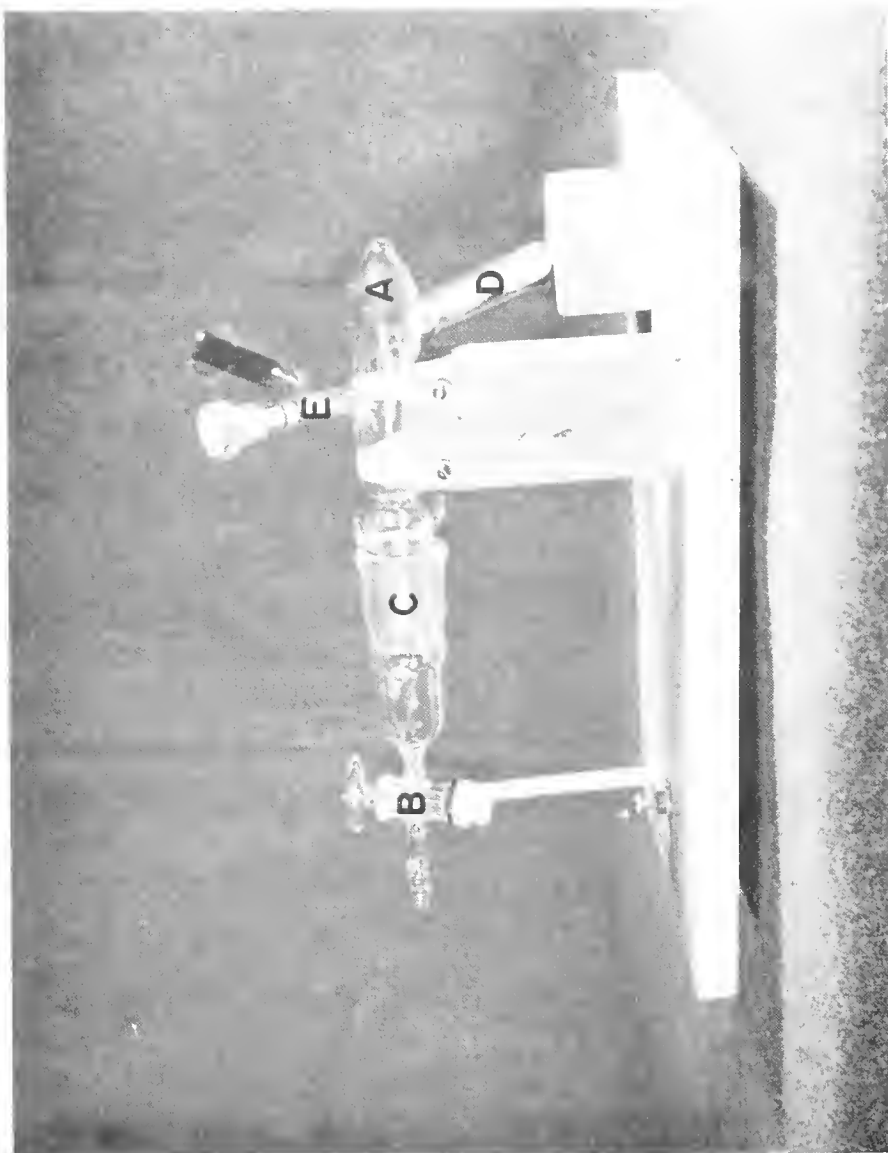


FIGURE 21. FILLING DEVICE; ADAPTED FROM WINSLOW (66)

The penetrometer, which houses the dry soil sample and ultimately the mercury, has a bulb volume of about 6 ml. and a precision bore capillary stem calibrated at 0.002 ml. intervals. Referring to Figure 21 the filling device consists of a two-chambered glass tube closed at one end, A, and with a stopcock, B, at the other end. This main tube can be separated at a ground joint, C, to allow the penetrometer to be positioned within the filling device. A side arm, D, which functions as a mercury reservoir, and another stopcock, E, used to introduce additional mercury between tests are also attached to the main chamber. A more detailed description of this apparatus is given by Winslow (66).

The volume measurement procedure is as follows:

1. The weight of the penetrometer of known volume is recorded.
2. The weight of the penetrometer and dry aggregates (freeze-dried (1) to control volume change upon drying) is recorded.
3. The penetrometer is placed in the double-chambered glass tube of the filling device, and the penetrometer and filling device are evacuated by means of a vacuum pump.
4. The system is evacuated to the lowest obtainable pressure. Typically this is 0.010 mm. Hg.
5. The system is isolated from the vacuum pump and mercury is allowed to cover the penetrometer stem by rotating

the filling device, thus elevating the side arm mercury reservoir.

6. A needle valve in the line connecting atmospheric pressure and the evacuated filling device is momentarily cracked, raising the pressure within the filling device and driving mercury into the evacuated penetrometer-soil aggregate system.

The desired pressure increase within the filling device is 30 to 50 mm. Hg. This initial pressure increment causes the penetrometer bulb to be flooded with mercury; the only space not occupied by the mercury is occupied by the soil aggregates. This is something of a simplification, however, since a small, but measurable volume of air is not evacuated from the penetrometer. The aggregates are in contact with each other and many are in contact with the inside glass surface of the penetrometer. Each such contact gives rise to what can be considered an air pore, with an ever-decreasing radius as the contact point is approached. The entrance of a liquid, mercury in this case, into a circular pore can be estimated by the following equation (65)

$$D = \frac{-4 \gamma \cos \theta}{p}$$

where

D = diameter of a circular pore

p = pressure difference between the intruding liquid and the pore interior

γ = surface tension of the intruding liquid, 484
 dynes per cm. for mercury in a vacuum at 25°C (15).
 θ = contact angle of intruding liquid on the pore
 wall, 146° for a mercury - kaolinite interface (11).

Since soil pores are not circular in section, the resulting pore sizes are spoken of as equivalent pore sizes.

In addition to the mercury-free volumes near the aggregate contact points, each aggregate is both surficially rough and contains a multitude of interconnected pores open to the surface of the aggregate. At low intrusion pressure, even the aggregate surface may be imperfectly wetted by the mercury, and the interior voids are most certainly mercury-free. See Figure 22. The objective is to wet the entire surface of each aggregate without intruding the mercury into the internal pore system of the aggregate, and to calculate the total aggregate volume at this time.

The task is simplified by the fact that the pores within the aggregates have much smaller effective radii than most of the surface irregularities, and all but a very small portion of the external volume is at contact points among the aggregates. Therefore, at some indeterminate intrusion pressure, each aggregate will be almost totally wetted, yet the mercury will not have intruded any interior pores.

As indicated previously, the initial mercury filling of the penetrometer containing the aggregates is accomplished

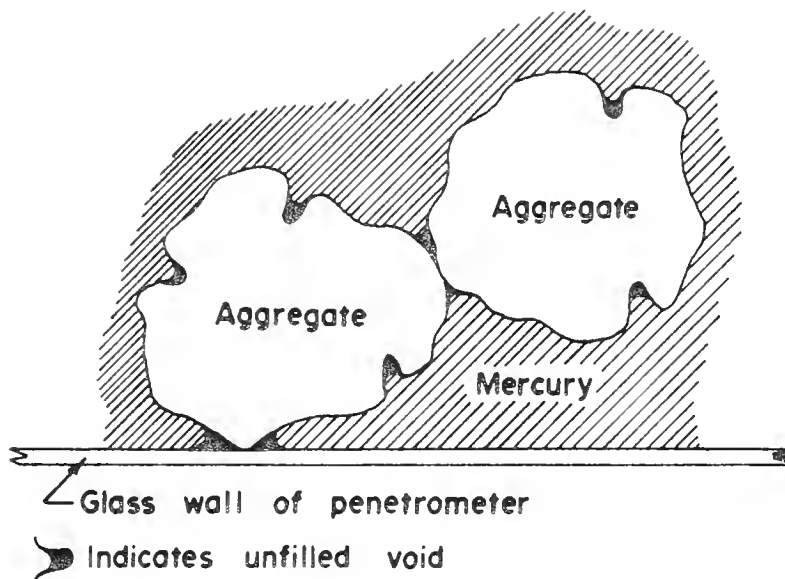


FIGURE 22. REPRESENTATION OF AGGREGATE-MERCURY SYSTEM WITHIN PENETROMETER AT INSUFFICIENT MERCURY PRESSURE TO COMPLETELY FILL INTER-AGGREGATE AND SURFACE VOIDS

at a relatively low intrusion pressure. When this has been accomplished, the filling device is rotated about its major axis enough to lower the side arm reservoir, thus draining the mercury away from the penetrometer and exposing the entire penetrometer stem. At this time the calibrated stem is read at the interface of mercury and low pressure near the open end. Typically the stem is full or nearly so. Any pressure increase in the filling device after this time drives the constant volume of mercury further into the penetrometer stem as smaller voids are intruded under the higher pressure. The void volume intruded under any pressure increment can be measured simply by reading the calibrated stem, making corrections for the various factors involved. The results of a typical test of this type are shown in Figure 23 showing the cumulative void penetration as a function of intrusion pressure. The point of zero cumulative void penetration corresponds to the total apparent volume occupied by the aggregates within the penetrometer. As can be seen, the first few increments of pressure increase result in comparatively large void penetration compared to the void penetration occurring due to pressure increments at higher pressures. The reason for this is that at the lower pressures, the individual aggregates are imperfectly wetted, and small pressure increases will drive the mercury further into the voids among the aggregates in contact with one another or the

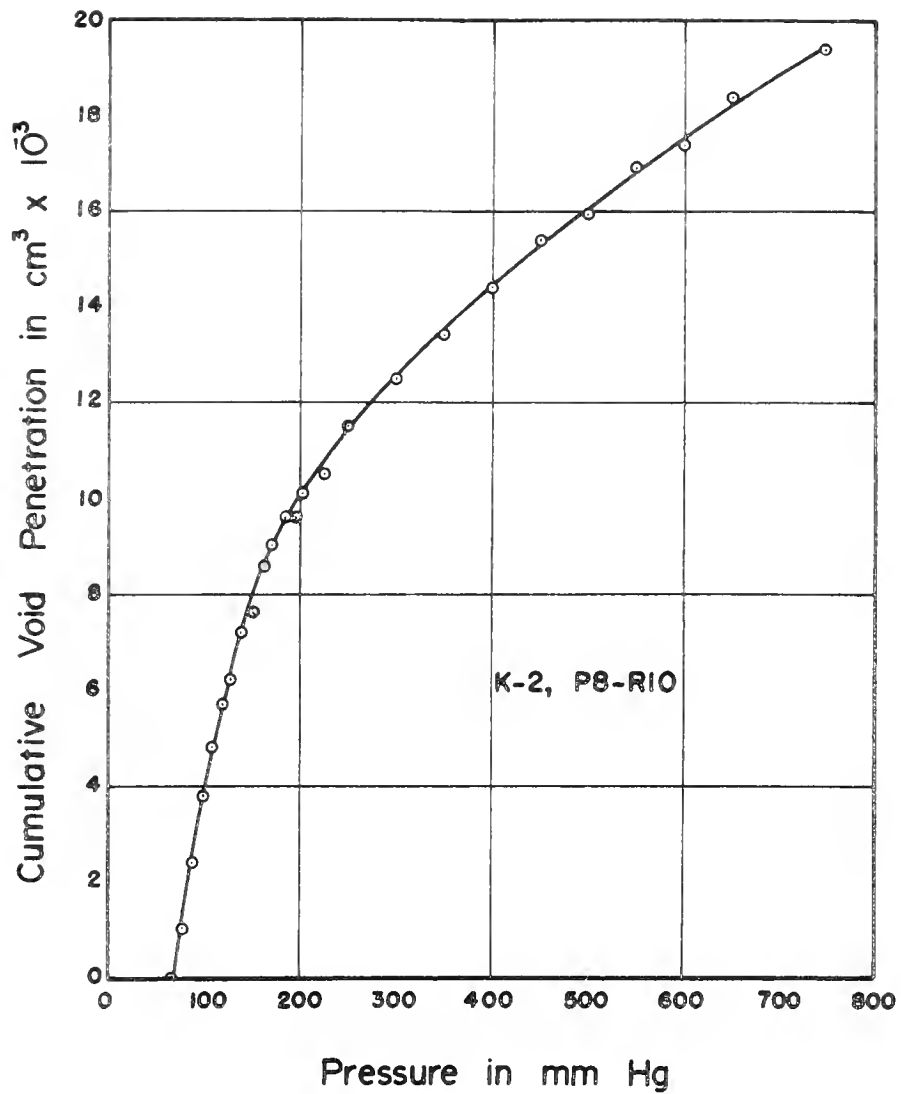


FIGURE 23, DETERMINATION OF INTER-AGGREGATE VOIDS ($V_v - \Sigma V_{va}$) FOR A LOOSE ASSEMBLAGE OF AGGREGATES

glass penetrometer and into the large radius surface voids. At successively higher pressures these voids have been filled and the mercury is being intruded into smaller and smaller pores within each aggregate. Although at this higher pressure many more pores are being intruded, their small size leads to a rather small volume change, as can be seen from the Figure.

There is some value of pressure which corresponds to the true volume of the aggregates (ΣV_a). At this value, the physical picture would show the group of aggregates, some in contact with one another, imperfectly wetted by the mercury, but with many of the aggregates having their largest internal voids already intruded by mercury. At this pressure value, the intruded intra-aggregate volume is equal to the inter-aggregate volume near the contact points which has not yet been intruded. As previously mentioned, this pressure value is indeterminate due to the complex void shapes and the simplifying assumption of circular pores used in the intruded pore size equation.

There is, however, little practical difficulty encountered here since the void penetration as a function of pressure increase is small over the entire range compared to the volume of the aggregates within the penetrometer. In Figure 23, which shows the relation between intrusion pressure and void penetration, the aggregates' volume at zero cumulative void penetration is 1.0863 cu cm, and the change in apparent volume due to intrusion from the filling pressure to

atmospheric pressure is about 2.5% of the apparent volume at the intrusion pressure. The aggregate volume at 100 mm. Hg. intrusion pressure was chosen as the best volume measure. Judging from the shape of the cumulative void penetration vs. intrusion pressure curves, this volume may be slightly too large.

A number of samples were run in this manner after first photographing the entire group of dried aggregates comprising each sample.

Although not a part of this study, this equipment, viz., the penetrometer, filling device, and an additional higher pressure porosimeter, can be used to study the pore-size distribution characteristics of compacted soils down to an equivalent pore size of a few hundred Å (1, 11, 58).

Photographic Measuring Technique for the Determination of Aggregate Volume

Numerous difficulties were encountered in the liquid displacement approach to measurement of aggregate volumes. In addition to those described in the previous section there is the practical difficulty of removing the molding water with insignificant volume change prior to the volume measure proper. This may be accomplished rather successfully by freeze drying, but special apparatus and technique is of course involved. Difficulties are also related to the aggregate size. The applicability of this technique to large aggregates is limited by the internal volume of the penetrometer. Also as the number of aggregates within



the penetrometer increases, the increased number of particle contacts seems to introduce a greater error due to incomplete wetting. Accordingly alternate techniques were sought and significant success was achieved with a photographic analysis.

The method chosen was an indirect one wherein the aggregates to be analyzed were photographed, the photos were enlarged as transparencies, and the diameters of the photo images of the aggregates were measured individually. Sample enlargement prints are shown as Figures 24 and 25. The diameters were measured by the use of a Zeiss Particle Size Analyzer, Model TGZ-3, an instrument specifically designed to measure particulate size, shape, roughness, etc. The analyzer functions by using (20) "... an iris diaphragm, illuminated from one side, which is imaged by a lens onto the plane of a plexiglass plate. An enlargement of the photograph is put on this plate. By adjusting the iris diaphragm the diameter of the sharply defined circular light spot appearing on the enlargement can be changed and its area made equal to that of the individual particles. If particles deviate from a circular shape, this circular measuring mark must be so adjusted that the total area of protruding portions of the particle becomes equal to that of the reentrant ones... The different diameters of the iris diaphragm are correlated, via a collector, with a number of telephone counters, each counter corresponding

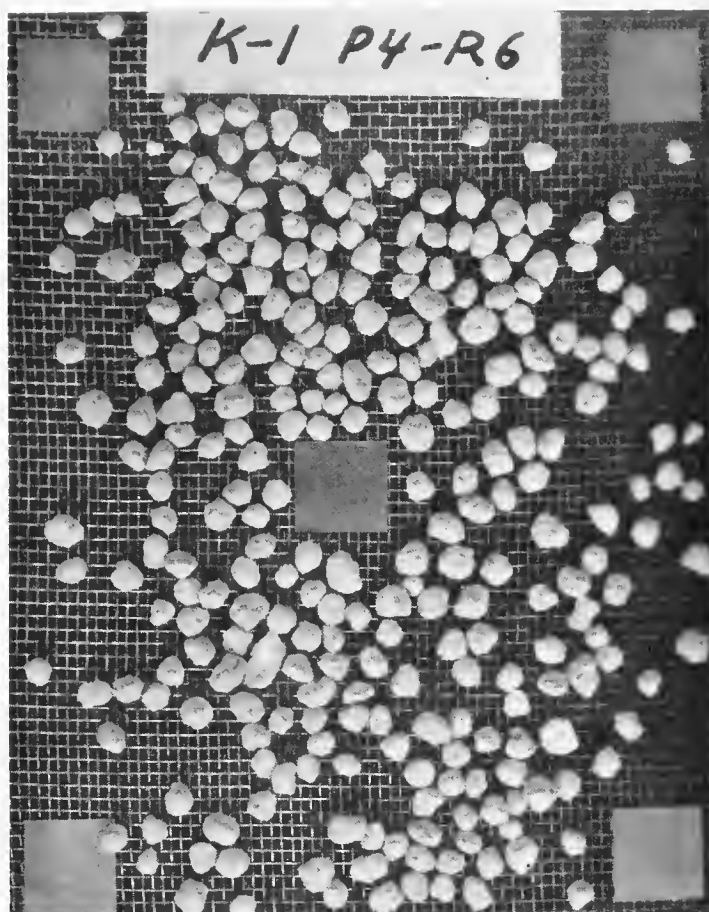


**FIGURE 24. SAMPLE ENLARGEMENT PRINT OF AGGREGATES
K-1, P4-R6**

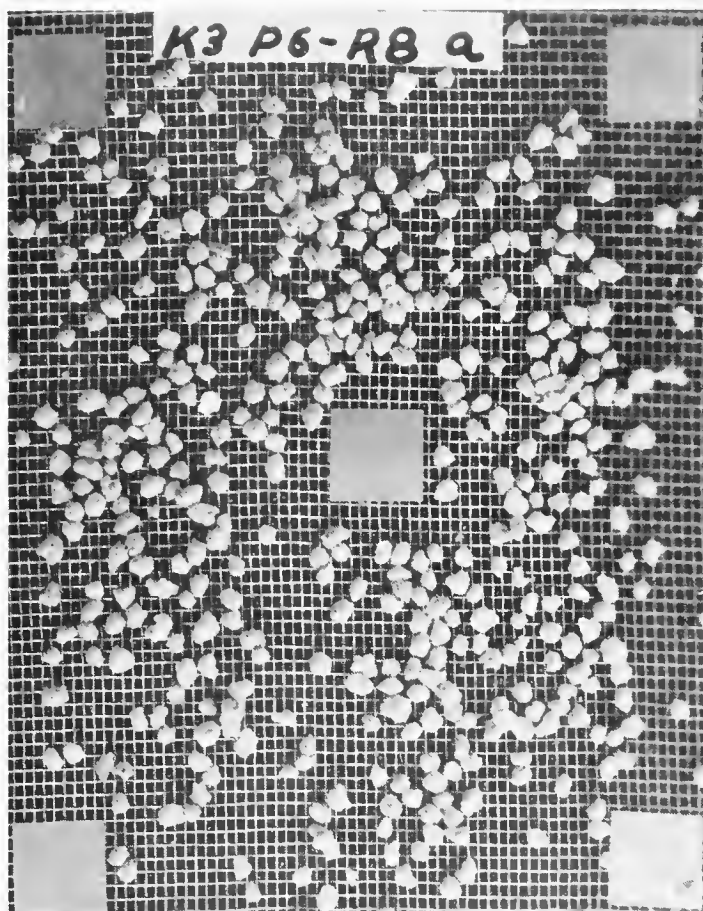


FIGURE 25. SAMPLE ENLARGEMENT PRINT OF AGGREGATES
K-3, P6-R8

to a certain aperture interval of the iris diaphragm. When the measuring mark is equalized with a particle in the photograph, the footswitch is depressed. Thus the correlated counter is actuated, and a puncher marks the counted particle on the photograph." The diameter measuring ranges with this machine are 1.0 to 9.2 mm. and 1.2 to 27.7 mm., with each range being tabulated in 48 parts, either equally or exponentially.

The diameter size distribution measurements, coupled with an assumption that the aggregates were spheres permitted the determination of an aggregate volume distribution. Such a frequency distribution could be plotted and characterized by an arithmetic mean and a coefficient of variation,¹ see Figure 26 for a sample. Reproducibility of results and variation from one operator to another were also checked with gratifying results. Table 3 shows the results of a check to determine the reproducibility of results using: (a) identical photos with two different operators, and (b) photos of the same sample at different magnifications with one operator.

Although the results from the particle analyzer are reproducible, there is no assurance that the lack of sphericity, preferential orientation of the aggregates on the background grid, and other unrecognized factors do not

1. Coefficient of variation is standard deviation (σ) :
mean (\bar{X}).

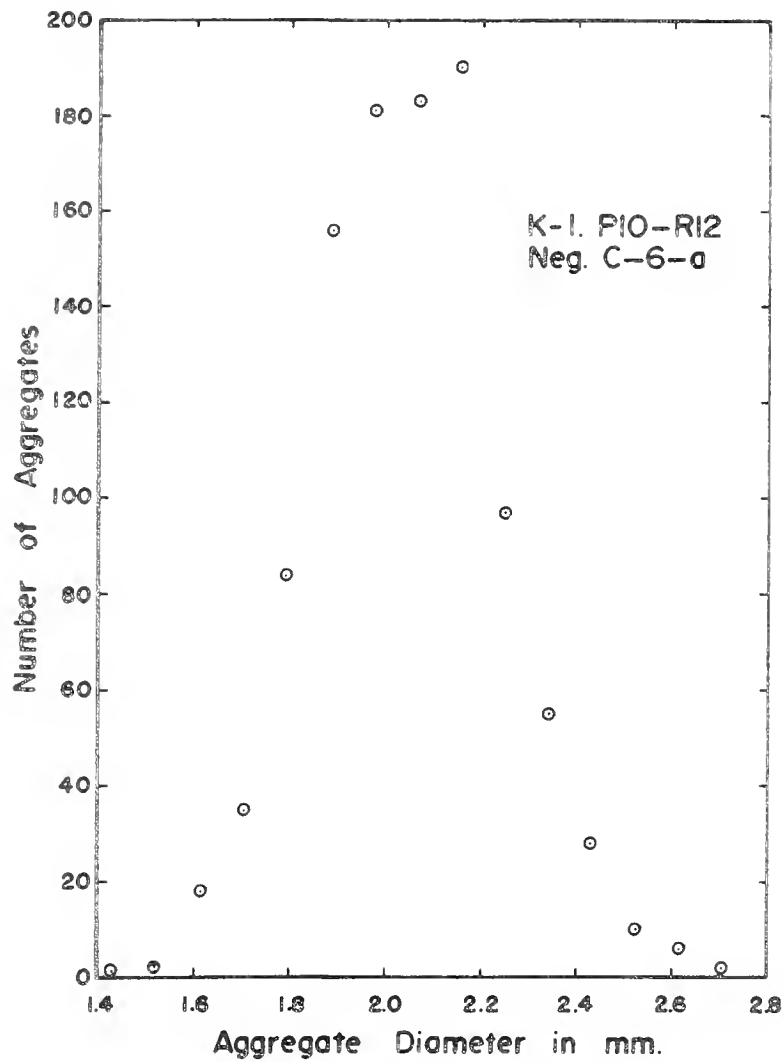


FIGURE 26. AGGREGATE DIAMETER FREQUENCY DISTRIBUTION

Table 3. Reproducibility Check on Photo Measurements.

Neg #	Size	Batch	Photo		(cm)		σ	(%) C.V.	(cm ³)		# agg.	Operator
			Mag.	Mag.	Mean	dia.			Mean	vol.		
					\bar{X}				\bar{X}			
C-6	P10-R12	K-1	1.96X		0.1996		.020297	10.17	.00400		1046	1
C-6	P10-R12	K-1	1.94X		0.2049		.022768	11.11	.00431		1059	2
C-6-a	P10-R12	K-1	2.02X		0.2046		.01923	9.40	.00436		1049	2

cause the calculated volumes to be in error. Accordingly, these measures were compared with those made by the mercury intrusion technique following freeze drying, i.e., the sample was weighed and photographed after freeze drying and then placed in the mercury penetrometer.

The photo for each sample was measured with the particle analyzer, and these results were compared with the aggregate volume results found with the mercury intrusion method. For each sample the ratio of the arithmetic mean aggregate volume by mercury intrusion (\bar{Y}) to the arithmetic mean aggregate volume by photo measurement (\bar{X}) was calculated and defined as the correction factor (CF).

$$CF = \frac{\bar{Y}}{\bar{X}}$$

The relationship between (\bar{X}) and CF was subjected to a least squares linear regression analysis, for which the equation is

$$CF = 0.82107 + 4.0909 \bar{X}$$

One can alternately view both measures as subject to significant errors and conclude that the above equation simply relates two somewhat incorrect values. Conversely, it can be concluded that both methods can yield volume values which are sufficiently precise to accomplish the comparisons needed in the research. The largest (P4-R6) and the smallest (P20-R40) aggregates were not used for the determination of the correction factor equation, and its application to them is by extrapolation.

Aggregate Weights and Weight-Volume Ratios

The weight of solids per aggregate, W_{SA} was determined for each material size of each batch by hand counting the number of aggregates in a sample, oven drying them at 110°C to constant weight, weighing the sample on an analytical balance, and dividing the resulting W_s by the number of aggregates. For the very small material, P12-R20 and P20-R40, the aggregates were photographed and counted on the photograph rather than by hand. However, even for these small sizes, some hand counts were performed.

For many sizes, three or even four independent determinations were made. All plausible determinations within a given batch and size were averaged for a final W_{SA} for that particular material. Sample results are shown below in Table 4.

Table 4. Sample Results of Aggregate Weight Determinations

<u>Size</u>	<u>Batch</u>	<u>Total No. of Aggs. Weighed</u>	<u>Avg. W_{SA} in gm.</u>
P4-R6	K-1	649	0.03915
P8-R10	K-2	926	0.00670
P20-R40	K-3	1372	0.000150

Using the W_{SA} the averaged aggregate volume from photographic measurements, and the correction factor for each volume, aggregate dry unit weights were obtained. All dry unit weights are shown under Results. Typical sample results are shown below in Table 5.

Table 5. Sample Results of Aggregate Dry Unit Weight Determinations

Size	Batch	(cm ³) Avg. \bar{X} vol.	Correction Factor	(cm ³) Corr. \bar{X} vol.	(gm) \bar{W}_{SA}	lbs/ft ³ γ_d
P4-R6	K-1	.03380	.959	.0324	.03915	75.5
P8-R10	K-2	.00603	.846	.00510	.00670	82.0
P20-R40	K3	.00018	.822	.000097	.000150	96.5

Description of Aggregate Deformation Test

In an effort to learn more about the load-deformation characteristics of the aggregates which were compacted into the gross specimens, tests were conducted on individual aggregates.

The equipment used consisted of a five pound capacity Statham load cell, a constant displacement rate Wykeham-Farrance loading press, a 1/4 inch thick polished aluminum lower platen, and a smooth lucite upper platen attached to the load cell. The output of the load cell was recorded on a Model 321 Sanborn strip-chart recorder.

The procedure used was to place a single aggregate on the lower platen, raise the lower platen until contact between the aggregate and the upper platen was imminent, and to then crush the aggregate at a constant displacement rate while recording the load being generated. No attempt was made to select particular aggregates to be tested, only aggregates which were obviously oversize or undersize due to incomplete sieving were discarded.

Typically the load increased linearly with the deformation to a point and then increased less rapidly or even decreased. This was followed by a rapid increase of the load as the fully-deformed aggregate was further squeezed between the platens. The displacement rate was chosen within the confines of undrained testing and protection of the fragile low-capacity load cell. Several displacement

rates were tried and the rate of 0.1 inches/106 seconds was finally used. Using this rate, a test was typically concluded in less than thirty seconds, and the final build-up of load was slow enough so that the press could be stopped before damage occurred. This rate was doubled for one duplicate series of tests, and the results did not indicate significant time dependence within this range.

FABRIC STUDIES

Such studies were carried out in a direct fashion by X-ray diffraction and to a lesser degree by the qualitative examination of stereomicrograms obtained with a modern scanning electron microscope.

Sample Preparation for Diffraction Study

The samples were prepared following, in general, the procedure outlined by Martin (36). The material used for impregnation was polyethylene glycol 6000 (commonly called carbowax), which has a strong affinity for water, is solid at room temperature, and melts at approximately 60°C.

Compacted samples were submerged in liquid carbowax, at a temperature of 65°C, as soon after compaction as was practical. Typically, the time lag was about 15 minutes, and during this time the sample was stored in a sealed moisture box. Initially, the carbowax was not allowed to completely surround the sample, some of the upper surface being open to the atmosphere so that entrapped air could escape. However, the low permeability of the soil and the rapid drying of the surface at the elevated temperature did not justify the slight benefits to be gained, and after 5 to 10 minutes, additional carbowax was added so that the sample was completely submerged.

The submerged samples were maintained at 65°C., and periodically the carbowax was decanted and replaced with freshly-melted carbowax. Several repetitions of this procedure were usually required to ensure complete removal and replacement of the water by carbowax. Removal of water was judged to be complete when a sample had been submerged in carbowax for a minimum of three weeks, the carbowax had been changed twice, and the decanted carbowax which was allowed to solidify was of the same color and hardness as carbowax which had not been in contact with the soil. If at this time the decanted carbowax remained soft after solidification, further submergence of the sample and carbowax changes were carried out until all water had been removed from the system.

Uncompacted aggregate samples were impregnated similarly, except that each quantity of aggregates was covered with liquid carbowax immediately, so that no moisture was lost through evaporation.

After impregnation, each sample was removed from the oven and allowed to cool to room temperature while remaining in its aluminum container. After the sample was cool and the carbowax solidified, it was stored in a dessicator at room temperature.

Each hardened sample was prepared for the X-ray diffraction study by removal from the tare and cutting of the carbowax from above its upper surface with a coarse-bladed

coping saw. After removal of the excess carbowax, approximately $\frac{1}{8}$ in. of the upper surface was also sawed off and discarded, with care being taken to maintain the upper and lower surfaces in a parallel condition. To smooth the sample's upper surface after sawing, it was lapped against a flat glass plate, using 60 grit carborundum powder and kerosene.

At this point, the sample was cut to a size which would fit the holder on the goniometer of the diffractometer. A one-inch square sample was cut from the central area of the original sample, this smaller sample's upper surface was lapped against the glass plate with 150 grit grinding powder and kerosene, and finally it was lapped again using 600 grit Crystolon 600B silicon carbide grinding powder and kerosene. This completed the preparation of the sample and its surface for the X-ray diffraction study.

Determination of Particle Orientation

The X-ray diffraction patterns were obtained using a General Electric XRD-5 diffractometer. Information concerning machine settings, radiation source, etc., is given in Appendix B.

Each sample was scanned from $2\theta = 15^\circ$ to $2\theta = 30^\circ$. This range allowed the 020 peak at $2\theta \approx 19.9^\circ$ and the 002 peak at $2\theta \approx 24.8^\circ$ to be observed.

The measure of particle orientation used was the ratio of the height of the 002 peak to the height of the 020 peak,

and the peak heights were measured from a base line connecting the trace of the background radiation at $2\theta = 18^\circ$ with that of the background radiation at $2\theta = 30^\circ$.

Random and well-oriented kaolinite samples were prepared according to the procedure suggested by Martin (36), and their 002/020 peak height ratios were used to evaluate the relative orientations of the samples examined.

Although there were exceptions (see Appendix C), eighteen X-ray diffraction patterns were obtained from each carbowax-impregnated sample, in the following manner. The sample was surfaced as previously described, mounted in the goniometer specimen holder, and the diffraction pattern between 15° and 30° was obtained three times, without moving the sample in its mount. At this point, the sample was rotated 90° so that the X-ray beam was diffracting from the same surface, but perpendicular to its previous path. After this rotation, three more patterns were generated without repositioning the sample in the mount. The sample was next removed from the mount and a new surface exposed by resurfacing the previously investigated face with 150 grit powder and kerosene, followed by 600 grit powder and kerosene. After resurfacing, six more patterns were obtained as described above, the sample was again resurfaced, and six more diffraction patterns were made, for a total of eighteen patterns over what can be considered six different sample

areas. The peak heights and peak height ratios for each individual pattern are given in Appendix C.

Direct Examination of Fabric

Visual examinations were made of the original kaolinite powder, of the aggregates prior to compaction, and of freshly fractured surfaces of compacted specimens. These examinations were undertaken with the aid of a Cambridge Scanning Electron Microscope and a Jeolco¹ Model JSM U-3 scanning electron microscope. Both instruments are similar in operation and availability governed the use of one or the other.

The sample requirements for scanning electron microscopy are that the sample be dry and that it conducts electricity. The first requirement is easily satisfied by starting with dry material (as was the case with the original kaolinite powder) or by removing the water by means of heat, freeze drying, or critical region drying (11). The second requirement, conductivity, is usually satisfied by applying a few molecular layers' thickness of metal to the sample's surface. Alternately, conductivity can be achieved by gluing the sample to the metal machine mount with silver paint. In this work samples were either initially dry or dried by freeze drying, and conductivity was achieved by both alternate techniques. That is, some specimens were coated with carbon followed by gold-palladium and some were

1. Japan Electron Optics Laboratory Company.

glued with silver paint. Both techniques gave acceptable results.

The observations confirmed the existence of domains. They also showed that discrete aggregates could be recognized in the compacted samples.

Sample Compaction

With reference to Figure 27, samples were compacted in a specially designed mold, A, with the effort being applied by an MTS Model 483.01 Servo-Hydraulic Tester, B. This combination along with a moderately high-speed Sanborn Model 321 Dual Channel Carrier Amplifier-Recorder, C, and a high speed Brush Model 16-2300 Oscillograph, D, allowed the achievement of sample densification to be monitored in detail.

In the full face coverage compaction process (generally termed "static"), it was possible to: control the rate of loading, monitor the axial deformation or compression, measure the input load, and measure the load transferred to the bottom of the mold by the sample, all as a function of time.

The compaction mold (referred to hereafter as the cell), fabricated especially for this research, is shown in Figures 28 and 29. It consists of a brass ring, a recessed lucite base containing silicon oil, a teflon membrane separating the silicon oil from the brass ring, an aluminum spacer within the brass ring, resting on the teflon membrane, and a Statham Model Number PG132TC-500-350, 500 psi strain gage pressure transducer. The brass ring was instrumented with

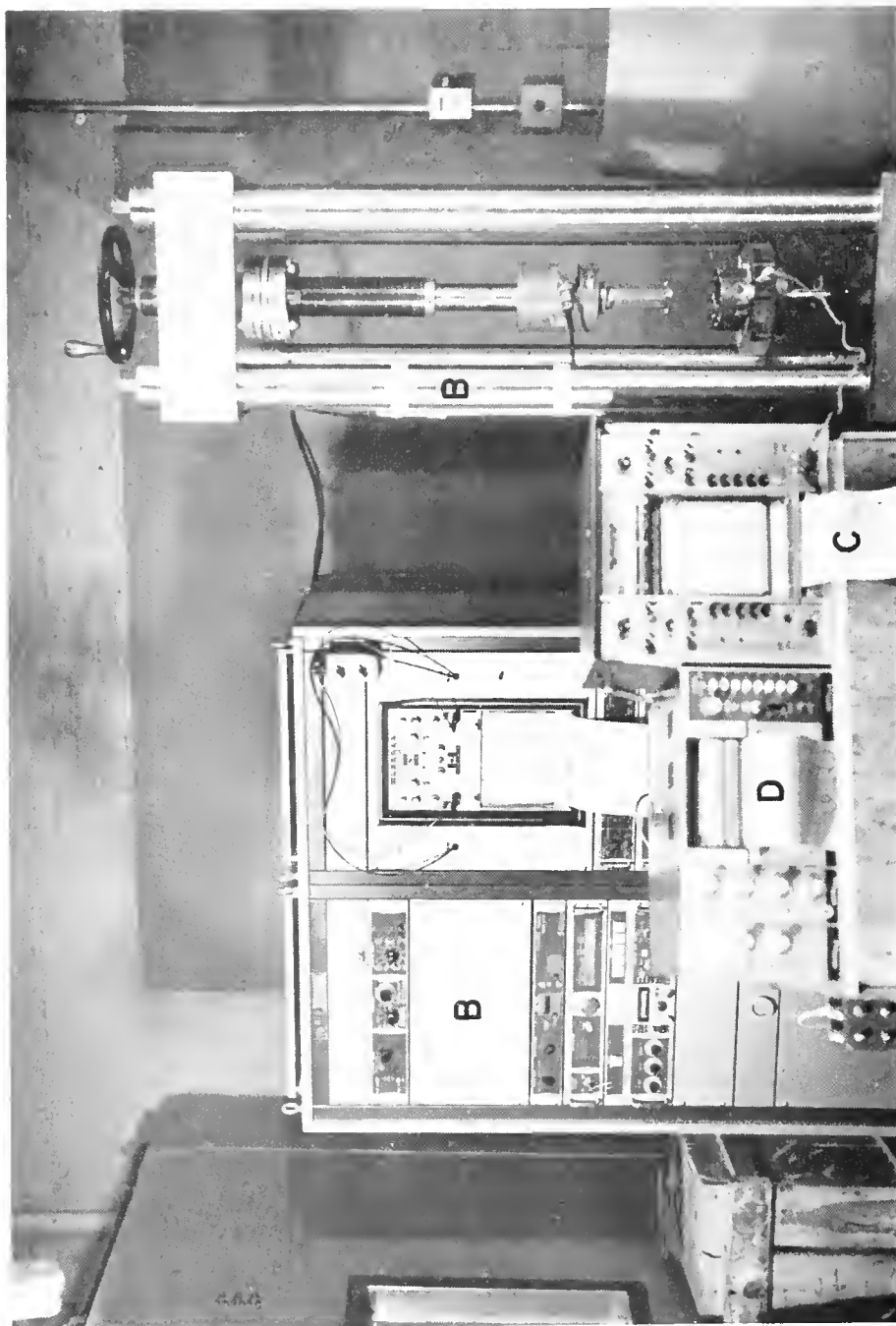


FIGURE 27. EQUIPMENT USED FOR SAMPLE COMPACTION

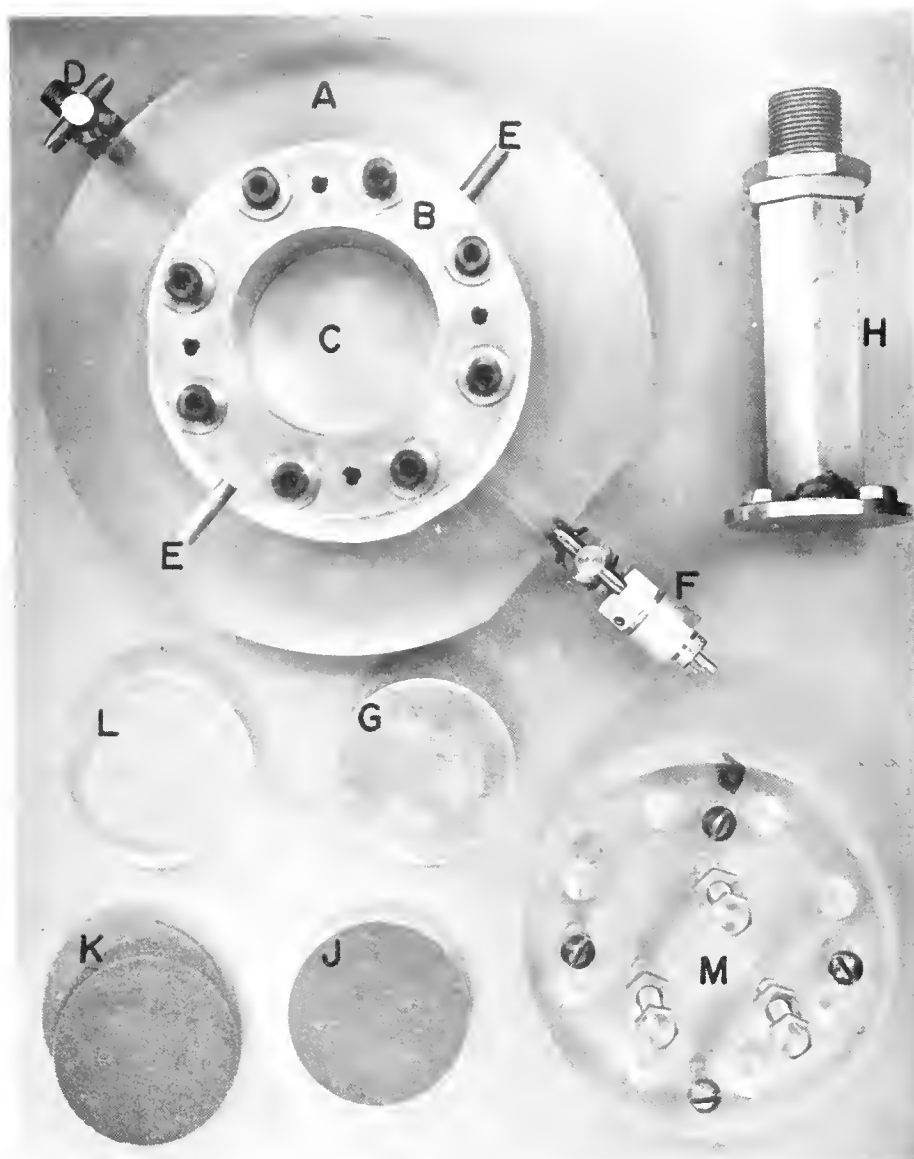


FIGURE 28. COMPACTION MOLD AND RELATED ACCESSORIES

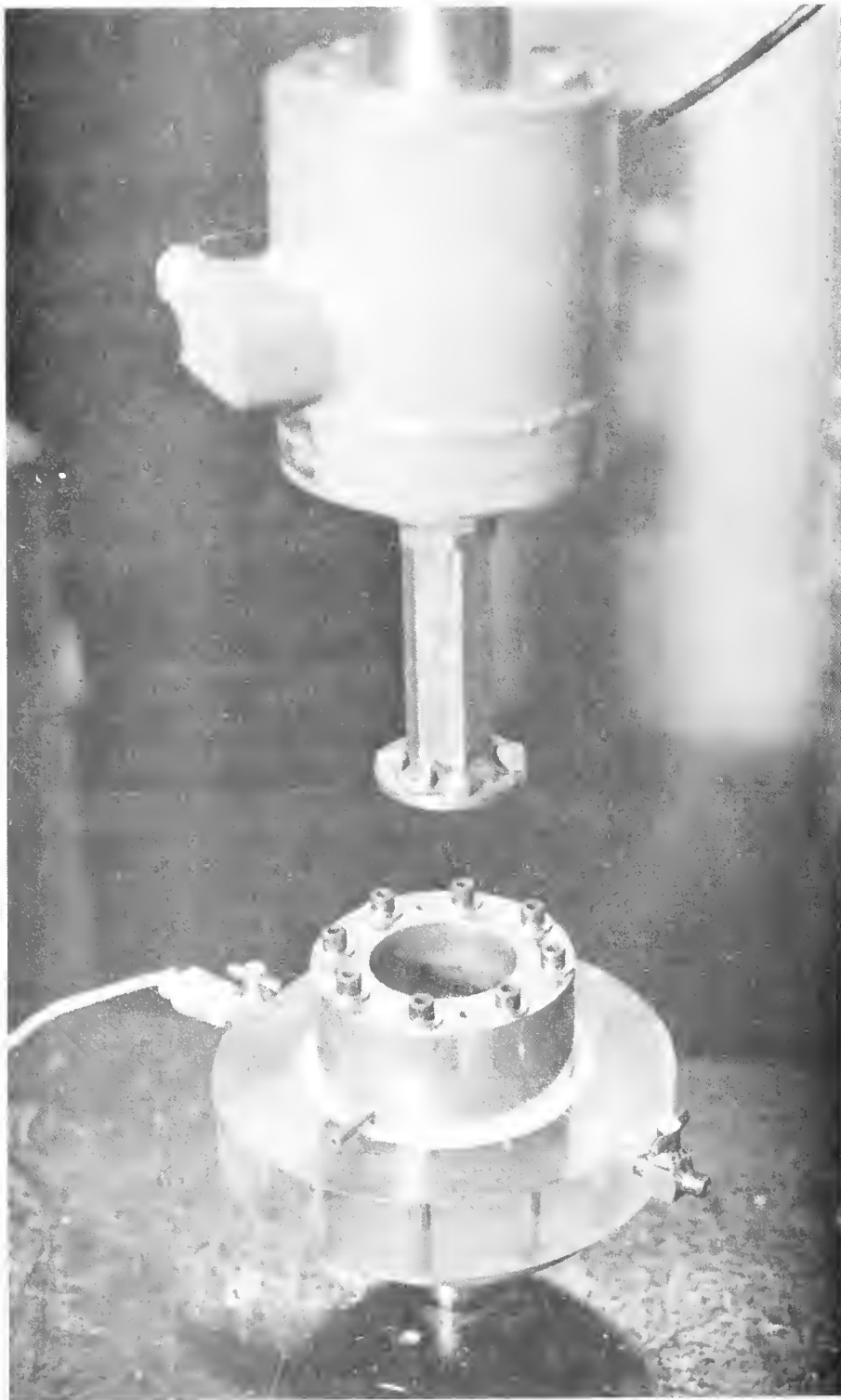


FIGURE 29. CELL, COMPACTOR FOOT AND LOAD CELL

a Fenwal Number EA33JM8 thermistor for temperature measurement during subsequent swelling pressure tests. To aid in sample removal as well as to provide access for water into the sample during the swelling pressure tests, two small-diameter holes were bored through the wall of the brass ring, one on each side, below the elevation of the upper surface of the aluminum spacer, and fitted with copper tubes. Figure 28 shows the lucite base, A; the brass ring, B; the teflon membrane, C; the silicon reservoir valve, D; the vent pipes, E; the Statham transducer, F; and the aluminum spacer, G. In addition Figure 29 shows the compaction foot, H; the aluminum calibration spacer, J; the upper and lower bronze porous stones, K; the perforated lucite top spacer, L; and the lucite upper restraining cap, M. The porous stones, perforated lucite spacer, and restraining cap are used during the swelling pressure tests. Not shown is the Fenwal thermistor embedded in the brass ring. The dimensions and details of the cell are shown in Appendix H.

Each sample was compacted by a single application of a full-coverage compaction foot. Because of the nature of the desired information and in part due to an inability to predict the input load vs. compacted unit-weight-achieved relationship, the independent variables were the rate of loading and the magnitude of the input load for the compaction machine and molding moisture content and aggregate size for the soil.

An extensive pilot study was made to study the load-displacement characteristics of the machine-soil system. Various loading functions such as the sine wave, linear ramp, spike or saw tooth, and half sine were investigated over a wide range of application rates. Desirable characteristics were reproducibility, ease of analysis, and a resemblance to the field loading condition.

The analysis of this preliminary study indicated that all functions were true to form and reproducible at modest loading rates. As the rate was increased, all functions deviated from the programmed shape, were plagued by overshoot, and were not reproducible as the soil's aggregate size and moisture content were changed. The primary reason for these difficulties was the testing machine's inability to "keep up" with the deformation of the soil. During the pilot study it was determined that loading rate rather than displacement rate would be a more meaningful independent variable. Therefore, when the soil response was large, i.e. when considerable one-dimensional compression occurred, the hydraulic pump was unable to supply the necessary amount of oil at the required pressure.

A comparison of the system's limitations and the research requirements led to the following standard test procedure: A single application of a full-coverage compaction foot applied at a loading rate of 3,000 lb. per second to a load of either 1,000 lb. or 1,500 lb. ("effort" was also a

variable). The ramp function was utilized; this can be described as a linear increase of the variable as a function of time to some programmed maximum value, and then the maintenance of the maximum value of this variable constant with time. The maximum load (1,000 lb. or 1,500 lb.) was maintained on the sample, allowing further densification to occur, for a period of two minutes.

The rapid rise time followed by a relatively long term continuation at constant load allowed the aggregate-aggregate interaction to be evaluated. No further compression, or increase in unit weight, of the sample after the initial load buildup indicates an immediate rearrangement of the aggregates into a denser packing by aggregate movement, aggregate fracture, and elastic straining. Long-term compression, on the other hand, indicates "plastic" behavior of the aggregates.

After the elapsed time of two minutes, the load was released and the compaction foot withdrawn. So that an independent direct check could be made on the sample height, each sample removed from the cell was measured with a vernier micrometer. To facilitate removal of the sample from the cell without disturbing it, compressed air was introduced at the previously-described ports in the lower portion of the ring. The air pressure easily forced the aluminum spacer, and the sample above it, out of the ring.

Before each group of samples was compacted, it was necessary to calibrate the entire system with respect to load and displacement. Displacement calibration of the Brush oscillograph was accomplished with the aid of machined spacers of known thickness. The calibration of the Sanborn recorder used to measure silicon oil pressure during compaction was accomplished by loading the teflon diaphragm and spacer with the compactor foot attached to the five-kip capacity load cell of the MTS machine. This load cell was checked periodically by MTS Company personnel. The Brush Oscillograph and the Sanborn recorder were calibrated simultaneously to the magnitude of the compaction load to be used. This allowed the compression of the cell and testing frame to be taken into account. Since a second Sanborn recorder was required to monitor swelling pressure after compaction, it also was calibrated prior to each test, with the use of a 700 lb. capacity proving ring.

At each testing session three replicate samples were compacted, no variables were introduced within this group. The first sample was used completely for a moisture content determination, the second was saved for carbowax impregnation, and the third was left in the cell after compaction for the swelling pressure test.

Swelling Pressure Measurements on Compacted Samples

As an aid to the determination of the macrostructure after compaction and its response to the forces generated by the addition of water, swelling pressure as a function of time was monitored for selected compacted samples. No gross volume change was permitted and the temperature was held constant as water was made available to the sample.

The apparatus used for these measurements consisted of the previously described cell equipped with lower and upper bronze stones and an upper cap to eliminate vertical swelling, a Sanborn Model 321 slow speed strip-chart recorder to monitor the vertical total stress by means of the Statham pressure transducer, and a constant temperature chamber ($\pm 0.2^{\circ}\text{C}$). Water was supplied to the cell from an inclined burette through a tygon tube. Figure 30 shows the cell with the upper cap bolted down, A; the Fenwal thermistor lead, B; the Statham pressure transducer, C; and the water reservoir, D. Not shown are the Sanborn recorder and the constant temperature cabinet into which the equipment shown in this figure was placed.

The test procedure was as follows. Before compacting the last sample of the three-sample group, the lower metal spacer within the mold was replaced by a dry bronze porous stone. After this substitution, the soil was placed into the mold and compacted as before. The sample was then allowed to remain in the mold. The slow speed recorder was

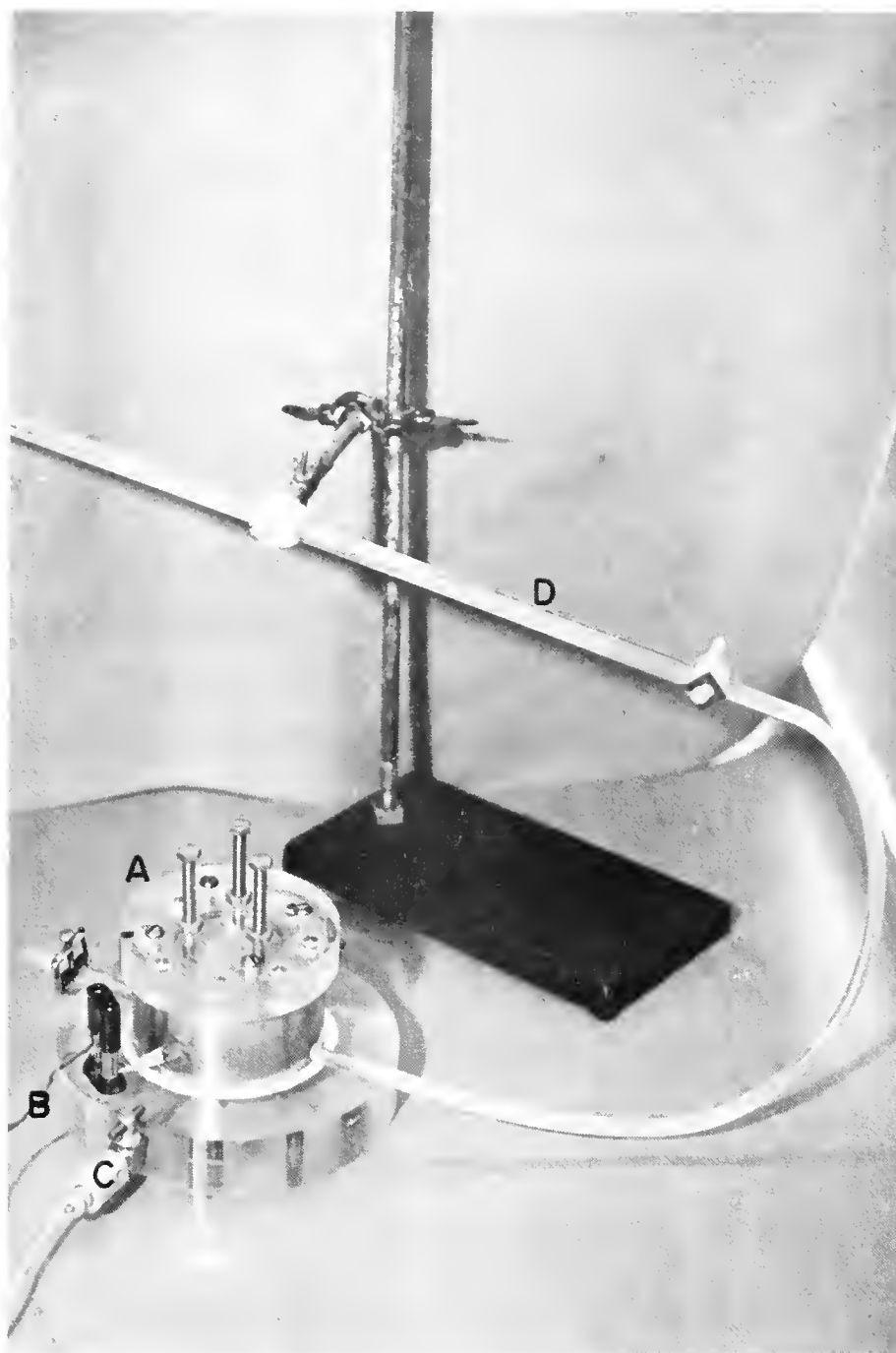


FIGURE 30. SWELLING PRESSURE TEST CELL AND WATER RESERVOIR

connected to the pressure transducer, the dry upper porous stone was placed into the ring and seated, as evidenced by an increase in the fluid pressure in the cell, a loose-fitting plastic spacer was placed above the stone, and the upper cap was bolted to the ring. The upper cap restrained the sample by means of three bolts which were tightened sufficiently to bear against the plastic spacer, which rested against the upper bronze stone. At this time the bolts were tightened sufficiently so that the transducer indicated approximately 50 pounds of load on the bottom of the sample. Finally, the cell was placed into the constant temperature chamber and allowed to come to equilibrium at the chamber temperature of approximately 29.5°C.

As the temperature of the soil-cell system increased, the fluid pressure, as measured by the Statham transducer, changed in response to the slight volumetric changes of the fluid and the metal and lucite parts of the cell. Equilibrium was achieved when the cell temperature, as measured by the embedded thermistor, ceased to change. This required a minimum of eight hours in the constant temperature chamber.

After equilibrium was achieved, the strip-chart speed was increased, and the water supply to the bottom porous stone was opened. The pressure head of the water supply at the bottom stone was essentially constant and of small magnitude in that it varied between 14 and 12 inches. The moisture movement through the soil was upward, allowing the

air to escape through the upper porous stone and perforated lucite spacer.

The constant volume swelling pressure-time relationship was recorded until an equilibrium pressure was reached, usually 24 to 48 hours for these particular samples, and during this period, the cell temperature was monitored and noted on the strip-chart several times. Although no attempt was made to change the cabinet temperature once a test was in progress, occasional cell temperature determinations were necessary to the analysis of the results because of the temperature dependence of the measured fluid pressure.

Upon completion of the test, the free water in the bottom ports was blown out with low air pressure, the upper confining cap was loosened and removed, the sample was removed by the air pressure technique, and it was weighed, dried, and reweighed so that water content and degree of saturation determinations could be made. Immediately after removing the sample from the cell, the cell was recalibrated in the manner previously explained.

RESULTS

The experimental results are arranged in the following order: particle orientation, both within uncompacted aggregates and within compacted samples; dry unit weights of aggregates; achievement of compacted unit weight; end results of compaction and saturation; swelling pressure; and aggregate deformation.

The reader is reminded that samples of batches are identified by the batch number and the sieve limits of aggregate size. For example, K-2, P8-R10 indicates batch number K-2 and aggregates which passed the number 8 sieve and were retained on the number 10 sieve. The moisture content of the batch increases with the batch number.

The prefix is modified from K to KL to indicate that the sample was compacted. If the sample was subjected to a swelling pressure test after compaction the prefix becomes KLS.

Particle Orientation

In Table 6 below are the average peak height ratios (002/020) for each impregnated (a) group of uncompacted aggregates (aggreg.) or (b) compacted sample examined by the X-ray diffraction technique. Individual values are shown in Appendix C.

Table 6. Particle Orientation by Peak Height Ratio

Sample	Batch	Size	Maximum Compacting Load	Peak Height Ratio, 002/020
aggreg.	K-1	P6-R8	--	1.53
KL-5	K-1	P6-R8	1000	1.73
KL-7	K-1	P6-R8	1500	1.96
aggreg.	K-2	P6-R8	--	1.80
KL-35	K-2	P6-R8	1000	2.09
KL-38	K-2	P6-R8	1500	2.28
aggreg.	K-3	P6-R8	--	2.03
KL-65	K-3	P6-R8	1000	2.53
KL-68	K-3	P6-R8	1500	2.35
aggreg.	K-1	P20-R40	--	1.83
KL-26	K-1	P20-R40	1000	2.01
KL-29	K-1	P20-R40	1500	2.13
aggreg.	K-2	P20-R40	--	1.64
KL-54	K-2	P20-R40	1000	2.06
KL-57	K-2	P20-R40	1500	2.36
aggreg.	K-3	P20-R40	--	1.78
KL-86	K-3	P20-R40	1000	2.47
KL-89	K-3	P20-R40	1500	2.81

Following Martin's procedure (36) the maximum and minimum peak height ratios were determined to be 3.5 and 1.0 for the most oriented and most random cases, respectively.

The relationships among peak height ratio, batch (moisture content), aggregate size, and compacting load are shown in Figures 31, 32, and 33 in the form of histograms.

The results show that the peak height ratio ranges from 1.53 for the K-1, P6-R8 aggregates to 2.81 for a K-3, P20-R40 specimen compacted with the 1,500 lb. load. Qualitatively the histograms indicate that the peak height ratio increases as the moisture content increases. This dependence holds for all three conditions, the aggregates and the compacted samples at both compaction effort levels. It is also indicated that the peak height ratio increases with increasing compactive load, from no load (aggregates) to the 1,500 lb. level when the moisture content and aggregate size are held constant.

Dry Unit Weights of Aggregates

The experimentally determined dry unit weights of the various size aggregates are reported in Table 7 in pounds per cubic foot. Results are not reported for K-3, P8-R10 because these aggregates were accidentally destroyed during the determination and could not be replaced.

No consistent trends are obvious for these results, and a detailed analysis will be made later in this paper under the heading Discussion of Results.

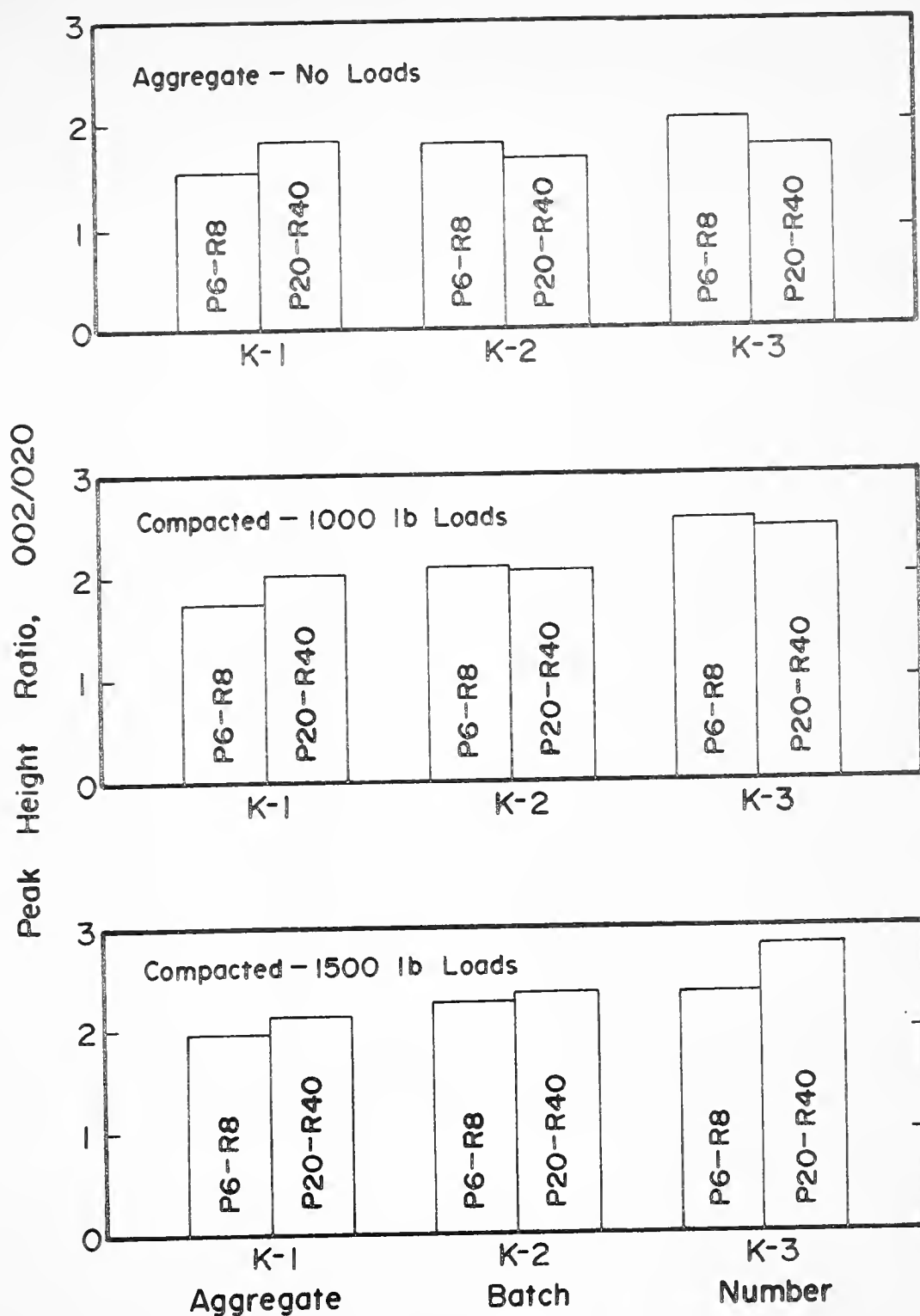


FIGURE 31. RELATIONSHIPS AMONG PEAK HEIGHT RATIO, AGGREGATE SIZE AND COMPACTIVE EFFORT

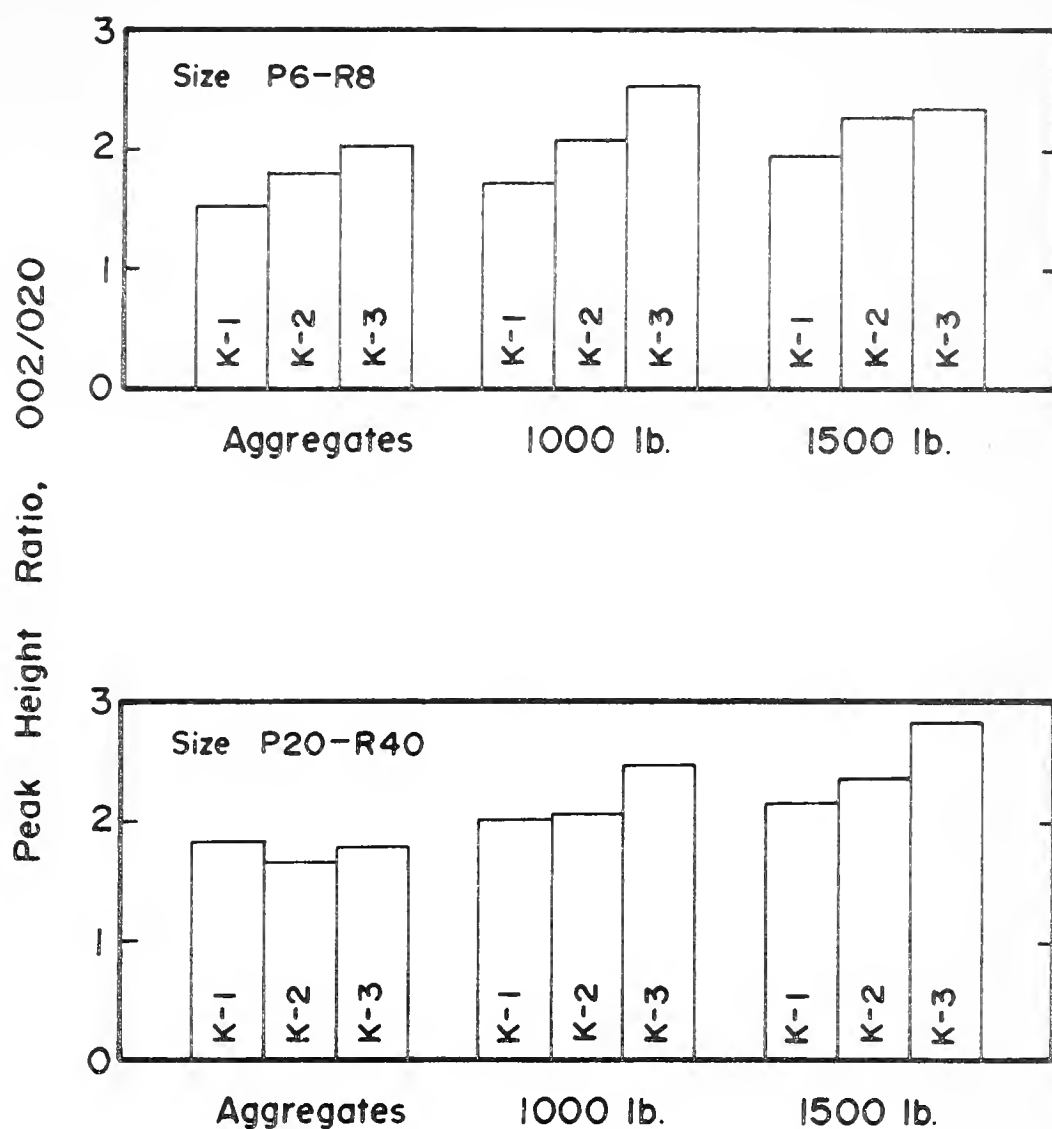


FIGURE 32. DEPENDENCE OF PEAK HEIGHT RATIO ON MOLDING WATER CONTENT

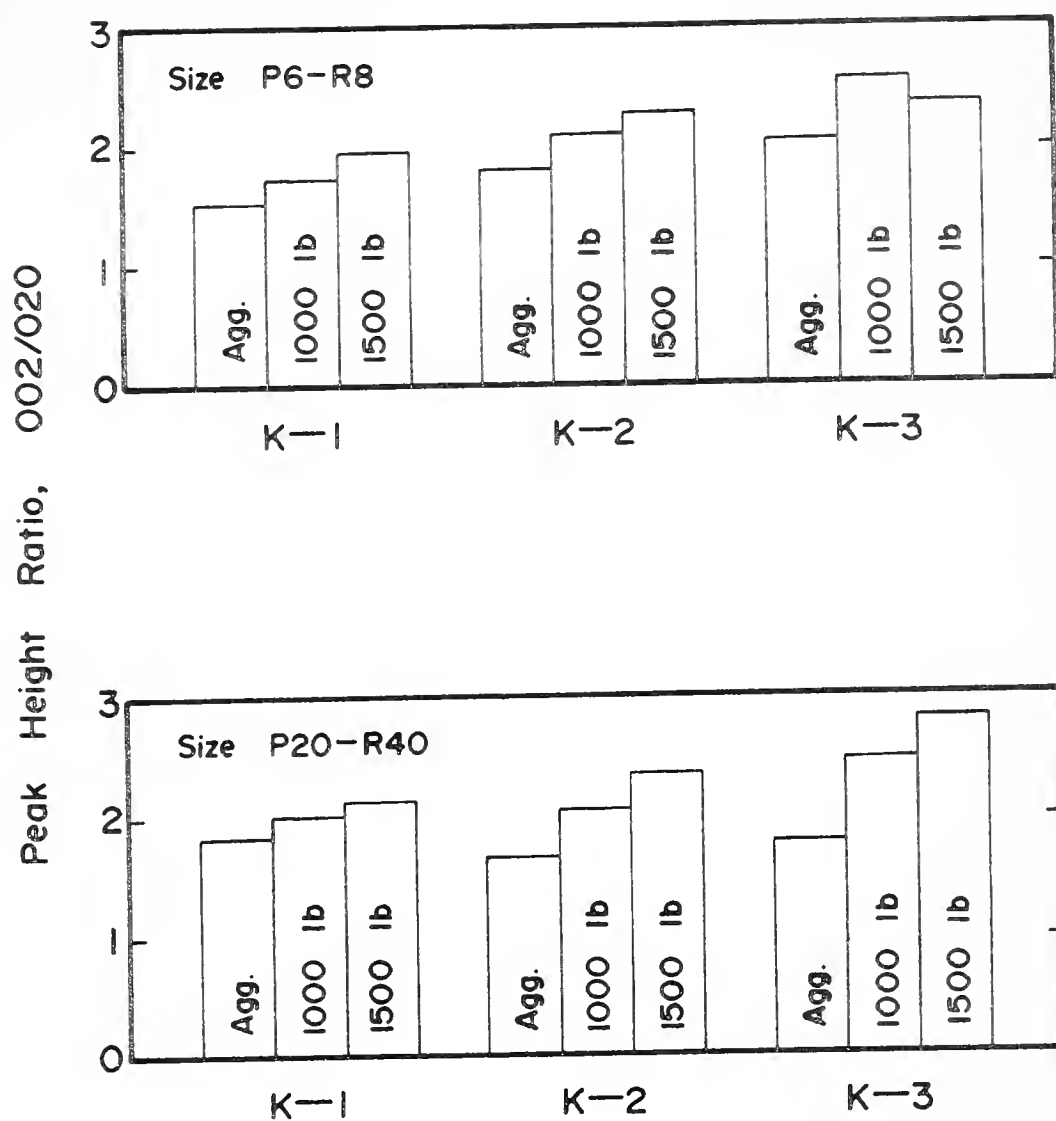


FIGURE 33. DEPENDENCE OF PEAK HEIGHT RATIO ON
COMPACTIVE EFFORT

Table 7. Dry Unit Weights of Aggregates

<u>Batch</u>	<u>Size</u>	<u>γ_d, pcf</u>
K-1	P4-R6	75.4
K-2	P4-R6	76.9
K-3	P4-R6	88.6
K-1	P6-R8	93.4
K-2	P6-R8	85.6
K-3	P6-R8	84.0
K-1	P8-R10	93.2
K-2	P8-R10	82.0
K-1	P10-R12	89.0
K-2	P10-R12	107.4
K-3	P10-R12	84.5
K-1	P12-R20	88.3
K-2	P12-R20	104.5
K-3	P12-R20	106.9
K-1	P20-R40	86.5
K-2	P20-R40	82.0
K-3	P20-R40	82.8

Achievement of Compacted Unit Weight

As previously described the relationship between load and deformation during the densification process was monitored for each compacted sample. This made it possible to define the relation between sample unit weight and the work applied to achieve that unit weight.

Figures 34 and 35 and Figures 36 and 37 show this relationship for the P6-R8 samples in terms of dry unit weight and total unit weight respectively. The remainder of these results are shown in Appendix D. The net energy absorbed was calculated by averaging the measured loads at the top and bottom of the sample at the beginning and end of an increment of the test data, averaging these two, and multiplying by the net compression of the specimen during this increment. Each increment for data reduction purposes was 100 pounds of input load. Averaging the loads at the top and bottom of the sample attempts to take into account the side friction between the soil and the confining ring. The net sample compression is the measured compression over the increment minus the compression of the mechanical system over the same increment as previously measured in calibration tests.

In general the results indicate the relation between unit weight and net energy absorbed by the soil during densification to be a simple one, that is, it does not appear to be mathematically complex. Furthermore with

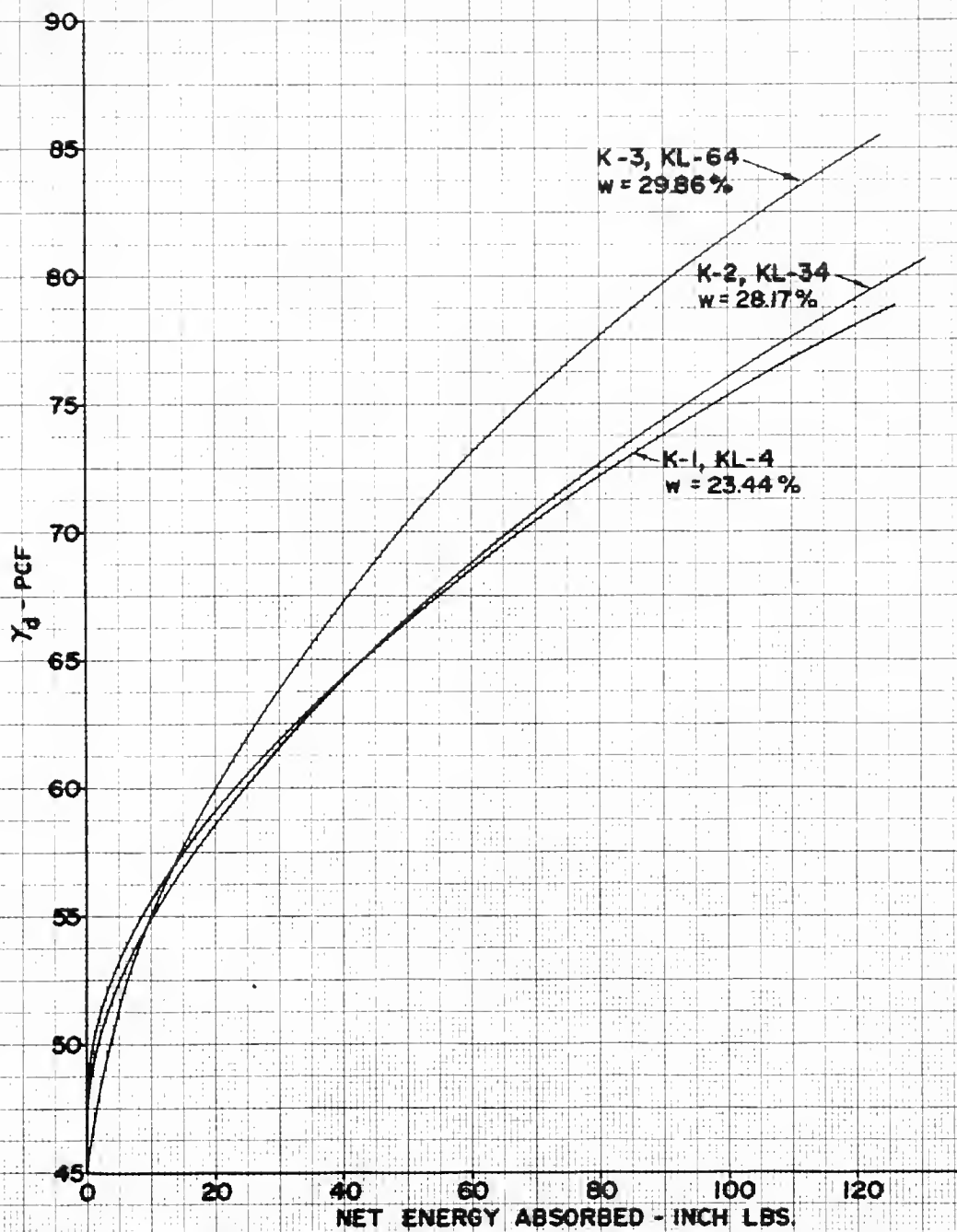


FIGURE 34. EFFECT OF MOISTURE CONTENT ON γ_d vs. ENERGY (P6-R8 KAOLINITE; 1000 LB LEVEL)

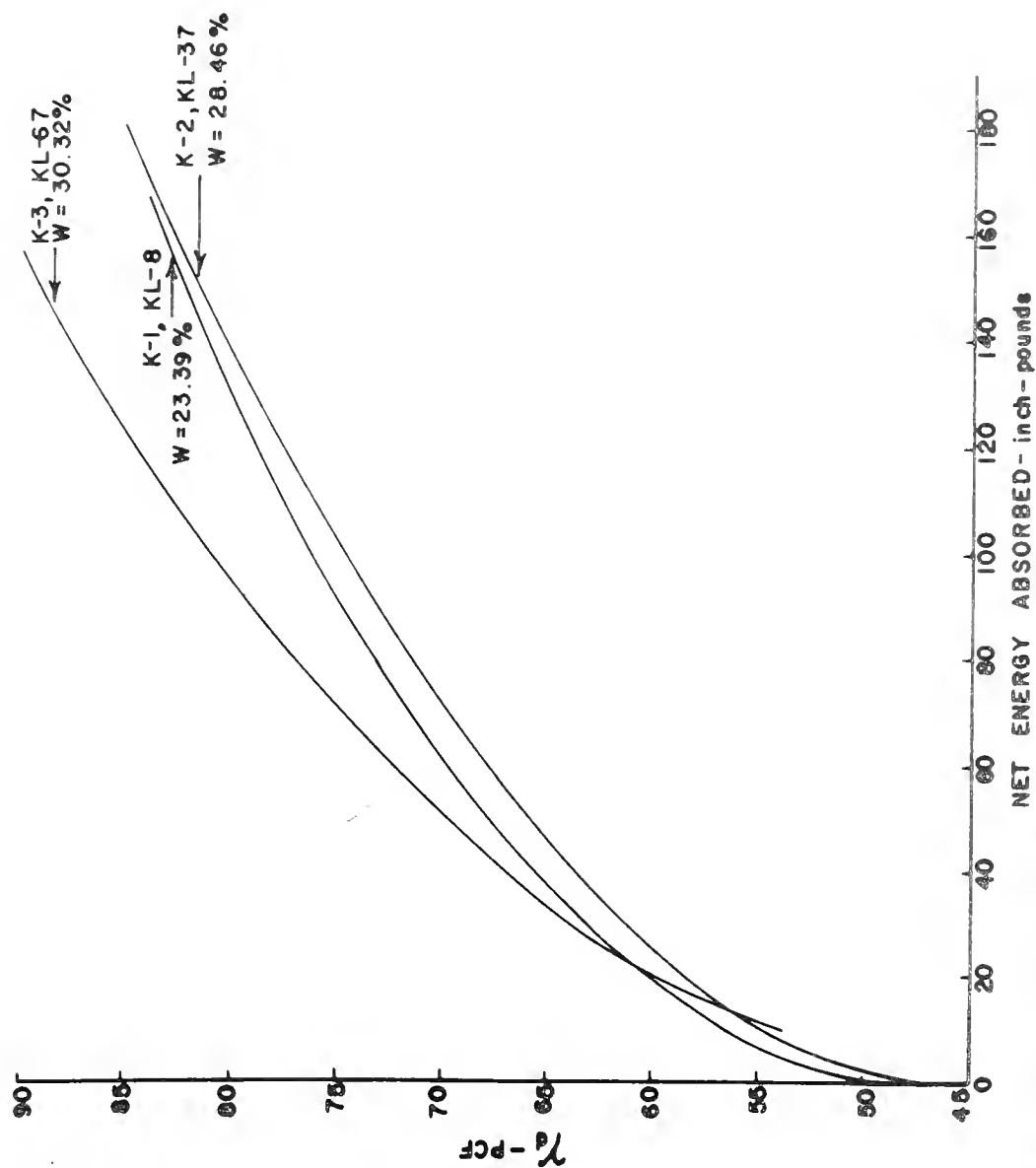


FIGURE 35. EFFECT OF MOISTURE CONTENT ON γ vs ENERGY (P6-R8)
KAOLINITE; 1500 LB LEVEL)

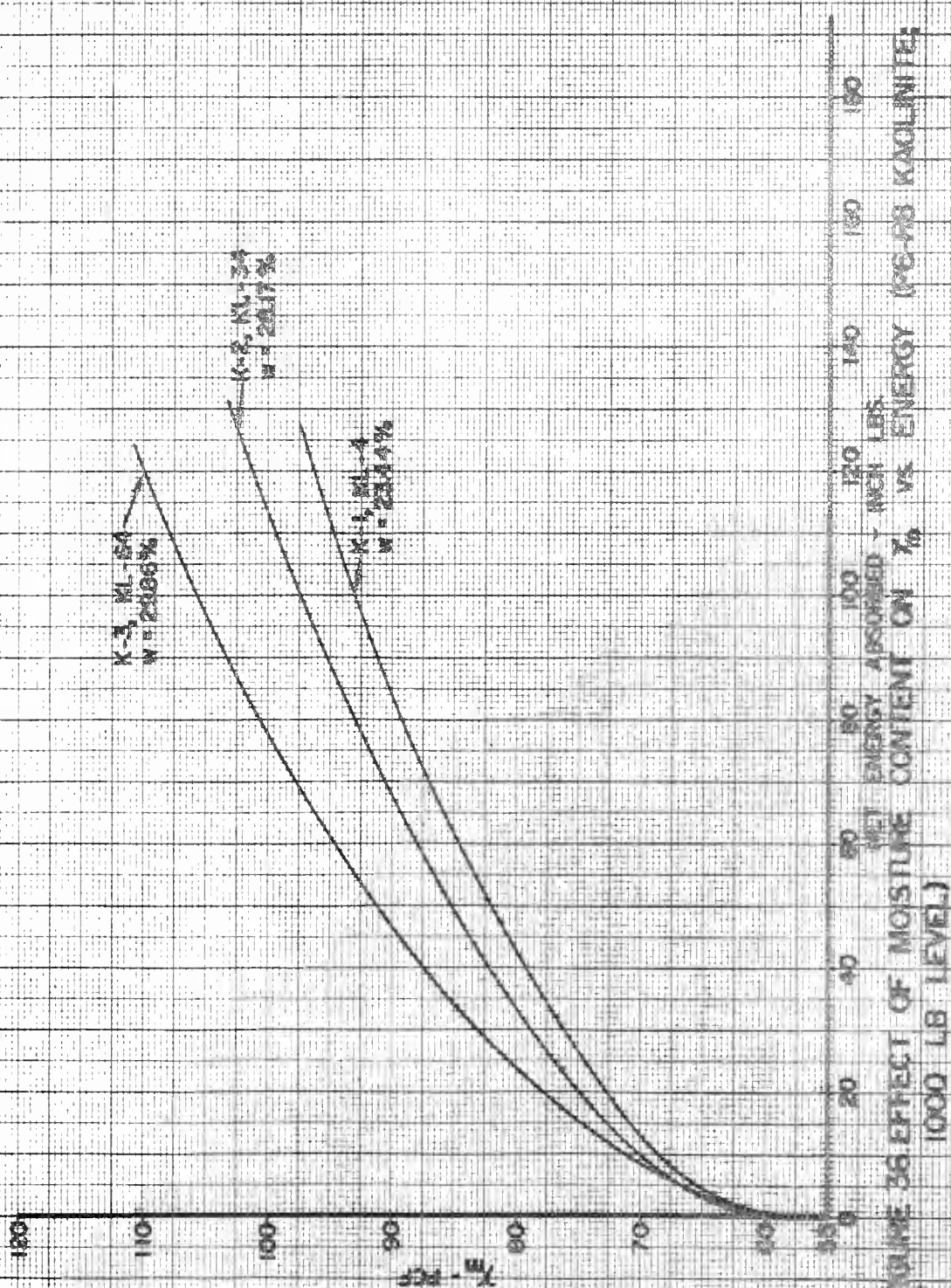


FIGURE 36. EFFECT OF MOISTURE CONTENT ON X_m VS ENERGY (K-3, K-4, K-5 KAOLINITES, 1000 LB LEVEL)

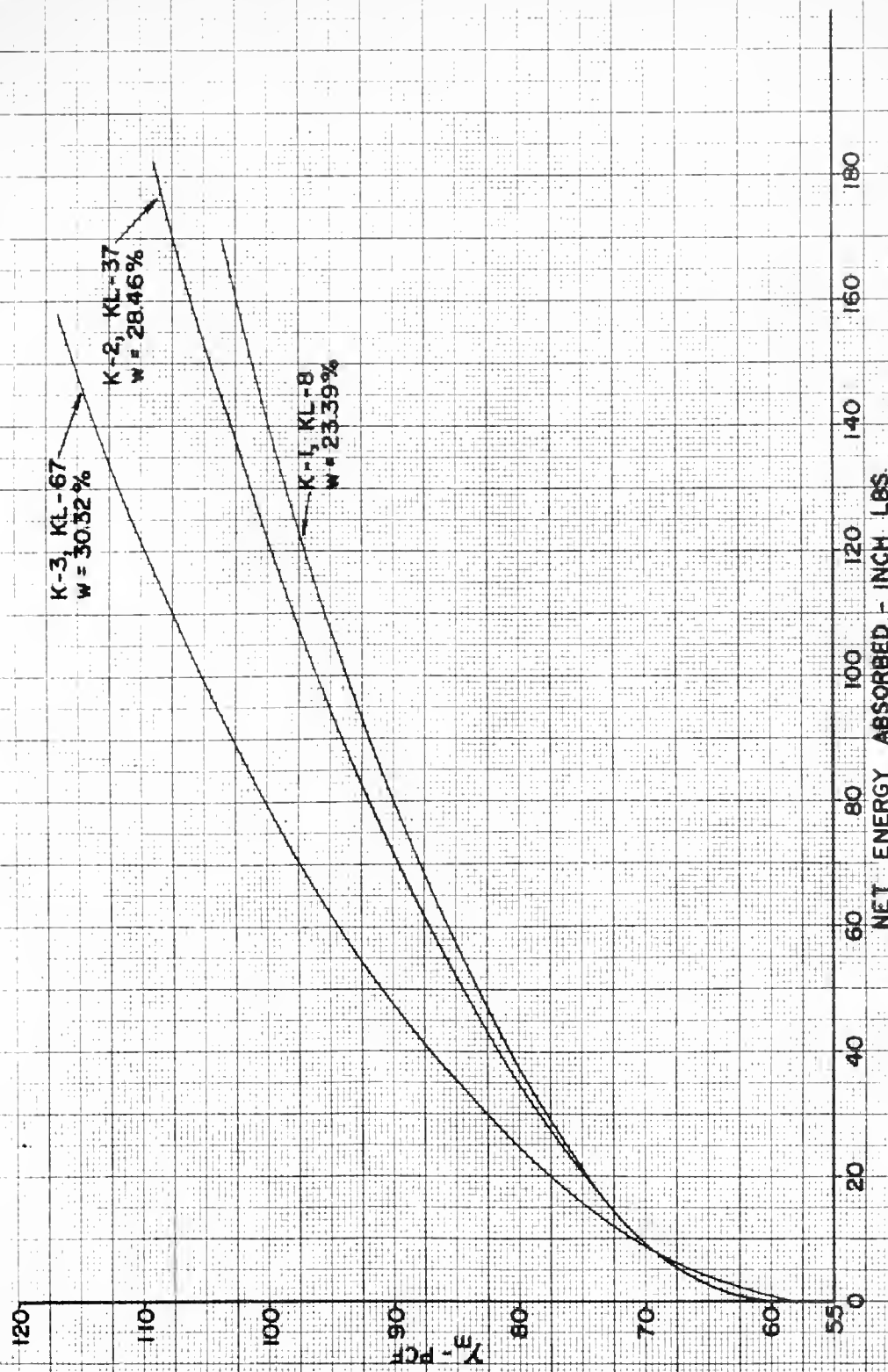


FIGURE 37: EFFECT OF MOISTURE CONTENT ON γ_m vs. ENERGY (P6-R8 KAOLINITE; 1500 LB LEVEL)

the exception of the samples made up of P4-R6 size aggregates the net energy required to achieve a given unit weight decreases as the compaction moisture content increases. Stated another way, holding the net energy absorbed constant the unit weight increases within the range of moisture content investigated in this study.

End Results of Compaction and Saturation

To aid in the understanding of these results a schematic diagram of the recorded output from a typical compaction test is shown in Figure 38. The output consists of three traces, each showing a variable as a function of time. Channel 1 records the compactive load at the compaction foot, channel 2 records the compactive load reaching the base of the soil sample, and channel 3 records the relative motion between the compaction foot and the pedestal on which the compaction cell rests. As mentioned previously, prior to each compaction test the cell and recorders are calibrated and the system compression, which will be subtracted from the total displacement, is measured. This calibration is shown in the left portion of Figure 38. Note that channels 1 and 2 are not to the same scale although they are measuring the same load at this time.

Referring to the letters along the time axis in the figure, A indicates the beginning of load application, B indicates that time when the maximum load (1,000 or 1,500

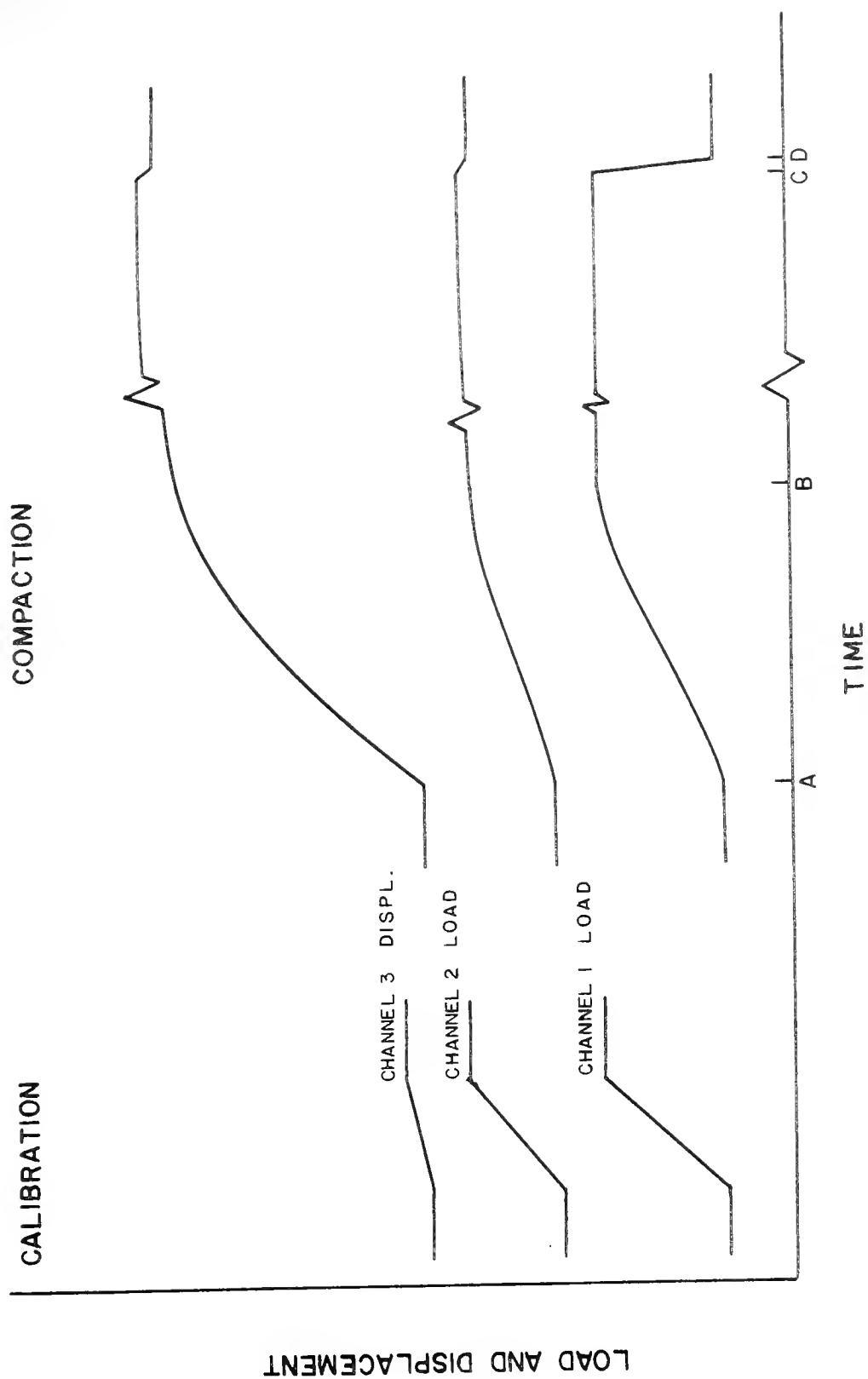


FIGURE 38. SCHEMATIC OUTPUT FROM COMPACTION TEST

lbs.) has been reached, C indicates that two minutes have elapsed and at this time the applied load is rapidly reduced to zero as indicated by D. Note that the base load measured by channel 2 continues to increase slightly after time B but is essentially constant by the time C is reached.

Table 8, which follows, contains the calculated dry unit weight, total unit weight, and degree of saturation for each specimen. The various quantities have been calculated for three different times after the start of the compactive loading.

"At Maximum Load" refers to that point in time (B) when the maximum compactive load has just been reached. "After Two Minutes of Maximum Load" refers to the time (C) just before the compactive load is released. "After Load Removal" is that condition (D) just after the applied load goes back to zero.

The "After Swell Pressure Test" degree of saturation was calculated using the "After Load Removal" volume measurement. That is, it was assumed that no volume increase occurred during the two to three minutes which elapsed between the removal of the compaction load and reconfinement of the soil for the swelling pressure test.

Occasionally, due to difficulties with the oscillograph, portions of the data were not recorded. The

Table 8

After Swell
Pressure Test

Size	ω W	σ Sr
P4-R6	---	---
P4-R6	---	---
F4-R6	35.71	101.6%
P4-R6	---	---
F4-R6	---	---
P4-R6	33.87	105.8%
P6-R8	---	---
P6-R8	---	---
P6-R8	38.16	*
P6-R8	---	---
P6-R8	37.44	96.3%
P6-R8	---	---
P6-R8	---	---
P6-R8	35.15	100.8%
P6-R8	---	---
P6-R8	---	---
P6-R8	33.71	104.8%
P8-R10	---	---
P8-R10	38.10	96.1%
P8-R10	---	---
P8-R10	36.38	101.9%
P8-R10	---	---
P8-R10	34.08	102.6%
P10-R12	---	---
P10-R12	37.91	99.6%
P10-R12	---	---
P10-R12	36.09	102.2%
P10-R12	---	---
P10-R12	33.96	105.8%

Table 8. End Results of Compaction and Saturation.

Size	Batch	Test #	lbs. Load	w % at comp.	At Max. Load			After 2 Min. of Max. Load			After Load Removal			After Swell Pressure Test	
					γ_d pcf	SR %	γ_m pcf	γ_d pcf	SR %	γ_m pcf	γ_d pcf	γ_m pcf	SR %	w %	SR %
P4-R6	K-1	KL-1	1000	23.93	87.5	72.9%	108.4	90.5	78.5%	112.2	110.3	89.0	75.6%	---	---
P4-R6	K-2	KL-31	1000	28.19	81.1	73.3%	104.0	84.7	80.1%	108.6	107.7	84.1	78.8%	---	---
F4-R6	K-2	KLS-32	1000	28.19	84.1	78.9%	107.8	86.2	83.0%	110.5	108.7	84.8	80.2%	35.71	101.6%
P4-R6	K-3	KL-59	1000	29.94	85.3	86.3%	110.8	89.3	95.2%	116.0	114.6	88.2	92.6%	---	---
F4-R6	K-3	KL-60	1000	29.94	84.9	85.4%	110.3	88.8	94.2%	115.4	114.0	87.7	91.6%	---	---
P4-R6	K-3	KLS-61	1000	29.94	85.7	87.1%	111.3	89.7	96.2%	116.6	115.1	88.6	93.6%	33.87	105.8%
P6-R8	K-1	KL-4	1000	23.44	79.0	57.9%	97.5	81.8	62.0%	101.0	99.4	80.5	60.1%	---	---
P6-R8	K-1	KL-5	1000	23.44	*	*	*	*	*	*	*	*	*	---	---
P6-R8	K-1	KLS-6	1000	23.44	*	*	*	*	*	*	*	*	*	38.16	*
P6-R8	K-1	KL-10	1000	23.00	78.4	55.9%	96.4	81.4	60.3%	100.2	99.0	80.5	58.9%	---	---
P6-R8	K-1	KLS-11	1000	23.00	78.6	56.1%	96.6	81.3	60.1%	100.0	99.2	80.7	59.1%	37.44	96.3%
P6-R8	K-2	KL-34	1000	28.17	80.6	72.3%	103.3	84.5	79.6%	108.3	106.1	82.8	76.4%	---	---
P6-R8	K-2	KL-35	1000	28.17	82.2	75.1%	105.3	84.5	79.6%	108.3	106.6	83.1	77.0%	---	---
P6-R8	K-2	KLS-36	1000	28.17	81.7	74.4%	104.8	86.1	82.8%	110.4	109.0	85.1	80.7%	35.15	100.8%
P6-R8	K-3	KL-64	1000	29.86	85.5	86.5%	111.0	89.5	95.6%	116.3	114.6	88.3	92.7%	---	---
P6-R8	K-3	KL-65	1000	29.86	85.5	86.5%	111.0	89.1	94.7%	115.8	113.8	87.6	91.2%	---	---
P6-R8	K-3	KLS-66	1000	29.86	85.5	86.4%	111.0	89.5	95.5%	116.2	114.7	88.4	92.8%	33.71	104.8%
P8-R10	K-1	KL-12	1000	22.83	78.3	55.4%	96.2	81.0	59.2%	99.5	98.4	80.1	57.9%	---	---
P8-R10	K-1	KLS-13	1000	22.83	78.1	55.1%	95.9	81.1	59.3%	99.6	98.1	79.9	57.6%	38.10	96.1%
P8-R10	K-2	KL-40	1000	28.11	80.0	71.1%	102.5	83.5	77.5%	107.0	105.7	82.5	75.7%	---	---
P8-R10	K-2	KLS-41	1000	28.11	82.2	75.0%	105.3	85.9	82.2%	110.0	107.8	84.2	78.8%	36.38	101.9%
P8-R10	K-3	KL-70	1000	29.36	84.6	93.1%	109.4	88.6	91.6%	114.6	113.1	87.4	89.2%	---	---
P8-R10	K-3	KLS-71	1000	29.36	84.9	83.9%	109.6	89.3	93.4%	115.5	112.6	87.1	88.4%	34.08	102.6%
P10-R12	K-1	KL-15	1000	23.31	77.6	55.6%	95.7	81.0	60.5%	99.9	99.0	80.3	59.4%	---	---
P10-R12	K-1	KLS-16	1000	23.31	80.3	59.3%	99.0	83.1	63.8%	102.5	100.5	81.5	61.2%	37.91	99.6%
P10-R12	K-2	KL-43	1000	27.85	82.2	74.3%	105.1	86.2	82.1%	110.2	*	*	*	---	---
P10-R12	K-2	KLS-44	1000	27.85	82.3	74.5%	105.2	86.0	81.6%	109.9	108.2	84.6	78.9%	36.09	102.2%
P10-R12	K-3	KL-74	1000	29.42	84.9	83.9%	109.8	88.5	91.7%	114.5	112.5	86.9	88.2%	---	---
P10-R12	K-3	KLS-75	1000	29.42	85.6	85.3%	110.7	89.2	93.4%	115.4	114.5	88.4	91.7%	33.96	105.8%

Table 8

After Swell
Pressure Test

Size	W %	Sr %
P12-R20	---	---
P12-R20	---	---
P12-R20	38.10	100.3%
P12-R20	---	---
P12-R20	---	---
P12-R20	36.95	103.3%
P12-R20	---	---
P12-R20	---	---
P12-R20	33.87	102.1%
P12-R20	---	---
P20-R40	---	---
P20-R40	---	---
P20-R40	38.06	94.9%
P20-R40	---	---
P20-R40	---	---
P20-R40	---	---
P20-R40	---	---
P20-R40	35.60	99.7%
P20-R40	---	---
P20-R40	---	---
P20-R40	34.21	*
P20-R40	---	---
P4-R6	---	---
P4-R6	32.82	106.7%
P4-R6	---	---
P4-R6	32.22	106.8%
P4-R6	---	---
P6-R8	---	---
P6-R8	---	---
P6-R8	34.37	103.9%
P6-R8	---	---
P6-R8	---	---
P6-R8	32.74	102.6%
P6-R8	---	---
P6-R8	---	---
P6-R8	---	---
P6-R8	32.91	107.7%
P6-R8	---	---

Table 8. (continued)

Size	Batch	Test #	lbs. Load	w % at comp.	At Max. Load			After 2 Min. of Max. Load			After Load Removal				After Swell Pressure Test	
					γ_d pcf	Sr %	γ_m pcf	γ_d pcf	Sr %	γ_m pcf	γ_m pcf	γ_d pcf	Sr %	w %	Sr %	
P12-R20	K-1	KL-19	1000	23.16	78.6	56.6%	96.8	81.3	60.5%	100.2	98.6	80.1	58.7%	---	---	
P12-R20	K-1	KL-20	1000	23.16	78.9	56.9%	97.1	81.3	60.5%	100.2	99.0	80.4	59.2%	---	---	
P12-R20	K-1	KLS-21	1000	23.16	80.1	58.7%	98.6	82.9	63.0%	102.1	100.5	81.6	61.0%	38.10	100.3%	
P12-R20	K-2	KL-47	1000	27.31	*	*	*	*	*	*	*	*	*	---	---	
P12-R20	K-2	KL-48	1000	27.31	81.8	72.3%	104.1	85.5	79.1%	108.9	107.1	84.1	76.5%	---	---	
P12-R20	K-2	KLS-49	1000	27.31	81.8	72.1%	104.1	85.4	79.0%	108.7	107.0	84.1	76.3%	36.95	103.3%	
P12-R20	K-3	KL-79	1000	29.20	84.7	83.0%	109.4	88.7	91.6%	114.6	112.9	87.4	88.7%	---	---	
P12-R20	K-3	KL-80	1000	29.20	83.5	80.6%	107.9	88.5	91.1%	114.3	112.9	87.4	88.6%	---	---	
P12-R20	K-3	KLS-81	1000	29.20	85.3	84.2%	110.2	88.6	91.3%	114.5	112.5	87.1	88.0%	33.87	102.1%	
P20-R40	K-1	KL-25	1000	22.40	78.1	54.0%	95.6	85.7	65.2%	104.9	102.4	83.7	62.0%	---	---	
P20-R40	K-1	KL-26	1000	22.40	76.6	52.1%	93.8	79.8	56.4%	97.7	96.2	78.6	54.8%	---	---	
P20-R40	K-1	KLS-27	1000	22.40	79.7	56.3%	97.6	82.9	60.8%	101.4	97.2	79.4	55.8%	38.06	94.9%	
P20-R40	K-1	KL-2	1000	22.87	87.7	69.9%	107.7	91.1	76.1%	111.9	109.6	89.2	72.5%	---	---	
P20-R40	K-1	KL-3	1000	22.87	*	*	*	*	*	*	*	*	*	---	---	
P20-R40	K-2	KL-53	1000	27.41	82.2	73.2%	104.7	85.5	79.5%	109.0	107.2	84.2	76.8%	---	---	
P20-R40	K-2	KL-54	1000	27.41	81.8	72.6%	104.3	85.5	79.5%	109.0	107.2	84.2	76.8%	---	---	
P20-R40	K-2	KLS-55	1000	27.41	82.1	73.1%	104.6	85.8	80.1%	109.4	107.2	84.1	76.7%	35.60	99.7%	
P20-R40	K-3	KL-85	1000	28.87	84.2	81.0%	108.5	87.7	88.4%	113.0	110.3	85.6	83.8%	---	---	
P20-R40	K-3	KL-86	1000	28.87	84.1	80.8%	108.4	*	*	*	*	*	*	---	---	
P20-R40	K-3	KLS-87	1000	28.87	84.6	81.8%	109.0	88.5	90.2%	114.1	*	*	*	34.21	*	
P4-R6	K-1	NONE	1500													
P4-R6	K-2	KLS-33	1500	28.19	87.2	85.1%	111.8	91.3	94.4%	117.1	115.6	90.2	91.7%	32.82	106.7%	
P4-R6	K-3	KL-62	1500	29.94	88.1	92.5%	114.5	90.4	97.9%	117.4	115.9	89.2	95.1%	---	---	
P4-R6	K-3	KLS-63	1500	29.94	90.1	97.3%	117.1	91.7	101.2%	119.2	118.2	90.9	99.3%	32.22	106.8%	
P6-R8	K-1	KL-8	1500	23.39	83.9	65.1%	103.5	87.0	70.3%	107.3	106.0	85.9	68.5%	---	---	
P6-R8	K-1	KL-7	1500	23.39	83.7	64.7%	103.2	86.8	69.9%	107.1	106.2	86.1	68.7%	---	---	
P6-R8	K-1	KLS-9	1500	23.39	84.8	66.5%	104.6	88.0	72.0%	108.5	107.6	87.2	70.7%	34.37	103.9%	
P6-R8	K-2	KL-37	1500	28.46	85.0	81.5%	109.2	89.0	90.0%	114.3	111.9	87.1	85.9%	---	---	
P6-R8	K-2	KL-38	1500	28.46	85.0	81.5%	109.2	88.6	89.1%	113.8	111.5	86.8	85.1%	---	---	
P6-R8	K-2	KLS-39	1500	28.46	87.6	86.7%	112.5	91.0	94.5%	116.9	113.9	88.7	89.2%	32.74	102.6%	
P6-R8	K-3	KL-67	1500	30.32										---	---	
P6-R8	K-3	KL-68	1500	30.32	88.2	94.0%	115.0	90.6	99.6%	118.0	116.5	89.4	96.7%	---	---	
P6-R8	K-3	KLS-69	1500	30.32	88.9	95.5%	115.8	92.0	103.3%	119.9	117.8	90.4	99.2%	32.91	107.7%	

Table 8

After Swell
Pressure Test

Size	W %	SR %
P8-R10	34.48	102.3%
P8-R10	32.81	107.5%
P8-R10	---	---
P8-R10	32.61	103.6%
P10-R12	---	---
P10-R12	33.53	---
P10-R12	---	---
P10-R12	33.18	106.6%
P10-R12	---	---
P10-R12	---	---
P10-R12	32.33	107.6%
P10-R12	---	---
P12-R20	---	---
P12-R20	---	---
P12-R20	34.24	104.2%
P12-R20	---	---
P12-R20	---	---
P12-R20	33.22	*
P12-R20	---	---
P12-R20	---	---
P12-R20	32.46	103.4%
P12-R20	---	---
P20-R40	---	---
P20-R40	---	---
P20-R40	---	---
P20-R40	---	---
P20-R40	---	---
P20-R40	32.64	99.8%
P20-R40	---	---
P20-R40	---	---
P20-R40	32.11	105.6%
P20-R40	---	---

Table 8. (continued)

Size	Batch	Test #	lbs. Load	At Max. Load				After 2 Min. of Max. Load				After Load Removal				After Swell Pressure Test	
				w % comp.	γ_d pcf	SR %	γ_m pcf	γ_d pcf	SR %	γ_m pcf	γ_m pcf	γ_d pcf	SR %	γ_m pcf	SR %	w %	SR %
P8-R10	K-1	KLS-14	1500	22.83	85.4	66.0%	104.9	88.3	70.9%	108.5	106.2	86.5	67.8%			34.48	102.3%
P8-R10	K-2	KLS-42	1500	28.11	87.8	86.2%	112.5	91.3	94.0%	116.9	115.9	90.5	92.1%			32.81	107.5%
P8-R10	K-3	KL-72	1500	29.36	88.7	92.1%	114.7	91.0	97.5%	117.7	114.3	88.3	91.2%			---	---
P8-R10	K-3	KLS-73	1500	29.36	88.9	92.5%	115.0	92.0	99.9%	119.0	115.5	89.2	93.3%			32.61	103.6%
P10-R12	K-1	KL-17	1500	23.31	83.1	64.4%	103.1	89.0	73.5%	109.7	102.7	83.3	63.9%			---	---
P10-R12	K-1	KLS-18	1500	23.31	86.1	68.5%	106.2	89.0	73.7%	109.7	---	---	---			33.53	---
P10-R12	K-2	KL-45	1500	27.85	87.8	85.4%	112.3	91.2	93.1%	116.7	114.2	89.3	88.6%			---	---
P10-R12	K-2	KLS-46	1500	27.85	87.8	85.4%	112.3	91.3	93.1%	116.7	114.7	89.7	89.5%			33.18	106.6%
P10-R12	K-3	KL-76	1500	29.37	88.8	92.4%	114.9	91.1	97.9%	117.9	114.9	88.8	92.4%			---	---
P10-R12	K-3	KL-77	1500	29.37	88.5	91.7%	114.6	91.1	97.9%	117.9	*	*	*			---	---
P10-R12	K-3	KLS-78	1500	29.37	89.2	93.1%	115.3	91.9	99.7%	118.9	117.8	91.1	97.8%			32.33	107.6%
P12-R20	K-1	KL-22	1500	22.96	83.6	63.5%	102.8	86.4	68.0%	106.2	104.5	85.0	65.7%			---	---
P12-R20	K-1	KL-23	1500	22.96	84.0	64.1%	103.3	86.8	68.7%	106.7	105.4	85.7	66.9%			---	---
P12-R20	K-1	KLS-24	1500	22.96	86.1	67.4%	105.8	89.1	72.5%	109.6	107.6	87.5	69.9%			34.24	104.2%
P12-R20	K-2	KL-50	1500	27.49	87.1	82.9%	111.1	90.9	91.1%	115.9	114.4	89.7	88.4%			---	---
P12-R20	K-2	KL-51	1500	27.49	87.1	83.0%	111.0	90.5	90.2%	115.4	113.4	89.0	86.8%			---	---
P12-R20	K-2	KLS-52	1500	27.49	87.4	83.5%	111.4	91.2	91.8%	116.3	*	*	*			33.22	*
P12-R20	K-3	KL-82	1500	29.18	88.9	92.0%	114.8	91.3	97.5%	117.9	114.9	88.9	92.0%			---	---
P12-R20	K-3	KL-83	1500	29.18	89.3	93.0%	115.4	91.3	97.6%	117.9	*	*	*			---	---
P12-R20	K-3	KLS-84	1500	29.18	89.3	93.0%	115.4	91.7	98.6%	118.4	115.4	89.3	93.0%			32.46	103.4%
P20-R40	K-1	KL-28	1500	22.55	83.9	62.8%	102.8	86.6	67.2%	106.1	*	*	*			---	---
P20-R40	K-1	KL-29	1500	22.55	83.9	62.8%	102.8	86.7	67.2%	106.2	104.5	85.3	64.9%			---	---
P20-R40	K-1	KLS-30	1500	22.55	85.9	66.0%	105.3	88.8	70.9%	108.9	107.0	87.3	68.4%			---	---
P20-R40	K-2	KL-56	1500	27.42	87.6	83.8%	111.6	91.1	91.3%	116.1	114.0	89.5	87.7%			---	---
P20-R40	K-2	KL-57	1500	27.42	87.7	83.8%	111.7	91.1	91.3%	116.1	114.1	89.5	87.8%			---	---
P20-R40	K-2	KLS-58	1500	27.42	88.4	85.4%	112.7	91.9	93.2%	117.1	111.7	87.7	83.8%			32.64	99.8%
P20-R40	K-3	KL-88	1500	27.88	88.3	86.6%	112.9	91.4	93.4%	116.8	114.2	89.3	88.7%			---	---
P20-R40	K-3	KL-89	1500	27.88	88.0	85.9%	112.5	91.0	92.7%	116.4	114.4	89.5	89.2%			---	---
P20-R40	K-3	KLS-90	1500	27.88	89.1	88.3%	113.9	92.6	96.4%	118.4	115.9	90.6	91.6%			32.11	105.6%

resulting omissions are marked with an asterisk (*) in Table 8.

The most obvious trends from these results are as follows:

A. At Maximum Load

1. Holding the aggregate size constant the compacted dry unit weight (γ_d) increases as the moisture content increases.
2. Holding the aggregate size constant the compacted total unit weight (γ_m) increases as the moisture content increases.
3. Holding the aggregate size constant the degree of saturation (S_r) increases as the moisture content increases.

B. After Two Minutes of Maximum Load

1. The trends stated above in A are still in evidence.
2. A comparison of the γ_d values with those from A above shows that the increase in γ_d during the two minutes of constant load increases with the increase in compaction moisture content at the 1,000 lb. level.
3. At the 1,500 lb. level the increase in γ_d during the two minutes of constant load

is largest at the intermediate (K-2) moisture content.

4. Many of the K-3 samples compacted with the 1,500 lb. load closely approached their limiting dry unit weights, i.e., S_r approached 100%.

C. After Load Removal

1. The decrease in γ_d upon removal of the compactive load increases as the aggregate size decreases at both levels of compaction.

D. After Swell Pressure Test

1. Within the limits of experimental verification the samples imbibed enough water so that they were essentially saturated.

Swelling Pressure

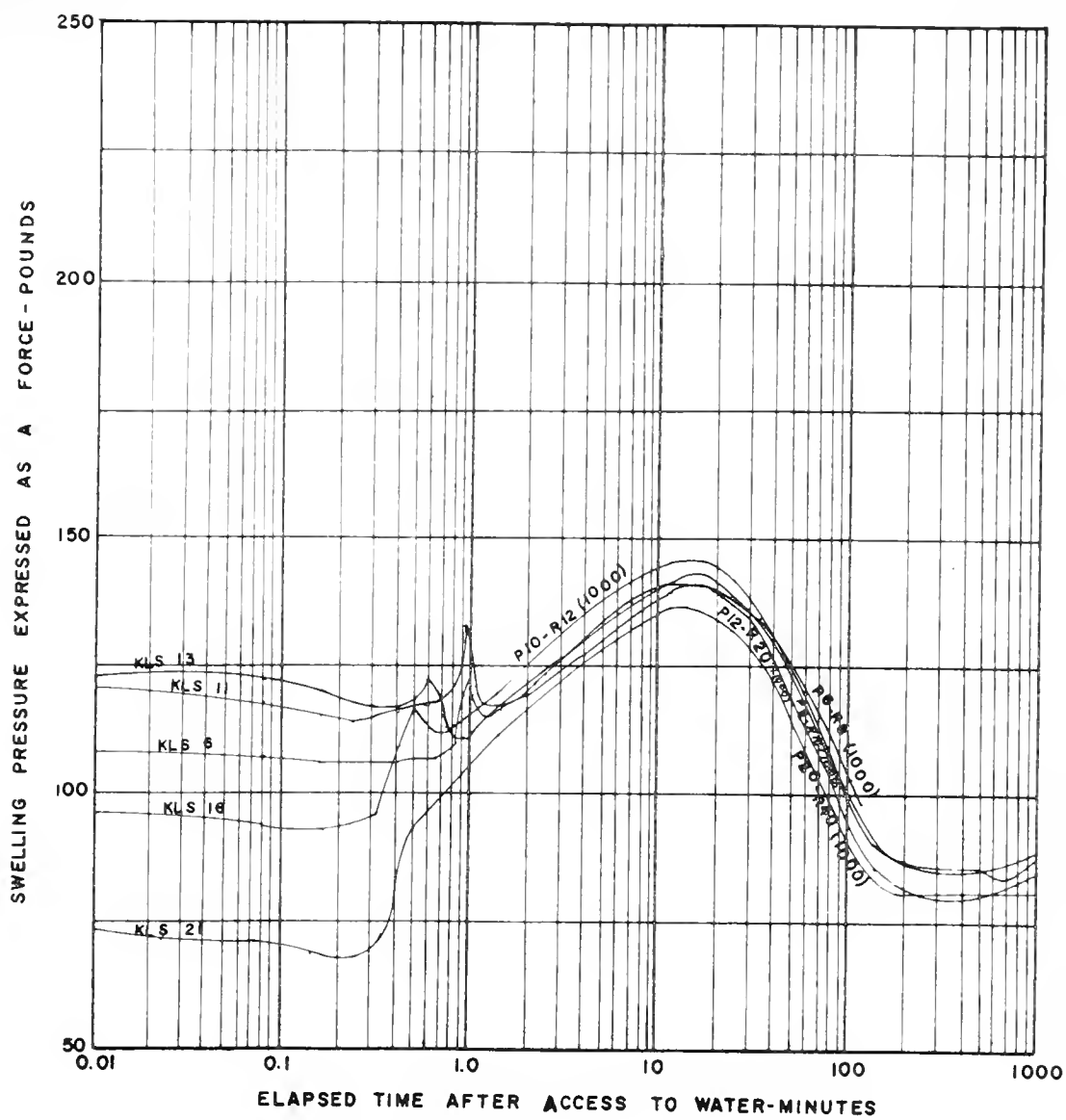
As explained previously, selected samples were allowed to remain in the mold after compaction. In this case the upper surface of the sample was restrained to prohibit any increase in total volume, the sample was allowed to imbibe water, and the swelling pressure expressed as a force was measured until equilibrium was essentially reached.

The swelling pressure was expressed as a force because it was felt that nothing would be gained by the

introduction of another constant, the surface area of each compacted specimen. It cannot be stated with absolute assurance that the "equilibrium" pressure measures were indeed long-term equilibrium values. Every effort was made to control the temperature of each specimen during these tests, however the chance of the average controlled temperature changing increases with the length of the test. In addition, when the true change in swelling pressure is quite small over a period of time, it can be masked by the effects of small ($\pm 0.1^{\circ}\text{C}$) temperature changes occurring from the normal temperature control technique. For these reasons there was a practical limit, a function of elapsed time and rate of change of pressure generated, beyond which no meaningful data could be derived. It was at this limit that the equilibrium value of swelling pressure was defined.

The results of these tests are shown in Figures 39 through 44. Each of the six figures shows the results as a function of aggregate size, with the batch (compaction moisture content) and level of compactive effort as constants.

In general for the samples compacted at the 1,000 lb. level of effort the results indicate that the maximum swelling pressure increases as the compaction water content increases. A general time-pressure pattern is also evident. The pressure rapidly reaches a maximum value after it has



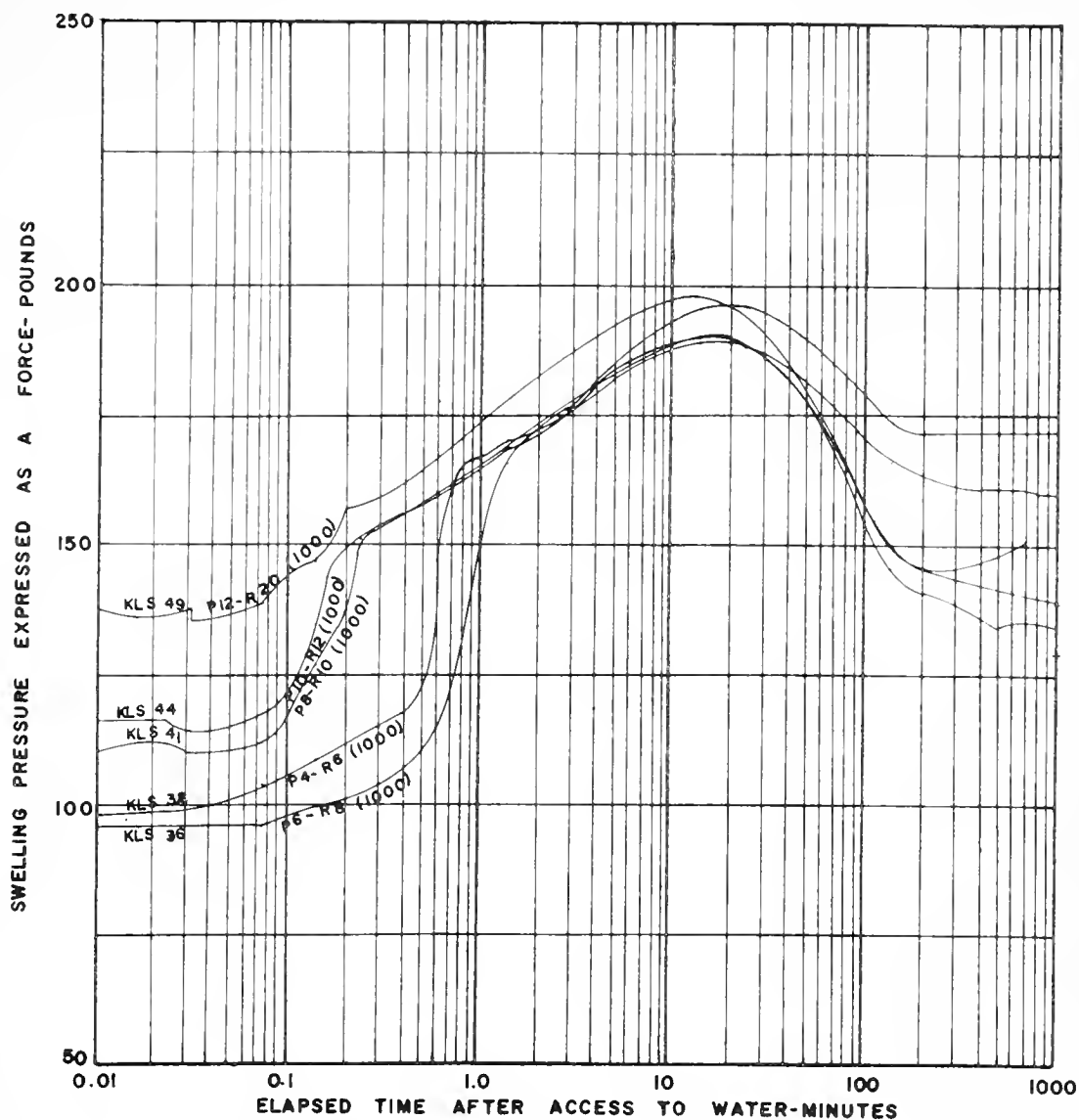


FIGURE 40. RESULTS OF SWELLING PRESSURE TESTS (K-2 AT 1000 POUND LEVEL)

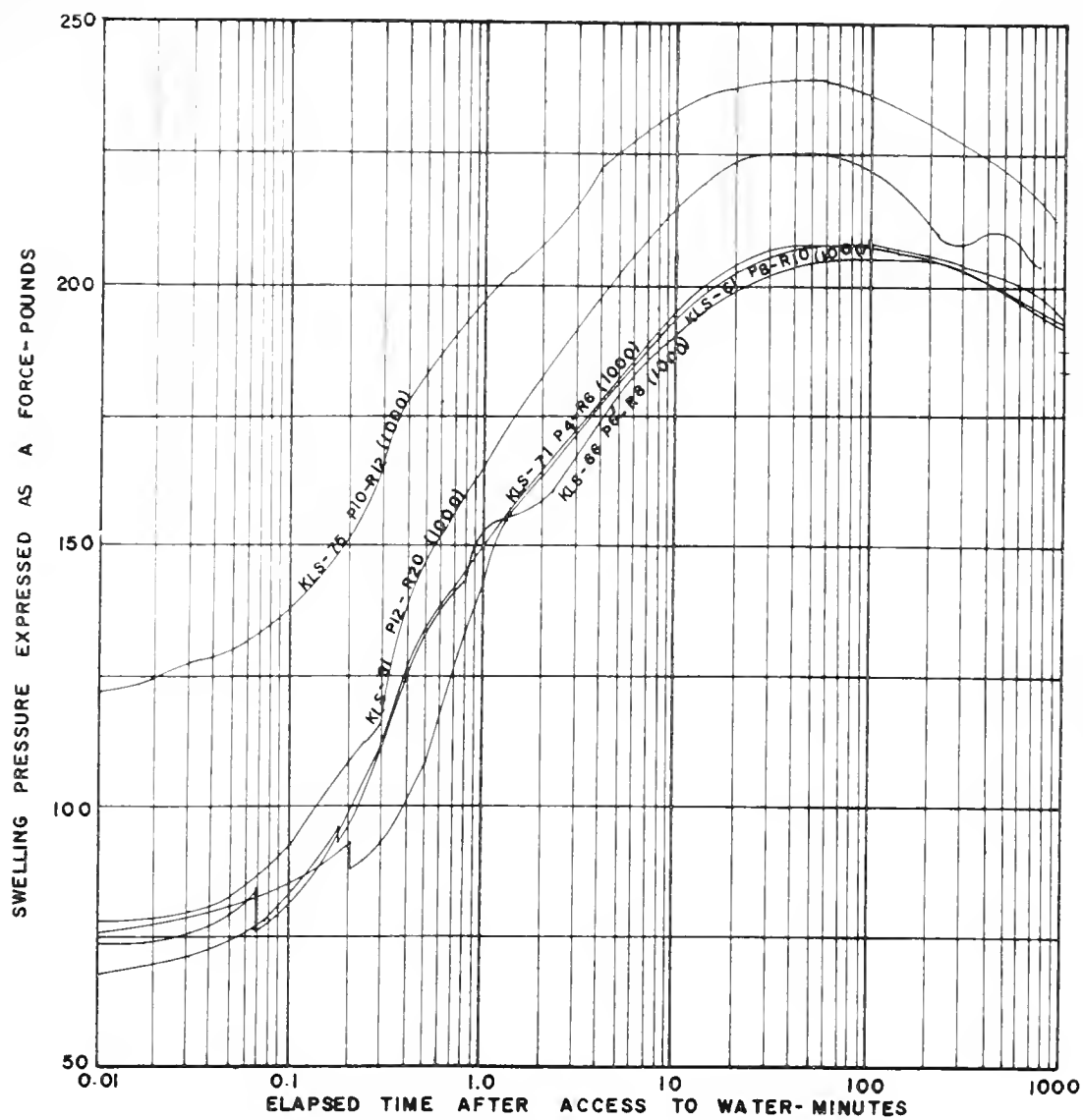


FIGURE 4I. RESULTS OF SWELLING PRESSURE TESTS (K-3 AT 1000 POUND LEVEL)

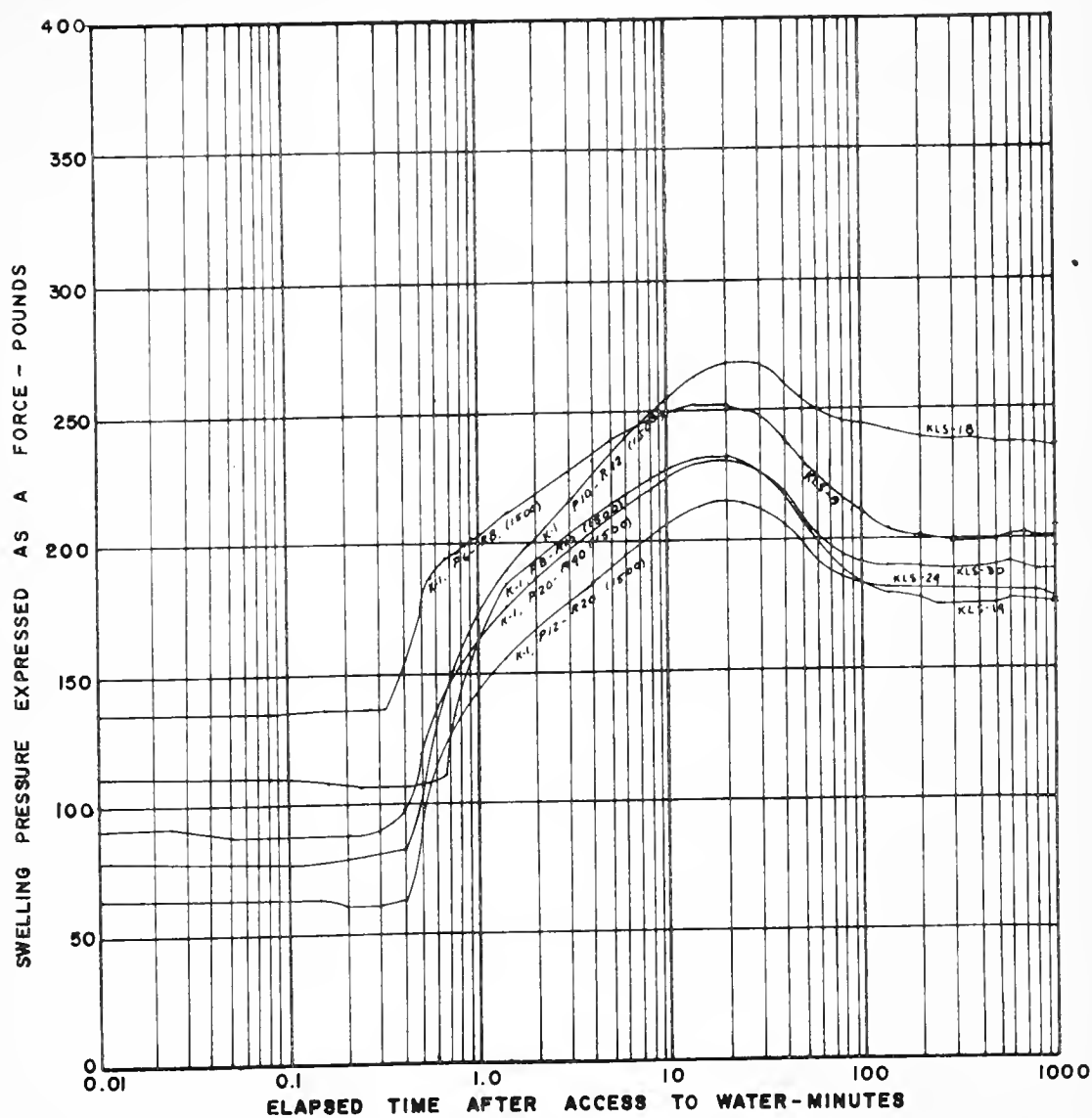


FIGURE 42. RESULTS OF SWELLING PRESSURE TESTS (K-1 AT 1500 POUND LEVEL)

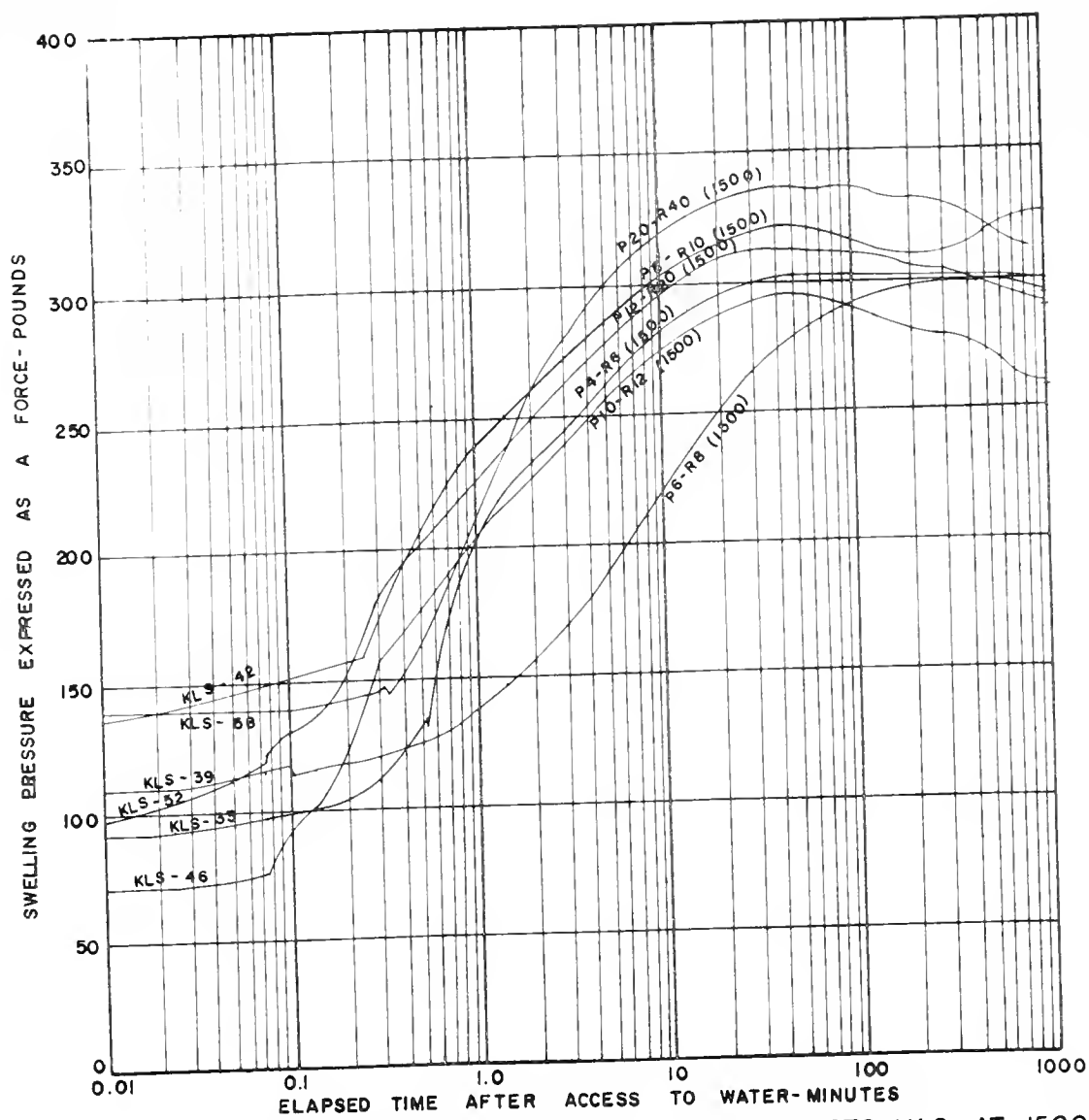


FIGURE 43 RESULTS OF SWELLING PRESSURE TESTS (K-2 AT 1500 POUND LEVEL)

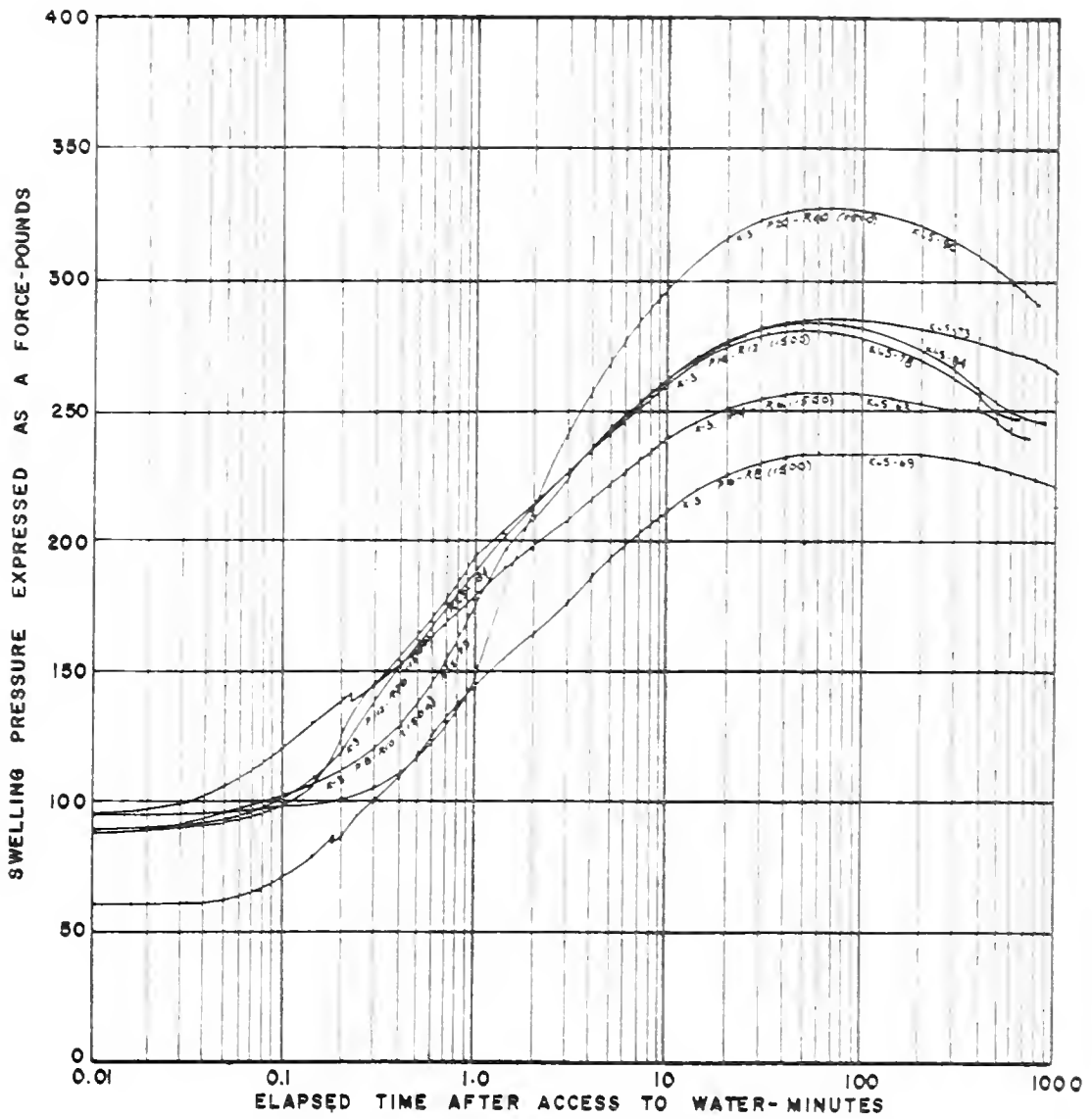


FIGURE 44. RESULTS OF SWELLING PRESSURE TESTS (K-3 AT 1500 POUND LEVEL)

been given access to water and decreases thereafter at a slower rate to some equilibrium value.

The time-pressure pattern for the samples compacted at the 1,500 lb. level showed this same general pattern. However whereas at the 1,000 lb. level for each aggregate size there was an increase in the maximum swelling pressure as the compaction moisture content increased, at the 1,500 lb. effort level all aggregate sizes, without exception, exhibited increases in their maximum swelling pressure from the low (K-1) to intermediate (K-2) moisture content and decreases from the intermediate (K-2) to high (K-3) compaction moisture content.

Another characteristic exhibited by some of the specimens was an apparent temporary drop in their swelling pressures before the maximum values were reached. This feature is most apparent in Figure 39.

Aggregate Deformation

The output from each aggregate compression test was the load required to deform an individual aggregate at a constant displacement rate as a function of the displacement. Thirty replicate tests were run for each aggregate size-water content combination tested. The results of the thirty tests were then averaged. These average results are shown in Figures 45, 46, and 47. Not all of the size-moisture content combinations were tested either because

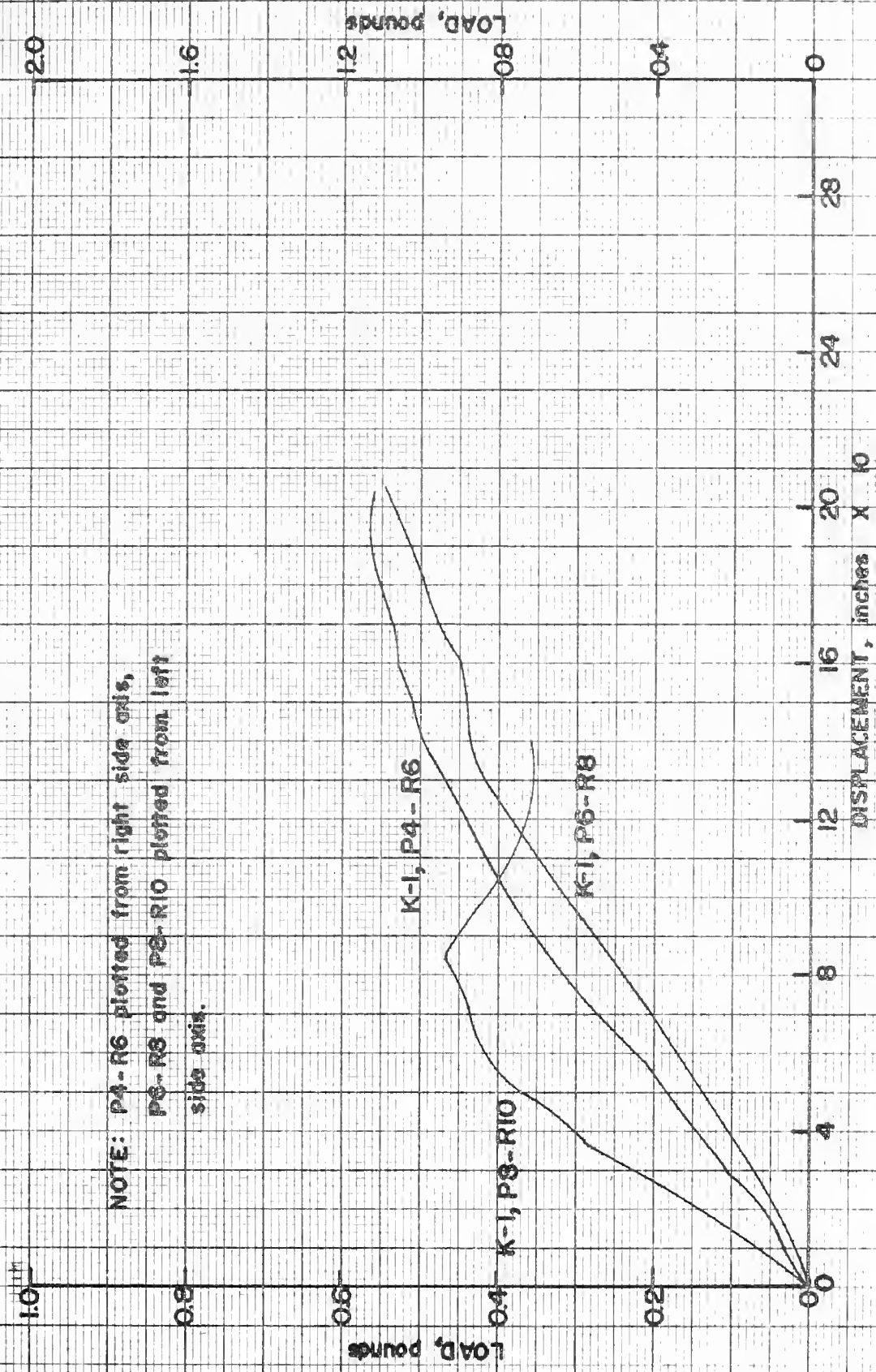


FIGURE 45. SINGLE AGGREGATE LOAD vs. DEFORMATION RESULTS, BATCH K-1

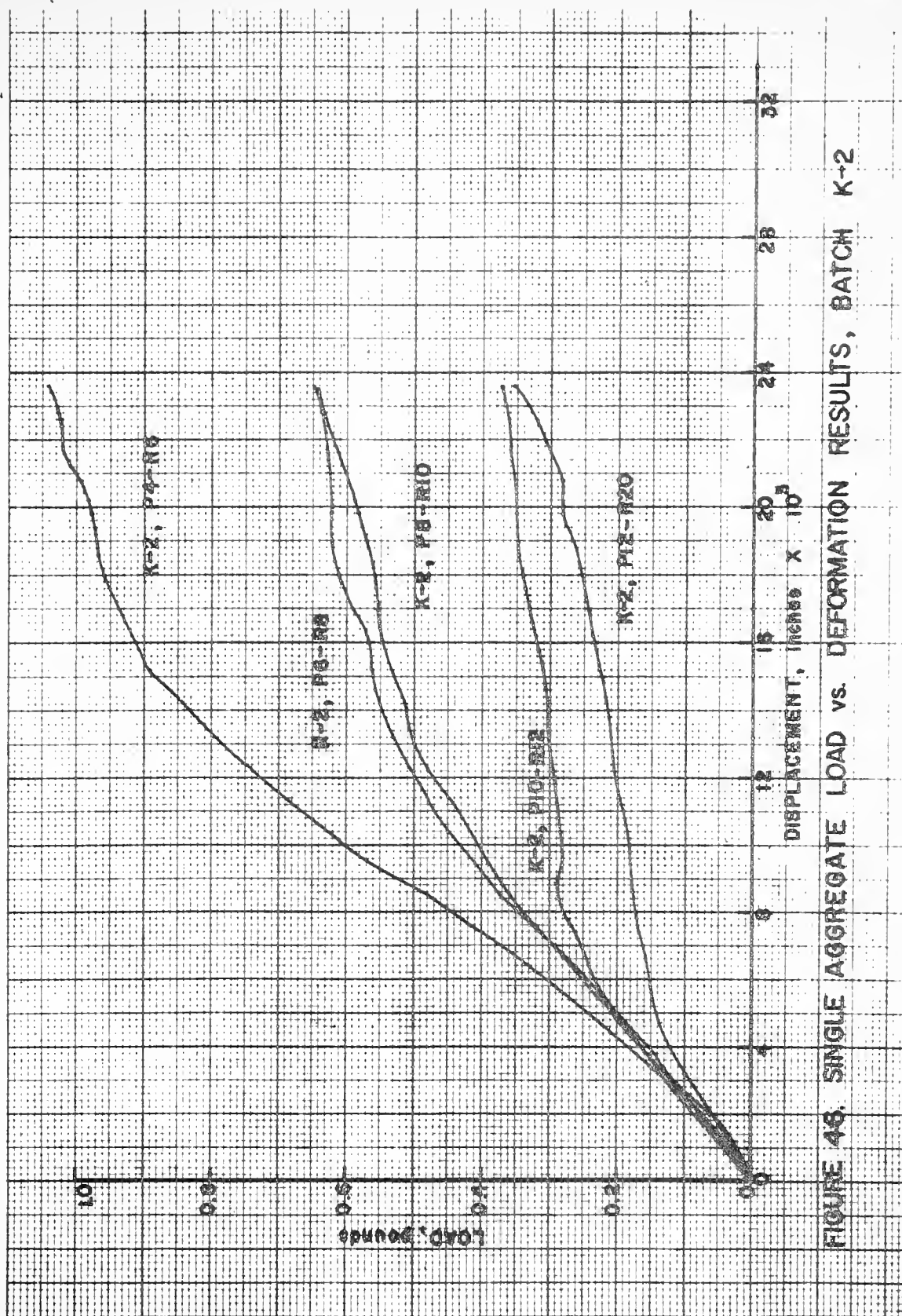


FIGURE 46. SINGLE AGGREGATE LOAD vs. DEFORMATION RESULTS, BATCH K-2

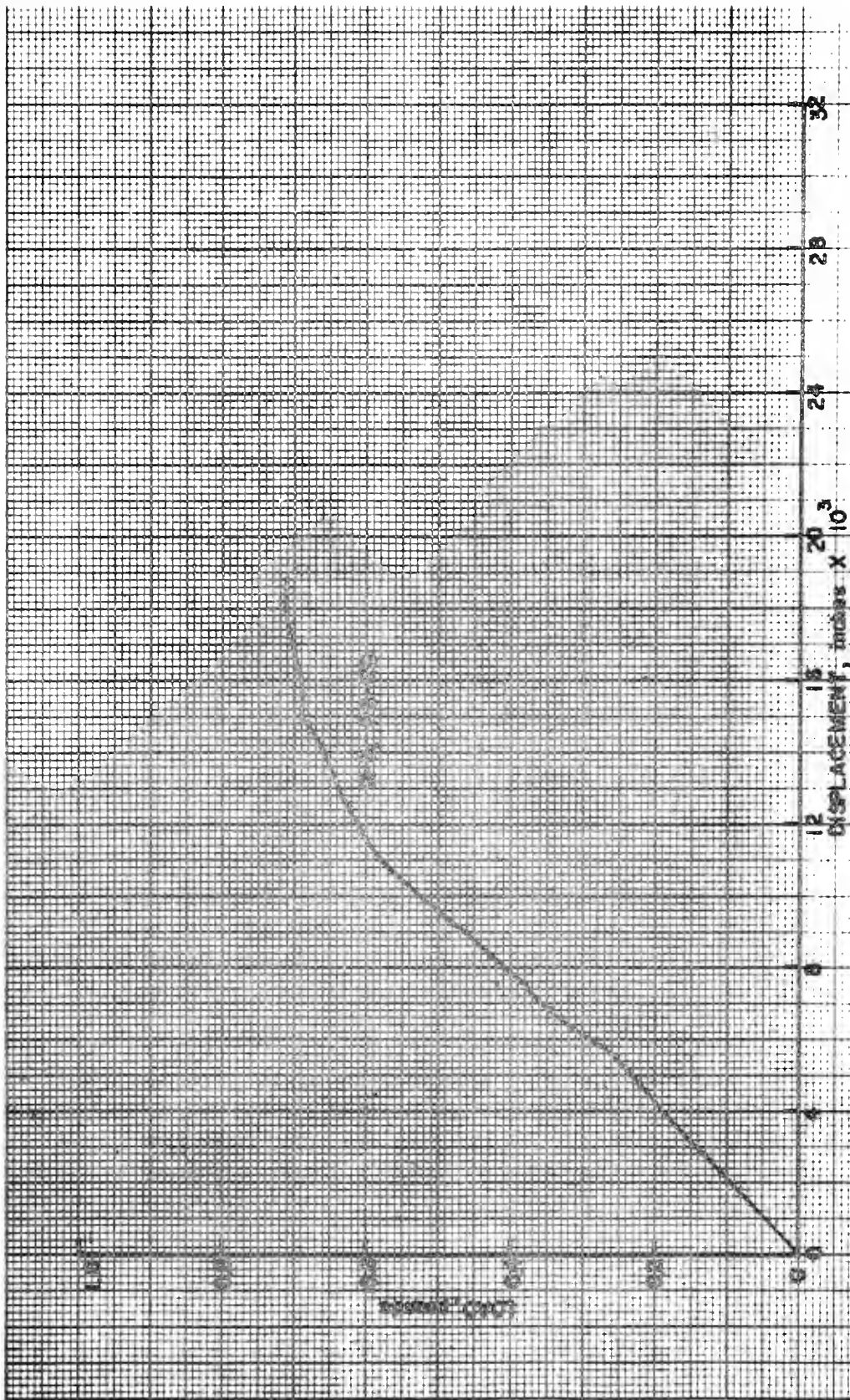


FIGURE 47. SINGLE AGGREGATE LOAD vs. DEFORMATION RESULTS, BATCH K-3

of their very small size or because they were judged to be atypical of the aggregates used in the compacted specimens.

The results show the load-deformation curves to be reasonably linear to some point beyond which the load buildup is more gradual. As can be seen in Figure 46, both the peak load for the linear portion of the curve and the slope of the curve depend on the aggregate size. As the aggregate size increases, both the peak load and the slope of the curve increase.

However load-deformation is not the most meaningful indicator of strength and elasticity when specimen size is a variable, and an analysis in terms of stress is made under DISCUSSION OF RESULTS.

DISCUSSION OF RESULTS

Particle Orientation

Relations among the variables as shown in part in Figures 31, 32, and 33 were analyzed statistically with the aid of the Wald-Wolfowitz run test (14). This device tests the hypothesis that two groups of observations are from the same population, and it does not depend on the normality of the samples.

The results of the application of this test are shown below in Table 9. An explanation of the test and the numerical values are given in Appendix E.

The dependence of peak height ratio on molding water content (Figure 32) for aggregates as well as compacted samples of size P6-R8 is, for the most part, confirmed. Of the nine null hypotheses tested only two could not be rejected, and both of these involve K-2 K-3 comparisons. The difference in compaction water content between K-2 and K-3 is smaller than that between K-1 and K-2, therefore, it is expected that fabric dependence on water content would be less well defined for the former pair. The comparison of mean values and the statistical tests indicate that for size P6-R8 the peak height ratio is dependent on moisture content and increases as the moisture content increases.

Table 9. Results of Wald-Wolfowitz Run Test

<u>Condition</u>		<u>Hypothesis</u>	<u>Code*</u>	<u>Result</u>
Aggregates	P6-R8	K-1 = K-2	(1)	Reject
		K-2 = K-3	(2)	Cannot Reject
		K-1 = K-3	(3)	Reject
1,000 lb.	P6-R8	K-1 = K-2	(4)	Reject
		K-2 = K-3	(5)	Reject
		K-1 = K-3	(6)	Reject
1,500 lb.	P6-R8	K-1 = K-2	(7)	Reject
		K-2 = K-3	(8)	Cannot Reject
		K-1 = K-3	(9)	Reject
Aggregates	P20-R40	K-1 = K-2	(10)	Cannot Reject
		K-2 = K-3	(11)	Cannot Reject
		K-1 = K-3	(12)	Cannot Reject
1,000 lb.	P20-R40	K-1 = K-2	(13)	Cannot Reject
		K-2 = K-3	(14)	Reject
		K-1 = K-3	(15)	Reject
1,500 lb.	P20-R40	K-1 = K-2	(16)	Reject
		K-2 = K-3	(17)	Reject
		K-1 = K-3	(18)	Reject
Aggregates	K-1	P6-R8 = P20-R20	(19)	Reject
	K-2	P6-R8 = P20-R40	(20)	Cannot Reject
	K-3	P6-R8 = P20-R40	(21)	Cannot Reject
1,000 lb.	K-1	P6-R8 = P20-R40	(22)	Reject
	K-2	P6-R8 = P20-R40	(23)	Cannot Reject
	K-3	P6-R8 = P20-R40	(24)	Cannot Reject
1,500 lb.	K-1	P6-R8 = P20-R40	(25)	Cannot Reject
	K-2	P6-R8 = P20-R40	(26)	Cannot Reject
	K-3	P6-R8 = P20-R40	(27)	Reject
P6-R8	K-1	Agg.=1,000 lb.	(28)	Reject
		1,000 lb.=1,500 lb.	(29)	Reject
		Agg.=1,500 lb.	(30)	Reject
P6-R8	K-2	Agg.=1,000 lb.	(31)	Reject
		1,000 lb.=1,500 lb.	(32)	Reject
		Agg.=1,500 lb.	(33)	Reject

* The code is used as the descriptor in Table E1, Appendix E.

Table 9. (continued)

P6-R8	K-3	Agg.=1,000 lb.	(34)	Reject
		1,000 lb.=1,500 lb.	(35)	Cannot Reject
		Agg.=1,500 lb.	(36)	Reject
P20-R40	K-1	Agg.=1,000 lb.	(37)	Reject
		1,000 lb.=1,500 lb.	(38)	Reject
		Agg.=1,500 lb.	(39)	Reject
P20-R40	K-2	Agg.=1,000 lb.	(40)	Reject
		1,000 lb.=1,500 lb.	(41)	Reject
		Agg.=1,500 lb.	(42)	Reject
P20-R40	K-3	Agg.=1,000 lb.	(43)	Reject
		1,000 lb.=1,500 lb.	(44)	Reject
		Agg.=1,500 lb.	(45)	Reject

This dependence is not as apparent for size P20-R40 (Figure 32). The statistical test does not indicate any dependence for the aggregates or for the low and intermediate water content pair compacted at the 1,000 lb. level. However, the dependence is confirmed for the high moisture content (K-3) at the 1,000 lb. level and for the entire moisture content range investigated at the 1,500 lb. compaction level.

A peak height ratio-compactive effort relation, shown in Figure 33, is confirmed. For the size P6-R8 only one anomaly exists, the failure to reject the null hypothesis for the K-3 1,000 and 1,500 lb. combination. The trend is established for the P20-R40 size material without exception.

The analysis of Figure 31 indicates, for batch K-1, that initially the particle orientation is size dependent and that this dependence disappears under high compaction pressure. This trend is not evident at an intermediate moisture content (K-2). In this case the statistical tests indicate the two sample sizes to have the same peak height ratios at all three conditions tested. The high moisture content samples of batch K-3 show no size dependence for the aggregate and 1,000 lb. load conditions, but the indication is that at the 1,500 lb. load size P20-R40 has a higher peak height ratio than size P6-R8. This last mentioned result seems to be inconsistent with the pattern

developed, viz., the trend that shows orientation dependence on size only at low moisture content with zero and moderate compaction loads.

If it is assumed that the peak height ratio observations for K-3, P6-R8 at 1,500 lb. load are erroneously low, the previously mentioned inconsistency would not occur. This same sample was responsible for the inability to reject the null hypothesis between K-2, P6-R8 and K-3, P6-R8 at the 1,500 lb. level in Figure 32 because its peak height ratios were too low.

In light of the trend that shows P6-R8 and P20-R40 to be from the same populations for all three K-2 states of compaction and for the K-3 aggregate and 1,000 lb. load conditions, the K-3, P20-R40 at 1,500 lb. load should be from the same population as the K-3, P6-R8 at 1,500 lb. load data. Replacing K-3, P6-R8 at 1,500 lb. with K-3, P20-R40 at 1,500 lb. and comparing this with the K-2, P6-R8 at 1,500 lb. data statistically shows that the null hypothesis is rejected. This further confirms the trend of Figure 32 which shows the peak height ratio to be dependent on the molding water content.

Making this same replacement and comparing K-3, P20-R40 at 1,500 lb. with K-3, P6-R8 at 1,000 lb. results in the null hypothesis also being rejected. This result improves the trend exhibited by Figure 33 to the point that there are no exceptions among the observed data to contradict

the observation that the peak height ratio measured is dependent on the compactive effort exerted on the specimen.

This analysis has shown that the relative degree of orientation tends to increase as the moisture content increases for uncompacted size P6-R8 aggregates as well as for both aggregate sizes in compacted samples at both levels of compactive effort. These results are predicted by both the Lambe model (27) and this writer's model.

For the uncompacted aggregates and if it is assumed that plasticity, the ability to deform without fracturing, increases as the moisture content increases, the wettest aggregates will incur the largest shear strains during mixing, and the clay plates (Lambe) or domains (Hodek) will become better oriented.

Similarly under the action of a compactive load, according to Lambe, the degree of orientation will increase as the water content increases since the clay particles can more freely move about into a more parallel and denser array. According to this writer, densification occurs by a rearrangement of the aggregates into a denser array, similar to the densification of granular soil, and by deformation of the aggregates to accommodate themselves to the shapes of the available voids. Both of these processes involve some intra-aggregate movements, localized surface smearing and general shear strains, respectively. Deformation of the aggregates tends to better align the domains and/or

plates parallel to the loading plane, and the compacted samples will exhibit the increasing orientation which was, in fact, measured.

Again the results which show that at constant moisture content the degree of orientation increases as the level of compactive effort increases are adequately predicted by both the Lambe and this writer's models. For the specimens examined, the unit weight increased as the compactive effort was increased, and this necessarily involved more inter- and intra-aggregate movements, at least some of which would re-orient the domains into a more orderly arrangement.

Dry Unit Weights of Aggregates

The results of the determinations of the dry unit weights of aggregates shown in Table 10 follow directly from two experimentally determined quantities, the average aggregate volumes and the corresponding weights of solids per aggregate. As stated previously the relationships among water content, aggregate size, and dry unit weight are not well defined.

To interpret these results additional ratios have been computed. They are the degree of saturation (S_r), the total or mass unit weight (γ_m), and the intra-aggregate void ratio (e). These values along with the aggregate moisture contents, aggregate volumes, aggregate dry weights, and aggregate dry unit weights are shown in Table 10.

The results can best be assessed in terms of the degree of saturation, since $S_r = 100\%$ is an upper bound on the

Table 10. Measured and Calculated Aggregate Characteristics.

Aggregate	Volume, $\text{cm}^3 \times 10^{-2}$	Aggregate Dry Wgt., $\times 10^{-2}$ gm/agg	Water Content %	Dry Unit Wgt., γ_d , pcf	Total Unit Wgt., γ_m , pcf	Degree of Saturation S., %	Void Ratio e
K-1, P4-R6	3.24	3.915	23.93	75.4	93.4	54.0	1.15
K-2, P4-R6	2.96	3.650	28.19	76.9	98.6	66.0	1.11
K-3, P4-R6	2.56	3.636	29.94	88.6	115.1	93.6	0.832
K-1, P6-R8	0.988	1.480	23.39	93.4	115.2	82.5	0.736
K-2, P6-R8	0.945	1.297	28.46	85.6	110.0	82.6	0.894
K-3, P6-R8	0.981	1.321	29.86	84.0	109.1	83.4	0.931
K-1, P8-R10	0.526	0.787	22.83	93.2	114.5	80.0	0.742
K-2, P8-R10	0.510	0.670	28.11	82.0	105.1	74.5	0.980
K-1, P10-R12	0.339	0.4835	23.31	89.0	109.8	73.6	0.821
K-2, P10-R12	0.252	0.4338	27.85	107.4	137.3	141.7	0.511
K-3, P10-R12	0.256	0.3467	29.37	84.5	109.3	83.1	0.919
K-1, P12-R20	0.141	0.1995	22.96	88.3	108.6	71.3	0.838
K-2, P12-R20	0.054	0.0910	27.31	104.5	133.0	128.4	0.553
K-3, P12-R20	0.050	0.0860	29.18	106.9	138.1	146.6	0.517
K-1, P20-R40	0.0114	0.0158	22.40	86.5	105.9	66.6	0.876
K-2, P20-R40	0.0156	0.0205	27.42	82.0	104.5	72.7	0.980
K-3, P20-R40	0.0113	0.0150	28.87	82.8	106.7	78.2	0.961

possible values. If the experimental results indicate that $S_r > 100\%$, it is certain that one or both of the measured variables are in error and reasonable adjustments must be made.

For all aggregates except K-2,P10-R12; K-2,P12-R20; and K-3,P12-R20 the degrees of saturation appear to be reasonable; that is, $S_r < 100\%$. They show that as the compaction water content increases, the degree of saturation of the aggregate increases. The relationship between aggregate size and degree of saturation is shown in Figure 48. In this Figure the computed degree of saturation is plotted versus the measured moisture content for each aggregate. The data have been divided into three groups, K-1, K-2, and K-3, and a straight line has been fitted to each data group by the method of least squares. For the least squares fits, K-1,P4-R6 and K-2,P4-R6 were not considered, since they do not conform to the general trend. This analysis indicates that the degree of saturation increases as the aggregate size increases.

This Figure also demonstrates that when the aggregate size is held constant and the water content is increased, the degree of saturation increases. This relationship bears out the hypothesis that the pore water pressure is negative within the aggregate. As more water is made available, it is drawn into the aggregate to satisfy this water deficiency.

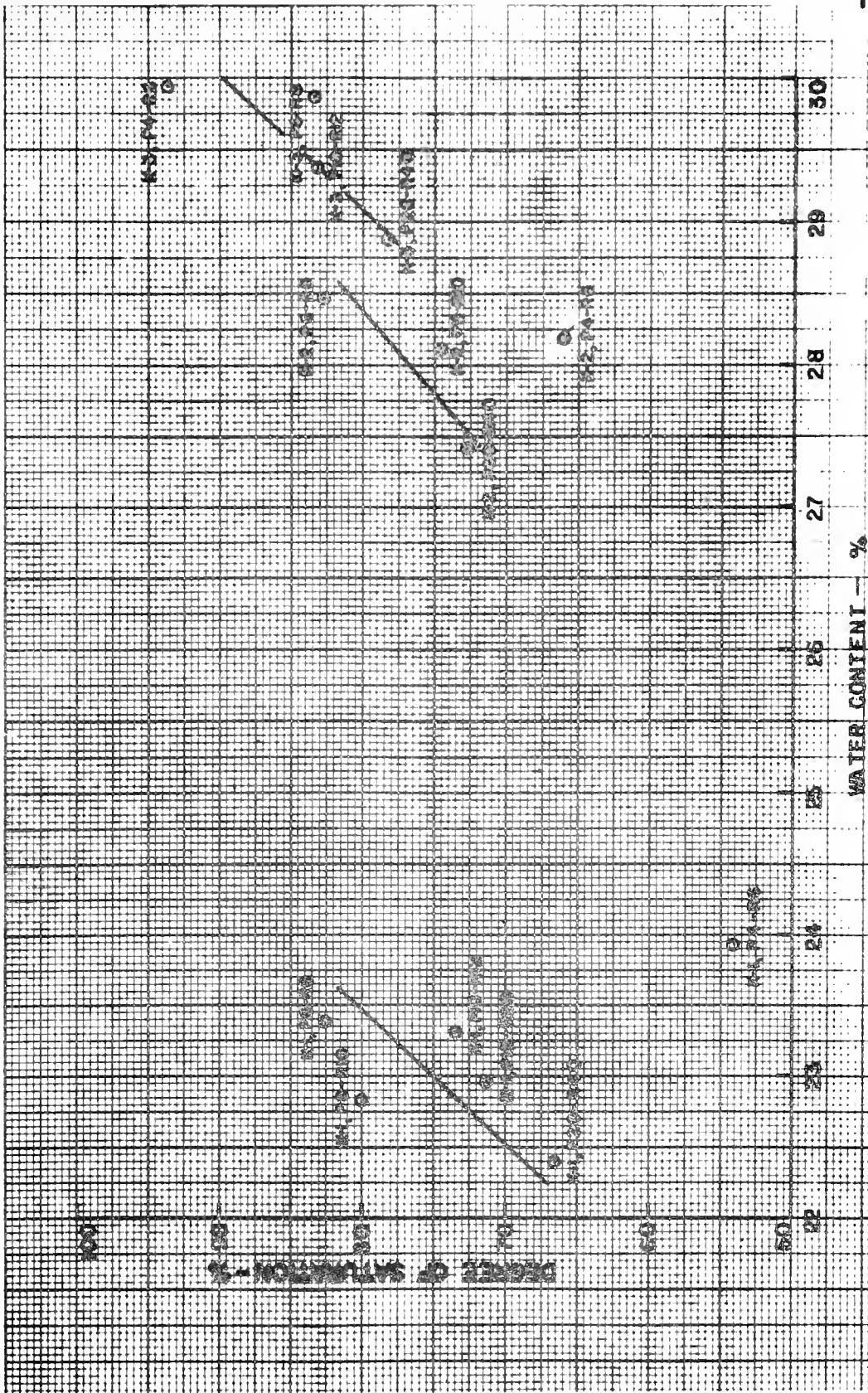


FIGURE 1. DEGREE OF SATURATION - WATER CONTENT RELATION FOR AGGREGATES

The relationship showing that the degree of saturation increases as the aggregate size increases can be attributed to the method of soil preparation. As previously explained the soil was agitated rather vigorously in the P-K solid-liquid blender as the water was added. This caused the aggregates to collide with each other, with the walls of the blender, and with the rotating beaters in the blender. The larger the aggregate's size, the larger its mass is, and the higher will be the contact stresses at impact. Thus the impacts cause some intra-aggregate compaction to occur, and the larger the aggregate is, the more compaction (reduction of air voids) occurs.

The erroneous results for K-2,P10-R12; K-2,P12-R20; and K-3,P12-R20 are apparent not only by an examination of their degrees of saturation but also by the void ratios tabulated in Table 10. These three exhibit void ratios which are noticeably lower than any others in the table. This indicates that the errors involve the void volumes and/or solid volumes, V_v and V_s respectively, since $e = V_v/V_s$. Both V_v and V_s are derived from the measured total volume, V , and the measured dry weight of an aggregate, W_s . The relationships are shown below:

$$V = V_v + V_s$$

$$V_s = W_s/G_s$$

$$V_v = V - W_s/G_s$$

where $G_s = 2.60$, the specific gravity of this kaolinite.

The locations of the experimental errors cannot be ascertained. However it should be pointed out that by substituting void ratios which are reasonable in comparison to the other void ratios exhibited in Table 10 the results are more plausible. Using a value of $e = 0.90$ the following results are obtained:

K-2,P10-R12	$S_r = 80.5\%$	$\gamma_d = 85.4$ pcf	$\gamma_m = 109.2$ pcf
K-2,P12-R20	$S_r = 78.9\%$	$\gamma_d = 85.4$ pcf	$\gamma_m = 108.7$ pcf
K-3,P12-R20	$S_r = 84.3\%$	$\gamma_d = 85.4$ pcf	$\gamma_m = 110.3$ pcf

Holding the batch (mixing water content) constant and comparing the water contents for the various sized aggregates shows that as the size increases the moisture content increases. According to the author's hypothesis for formation of the aggregates during mixing this is an expected result.

The hypothesis states that aggregate-domain and aggregate-aggregate growth is dependent on an abundance of water being temporarily present on the surface of the aggregate. It is the mutual desire for this water that causes aggregates to remain together after a collision. The more water there is present, the larger the size to which the aggregate can grow, i.e., the larger aggregates are expected to have a higher moisture content than the smaller ones.

Achievement of Compacted Unit Weight

Analysis of the samples used for the swelling pressure determinations indicates, with one anomaly, that the residual unit weight (rebound allowed after two minutes of application of the compactive load) varies directly as the moisture content. This indicates that in the usual terminology these samples, with the exception of batch K-3 compacted at the 1,500 lb. level, were compacted at water contents dry of optimum for the static compaction involved. The high final degree of saturation (Table 8) indicates that the K-3 at 1,500 lb. samples were wet of the omc.

It is commonly known that increasing the compactive effort input results in a higher unit weight at a constant moisture content and a lower optimum moisture content. That is, as the compactive effort increases, the $w-\gamma$ curve shifts up and to the left. This relation has been shown countless times for laboratory compaction and to a lesser but sufficient extent for field compaction (59). It is also known that if the type of compaction and compactor rating are held constant and only the number of blows per layer or number of passes in the procedure are allowed to vary, a condition is reached beyond which no additional permanent densification will occur. A combination of compaction and soil variables has been reached where no further densification occurs and no further net energy is transferred to the compacted mass, i.e., the soil behaves elastically. However a heavier

roller in the field or a heavier hammer in the laboratory will cause the soil to accept additional net energy until a new plateau is reached.

This can be understood in terms of the second-order skeleton. The skeletal strength increases during densification until its shear strength is equal to the compaction shear stresses. If the compaction stresses are increased by a procedural change or change in equipment rating, further densification will occur until a new equilibrium is reached between the skeletal shear strength and the imposed shear stress system. Beyond a certain combination of stress input and compaction moisture content (or aggregate strength) the skeleton structure is effectively destroyed.

For a given soil and type of compaction the optimum moisture content is essentially dependent on the degree of saturation. For a given moisture content the upper limit on the compacted unit weight is imposed by the compacted soil reaching a particular degree of saturation. As shown by others (27) a marked decrease in air permeability occurs at this point and this indicates a rapid decrease of the interconnected or continuous air voids. The moisture content controls the intra-aggregate strength and thus the effort necessary to break down the aggregate structure. The type of compaction and the aggregate size distribution control the degree of saturation at which the air voids become discontinuous. Once the air voids become

discontinuous very little further densification will occur regardless of the input effort. This is demonstrated by the fact that as the moisture content is increased wet of optimum, a common water content-unit weight relation develops which is independent of input energy. An example of this is shown in Figure 49.

The conventional compaction test does not allow the comparison of unit weights achieved at different moisture contents for a constant value of net energy imparted to the sample. The experimental procedure used for the preparation of compacted samples in this investigation does allow this comparison to be made. The unit weights achieved at various moisture contents can be compared at the same level of net energy absorbed. This is shown in terms of γ_m in Figures 50 through 60 and in terms of γ_d in the figures of Appendix F. In effect, this allows the efficiency of densification at various moisture contents to be evaluated. One variable, the heretofore unknown wasted or elastic energy, has been removed. All energies shown in the figures and tables can be considered to be comparable from sample to sample, that is, they can be considered to have been normalized with respect to the weight of the solids, W_s , for each test. They were not normalized, however for each compacted sample $W_s = 67.4 \pm 0.3$ grams, so that the effect is the same as normalization

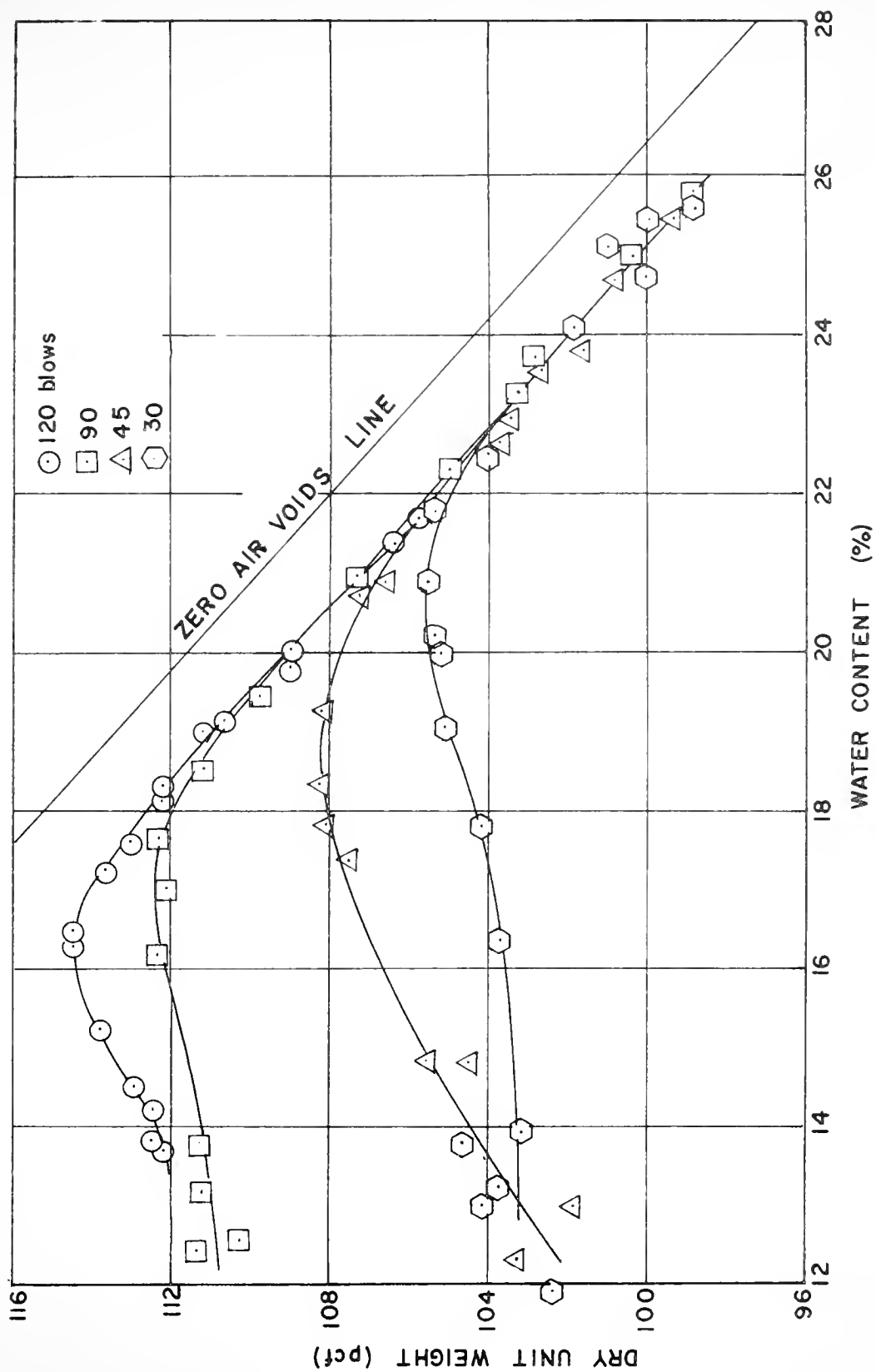


FIGURE 49. IMPACT COMPACTION CURVES FOR GRUNDITE AFTER PERLOFF (44)

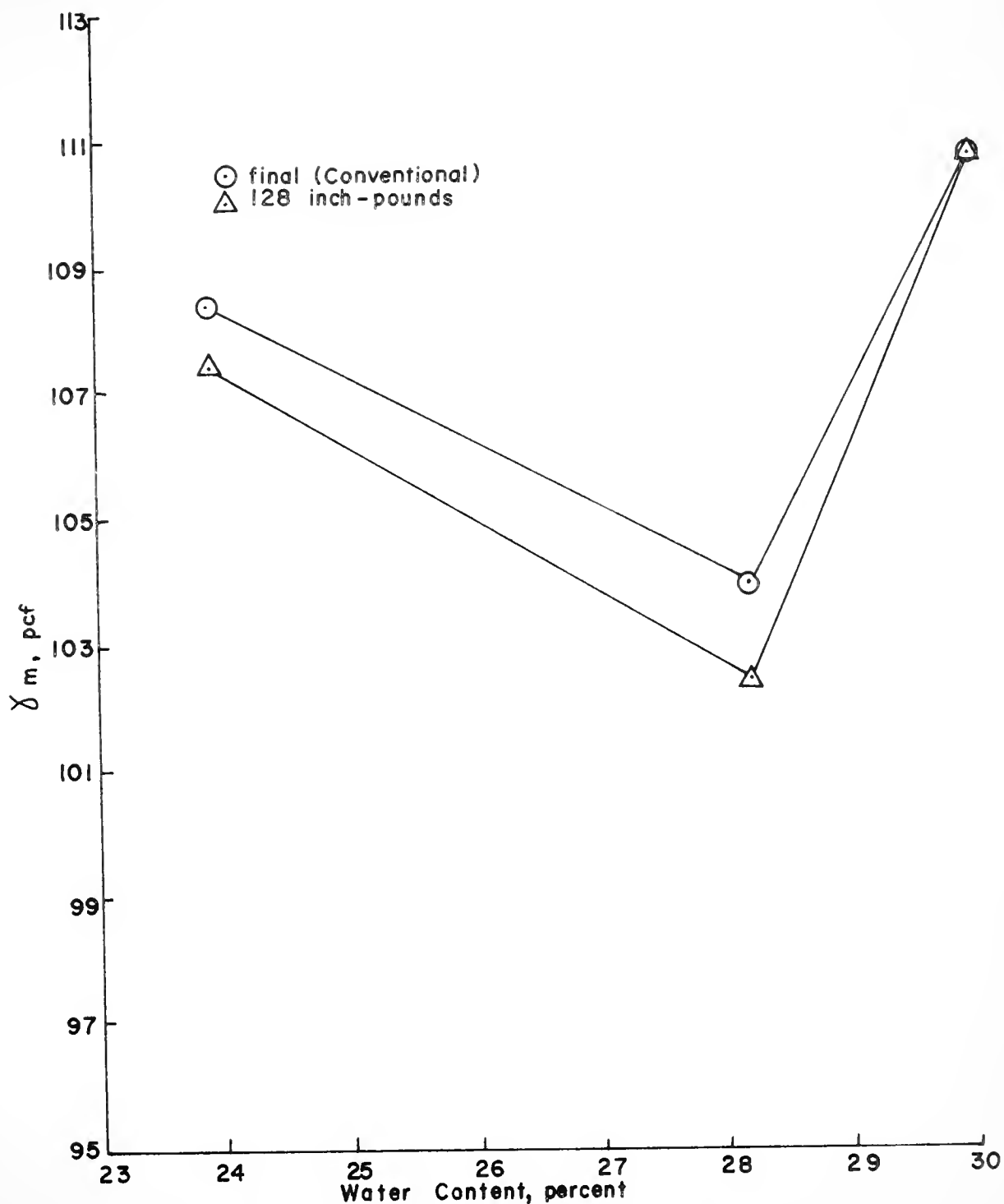


FIGURE 50. CONVENTIONAL AND EQUAL NET INPUT ENERGY
MOISTURE-TOTAL UNIT WEIGHT RELATIONS
(P4-R6; 1000 LB LEVEL)

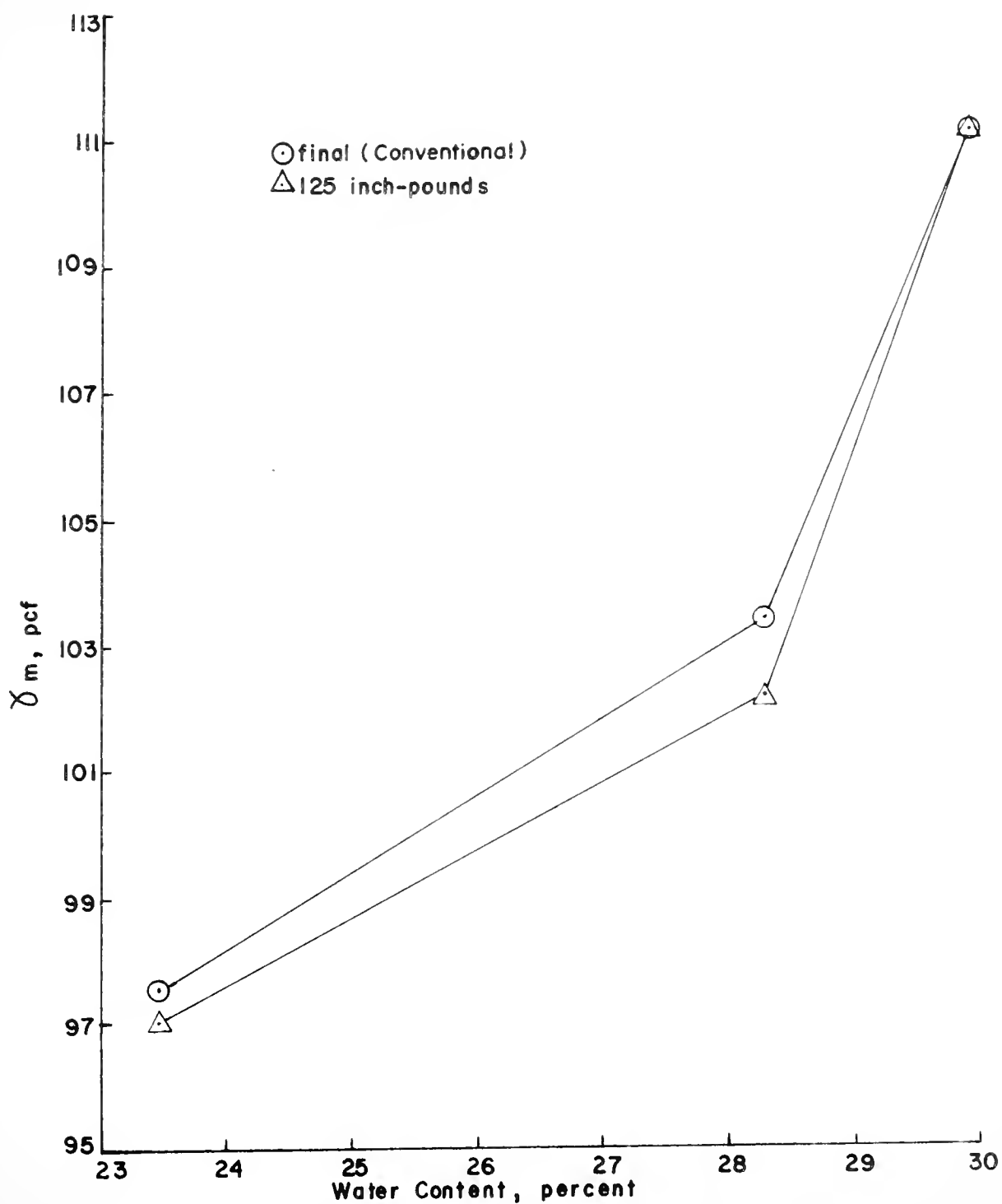


FIGURE 51. CONVENTIONAL AND EQUAL NET INPUT ENERGY
MOISTURE-TOTAL UNIT WEIGHT RELATIONS
(P6-R8; 1000 LB LEVEL)

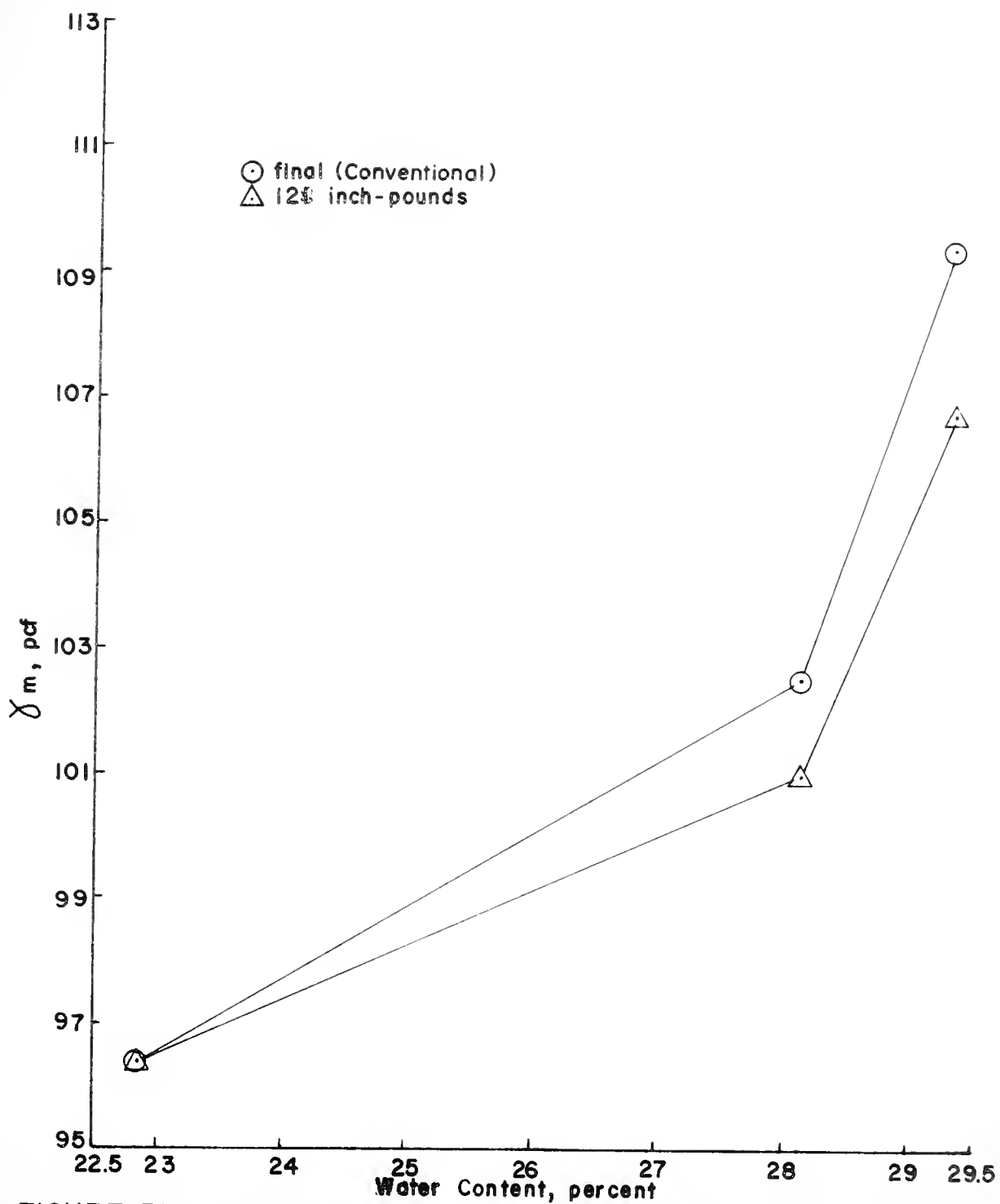


FIGURE 52. CONVENTIONAL AND EQUAL NET INPUT ENERGY
MOISTURE-TOTAL UNIT WEIGHT RELATIONS
(P8-R10; 1000 LB LEVEL)

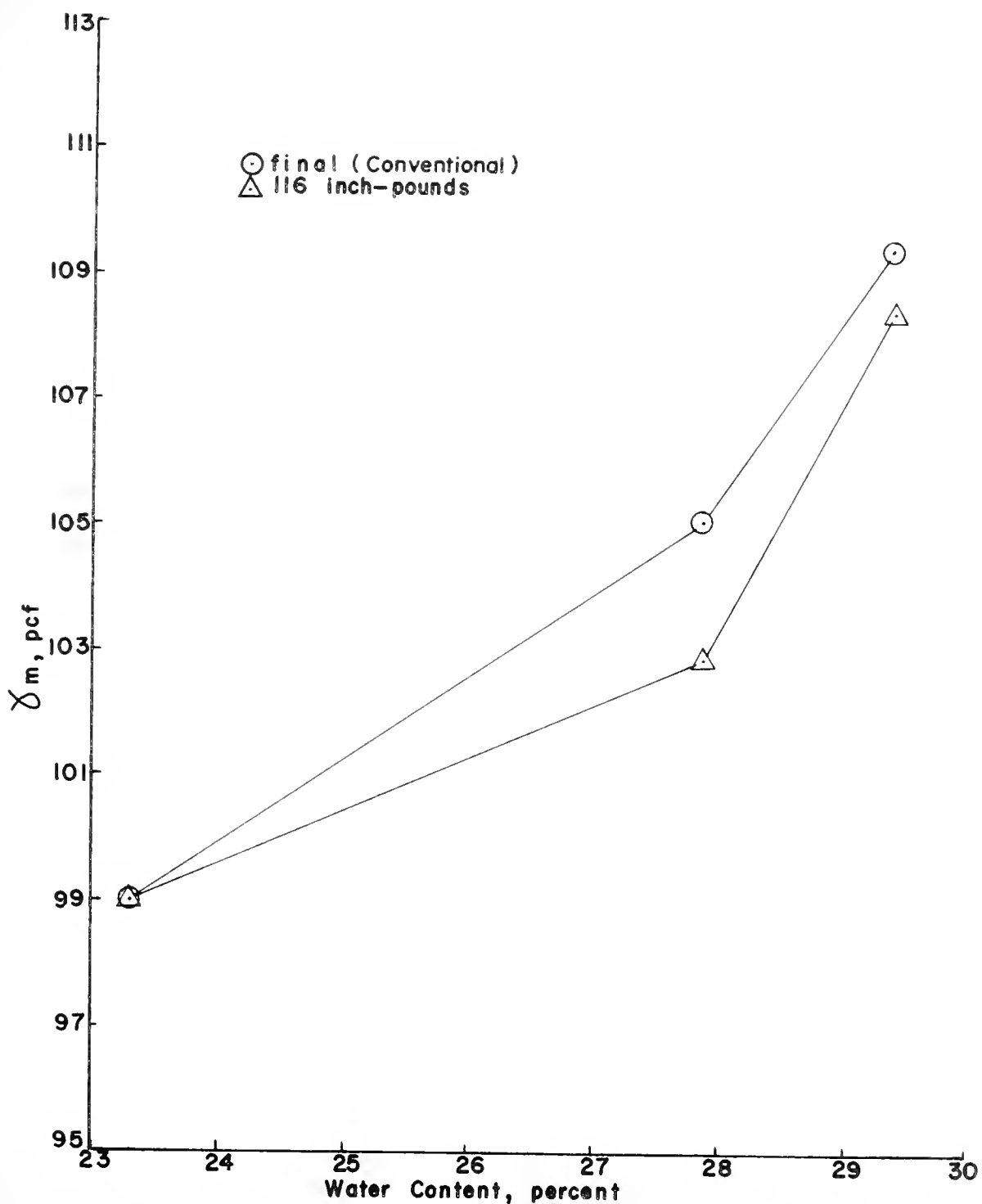


FIGURE 53. CONVENTIONAL AND EQUAL NET INPUT ENERGY
MOISTURE-TOTAL UNIT WEIGHT RELATIONS
(PIO-R12; 1000 LB LEVEL)

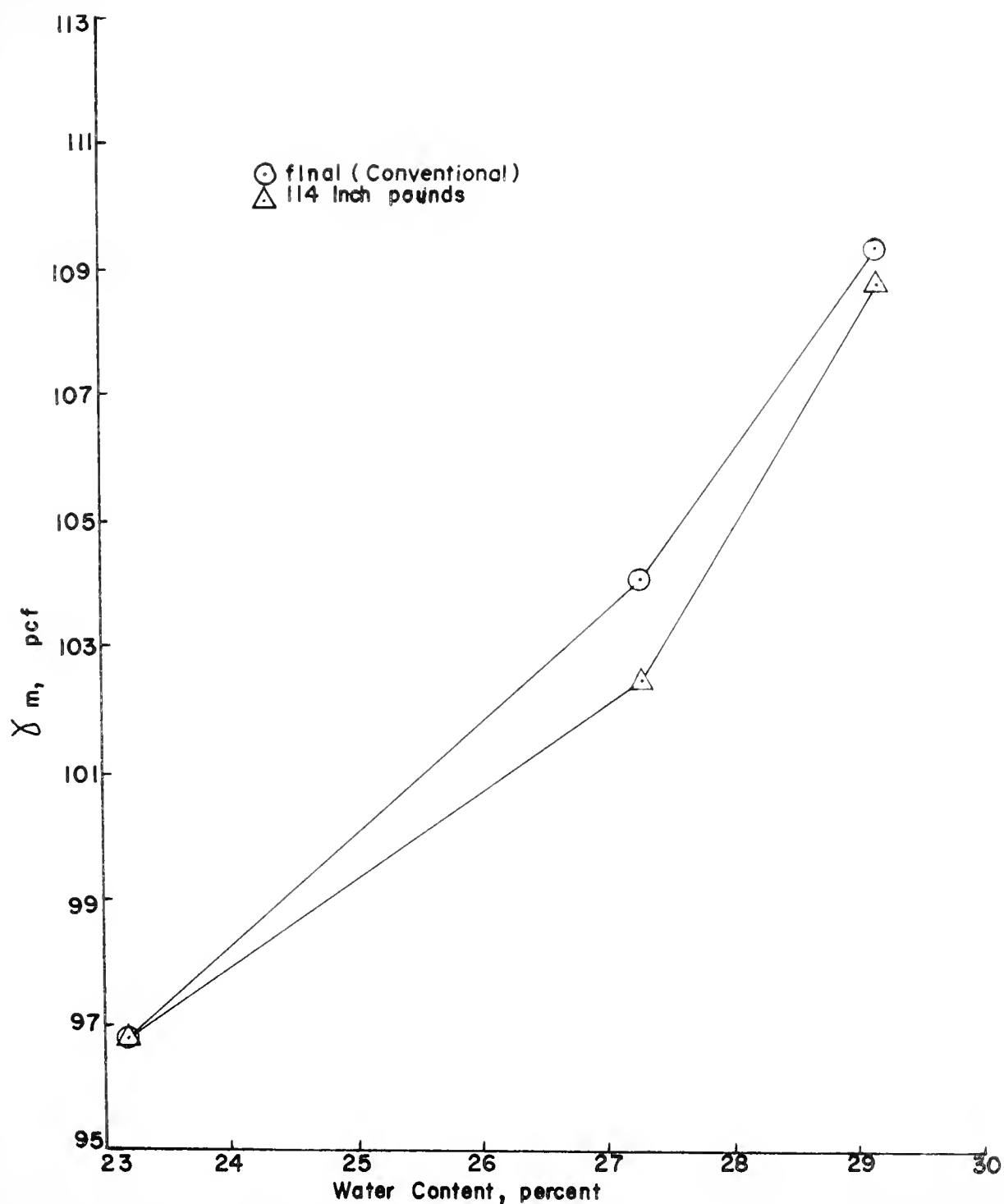


FIGURE 54. CONVENTIONAL AND EQUAL NET INPUT ENERGY
MOISTURE-TOTAL UNIT WEIGHT RELATIONS
(PI2-R20; 1000 LB LEVEL)

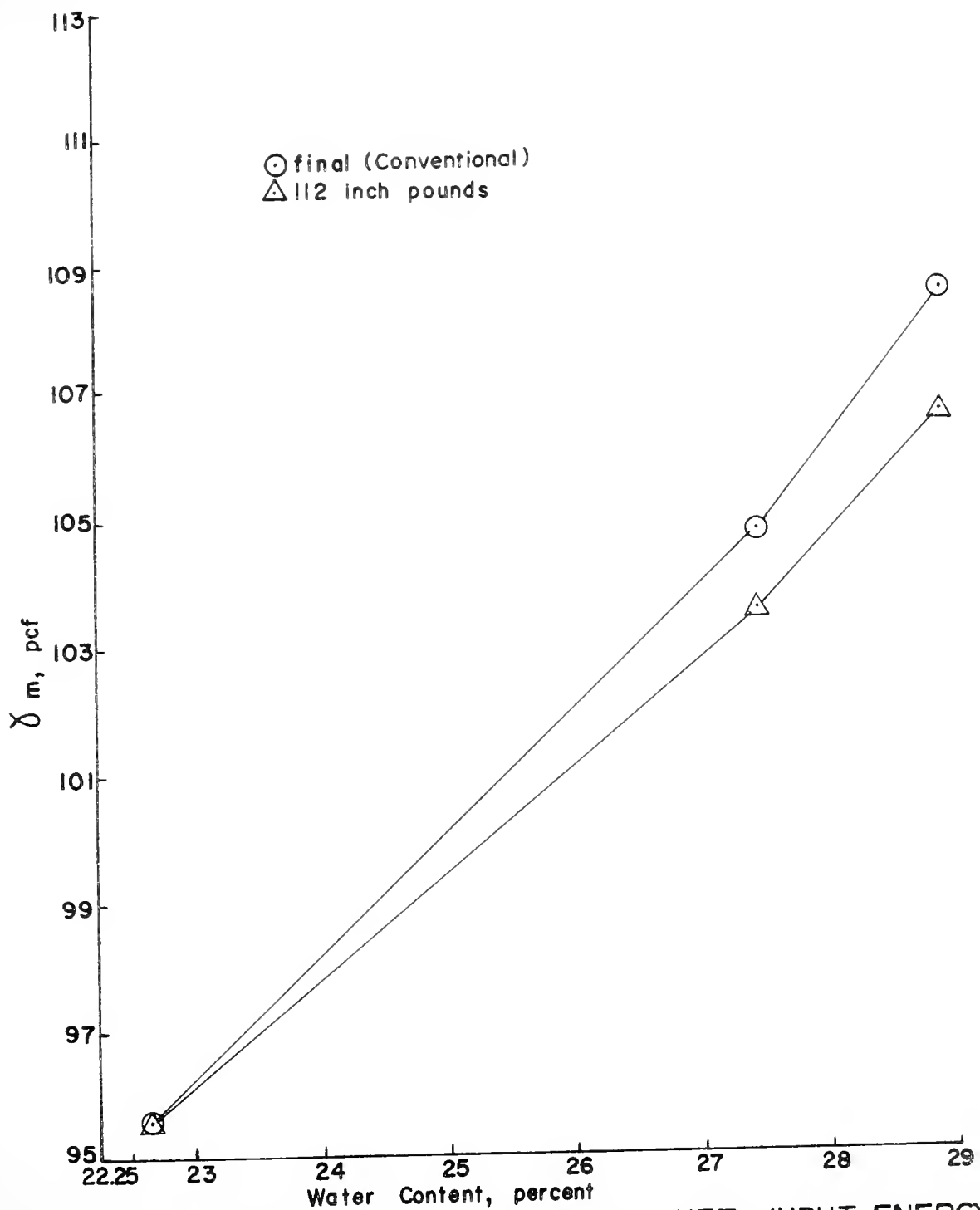


FIGURE 55. CONVENTIONAL AND EQUAL NET INPUT ENERGY
MOISTURE-TOTAL UNIT WEIGHT RELATIONS
(P20-R40; 1000 LB LEVEL)

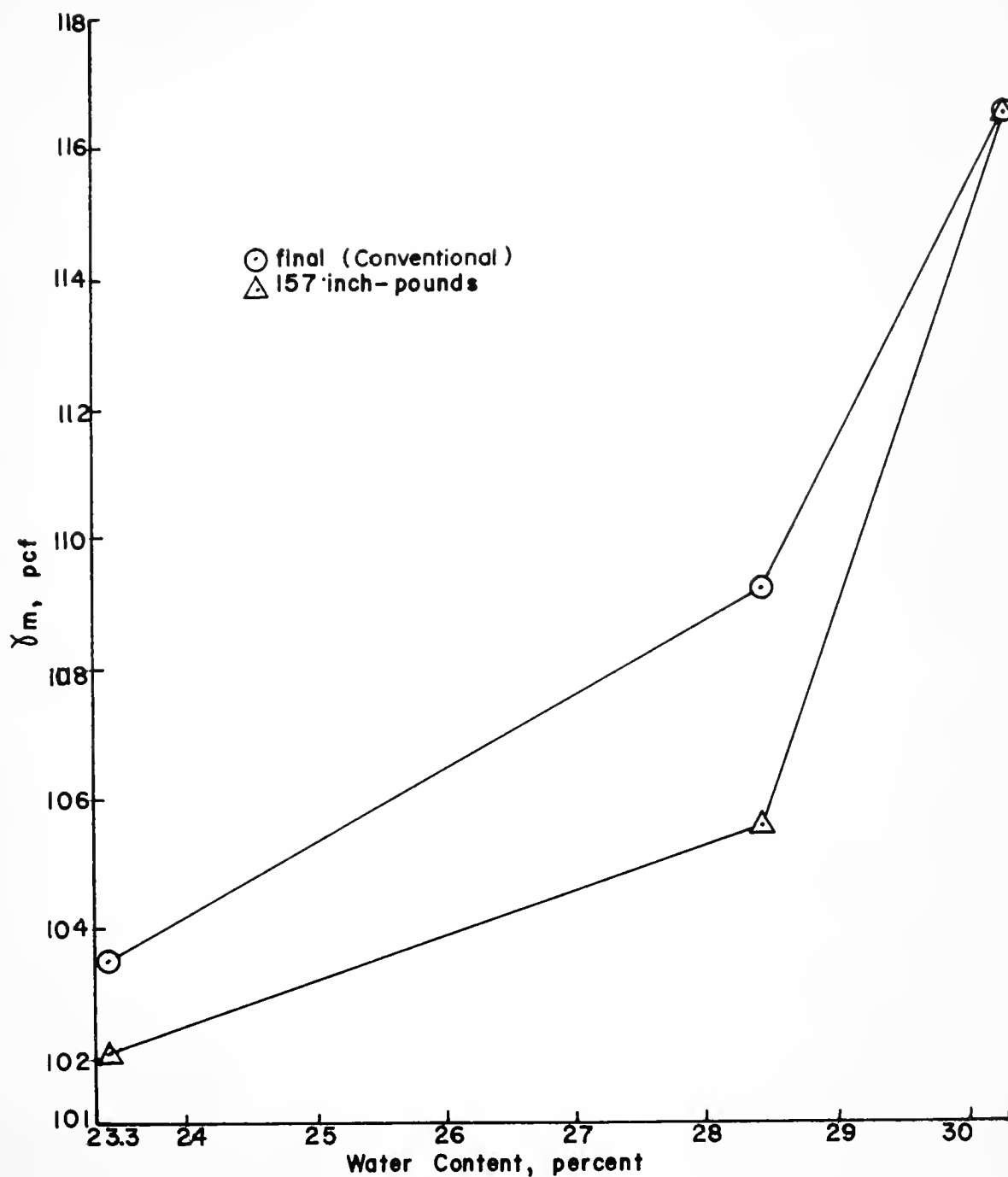


FIGURE 56 CONVENTIONAL AND EQUAL NET INPUT ENERGY
MOISTURE-TOTAL UNIT WEIGHT RELATIONS
(P6-R8; 1500 LB LEVEL)

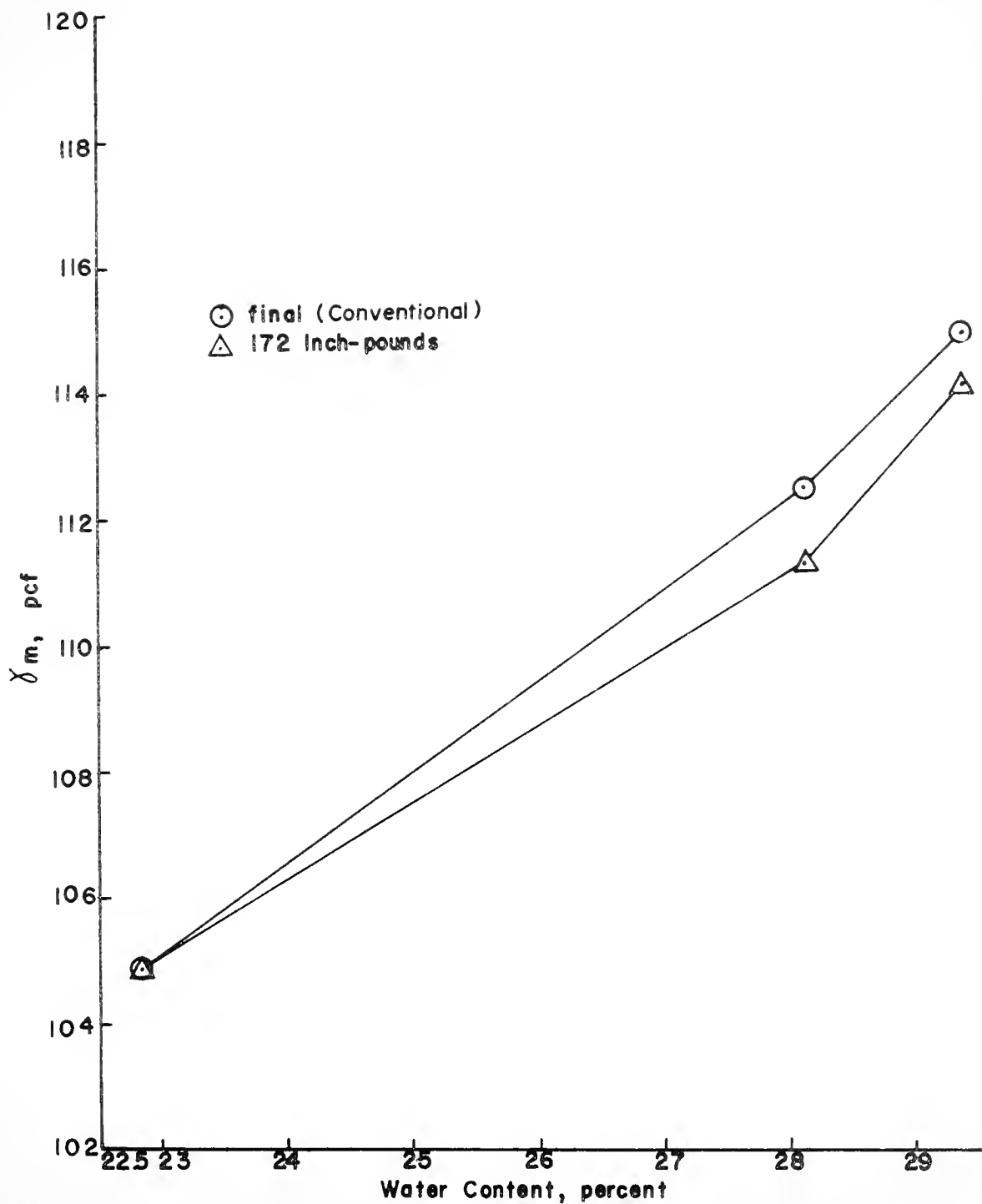


FIGURE 57. CONVENTIONAL AND EQUAL NET INPUT ENERGY
MOISTURE-TOTAL UNIT WEIGHT RELATIONS
(P8-R10; 1500 LB LEVEL)

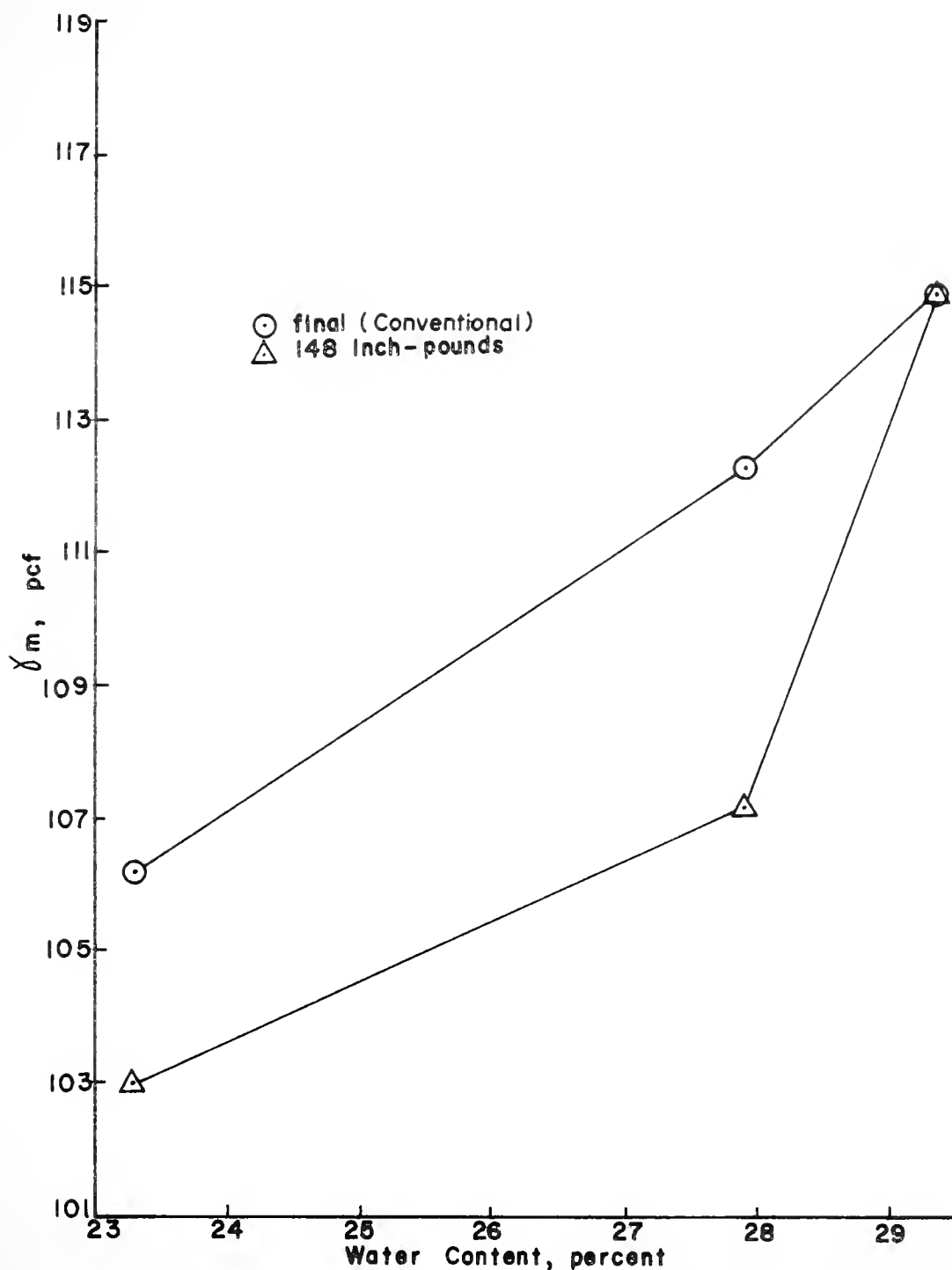


FIGURE 58. CONVENTIONAL AND EQUAL NET INPUT ENERGY
MOISTURE-TOTAL UNIT WEIGHT RELATIONS
(PIO-R12; 1500 LB LEVEL)

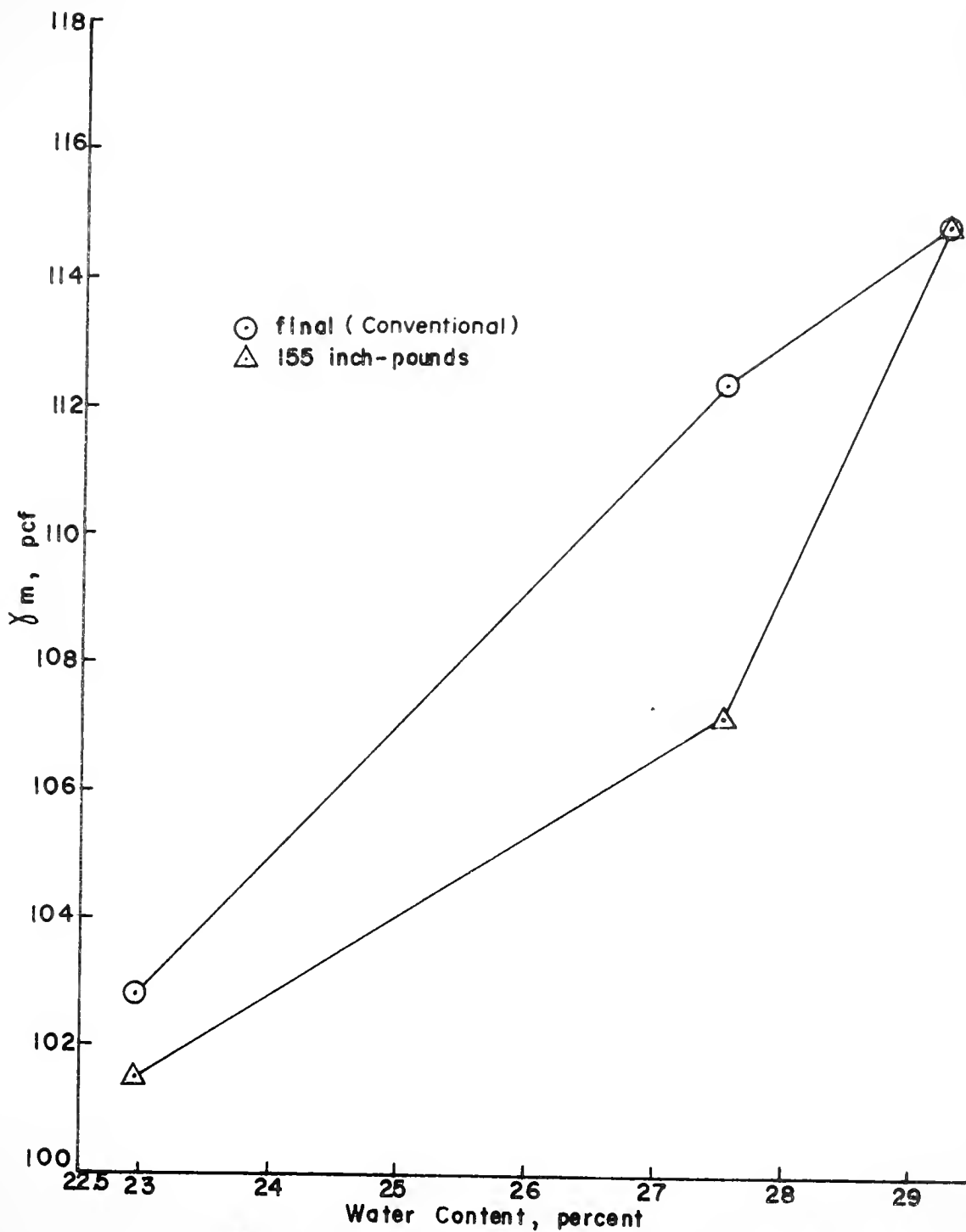


FIGURE 59. CONVENTIONAL AND EQUAL NET INPUT ENERGY
MOISTURE-TOTAL UNIT WEIGHT RELATIONS
(PI2-R20; 1500 LB LEVEL)

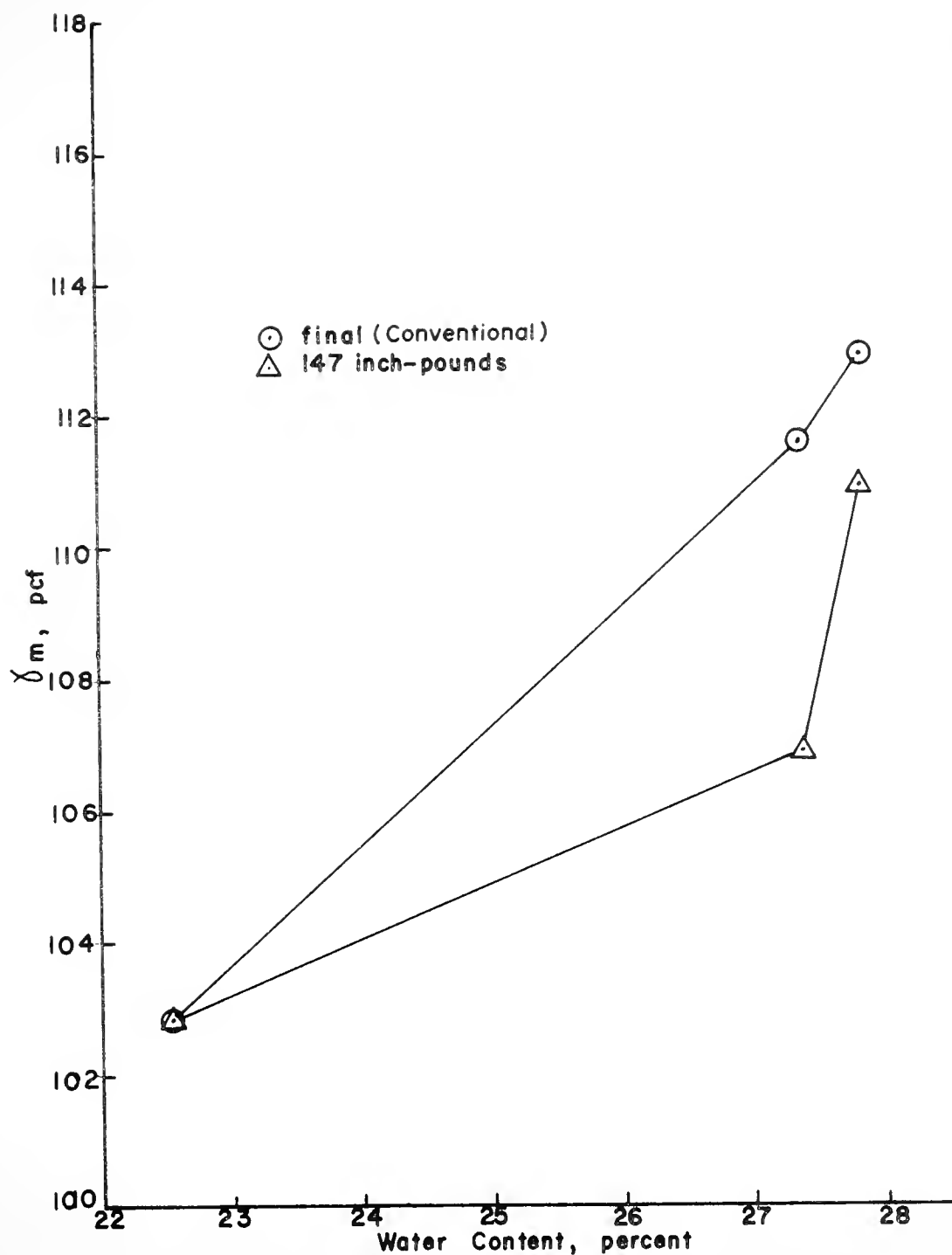


FIGURE 60. CONVENTIONAL AND EQUAL NET INPUT ENERGY
MOISTURE-TOTAL UNIT WEIGHT RELATIONS
(P20-R40; 1500 LB LEVEL)

with respect to W_s . By dividing all expressed energies by the same constant, the dimensions would be inch-pounds per gram of solids.

These figures show the conventional or end-result moisture content-unit weight relations as well as those at equal net input energy levels. For each figure the energy level chosen was the maximum energy for the specimen which accepted the least energy. Therefore these figures cannot be directly compared. However the effect of moisture content can be seen as the slopes of the lines. It is evident that two different moisture-unit weight relationships exist.

It is interesting to note that for the P4-R6 size soil shown in Figure 50 a rather odd relationship exists for both curves. That is, the driest soil, K-1, exhibits the highest compacted unit weight. This can be explained by the fact that the K-1, P4-R6 material as prepared consisted of smaller aggregates weakly held together as larger aggregates of the P4-R6 size. This was not as visually apparent at the K-2 and K-3 water content levels. The K-1 skeleton was quite weak and suffered degradation as the aggregates prematurely broke down to a smaller and more stable size.

The ease with which the soil can be densified can also be shown by measuring the net energy required to achieve a particular unit weight at various moisture contents. This is shown in Table 11. It is clearly

Table 11. Energy Required to Achieve a Given Unit Weight.

<u>Description</u> <u>1000 lb. Level</u>	Energy required, inch - lb.	
	<u>$\gamma_m = 95.0$ pcf</u>	<u>$\gamma_d = 77.5$ pcf</u>
K-1, P4-R6	74	78
P6-R8	112	115
P8-R10	117	116
P10-R12	93	97
P12-R20	103	105
P20-R40	108	107
K-2, P4-R6	89	109
P6-R8	89	109
P8-R10	91	111
P10-R12	79	97
P12-R20	77	94
P20-R40	72	89
K-3, P4-R6	65	83
P6-R8	61	79
P8-R10	72	91
P10-R12	62	80
P12-R20	59	77
P20-R40	63	81
1500 lb. level	$\gamma_m = 102.5$ pcf	$\gamma_d = 82.5$ pcf
K-1, P6-R8	161	155
P8-R10	154	146
P10-R12	143	138
P12-R20	163	157
P20-R40	145	(extrapolated) 131
K-2, P6-R8	138	159
P8-R10	119	137
P10-R12	120	138
P12-R20	125	143
P20-R40	122	138
K-3, P6-R8	89	122
P8-R10	109	129
P10-R12	84	102
P12-R20	89	109
P20-R40	100	116

evident that, holding the aggregate size constant, the energy required decreases as the moisture content increases.

The ease of densification can also be thought of as the slope of the curve defined for the moisture content-unit weight relationship. Using a secant slope, Table 12 defines these slopes for the previously shown relationships. As used in the figures \odot refers to the conventional $\gamma_m - w$ relationships and Δ refers to the $\gamma_m - w$ relationships defined for equal net input energies. Disregarding the P4-R6 slopes, the Δ slopes in the narrow moisture content range (K-2 to K-3) at the 1,000 lb. level of compaction exhibit a decreasing slope as the aggregate size decreases, i.e., the soil becomes "stiffer" with decreasing aggregate size. This same trend is not evident at the 1,500 lb. compaction level, probably because destruction of the aggregates, regardless of their size, has been more complete at this higher level. Over a larger moisture content range (K-1 to K-2), neither level of compaction shows a consistent relationship. This may be due to the fact that the moisture content range is too wide to provide a systematic guide to the achievement of densification. It should be noted that because of the extra variable, net energy input, the increasing stiffness as the aggregate size decreases is not apparent from the slopes defined by the conventional $\gamma_m - w$ relationship.

Table 12. Slopes of the γ_m - w Relationships.

Compaction Level	Size	Increase in unit weight, pcf per % increase in moisture			
		K-1 to K-2		K-2 to K-3	
		⊙	△	⊙	△
1,000 lb	P4-R6	-1.03	-1.15	3.88	4.74
	P6-R8	1.23	1.08	4.56	5.26
	P8-R10	1.19	0.91	5.52	4.56
	P10-R12	1.34	0.86	2.99	3.50
	P12-R20	1.76	1.37	2.81	3.33
	P20-R40	1.82	1.58	2.60	2.12
1,500 lb	P6-R8	1.12	0.69	3.98	5.91
	P8-R10	1.44	1.21	2.00	2.32
	P10-R12	1.34	0.93	1.71	5.06
	P12-R20	1.81	1.28	2.25	4.44
	P20-R40	1.81	0.84	2.82	8.70

Lambe's theory of compaction (27) does not explicitly explain the interactions which must be occurring during the achievement of compacted unit weight, i.e., from the loose (high void ratio) clay soil mass to the dense (low void ratio) compacted mass. Its essential starting point is a compacted condition on the dry side of the optimum moisture content on a moisture-density curve for low (typically Standard AASHTO) compactive effort.

Olson's explanation of compaction (38) is given in terms of normal stresses, pore fluid pressures, and the changes that occur in them with the application of the compactor foot. His ideas were developed for laboratory compaction where the foot covers only a portion of the end area of the mold. His explanation is logical but as previously stated he does not explicitly identify the soil model to which he is applying the stress system. In his closure (40) to his previous paper (38) he points out to the discussers that to improve his theory

"...it would be necessary to obtain measurements of both the pore air and pore water pressures within the soil mass at many locations since the state of stress beneath a compaction foot is complex. ...then it would be necessary to develop a generalized stress-strain theory for unsaturated soils plus a bearing capacity theory that would allow complete calculation of the state of stress beneath a dynamically loaded footing for all stresses to those that produce failure."

This writer feels that his explanation best describes the movements necessary within the soil volume being compacted to achieve a denser mass, and that Olson's explanation, suitably modified, can describe the intra-aggregate strength changes which occur during deformation of the aggregates.

The various curves relating the unit weight achieved (γ_m) to the net energy absorbed (E) are mathematically uncomplicated, and by using existing Purdue software, regression analyses supplied quadratic equations which adequately fit the experimental results. A few examples are shown below and the complete set of equations describing the total unit weight vs. net input energy relationships at the 1,500 lb. compaction level are given in Appendix G.

For K-1, P6-R8 at 1,500 lb.

$$\gamma_m = 64.687 + 0.41086 E - 0.00112 E^2, \text{ pcf}$$

For K-3, P12-R20 at 1,500 lb.

$$\gamma_m = 66.18 + 0.58045 E - 0.00178 E^2, \text{ pcf}$$

Grouping the linear terms of the quadratic equations at constant moisture contents shows a definite correlation; as the aggregate size decreases, the coefficient of the linear term increases. Grouping the linear terms of the quadratic equations by aggregate size also shows a definite correlation; in general, as the moisture content

increases, the coefficient of the linear term also increases. These groupings are shown in Table 13.

The adaptation of these techniques to the conventional laboratory impact control test and finally to the generation of field equipment moisture content-unit weight relations will be experimentally difficult. However, the rewards in terms of a better understanding of the mechanism of densification and the ability to predict and intelligently choose field equipment and compaction moisture content on the basis of economics are quite attractive.

End Results of Compaction and Saturation

The results of Table 8 showing that γ_d , γ_m , and S_r increase as the moisture content increases for the "At Maximum Load" case are not surprising. They are exactly what would be predicted from a knowledge of the end results of the usual impact compaction tests on various soils when compacted dry of their optimum moisture contents.

However the results "After 2 Minutes of Maximum Load", using the change in the dry unit weight as a descriptor, are less commonly known and tend to verify in part the compaction mechanism postulated in this paper. As indicated in Table 14 the increase in dry unit weight, expressed as a percentage, achieved during the two minute period of constant load is a function of the aggregate moisture content. To aid in the interpretation, the

Table 13. Correlation by Quadratic Equation.

<u>Identification</u>	<u>Constant</u>	<u>Linear Term of Equation</u>
KL-8, K-1, P6-R8	water content	0.41086 E
KLS-18, K-1, P10-R12		0.44353 E
KL-37, K-2, P6-R8	water content	0.42488 E
KLS-42, K-2, P8-R10		0.46312 E
KLS-14, K-1, P8-R10	water content	0.41566 E
KL-22, K-1, P12-R20		0.42652 E
KL-28, K-1, P20-R40		0.51943 E
KLS-73, K-3, P8-R10	water content	0.49482 E
KL-76, K-3, P10-R12		0.64268 E
KL-82, K-3, P12-R20		0.58045 E
KL-8, K-1, P6-R8	size	0.41086 E
KL-37, K-2, P6-R8		0.42488 E
KL-67, K-3, P6-R8		0.62912 E
KLS-14, K-1, P8-R10	size	0.41566 E
KLS-42, K-2, P8-R10		0.46312 E
KLS-73, K-3, P8-R10		0.49482 E
KLS-18, K-1, P10-R12	size	0.44353 E
KLS-46, K-2, P10-R12		0.45281 E
KL-76, K-3, P10-R12		0.64268 E
KL-22, K-1, P12-R20	size	0.42652 E
KL-51, K-2, P12-R20		0.42501 E
KL-82, K-3, P12-R20		0.58045 E
KL-28, K-1, P20-R40	size	0.51943 E
KL-56, K-2, P20-R40		0.46175 E
KL-88, K-3, P20-R40		0.51736 E

Table 14. Increase in Dry Unit Weight at Constant Load.

Compactive Load	Identification		Average Increase in γ_d , %		S_r After
			Ave.		2 Min., %
1,000 lb.	P4-R6	K-1	3.4	3.87	78.5
		K-2	3.5		81.6
		K-3	4.7		95.2
	P6-R8	K-1	3.6	4.17	60.8
		K-2	4.3		80.7
		K-3	4.6		95.3
	P8-R10	K-1	3.6	4.33	59.3
		K-2	4.4		79.9
		K-3	5.0		92.5
	P10-R12	K-1	3.9	4.27	62.2
		K-2	4.7		81.9
		K-3	4.2		92.6
	P12-R20	K-1	3.3	4.23	61.3
		K-2	4.5		79.1
		K-3	4.9		91.3
	P20-R40	K-1	4.1	4.30	64.4
		K-2	4.4		79.7
		K-3	4.4		89.3
1,500 lb.	P4-R6	K-2	4.7	4.00	94.4
		K-3	3.3		99.0
	P6-R8	K-1	3.7	3.70	70.7
		K-2	4.3		91.2
		K-3	3.1		99.8
	P8-R10	K-1	3.4	3.47	70.9
		K-2	4.0		94.0
		K-3	3.0		98.7
	P10-R12	K-1	3.4	3.37	73.7
		K-2	3.9		93.1
		K-3	2.8		98.5
	P12-R20	K-1	3.4	3.40	69.7
		K-2	4.2		91.0
		K-3	2.6		97.9
	P20-R40	K-1	3.3	3.63	68.4
		K-2	4.0		91.9
		K-3	3.6		94.2

average degrees of saturation at the end of the two minute loading period are also tabulated.

Table 14 shows at the 1,000 lb. compaction level that as the moisture content increases (K-1 to K-3), the increase in dry unit weight as a percentage also increases. This can be explained by the fact that for any aggregate size as the moisture content increases, the stiffness and the strength of the aggregate decrease. (These aggregate characteristics are discussed later under the heading Aggregate Deformation.) Under the compactive load the wetter, i.e., weaker, aggregates will be plastically deformed to fit the available voids more readily than will the drier and stronger aggregates.

For the 1,500 lb. level of compaction, Table 14 shows that the intermediate or K-2 moisture content gives the largest percentage gain in dry unit weight. However this is not in conflict with this author's explanation. An examination of the K-3 degrees of saturation shows that the limiting case has essentially been reached and regardless of the aggregate characteristics no further densification can occur without expulsion of pore water.

The averages of the average increase in γ_d shown in Table 14 demonstrate that the densification at constant load is related to aggregate size. As the aggregate size decreases, the percent change in dry unit weight increases. This trend is more evident at the 1,000 lb. level of

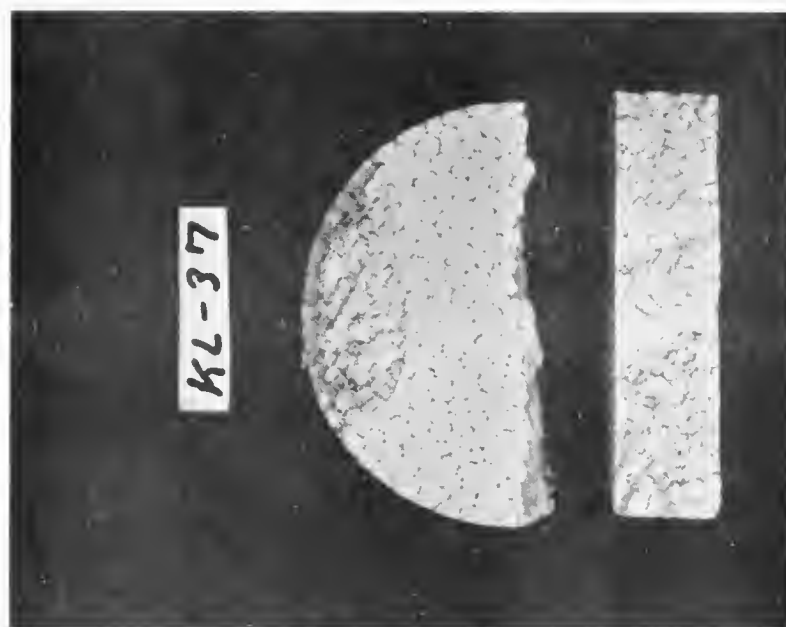
compaction than at the 1,500 lb. level, due to the fact that at the 1,500 lb. level the individual aggregates, regardless of their size, lose their identity during compaction. This can be observed qualitatively in Figures 61 and 62. Figure 61 shows samples made up of K-2, P6-R8 aggregates compacted at (a) the 1,000 lb. level and (b) the 1,500 lb. level. Figure 62 shows K-1, P12-R20 aggregates also compacted at the (a) 1,000 lb. level and (b) 1,500 lb. level. In both figures it can be seen that the aggregate structure is less apparent at the 1,500 lb. compaction level.

The rebound or decrease in the dry unit weight upon release of the compactive load also depends on the aggregate's moisture content and size. The rebound results are shown in Table 15 as the decrease in γ_d as a percentage of γ_d just before the load was released. These percentages are also presented as average values for each aggregate size and compactive load (1,000 or 1,500 lb.).

As explained previously, the sample height immediately after removal of the compactive load is experimentally difficult to measure and is therefore less accurately measured than would be desired. The author feels that this explains the lack of an obvious relationship between the percent decrease in γ_d and moisture content for the various aggregate sizes.



a) Compacted at 1000 lb. level



b) Compacted at 1500 lb. level

FIGURE 61. SAMPLES COMPACTED OF K-2, P6-R8 AGGREGATES



a) Compacted at 1000 lb. level



b) Compacted at 1500 lb. level

FIGURE 62. SAMPLES COMPACTED OF K-1, PI2-R20 AGGREGATES

Table 15. Decrease in Dry Unit Weight Upon Release of Load.

Compactive Load	Identification		Average Decrease in γ_d , %	
			Average	
1,000 lb.	P4-R6	K-1	1.66	1.35
		K-2	1.17	
		K-3	1.23	
	P6-R8	K-1	1.14	1.39
		K-2	1.61	
		K-3	1.42	
	P8-R10	K-1	1.30	1.60
		K-2	1.59	
		K-3	1.91	
	P10-R12	K-1	1.40	1.46
		K-2	1.63	
		K-3	1.35	
	P12-R20	K-1	1.38	1.48
		K-2	1.58	
		K-3	1.47	
	P20-R40	K-1	2.53	2.20
		K-2	1.67	
		K-3	2.39	
1,500 lb.	P4-R6	K-2	1.20	1.15
		K-3	1.10	
	P6-R8	K-1	1.00	1.59
		K-2	2.23	
		K-3	1.53	
	P8-R10	K-1	2.04	1.98
		K-2	0.88	
		K-3	3.01	
	P10-R12	K-1	6.40	3.34
		K-2	1.92	
		K-3	1.69	
	P12-R20	K-1	1.57	1.89
		K-2	1.49	
		K-3	2.62	
	P20-R40	K-1	1.65	2.07
		K-2	2.70	
		K-3	1.87	

However the average percentage decrease in γ_d for the three moisture contents at each aggregate size also shown in Table 15 does indicate that this decrease is related to the aggregate size present, and that as the aggregate size decreases the percent rebound increases. This result also can be explained in terms of the aggregate compaction model.

It has been shown by Marsal (35) that for a given load as the particle sizes in a soil fill sustaining a load decrease, the contact stresses between the particles also decrease. He has used this evidence to explain the unexpected settlements exhibited by some high rockfill structures. The rocks are large enough so that the contact stresses exceed the strength of the rock. This results in fracturing, degradation, and a decrease in the void ratio of the rockfill. He also showed that as long as their various geometric ratios were similar, particles of different average sizes would have the same number of contacts per particle.

At the same compactive load, aggregates of different sizes do not experience the same inter-aggregate contact stresses. These contact stresses increase as the average aggregate size increases, that is, as the total number of contacts available to sustain the force decreases. The more permanent degradation (fracturing and/or plastic flow) that occurs, the less stored energy is available for

release upon removal of the compactive load. This energy release is exhibited as a decrease in the dry unit weight.

An inspection of the "After Swell Pressure Test" results shown in Table 8 shows that within the limits of experimental accuracy the samples imbibed enough water during the period of swelling pressure measurements that they were essentially saturated ($S_r \approx 100\%$). This tends to confirm the hypothesis that double layer expansion contributes to the measured swelling pressure. Prior to compaction $S_{r_{agg}} < 100\%$ and after compaction $S_r < 100\%$ also. But after the swelling pressure tests were completed, $S_r \approx 100\%$. So it appears that not only are the inter-aggregate voids filled, but the intra-aggregate voids also fill with water.

Swelling Pressure Tests

The swelling pressure tests show two characteristics which to the writer's knowledge have not previously been reported in the literature. The first pattern is that the swelling pressure for most samples tested increased and then decreased as a function of the elapsed time after initial access to water. The second characteristic, which is most apparent in Figure 39, is the temporary decrease of the swelling pressure after an elapsed time of about one minute.

Both the short-term (temporary) and the long-term decrease of the swelling pressure can be explained with the aid of the compacted soil model used in this study. The first-order system, the aggregate, is partly saturated, and the porewater pressure is negative due to the deficiency of water available to fulfill double-layer requirements. The stress-strain character can be described as linear-elastic with a high modulus of elasticity and a low yield point at a low moisture content. At a high moisture content it would be better characterized as elasto-plastic.

The second-order system is the totality of the many aggregates within the compaction mold. The aggregates are somewhat deformed and in intimate contact with each other so that double layer water may be continuous between aggregates. Inter-granular or inter-aggregate compressive stresses, aggregate-mold base compressive stresses, and normal and shear aggregate-mold wall stresses exist. An equilibrium exists at some particular interaggregate void ratio due in the gross sense to interlocking among the aggregates, but actually due to the negative pore water pressure which gives each aggregate strength and integrity.

The addition of bulk water to this system causes a decrease in strength at the aggregate-aggregate contacts as the menisci are destroyed. This is manifested by

adjustments of the second-order system into a denser packing as well as a decrease in the equilibrium base pressure.

The addition of bulk water also causes the individual aggregates to swell as the double-layers expand. This has the effect of increasing the measured swelling pressure (the force exerted on the chamber's base by the soil) as long as the aggregate-aggregate skeleton remains rigid. However since strength is a function of moisture content, the strength of each aggregate will decrease as its moisture content increases. This will cause the aggregates to deform and flow plastically into the void spaces of the second order system. In this manner the volume of the summation of first order systems can increase even though the total volume available within the mold is not changed. As long as the aggregates are allowed to change in the fashion described, a decrease in the swelling pressure generated can be expected.

A schematic representation of the aggregate skeleton as it may change during the swelling pressure test is shown in Figure 63. Although the gross volume within the mold was constant during a test, the skeletons shown in Figure 63 are of different height as denoted by the upper and lower horizontal lines. An increase in the skeleton height is analogous to a higher vertical pressure, and similarly a decrease in the aggregate-skeleton height indicates a smaller vertical pressure. Figure 63 (a) shows the skeleton at equilibrium with the boundary normal stresses before being given access to water. In (b) upon being given access to water the

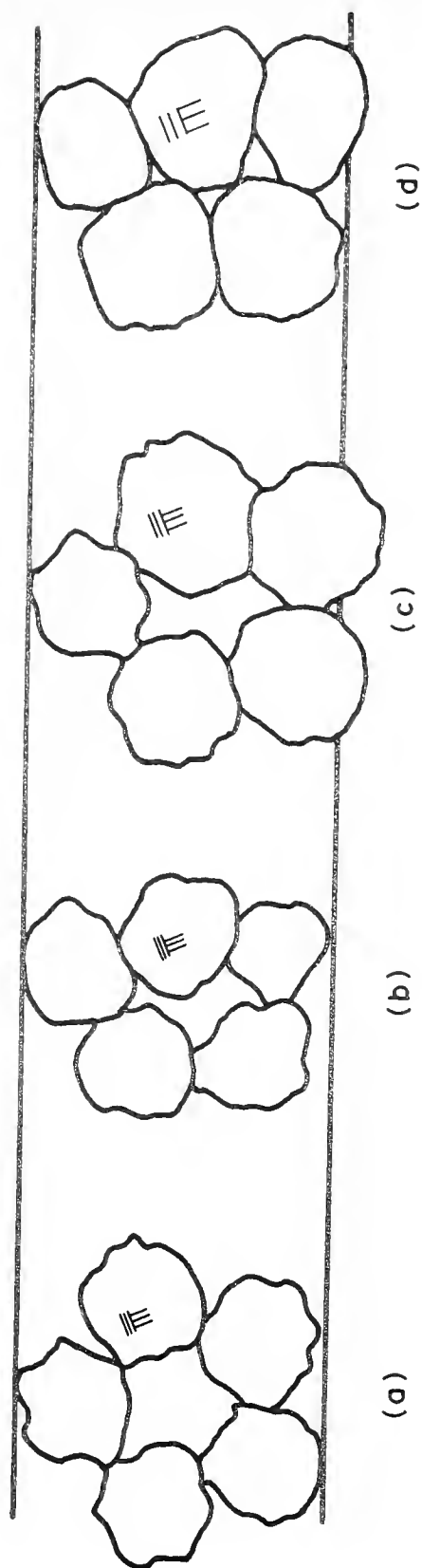


FIGURE 63. IDEALIZED REPRESENTATION OF THE EFFECTS OF SWELLING ON THE AGGREGATE SKELETON

aggregate skeleton collapses to a lower inter-aggregate void ratio due to local softening at aggregate-aggregate contacts. This action is similar to increasing the gross volume and results in a decrease of the vertical pressure. As shown in (c), the availability of water causes the aggregates to swell. If the skeleton can resist these increasing pressures an increase in the vertical pressure will result. Further swelling beyond the condition shown in (c) can result in a further decrease of the inter-aggregate void ratio due to the aggregates swelling and further rearrangement of the skeleton. This may result in no change in the vertical stress or a decrease as indicated in (d). The outcome in (d) depends on the volume change due to the skeletal rearrangement as well as the repulsive force vs. plate spacing relationship for the particular clay involved.

It can be seen that the effects of water on this system are not additive. Structural collapse and plastic deformation of the aggregates have the same effect as increasing the gross volume, i.e., they decrease the measured swelling pressure, and expansion of the aggregates as the double layers swell leads to an increase in the measured swelling pressure. Since all three phenomena are occurring simultaneously the resulting swelling pressure merely reflects the dominant mechanism occurring during some time increment.

Let us apply this reasoning to the schematic results of a typical swelling pressure test shown in Figure 64. From the beginning of the test to Point A, structural collapse

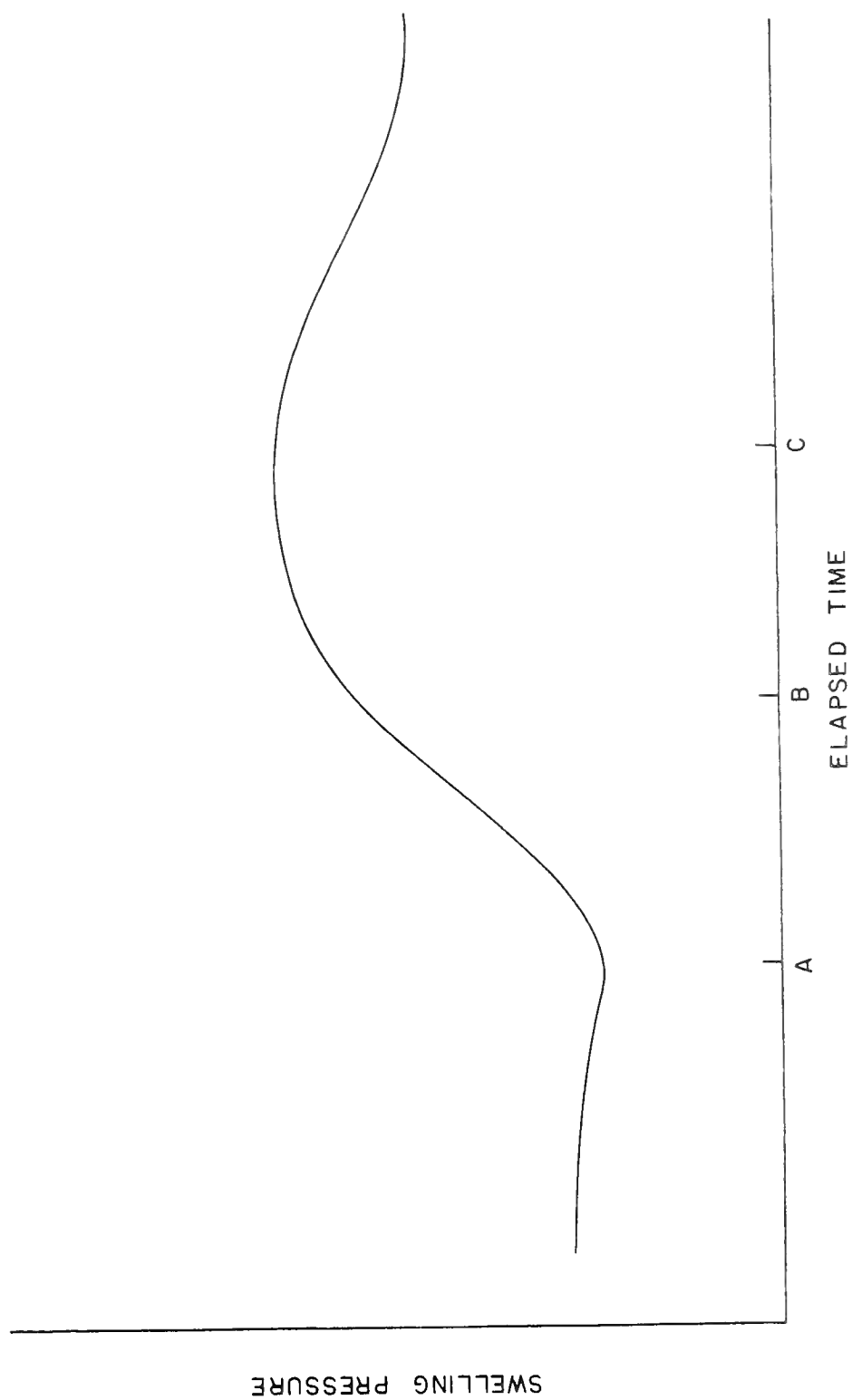


FIGURE 64. IDEALIZED RESULTS OF A SWELLING PRESSURE TEST

predominates; from Point A to Point B the skeleton is strong enough so that increasing stresses due to double layer swelling can be transferred to the lower boundary; from Point B to Point C a transition is occurring where the swelling is into inter-aggregate voids at constant skeletal stress (required strength = available strength); and from Point C to the equilibrium condition the aggregates have weakened enough so that gross deformations occur (required strength > available strength) and the net result is a progressive collapse of the skeleton and a concomitant decrease in the measured swelling pressure.

An examination of Table 16 indicates that at the 1,000 lb. compaction level for each aggregate size the maximum swelling pressure generated increased as the compaction moisture content increased, without exception. However, at the 1,500 lb. level of compaction the unit weight also increased as the water content increased (only Test KLS-73 is an exception to this), but in all cases the swelling pressure generated by the sample with the highest moisture content (K-3) was less than that generated by the intermediate water content sample (K-2).

The final swelling pressures tabulated in Table 16 exhibit these same trends. Namely, at the 1,000 lb. level of compaction the final swelling pressure increases with increasing compaction moisture content, and at the 1,500 lb. level of compaction the intermediate moisture content yields the largest swelling pressure. It should be noted that these

Table 16. Tabulated Results of Swelling Pressure Tests.

Identification	Unit Weight		Initial Side Friction, lb.	Swelling Pressure, lb.	
	γ_m	to Test, pcf		Maximum	Final
		γ_d			
KLS-32 (K-2,P4-R6)	108.7	84.8	14	189@15 min.	160
KLS-61 (K-3,P4-R6)	115.1	88.6	41	208@50 min.	183
KLS-6 (K-1,P6-R8)	--	--	30	141@15 min.	98
KLS-11 (K-1,P6-R8)	99.2	80.7	27	142@15 min.	89
KLS-36 (K-2,P6-R8)	109.0	85.1	27	196@15 min.	172
KLS-66 (K-3,P6-R8)	114.7	88.4	43	205@60 min.	186
KLS-13 (K-1,P8-R10)	98.1	79.9	29	141@12 min.	85
KLS-41 (K-2,P8-R10)	107.8	84.2	27	190@15 min.	139
KLS-71 (K-3,P8-R10)	112.6	87.1	43	208@40 min.	187
KLS-16 (K-1,P10-R12)	100.5	81.5	34	145@12 min.	92
KLS-44 (K-2,P10-R12)	108.2	84.6	18	190@12 min.	151
KLS-75 (K-3,P10-R12)	114.5	88.4	17	239@30 min.	213
KLS-21 (K-1,P12-R20)	100.5	81.6	40	136@12 min.	83
KLS-49 (K-2,P12-R20)	107.0	84.1	16	198@12 min.	129
KLS-81 (K-3,P12-R20)	112.5	87.1	44	225@30 min.	204
KLS-27 (K-1,P20-R40)	97.2	79.4	36	131@10 min.	80
KLS-55 (K-2,P20-R40)	107.2	84.1	30	200@15 min.	149
KLS-87 (K-3,P20-R40)	--	--	51	218@30 min.	190

Table 16, continued

Identification	Unit Weight Prior to Test, pcf γ_m	γ_d	Initial Side Friction, lb.	Swelling Pressure, lb. Maximum	Final
KLS-33 (K-2,P4-R6) 1500	115.6	90.2	--	303@50 min.	300
KLS-63 (K-3,P4-R6) 1500	118.2	90.9	30	257@45 min.	240
KLS-9 (K-1,P6-R8) 1500	107.6	87.2	29	252@15 min.	204
KLS-39 (K-2,P6-R8) 1500	113.9	88.7	34	298@250 min.	295
KLS-69 (K-3,P6-R8) 1500	117.8	90.4	52	233@50 min.	213
KLS-14 (K-1,P8-R10) 1500	106.2	86.5	36	232@17 min.	176
KLS-42 (K-2,P8-R10) 1500	115.9	90.5	8	321@40 min.	324
KLS-73 (K-3,P8-R10) 1500	115.5	89.2	31	283@50 min.	254
KLS-18 (K-1,P10-R12) 1500	*		39	268@20 min.	236
KLS-46 (K-2,P10-R12) 1500	114.7	89.7	13	294@40 min.	258
KLS-78 (K-3,P10-R12) 1500	117.8	91.9	30	280@49 min.	246
KLS-24 (K-1,P12-R20) 1500	107.6	87.5	42	215@18 min.	177
KLS-52 (K-2,P12-R20) 1500	--	--	25	312@40 min.	288
KLS-84 (K-3,P12-R20) 1500	115.4	89.3	40	283@40 min.	245
KLS-30 (K-1,P20-R40) 1500	107.0	87.3	38	231@20 min.	196
KLS-58 (K-2,P20-R40) 1500	111.7	87.7	27	336@40 min.	311
KLS-90 (K-3,P20-R40) 1500	115.9	90.6	45	328@60 min.	288

*Irregular Test - "extra" effort.

final values are not universally claimed to be the equilibrium values. However in many cases they are, and in others they approach the equilibrium. For some samples the rate of change of pressure with respect to time was so small that the tests were terminated.

Both trends seem to contradict the published observations of Seed and Chan (55). According to Seed and Chan the swelling pressure decreases as the moisture content, and thus the compacted unit weight on the dry side of optimum, increase for a constant effort and type of laboratory compaction. This was observed by them for "approximately constant volume" tests. It is presumed that their results were achieved using the equipment described in a later paper co-authored by Mitchell (56). In this later paper the authors showed the effects of slight total volume changes on the resulting swelling pressure measured. They also indicated that a measurable volume increase did occur in their apparatus. As shown previously in Figure 10 they also reported volumetric swell as a function of elapsed time for a sandy clay.

Two explanations evolve to reconcile this contradiction. It is possible that the soil reported, a sandy clay, does not behave the same as the kaolinite used in this study or that the effects were masked or altered. The effects (one would expect a collapse or negative swell for Specimen No. 1 in Figure 10 at a small elapsed time) may have been masked by an inability to record data in the early minutes of the tests. The first data appear at an

elapsed time of ten minutes. It is more probable, however, that due to the wide gradation of the material, the mechanism previously stated is less visible. The volume change characteristic inherent to Seed and Chan's device undoubtedly influenced the peak swelling pressures generated. In fact, yielding of the containing vessel would affect the low moisture content specimens more than it would the wetter samples, according to this author's mechanism.

As stated earlier in this thesis, Seed and Chan (55) also reported that as the degree of orientation increases, the swelling tendency decreases in the presence of free water, and shrinkage increases as the water is removed from the sample. They based their statement on experimental results and on assumption. In their words: "The marked increase in swelling tendencies of dry side compacted samples (and presumably, therefore, of flocculated structures) is readily apparent."

It is not at all obvious why, based on microstructure alone, a flocculated specimen should swell more than a dispersed sample, both samples being prepared at the same dry unit weight. This author would explain their results on the basis of the second order macrostructure model described previously. Referring to their results shown in Figure 7, on the dry side ($w = 12.4\%$) the aggregates are strong enough to maintain their integrity so that

essentially the same packing occurs regardless of the type of compaction. Therefore the shrink-swell behavior of the compacted samples should be, and is, independent of compactive type. For the pair of samples compacted wet of optimum it is hypothesized that the static compacted sample was made up of a relatively rigid skeleton of aggregates capable of supporting the side-wall stresses imposed by the mold without collapsing as it swelled upon access to water. The kneading sample, on the other hand, has a poorly developed aggregate skeleton due to the very nature of the compaction used. Therefore the swelling upon access to water could be more nearly accommodated within the gross volume of the sample. This same structural skeleton model explanation adequately predicts the very stress-strain results reported by Seed and Chan in the same paper (55). These results are reproduced as Figure 65.

The macrostructure is quite apparent after compaction. This can be observed in Figure 66 (a), a photo which shows the macrostructure of specimen KL-8 compacted at the 1,500 lb. level. Figure 66 (b) shows specimen KLS-9, a replicate of KL-8, after the swelling pressure test. Both samples are made up of K-1, P6-R8 aggregates. A comparison of the two photos shows that after the swelling pressure test the aggregates are more deformed and the inter-aggregate voids are better filled, although the aggregate skeleton or macrostructure is still quite visible.

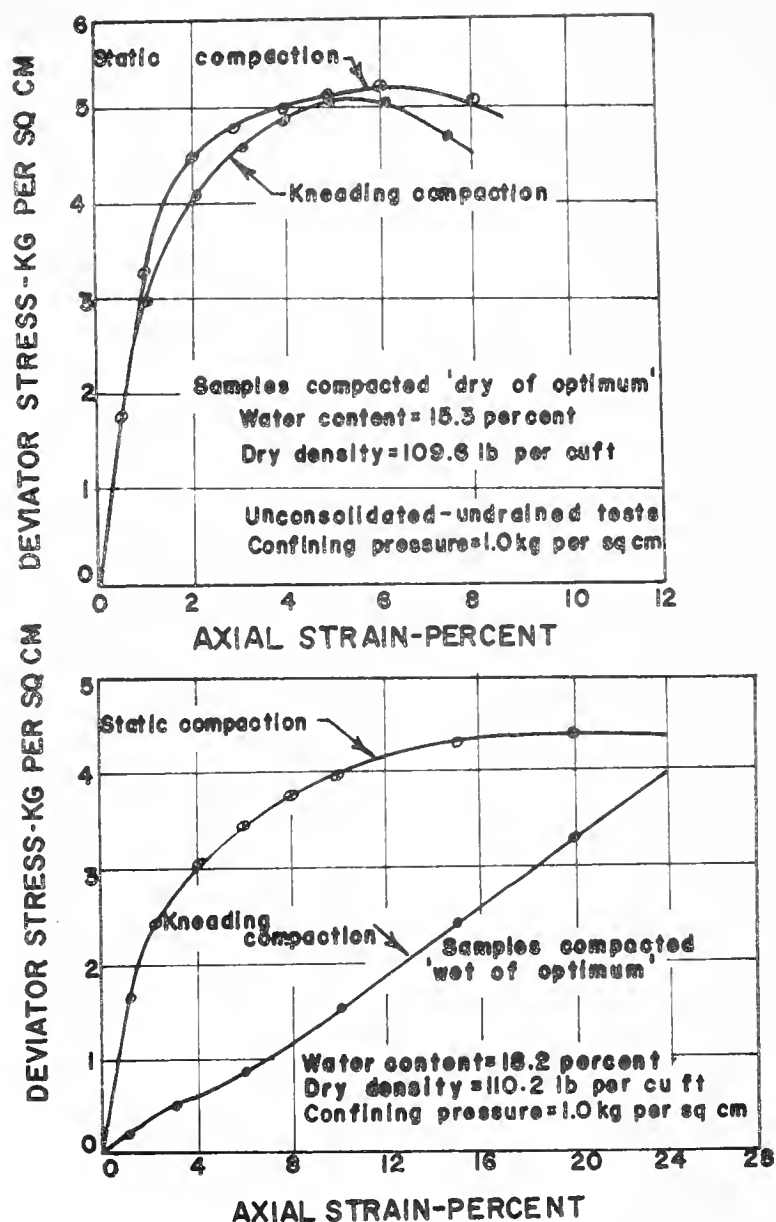
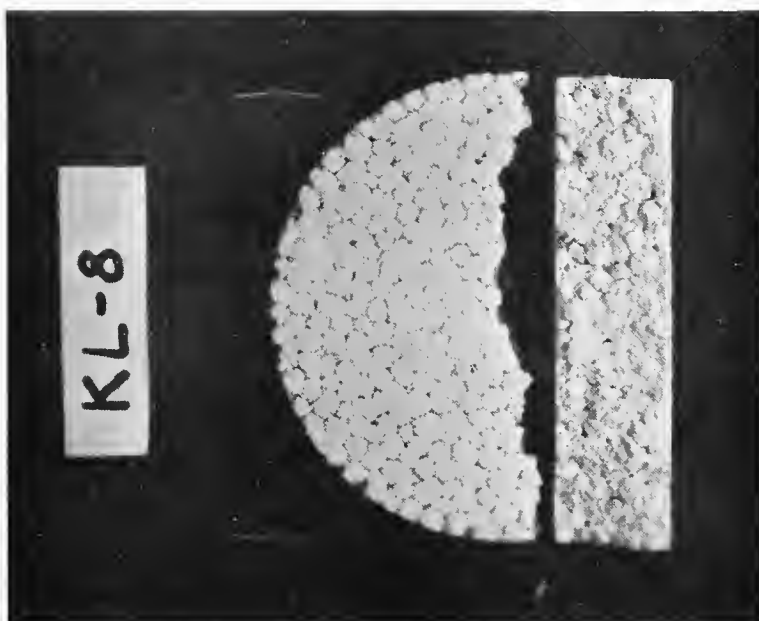
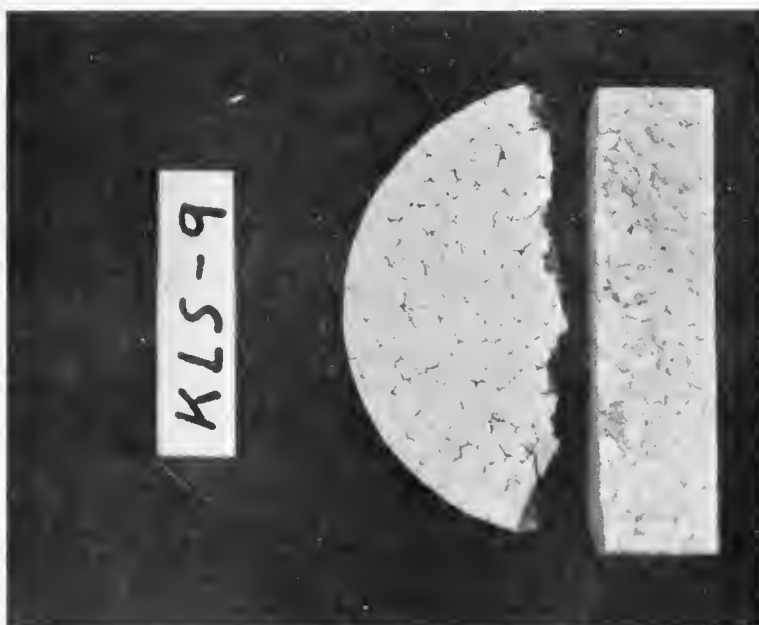


FIGURE 65 STRESS vs DEFORMATION RELATIONSHIPS FOR SAMPLES OF SILTY CLAY PREPARED DRY AND WET OF OPTIMUM BY KNEADING AND STATIC COMPACTION AFTER SEED AND CHAN (55)



a) Compacted at 1000 lb. level



b) Compacted at 1500 lb. level

FIGURE 66. COMPACTED SAMPLES OF K-1, P6-R8 AGGREGATES

Parcher and Liu (43) have presented some interesting results in conjunction with their studies of the swelling (not swelling pressure) characteristics of a compacted and a naturally consolidated clay. Some of their results are reproduced as Figures 67 and 68. For simplicity their data points have been omitted.

Figure 67 shows the percent horizontal and vertical swell for two compacted specimens, both prepared at approximately the same moisture content, 17.4% for the static sample and 17.22% for the kneading sample. Their initial dry unit weights were also the same, 1.747 grams per cubic centimeter. Both the horizontal and vertical swells were larger for the static than the kneading prepared sample. This is predicted by this writer's hypothesis.

The relations between horizontal and vertical swell are also quite informative. The kneading sample shows no particular directional dependence although Lambe's theory predicts a preferential particle alignment. The swelling of the static sample, on the other hand, is much larger in the direction perpendicular to the axis of loading. Existing theories of microstructure after compaction or consolidation would predict the particle alignment to be such that the clay plates are oriented perpendicular to the axis of loading also. It seems more logical to invoke the concept of a "locked-in" horizontal stress.

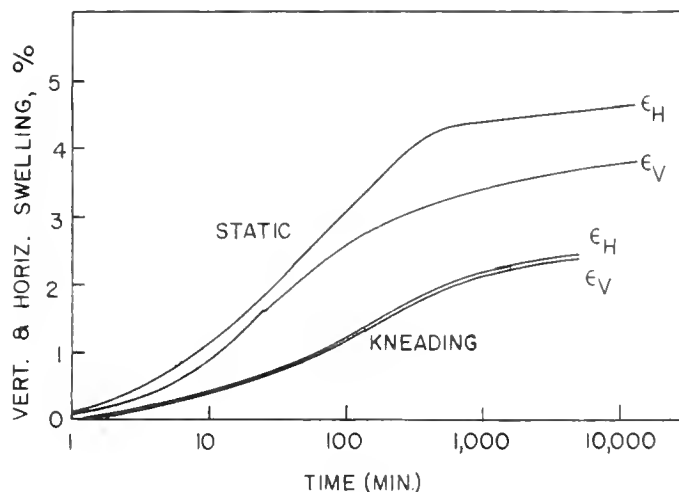


FIGURE 67. SWELLING - TIME CURVES, KNEADING AND STATIC COMPACTION, SOIL B2 AFTER PARCHER AND LIU (43)

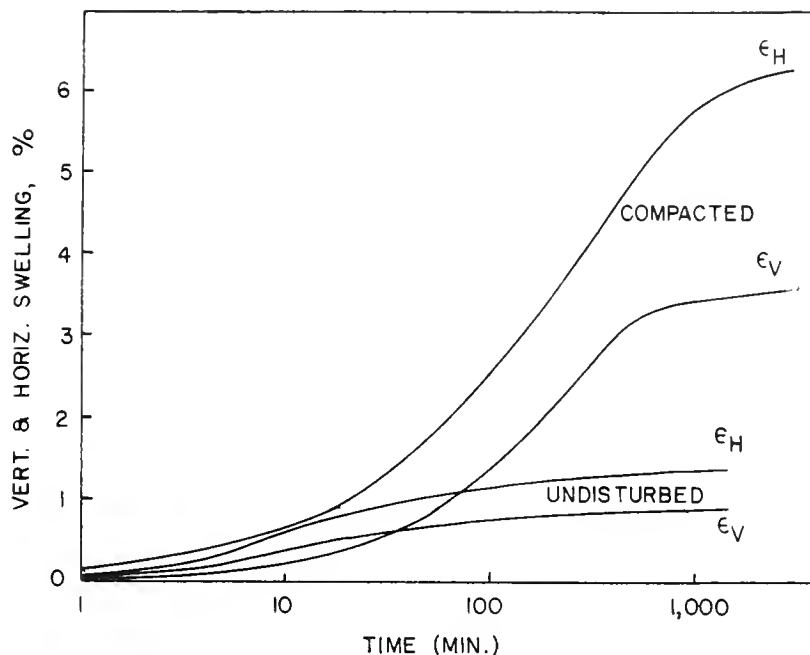


FIGURE 68. SWELLING - TIME CURVES, UNDISTURBED AND COMPACTED STATES, SOIL B1 AFTER PARCHER AND LIU (43)

This concept is well accepted for overconsolidated clays, for sedimentary rocks, and for field compacted clays. In brief for the case of plane strain, an increase in one principal effective stress causes an increase in the other principal stress. Upon removal of the stress change the other stress also decreases, but by less than its previous increase. It is not uncommon for the existing lateral effective stress in the ground to be much larger than the existing effective overburden pressure at that point.

The kneading compaction by its very action destroys the soil's aggregate structure and interlocking ability, and at the end of compaction the axial effective stress and the lateral effective stress are not too dissimilar. Static compaction fits and deforms the existing aggregates into a strong rigid mass and upon removal of the axial compactive stress the lateral stress is better maintained due to the rigidity of the mass. Upon access to water under the condition of free swell, the stresses manifest themselves as strains upon relaxation, as shown in Figure 67.

Figure 68 shows Parcher and Lius' results comparing a "heavily overconsolidated" undisturbed clay with a compacted sample of the same clay prepared at exactly the same moisture content and dry unit weight ($w = 22.1\%$ and $\gamma_d = 1.680 \text{ gm/cm}^3$). One would expect the heavily overconsolidated clay to have much better particle orientation

than the compacted sample, yet it swells considerably less. If it were not for the unknowns of particle bonding and cementation in the undisturbed sample, one would conclude that double-layer swelling plays a minor role in the swelling behavior of this soil.

Previously it was noted that at the 1,000 lb. compaction level the maximum swelling pressure increased as the compaction moisture content increased, while at the 1,500 lb. compaction level the maximum swelling pressure obtains at the intermediate moisture content. This can now be understood in terms of the model. At the 1,000 lb. compaction level each successively higher molding moisture content resulted in a stronger aggregate skeleton with better interlocking. However by increasing the input to the 1,500 lb. level the strength of the skeleton at the high moisture content was exceeded, the skeleton was partially collapsed, and it no longer was able to transfer the swelling pressure without undue internal yielding. This can be visualized as a surface in three-dimensional space with axes of moisture content, skeleton strength, and compactive effort or compacted unit weight. An idealized representation is shown below in Figure 69.

The so-called initial side friction, the residual load on the base of the compaction mold measured just before the upper restraining cap was secured, was also observed and is shown in Table 16. However there is no conclusive trend

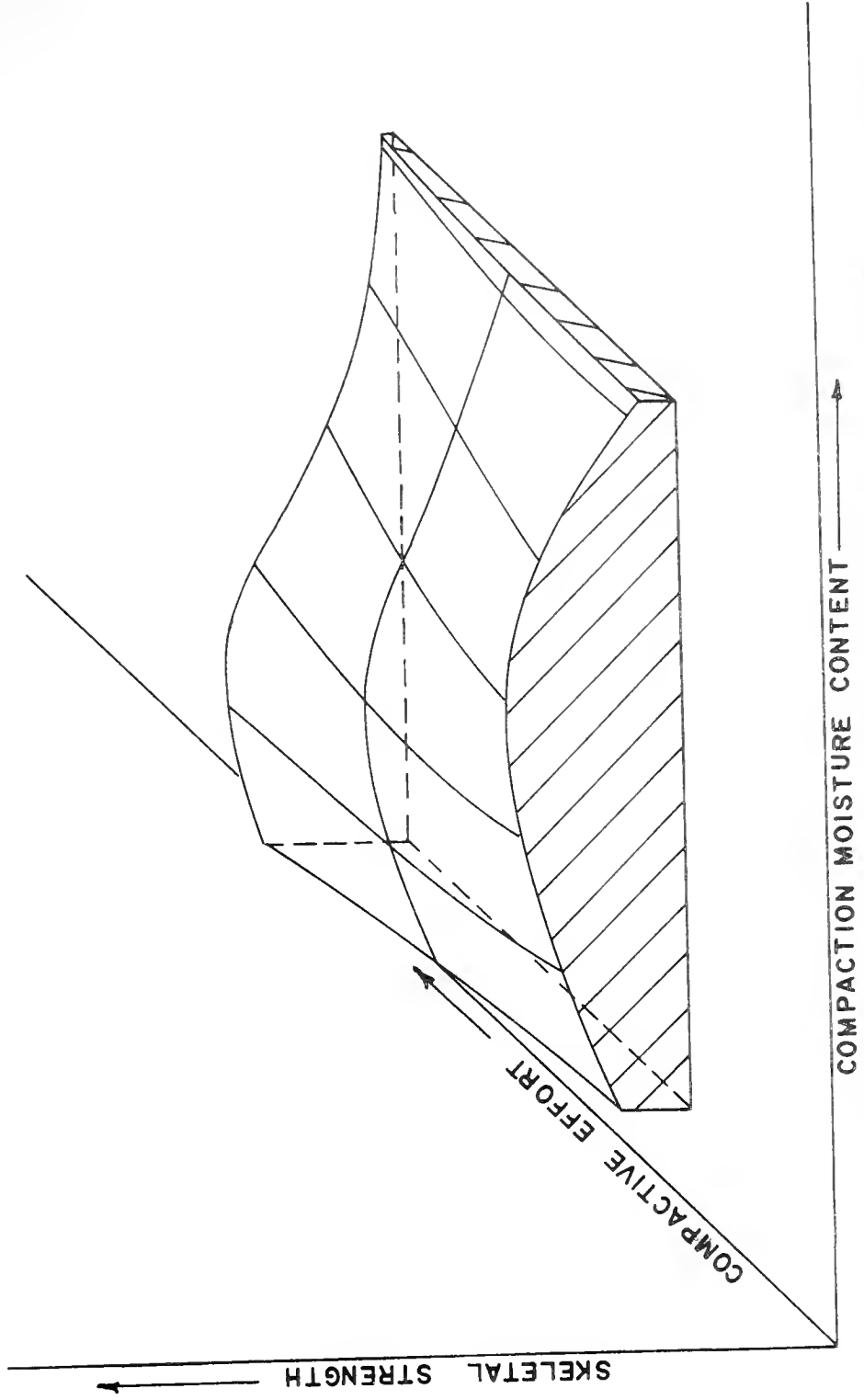


FIGURE 69. SKELETAL STRENGTH AS A FUNCTION OF EFFORT AND MOISTURE CONTENT

evident. There obviously is a relationship among the variables and this base load. However due to the sensitivity of the transducer and the adhesion between the loading ram and the specimen as the ram was withdrawn upon the completion of compaction, a very small axial displacement of the specimen can completely mask the true measurement.

There is an apparent lack of dependence of the maximum swelling pressure generated on the pre-test restraining load. Specimens KLS-6 and KLS-11 are duplicates. KLS-11 was prepared because some of the load-deformation data during the compaction of KLS-6 was lost due to a recorder failure. Their initial side frictions varied by 10% (Table 16), their initial preloads (not shown) varied by about 11%, yet their maximum swelling pressures were almost identical. As previously stated it was shown by Leonards (30) that a linear relation exists between the swelling pressure and the compaction pressure for static compaction. This writer advances the opinion that for constant volume swelling pressure determinations and unless the initial preload exceeds some fraction of the compaction pressure or maximum past pressure, the maximum swelling pressure will not be affected.

In summary this writer's model adequately explains the results of his swelling pressure tests. It also aids in the understanding of previously published swelling pressure and volumetric swell information.

Aggregate Deformation

The results of the aggregate deformation tests are of limited use in their "rough" form. The needed parameters are some measure of the aggregate strength expressed as a stress and a measure of the modulus of elasticity.

The general elastic solution for stress and deformation between two spheres in contact, along with the specific solution for a plate and a sphere, where both have the same modulus of elasticity has been shown by Timoshenko and Goodier (63). Those solutions were extended to the system of a sphere and a plate, each having a different modulus of elasticity.

Using the assumptions that the modulus of elasticity of aluminum or lucite is much larger than that of the soil aggregates, and that Poisson's ratio is 0.3 for all three materials yields the following equations:

$$\alpha = 1.67 \sqrt[3]{\frac{P^2}{E^2 R}} \quad (1)$$

$$q_o = 0.615 \sqrt[3]{\frac{PE^2}{R^2}} \quad (2)$$

where: α is the compression measured from the center of the aggregate to the platen, i.e., 1/2 the movement between the platens in inches.

P is the load in pounds at α compression.

E is the modulus of elasticity of the soil aggregate in pounds/inch².

R is the radius of the soil aggregate before compression, in inches.

q_0 is the maximum normal stress in pounds/inch² between the sphere and plate in contact and occurs at the center of the circular area of contact.

Values for α and P were determined from a secant modulus describing the slope of the average load-deformation relationship for each aggregate size and moisture content. Thus q_0 is the maximum normal stress attained before yielding or fracture of an aggregate occurred.

Due to the limited number of aggregates available after previous tests had been completed, and due to the experimental difficulties involved in testing extremely small aggregates, a complete set of results is not available.

Table 17, below, shows the results of applying equations (1) and (2) above to the results of the aggregate deformation tests.

Table 17. Elastic Properties of Aggregates

<u>Identification</u>	<u>Modulus of Elasticity, psi</u>	<u>q_0, psi</u>
K-1,P4-R6	11,500	1,600
K-1,P6-R8	9,980	1,540
K-1,P8-R10	27,800	3,410
K-2,P4-R6	11,100	1,640
K-2,P6-R8	11,220	1,740
K-2,P8-R10	10,520	1,910
K-2,P10-R12	17,930	2,490
K-2,P12-R20	21,280	3,120
K-3,P6-R8	11,650	1,920

Table 17 indicates that, in general, aggregate strength as expressed by q_0 increases as the aggregate size decreases at constant moisture content. It further shows that the modulus of elasticity increases with decreasing particle size at constant moisture content. Neither of these trends is surprising when viewed in terms of the mechanism of aggregate growth hypothesized previously.

The results show no water content dependence for the largest (P4-R6) aggregates; they indicate for the P6-R8 size that both E and q_0 increase as the water content increases, and the incomplete results for size P8-R10 indicates a reversal of this trend. That is, E and q_0 decrease as the water content increases. Since there is no information concerning K-3, the values for K-2 and K-1 are suspect.

Based on the trend of E and q_0 increasing as size decreases at constant moisture content, the E and q_0 values for K-2, P8-R10 seem to be reasonable. The reader is reminded that the K-1, P8-R10 results shown are the average relation obtained from thirty aggregate deformation tests and are reasonably certain. Referring to the results of aggregate unit weights, the dry unit weight of K-1, P8-R10 is considerably higher than that of K-2, P8-R10. This in itself would lead one to conclude that it is not unreasonable to expect that K-1, P8-R10 is stiffer and stronger than K-2, P8-R10.

The most obvious reason why the results of the aggregate deformation tests are inconclusive is that changes occurred in the aggregates between the time of sample compaction and aggregate deformation testing. The most likely change that occurred to influence the aggregate strengths is a slight decrease in the moisture content. A loss of moisture will increase the aggregate's strength.

According to the writer's hypothesis concerning the formation of aggregates, the larger aggregates have a higher moisture content than the smaller ones. This was shown to be true experimentally. From this it follows that the pore water pressure in the larger aggregates is less negative than in the smaller aggregates and that the undrained strength of the larger aggregates is less than that of the smaller aggregates.

Model Used by Other Investigators

In a parallel but independent investigation Barden and Sides (4) have adopted a compacted soil model similar to the one used in this study. Their verification of the correctness of this model consists of an analysis of air and water permeabilities and volume change characteristics of the compacted samples, as well as micrographs of the compacted clay showing the existence of aggregates or "macro-peds" as they call them.

SUMMARY AND CONCLUSIONS

Summary

In this study a model or mechanism has been developed to explain the achievement of the compacted unit weight for the laboratory static compaction of kaolinite. The mechanism takes into account the pre-compaction soil preparation and conditioning as well as the soil interactions which occur during compaction.

To validate this compaction mechanism an experimental program was developed. The significant independent variables investigated were compactive effort, moisture content, and aggregate size. Among the properties and characteristics measured were the aggregate strength, particle orientations for various conditions, the relation between compactive load and densification during the period of compaction, and the continued densification at a constant level of applied stress. Others were the decrease in unit weight upon release of the compactive load and the swell pressure-time relation when compacted samples were given access to water while being restrained at constant volume.

The most important findings are summarized below.

Aggregate Studies

Particle orientation increases as the moisture content increases (Figure 32, Table 9). The degree of saturation for the aggregates increases as the moisture content increases (Figure 48). The degree of saturation also increases as the aggregate's size increases (Table 10). At constant gross (batch) moisture content the water contents of the various sized aggregates making up the batch increase as the aggregate size increases (Table 10). The strength and modulus of elasticity of the aggregates increase as the aggregate size decreases (Table 17).

Achievement of Compacted Unit Weight

The concept of net input energy, as opposed to the gross applied energy, was introduced and shown to produce significantly different results from the common moisture content-unit weight relationship (Figures 50 through 60). It has been shown, based on this concept, that for the moisture contents investigated, the energy required to achieve a given unit weight decreases as the moisture content increases (Table 11). The net energy required to move from one position to another on the moisture content-unit weight curve is related to the aggregate size; as the aggregate size decreases the energy required increases (Table 12). It has further been shown that simple relations exist and can be quantified to describe the achievement of unit weight as a function of the net energy input (Table G1).

End Results of Compaction

The so-called end results of compaction indicate that during the two-minute period in which the compactive load is held constant the change (increase) in dry unit weight depends on both the compaction moisture content and the magnitude of the compactive load (Table 14). Further, the increase in dry unit weight also increases during this period of time as the aggregate size decreases. It has been shown that the rebound or immediate decrease of the dry unit weight upon release of the compactive load increases as the aggregate size decreases (Table 15). The measured degree of particle orientation increases with the compactive effort and the compaction moisture content (Figures 32 and 33).

Swelling Pressure

Many of the swelling pressure tests exhibited a temporary collapse or at least a decrease of the swelling pressure generated (Figures 39 through 44). This was especially true of those samples compacted at the 1,000 lb. level. Almost universally these tests displayed final swelling pressures which were considerably smaller than their peak values. The maximum swelling pressure increased as the compaction moisture content increased for the lower level of compaction. But at the higher compaction level the intermediate compaction moisture content resulted in the largest swelling pressure. The final measured swelling pressures have this same relationship to the compactive load-compaction moisture content combination.

Conclusions

The results have been discussed and interpreted in previous sections and have been shown to be in accord with the writer's model for the mechanism of compaction for kaolinite. In addition the published results of various authors have been analyzed and shown to be compatible with this model.

It is noted that Lambe's compaction theory (27) does predict the changes in particle orientation which were experimentally observed. Furthermore it is suggested, without verification, that Olson's effective stress theory of compaction (38) may be appropriate when considering the aggregate skeleton model. Some characteristics (particle orientation in particular) are adequately predicted by the one-level microstructure model, but it appears that engineering behavior can be better predicted and explained in terms of the deformable aggregate model.

It is therefore concluded that the deformable aggregate model is an appropriate one for use in aiding the interpretation of swell and compaction characteristics for laboratory static compacted kaolinite in the range of moisture content studied and for the preparation technique used. It is further concluded that the use of single-sized clay aggregates for sample preparation allows certain characteristics to be seen which may be otherwise masked.

RECOMMENDATIONS

As stated in the Introduction the objective of this research is the production of a mechanistic model which adequately explains the laboratory compaction of fine-grained soils. To further confirm this model and to extend its relevance the following tasks should be undertaken:

- 1) Verify the aggregate-skeleton concept for other fine-grained soils (including natural ones) in the laboratory. Two recently developed technologies can help enormously in this effort. These are: measure of pore size distribution by mercury porosimetry, and fabric measures with the scanning electron microscope. Undoubtedly, the model will need to be expanded from two dimensions to three to take full advantage of its predictive potential.
- 2) Verify this concept for laboratory impact and kneading types of compaction, and with particular attention to the potential importance of optimum moisture contents.
- 3) Extend the usefulness of the equations relating net input energy to unit weight increase by quantifying the effects of moisture content and aggregate size.

The emphasis here is on the generation of predictive equations.

- 4) Examine the usefulness of the net energy input concept in correlating the effects of the different modes and levels of laboratory compaction.
- 5) Determine the validity of the aggregate-skeleton model for field compacted soils.

The author intends to continue along this path of investigation with the ultimate objective of improving the engineer's predictive capabilities. If achieved, this would allow more extensive and rational use of the procedural type of specification for the field compaction of fine-grained soils.

LIST OF REFERENCES

LIST OF REFERENCES

Notations

ASCE is American Society of Civil Engineers
 ASTM is American Society for Testing and Materials
 JSMFD is Journal of the Soil Mechanics and
 Foundations Division
 HRB is Highway Research Board

1. Ahmed, S., "Pore Size Distribution and Its Effect on the Behavior of a Compacted Clay," MSCE Thesis, Purdue University, 1971.
2. Barber, E. S., Discussion of "Engineering Properties of Expansive Clays," by W. G. Holtz and H. J. Gibbs, Transactions, ASCE, Vol. 121, 1956, pp. 669-673.
3. Barden, L., Madedjar, A. O., and Sides, G. R., "Volume Change Characteristics of Unsaturated Clay," JSMFD, ASCE, Vol. 95, No. SM1, Jan. 1969, pp. 33-51.
4. Barden, L., and Sides, G. R., "Engineering Behavior and Structure of Compacted Clay," JSMFD, ASCE, Vol. 96, No. SM4, July 1970, pp. 1171-1200.
5. Bishop, A. W., "The Measurement of Pore Pressure in the Triaxial Test," Proceedings, Conference on Pore Pressure and Suction in Soils, 1961, pp. 38-46.
6. Bishop, A. W., "Discussion," Proceedings, Conference on Pore Pressure and Suction in Soils, 1961, pp. 63-66.
7. "Bituminous Materials; Soils; Skid Resistance," ASTM Standards, Part 11, March, 1967.
8. Bolt, G. H., "Physico-Chemical Analysis of the Compressibility of Pure Clays," Geotechnique, Vol. 6, No. 2, 1956, pp. 86-93.
9. Campanella, R. G., and J. K. Mitchell, "Influence of Temperature Variations on Soil Behavior," JSMFD, ASCE, Vol. 94, No. SM3, May 1968, pp. 709-734.
10. Casagrande, A., "The Structure of Clay and Its Importance in Foundation Engineering," Journal of the Boston Society of Civil Engineers, Vol. 19, April 1932, pp. 168-209.

11. Diamond, S., "Pore Size Distributions in Clays," Clays and Clay Minerals, Vol. 18, 1970, pp. 7-23.
12. Grim, R. E., Clay Mineralogy, McGraw-Hill, New York, 1953.
13. Dudley, J. H., "Review of Collapsing Soils," JSMFD, ASCE, Vol. 96, No. SM3, May 1970, pp. 925-947.
14. Guttman, I., Wilkes, S. S. and Hunter, J. S., "Chapter 14, Nonparametric Tests," Introductory Engineering Statistics, Second Ed., Wiley, New York, 1971, pp. 325-338.
15. Handbook of Chemistry and Physics, Chemical Rubber Publishing Co., Cleveland.
16. Heiselman, C. F., "Air Entrainment in Compacted Earth Embankment," Proceedings, Second International Conference on Soil Mechanics and Foundation Engineering, Vol. V, 1948, pp. 239-242.
17. Hogentogler, C. A., Jr., "Essentials of Soil Compaction," Proceedings, HRB, 16th Annual Meeting, 1936, pp. 309-316.
18. Holtz, W. G., and Gibbs, H. J., "Engineering Properties of Expansive Clays," Transactions, ASCE, Vol. 121, 1956, pp. 641-663.
19. Holtz, W. G. and Lowitz, C. A., "Compaction Characteristics of Gravelly Soils," STP No. 232, ASTM, 1957, pp. 67-86.
20. "Instructions for Use of the Particle Size Analyzer TGZ-3," Carl Zeiss Co., West Germany.
21. Johnson, A. W. and Sallberg, J. R., "Factors that Influence Field Compaction of Soils," HRB Bulletin 272, 1960.
22. Kassiff, G. and Baker, R., "Aging Effects on Swell Potential of Compacted Clay," JSMFD, ASCE, Vol. 97, No. SM3, March 1971, pp. 529-540.
23. Kruyt, H. R., editor, Colloid Science, Vol. I, Elsevier Co., New York, 1952.
24. Ladd, C. C., "Swelling of Compacted Clay," Master's Thesis, Massachusetts Institute of Technology, 1957.

25. Ladd, C. C., "Mechanisms of Swelling by Compacted Clay," HRB Bulletin 245, 1960, pp. 10-26.
26. Lambe, T. W., "The Structure of Inorganic Soil," Separate No. 315, ASCE, 1953.
27. Lambe, T. W., "Compacted Clay: Structure," Transactions, ASCE, Vol. 125, 1960, pp. 682-717.
28. Lambe, T. W., "Compacted Clay: Engineering Behavior," Transactions, ASCE, Vol. 125, 1960, pp. 718-756.
29. Lambe, T. W. and Whitman, R. V., Soil Mechanics, J. Wiley & Sons, Inc., New York, 1969.
30. Leonards, G. A., Discussion of "Effect of Compaction on Soil Properties," by S. D. Wilson, Proceedings of the Conference on Soil Stabilization, M.I.T., 1952, pp. 159-161.
31. Leonards, G. A. and Altschaeffl, A. G., Discussion of "Review of Collapsing Soils," by J. H. Dudley, JSMFD, ASCE, Vol. 97, No. SM1, Jan. 1971, pp. 269-271.
32. Low, P. F., Discussion of "Physico-Chemical Properties of Soils: Ion Exchange Phenomena," by A. W. Taylor, JSMFD, ASCE, Vol. 85, No. SM2, April 1959, pp. 79-89.
33. McRae, J. L., Discussion of "Structure and Strength Characteristics of Compacted Clays," Transactions, ASCE, Vol. 126, Part I, 1961, pp. 1393-1397.
34. McRae, J. L., and Turnbull, W. J., Discussion of "Effective Stress Theory of Soil Compaction," by R. Olson, JSMFD, ASCE, Vol. 89, No. SM6, Nov. 1963, pp. 101-108.
35. Marsal, R. J., "Contact Forces in Soils and Rockfill Materials," Proceedings, Second Panamerican Conference on Soil Mechanics and Foundation Engineering, Vol. II, 1963, pp. 67-98.
36. Martin, R. T., "Research on the Physical Properties of Marine Soils," Research Report R62-42, Soil Engrg. Div. Pub. No. 127, 56 pp., M.I.T., Nov. 1962.

37. Norrish, K., "The Swelling of Montmorillonite," Discussions of the Faraday Society, Vol. 18, 1954, pp. 120-134.
38. Olson, R. E., "Effective Stress Theory of Soil Compaction," JSMFD, ASCE, Vol. 89, No. SM2, March 1963, pp. 27-45.
39. Olson, R. E., Closure of "Effective Stress Theory of Soil Compaction," JSMFD, ASCE, Vol. 90, No. SM2, March 1964, pp. 171-184.
40. Olson, R. E. and Scott, J. D., Discussion of "Structure and Strength Characteristics of Compacted Clays," by H. B. Seed and C. K. Chan, Transactions, ASCE, Vol. 126, 1961, pp. 1398-1404.
41. Overbeck, J. Th. G., Colloid Science, H. R. Kruyt, ed., Vol. 1, Parts II, IV, and VI, Elsevier Co., Amsterdam, 1952.
42. Pacey, John G., Jr., "The Structure of Compacted Soils," S.M. Thesis, M.I.T., 1956.
43. Parcher, J. V. and Lin, P. C., "Some Swelling Characteristics of Compacted Clays," JSMFD, ASCE, Vol. 91, No. SM3, May 1965, pp. 1-17.
44. Perloff, W. H., Jr., "Study of Long-Term Deformation of Compacted Cohesive Soil Embankments," Final Report, Research Project EES-260, Ohio State University, Transportation Engineering Center, Jan. 1966.
45. Procedures for Testing Soils, ASTM, Fourth Edition, December, 1964.
46. Proctor, R. R., "Fundamental Principles of Soil Compaction," Engineering News-Record, Vol. 111, No. 9, Aug. 31, 1933, pp. 245-248.
47. Proctor, R. R., "Description of Field and Laboratory Methods," Engineering News-Record, Vol. 111, No. 10, Sept. 7, 1933, pp. 348-351.
48. Proctor, R. R., "Field and Laboratory Verification of Soil Suitability," Engineering News-Record, Vol. 111, No. 12, Sept. 21, 1933, pp. 348-351.
49. Proctor, R. R., "New Principles Applied to Actual Dam-Building," Engineering News-Record, Vol. 111, No. 13, Sept. 28, 1933, pp. 372-376.

50. Proctor, R. R., "Laboratory Soil Compaction Methods, Penetration Resistance Measurements, and the Indicated Saturated Penetration Resistance," Proceedings, Second International Conference on Soil Mechanics and Foundation Engineering, Rotterdam, Vol. V, 1948, pp. 242-247.
51. Quirk, J. P., "The Role of Interparticle Forces in Soil Structure," Interparticle Forces in Clay-Water-Electrolyte Systems, Commonwealth Scientific and Industrial Research Organization, Melbourne, Australia, 1960, pp. 2-1 - 2-8.
52. Quirk, J. P., "Discussion," Interparticle Forces in Clay-Water-Electrolyte Systems, Commonwealth Scientific and Industrial Research Organization, Melbourne, Australia, 1960, pg. 3-1.
53. Schofield, R. K., and Samson, H. R., "Flocculation of Kaolinite Due to the Attraction of Oppositely Charged Crystal Faces," Discussions of the Faraday Society, Vol. 18, 1954, pp. 135-145.
54. Seed, H. B., and Chan, C. K., "Compacted Clays - Undrained Strength After Soaking," Transactions, ASCE, Vol. 126, 1961, pp. 1408-1425.
55. Seed, H. B. and Chan, C. K., "Structure and Strength Characteristics of Compacted Clays," Transactions, ASCE, Vol. 126, 1961, pp. 1344-1385.
56. Seed, H. B., Mitchell, J. K., and Chan, C. K., "Studies of Swell and Swell Pressure Characteristics of Compacted Clays," HRB Bulletin 313, 1962, pp. 12-39.
57. Skempton, A. W., "The Pore-Pressure Coefficients A and B," Geotechnique, Vol. IV, No. 4, Dec. 1954, pp. 143-147.
58. Sridharan, A., Altschaeffl, A. G., and Diamond, S., "Pore Size Distribution Studies," JSMFD, ASCE, Vol. 97, No. SM5, pp. 771-785, 1971.
59. Standard Specifications for Highway Materials and Methods of Sampling and Testing, Part II, AASHO, 1966.
60. Terzaghi, K., Erdbaumechanik auf bodenphysikalischer Grundlage, Franz Deuticke, Leipzig, 1925.
61. Terzaghi, K., "Correspondence," Geotechnique, Vol. VI, No. 4, Dec. 1956, pp. 191-192.

62. Thiessen, P. A., "Wechselseitige Adsorption von Kolloiden," Z. Elektrochem., Vol. 48, 1942, pp. 675-681.
63. Timoshenko, S. P. and Goodier, J. N., Theory of Elasticity, Third Ed., McGraw-Hill, New York, 1970, pp. 409-414.
64. Van Olphen, H., An Introduction to Clay Colloid Chemistry, Interscience, New York, 1963.
65. Washburn, E. W., "Note on a Method of Determining the Distribution of Pore Sizes in a Porous Material," Proceedings of the National Academy of Science (US) Vol. 7, pp. 115-116, 1921.
66. Winslow, D. N., "The Pore Size Distribution of Portland Cement Paste," MSCE Thesis, Purdue University, 1969.

APPENDICES

Appendix A:

Aggregate Size Distribution Curves

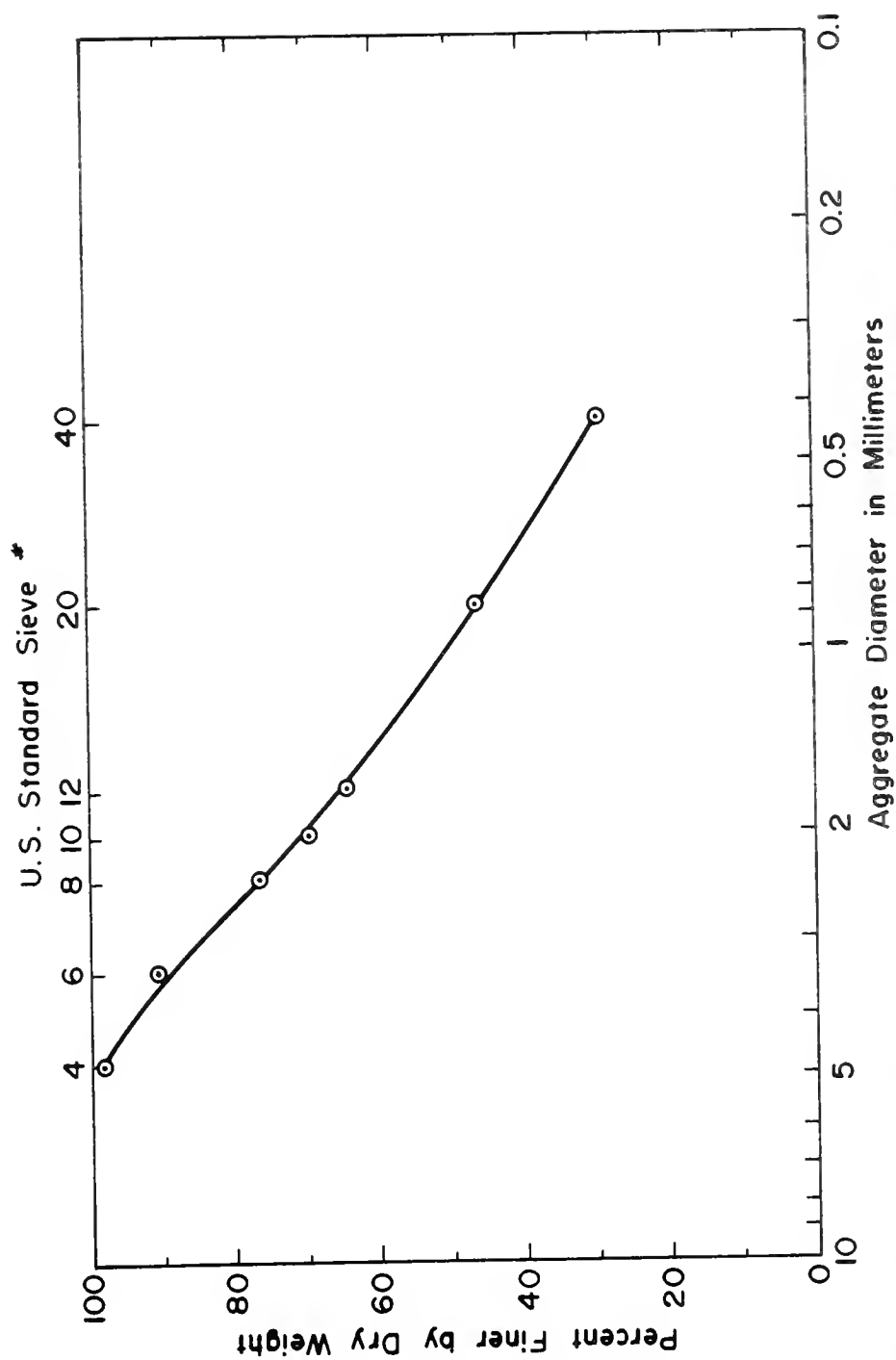


FIGURE A1. AGGREGATE SIZE DISTRIBUTION CURVE FOR BATCH K-1

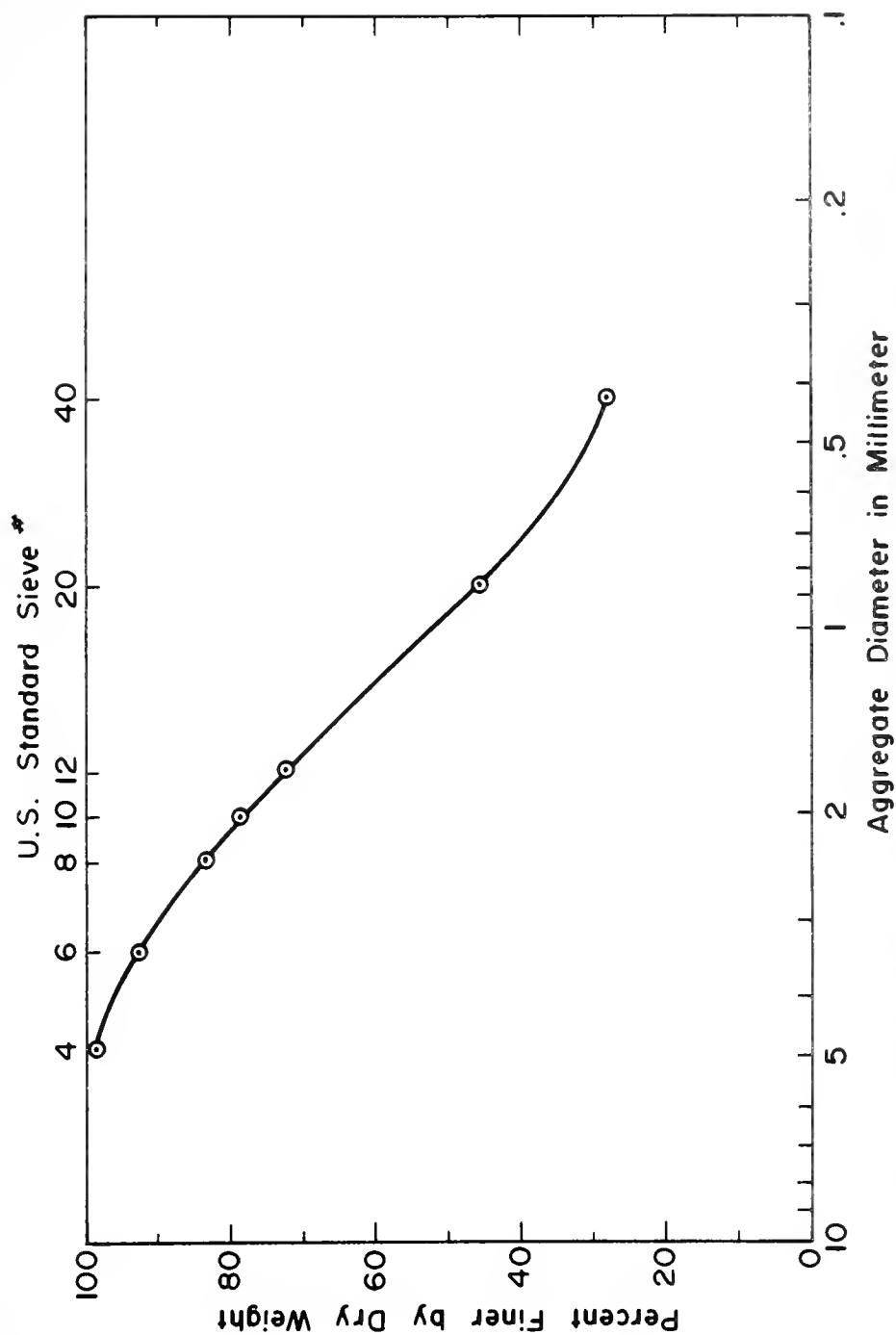


FIGURE A2. AGGREGATE SIZE DISTRIBUTION CURVE FOR BATCH K-2

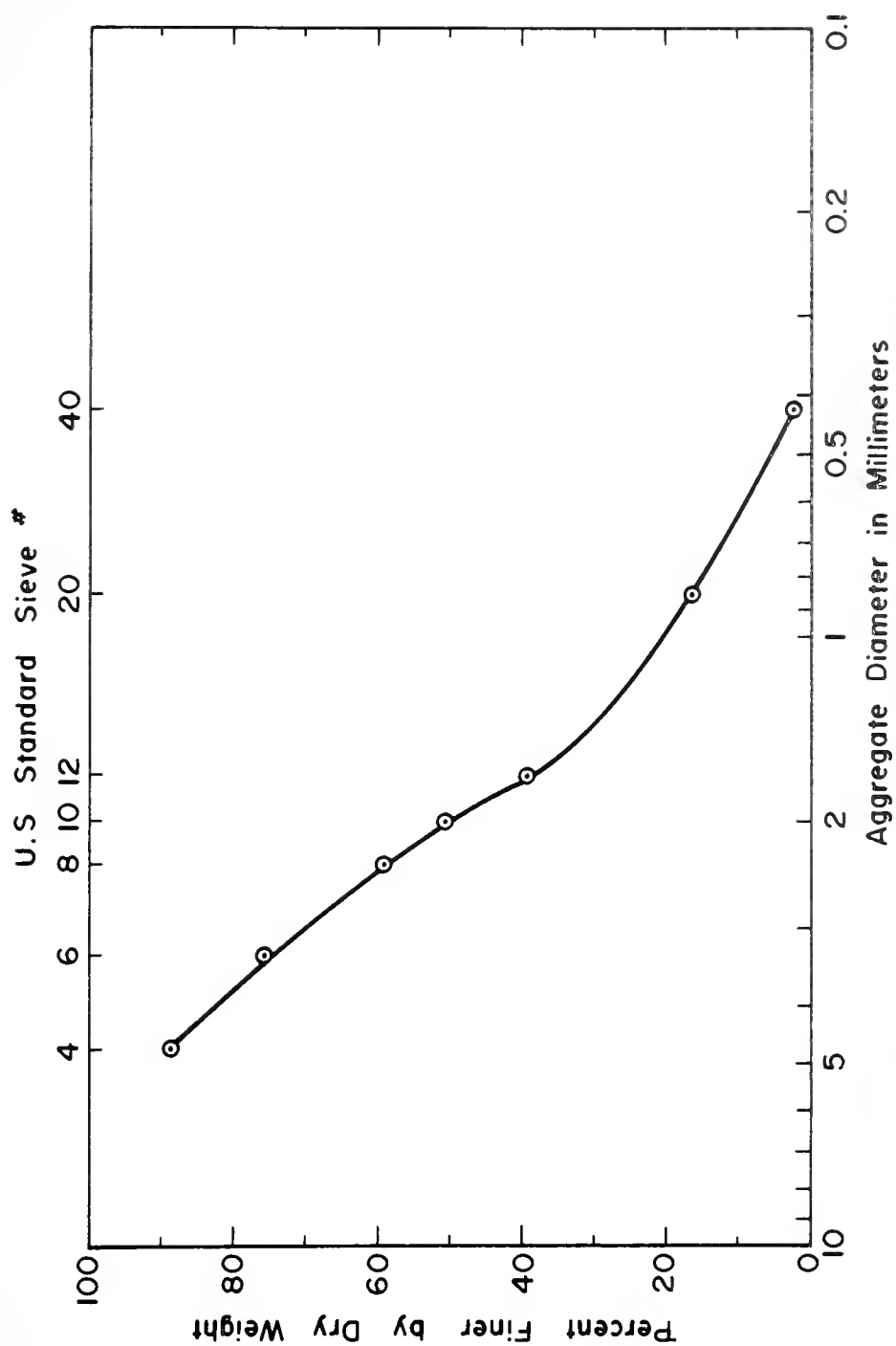


FIGURE A3. AGGREGATE SIZE DISTRIBUTION CURVE FOR BATCH K-3

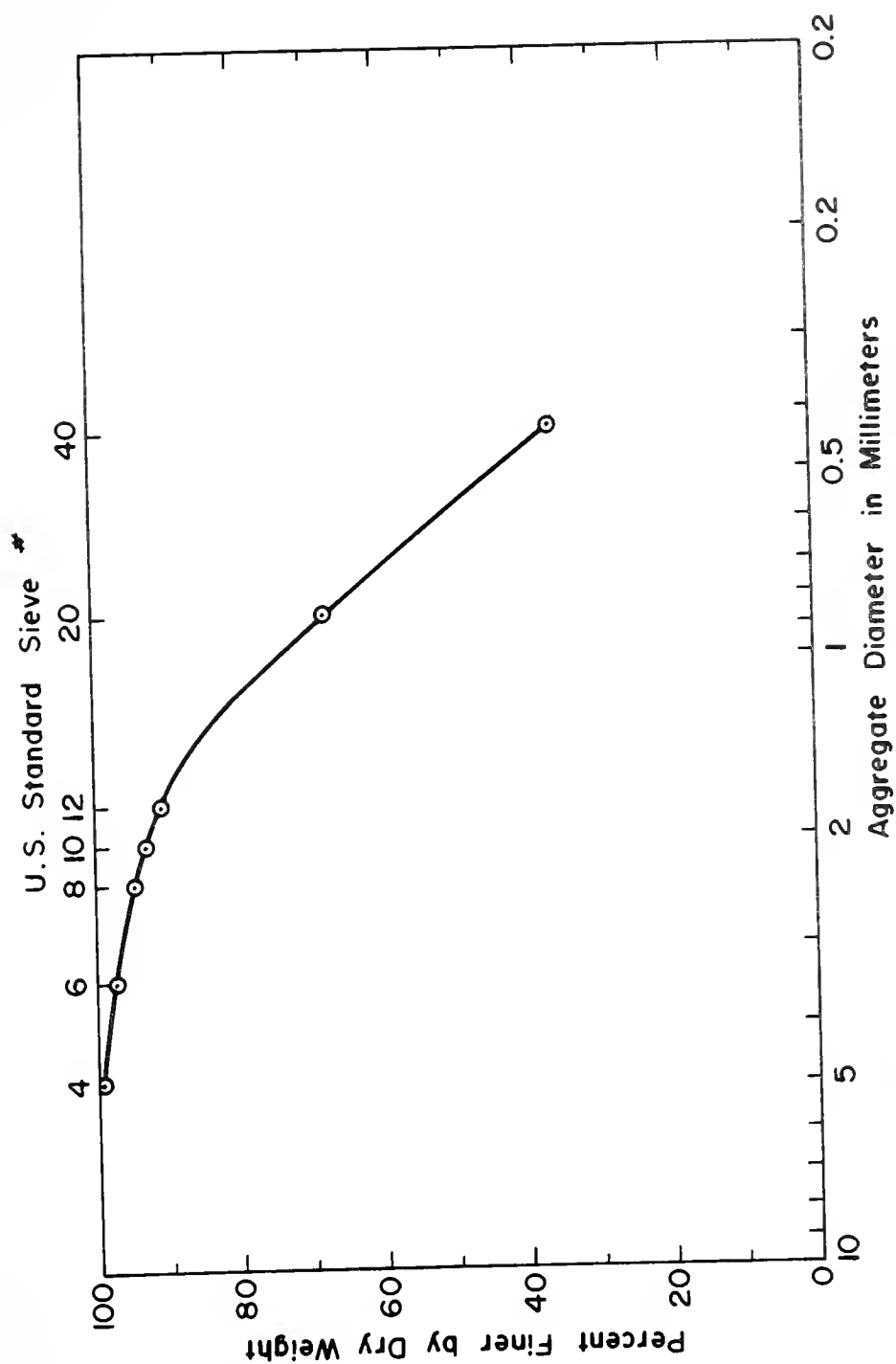


FIGURE A4. AGGREGATE SIZE DISTRIBUTION CURVE FOR BATCH K-4

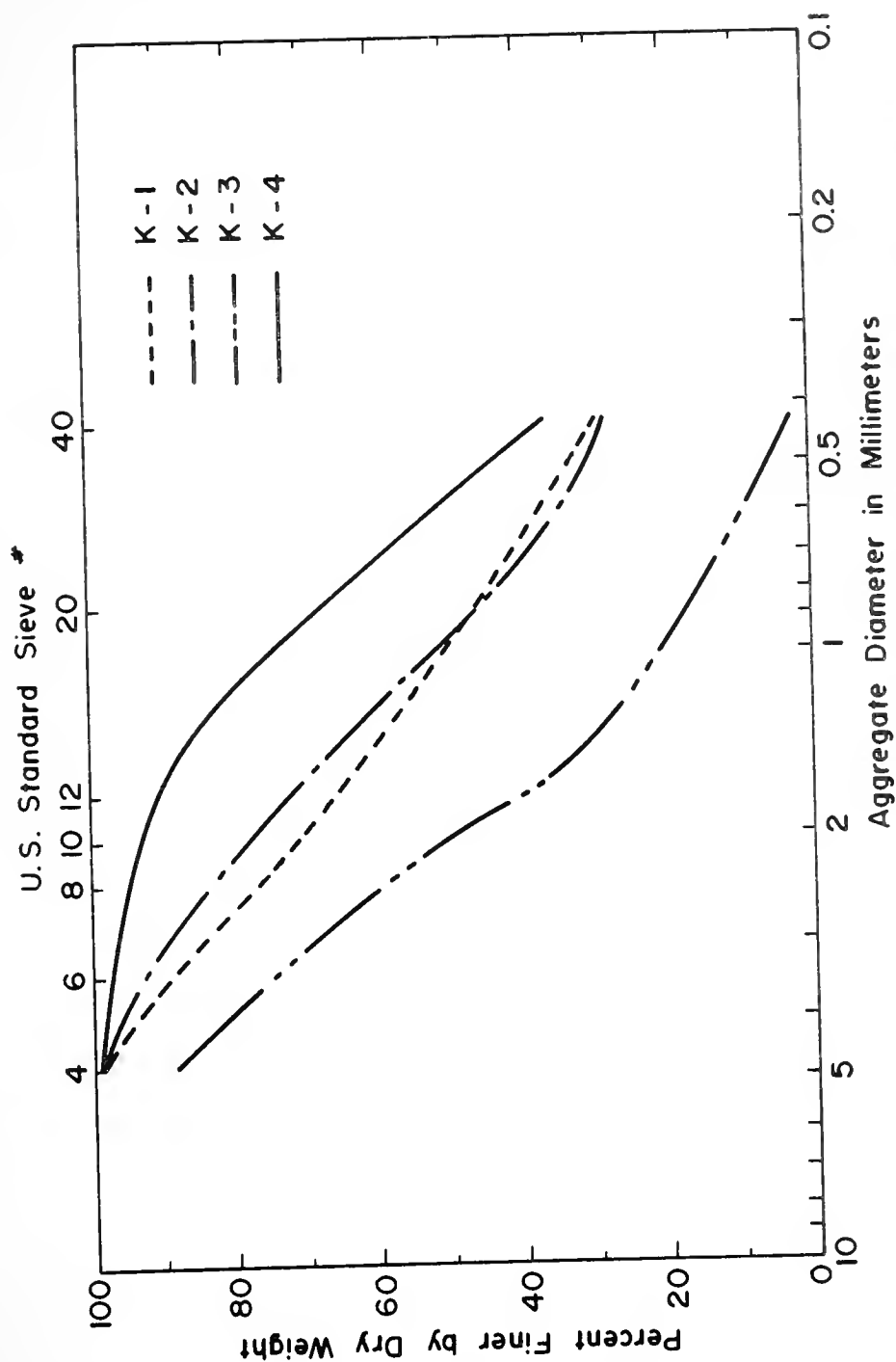


FIGURE A5. AGGREGATE SIZE DISTRIBUTION CURVES FOR BATCHES K-1 THROUGH K-4

Appendix B:X-Ray Diffractometer Settings

General Electric XRD-5 diffractometer

chart speed - C, 60 inches/hour

preset multiplier - 1

operation - preset time

preset time - 10 seconds

function - X 1

input sensitivity - 3.5 v

gain - 10

ΔE - 10 v

E - 5 v

range - 1,000 cps

time constant - 2.0 seconds

linear

H.V. adjust - 638

goniometer speed - 2 degrees per minute

power - 50 KV, 16 milliamps

Copper K_{α} radiation

Appendix C:Peak Height Ratios

The following table includes the results of each X-ray diffraction pattern obtained from the various impregnated samples. For ease of identification, each determination is lettered and numbered, since 18 X-ray patterns were obtained from each sample. A change in the letter indicates that the sample was resurfaced, while the numbers merely indicate repetitions without resurfacing or remounting the sample in the goniometer.

Table C1. Particle Orientation by Peak Height Ratio.

Sample	Batch	Size	Effort, lbs.	A, B or C	Peak Height Ratio, 002/020					
					1	2	3	4	5	6
aggreg.	K-1	P6-R8	--	A	1.49	1.55	1.50	1.42	1.62	1.58
				B	1.55	1.52	1.57	1.62	1.67	1.64
				C	1.56	1.41	1.57	1.41	1.42	1.39
KL-5	K-1	P6-R8	1000	A	1.75	1.80	1.79	1.91	1.72	1.80
				B	1.55	1.52	1.56	1.70	1.78	1.59
				C	1.85	1.76	1.88	1.73	1.67	1.78
KL-7	K-1	P6-R8	1500	A	1.75	1.94	1.74	2.04	2.04	2.08
				B	2.16	2.15	2.19	1.81	2.00	1.88
				C	1.96	1.96	1.82	1.88	1.88	1.98
aggreg.	K-2	P6-R8	--	A	2.35	2.06	1.97	1.72	1.68	1.63
				B	1.88	1.80	1.91	1.72	1.75	1.82
				C	1.69	1.74	1.81	1.54	1.64	1.71
KL-35	K-2	P6-R8	1000	A	2.27	2.05	2.08	2.11	1.95	2.00
				B	2.10	2.05	2.08	1.95	2.10	2.13
				C	2.25	2.13	2.11	2.05	2.10	2.14
KL-38	K-2	P6-R8	1500	A	2.43	2.16	2.30	2.47	2.43	2.46
				B	2.14	2.16	2.31	2.22	2.35	2.38
				C	2.15	2.13	2.38	2.25	2.20	2.14
aggreg.	K-3	P6-R8	--	A	2.23	2.15	2.06	2.30	2.12	2.23
				B	2.10	2.38	2.03	2.00	1.82	1.91
				C	1.91	1.64	1.70	1.92	2.07	1.94
KL-65	K-3	P6-R8	1000	A	2.48	2.25	2.62	2.23	2.28	2.38
				B	2.64	2.56	2.67	2.63	2.60	2.64
				C	2.66	2.72	2.61	2.51	2.64	2.77
KL-68	K-3	P6-R8	1500	A	2.32	2.38	2.18	2.40	2.68	2.57
				B	2.17	2.23	2.31	2.43	2.57	2.55
				C	2.37	2.28	2.28	2.27	2.19	2.10

Appendix D:Additional Results of Achievement of Compacted Unit Weight

The figures in Appendix D show the effect of moisture content on γ_d and γ_m versus energy for the 1000 lb and 1500 lb levels.

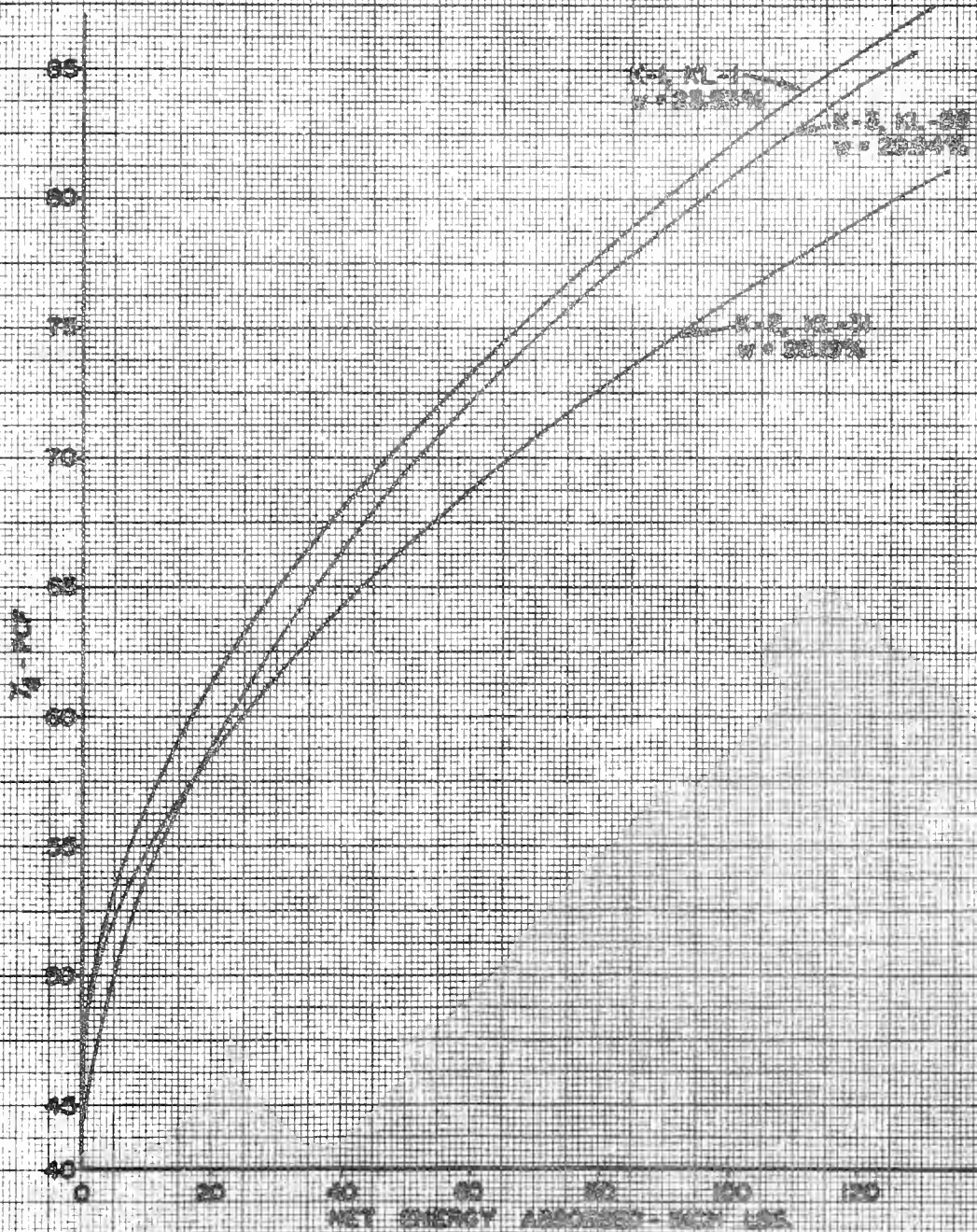


FIGURE D1 EFFECT OF MOISTURE CONTENT ON % VS. ENERGY (P4-R6 KALINITE-1000 LB LEVEL)

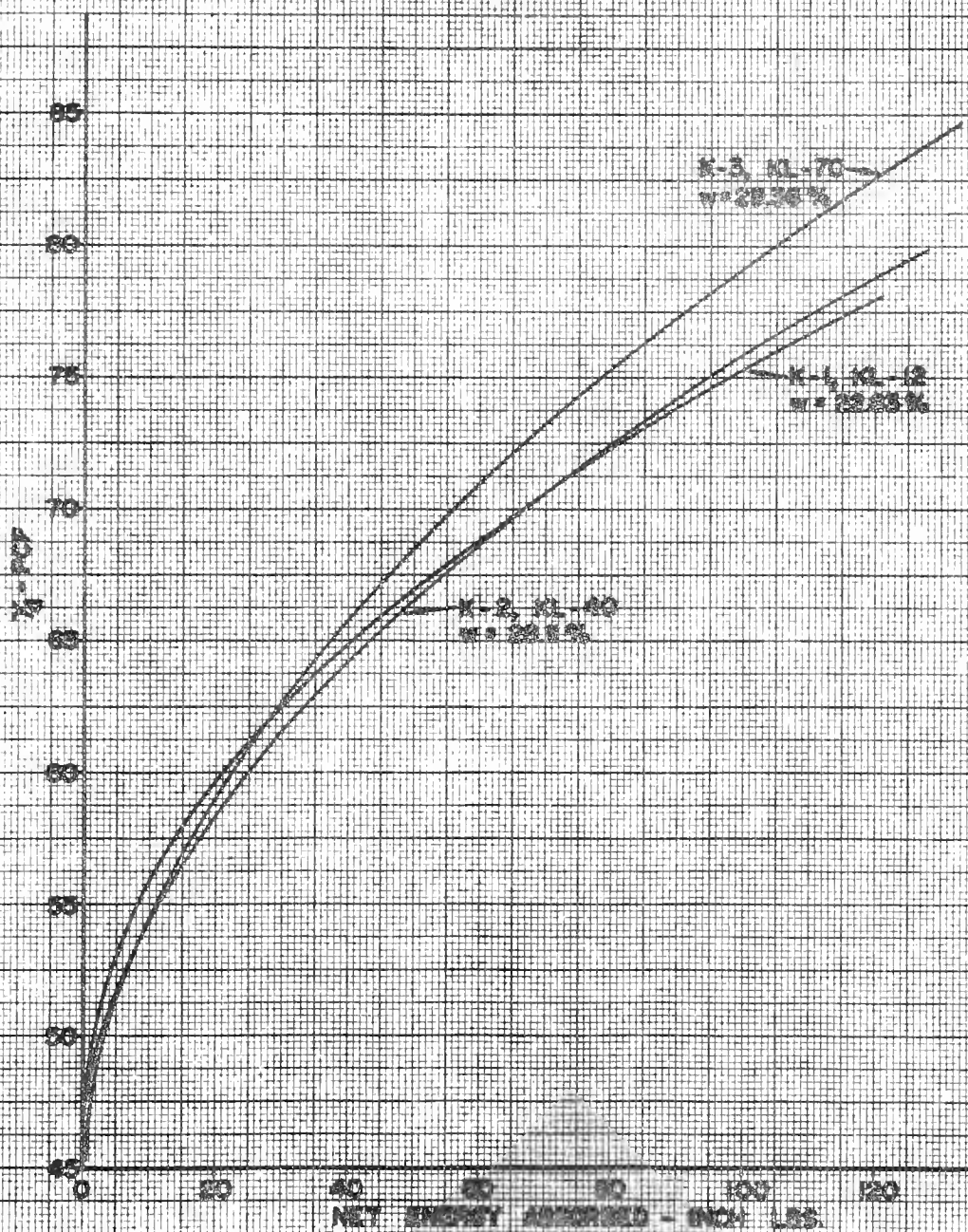


FIGURE D2.EFFECT OF MOISTURE CONTENT ON γ vs. ENERGY (PS-RIO KAOLINITE; 1000 LB LEVEL)

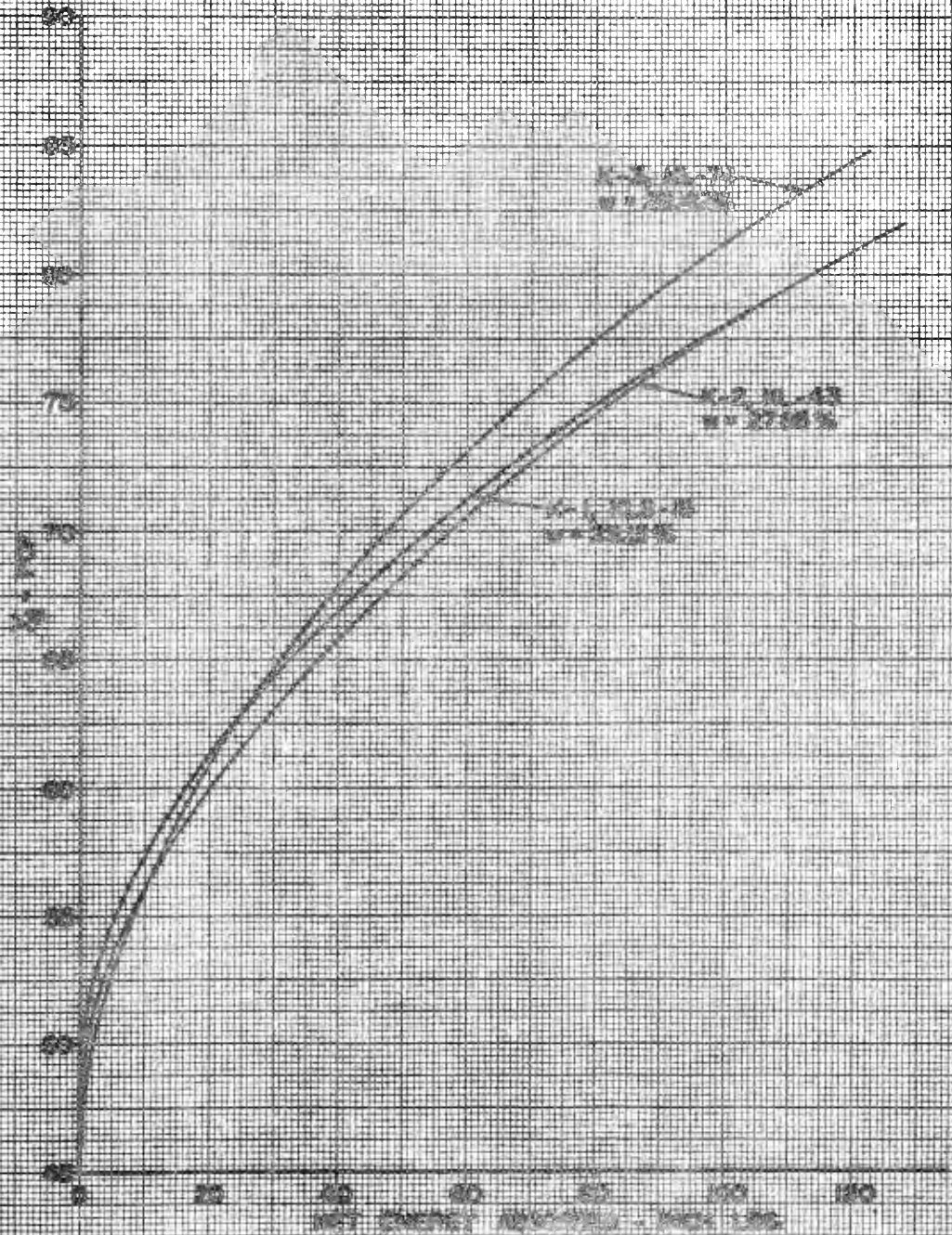


FIGURE 03 EFFECT OF MOISTURE CONTENT ON % W. ENERGY (P10-R12 KALINITE 1000 LB LEVEL)

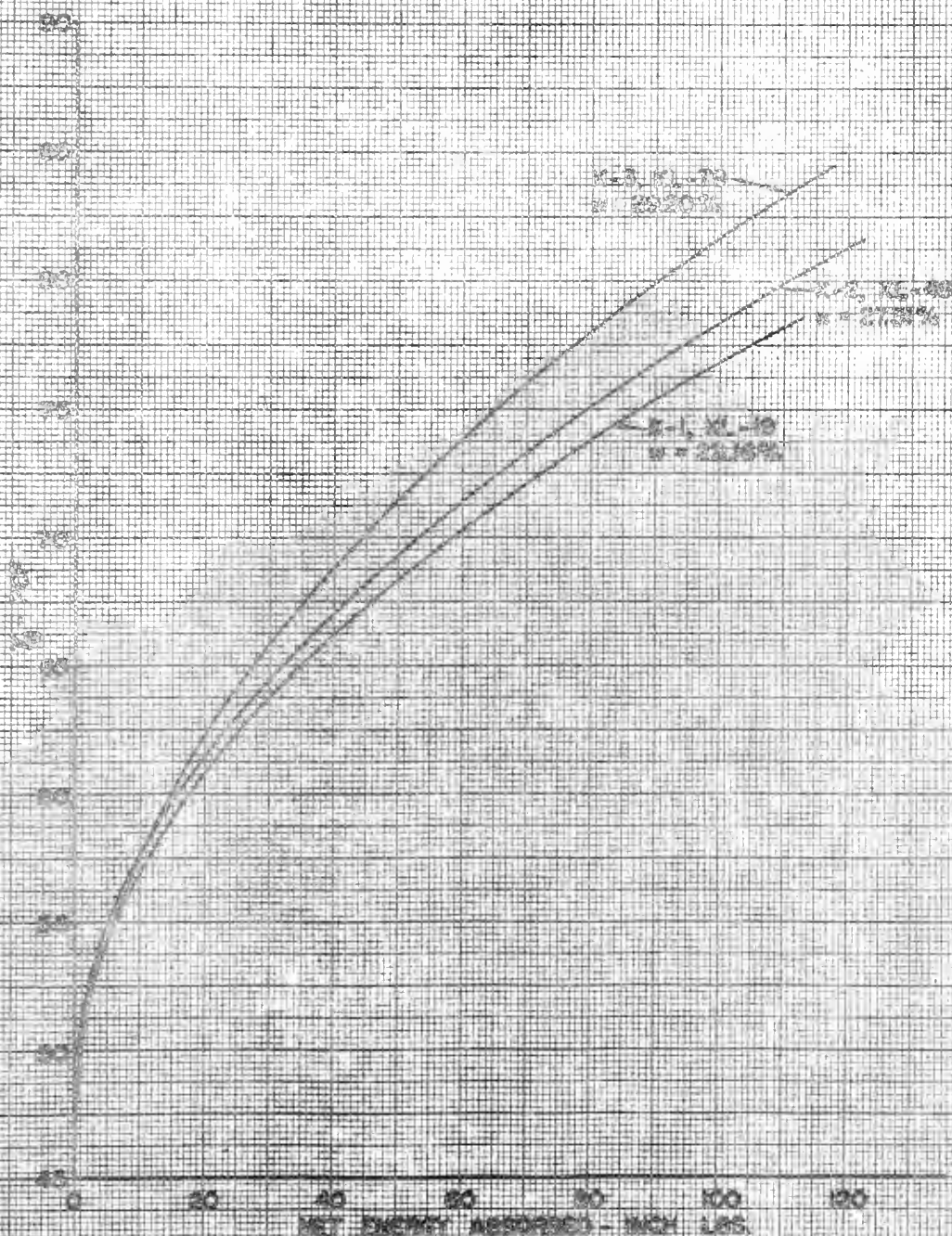


FIGURE D4 EFFECT OF MOISTURE CONTENT ON \bar{X} VS. ENERGY (P12-P25) (MOLARITE 1000 LB LEVEL)

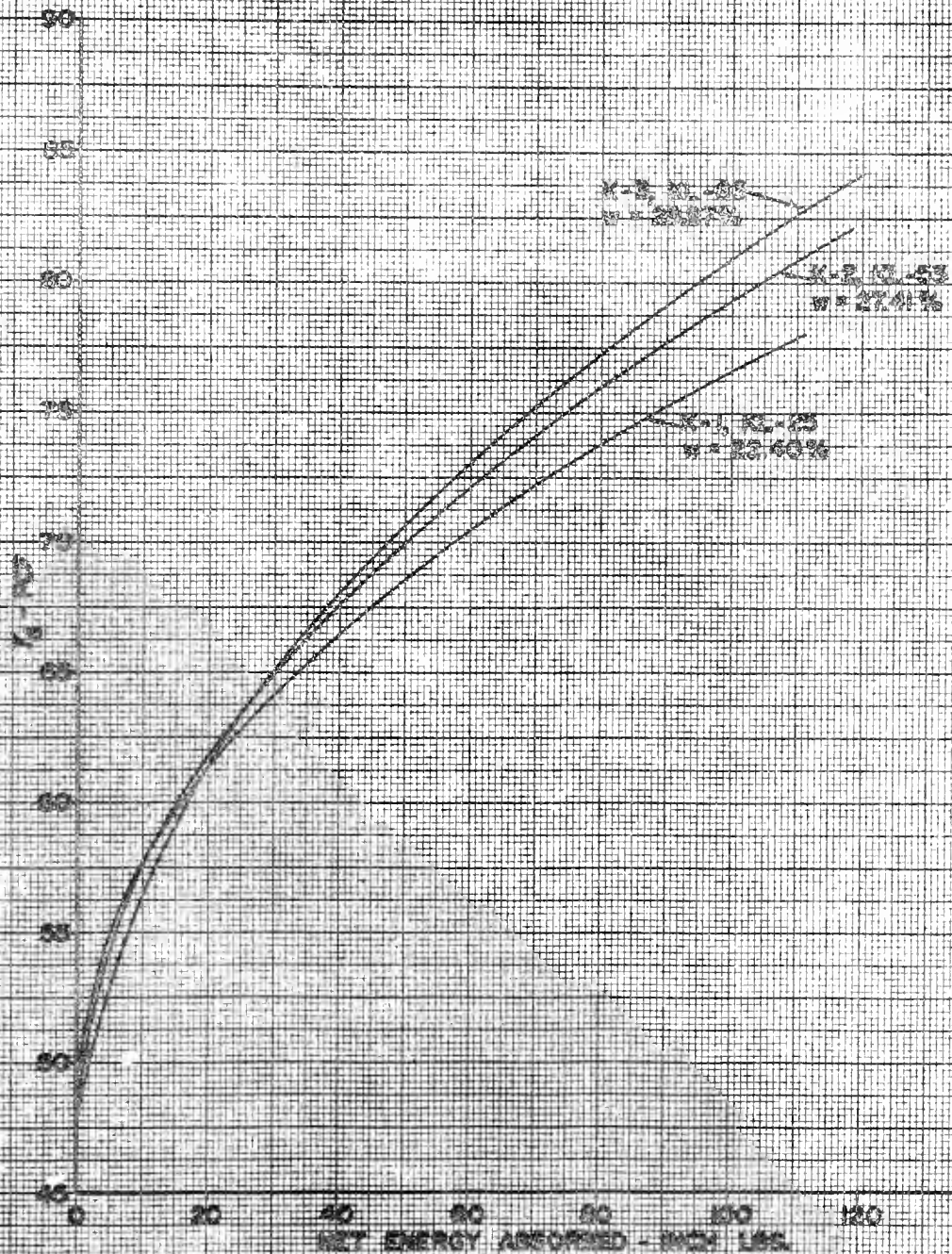


FIGURE D5 EFFECT OF MOISTURE CONTENT ON Z, VS. ENERGY (P20-P40 KAOLIN; 1000 LB LEVEL)

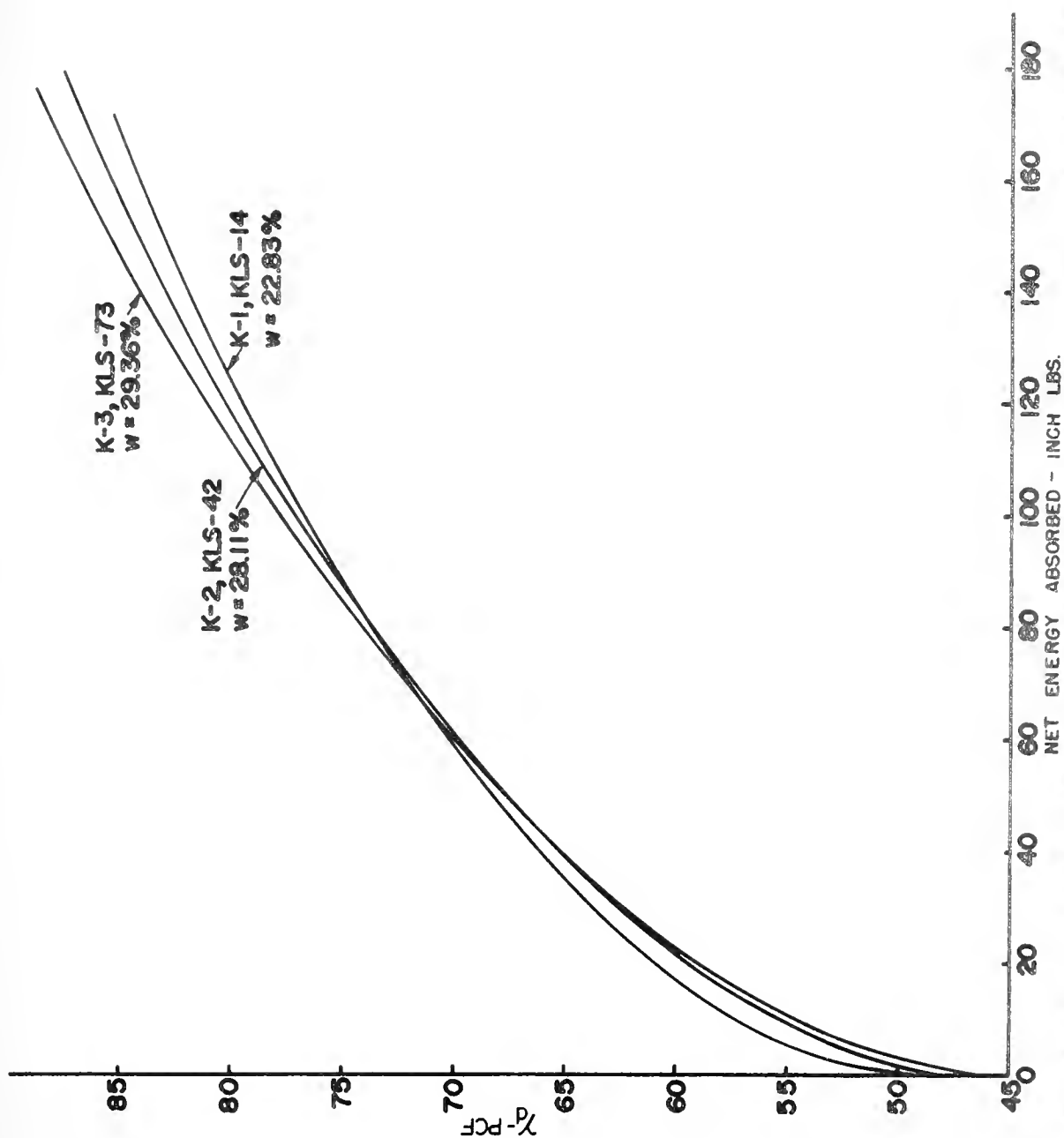


FIGURE D6. EFFECT OF MOISTURE CONTENT ON NET ENERGY ABSORBED - INCH LBS. vs. ENERGY (PB-RIO KAOLINITE; 1500 LB LEVEL)

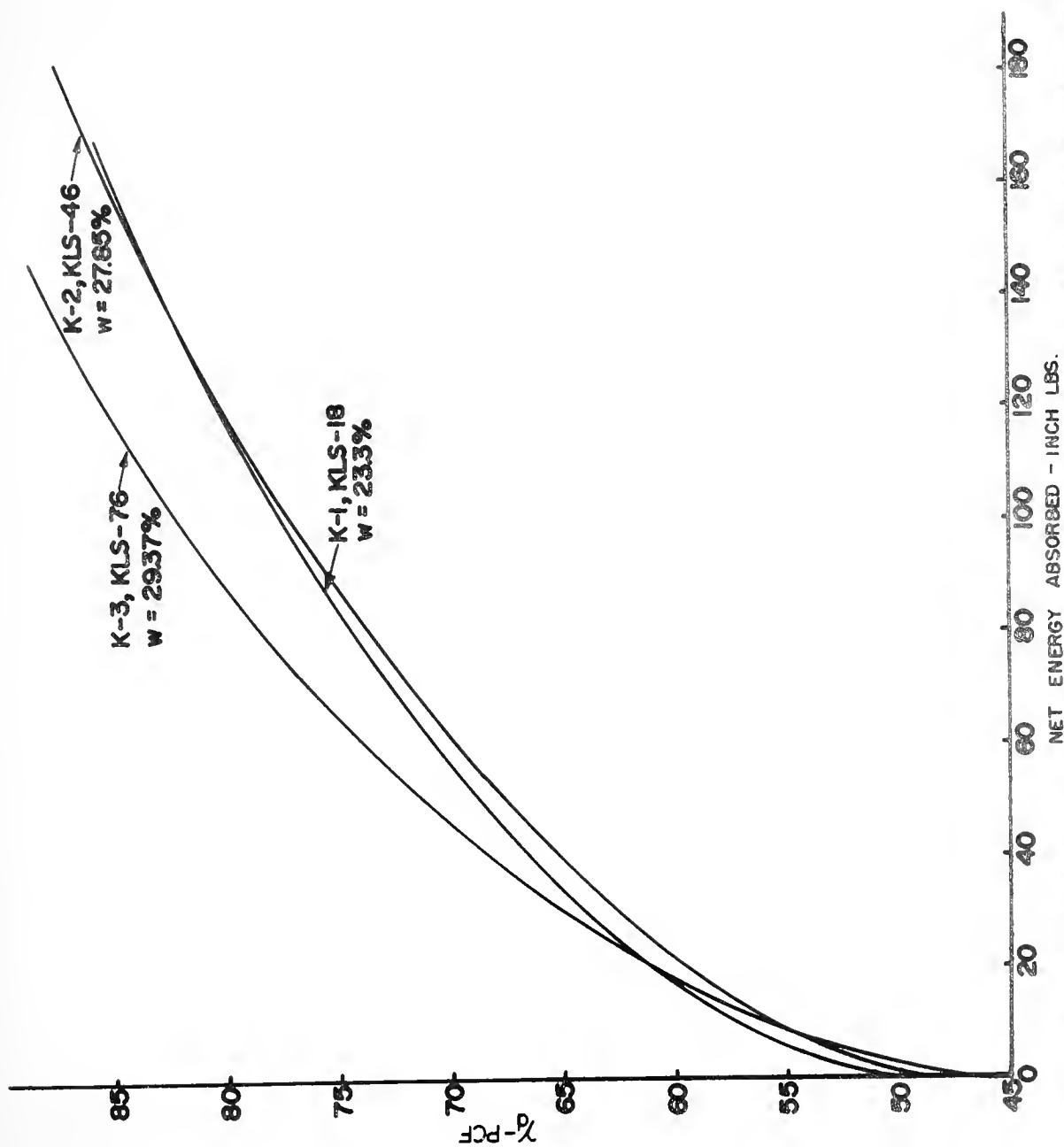


FIGURE D7. EFFECT OF MOISTURE CONTENT ON γ_{PCF} vs. ENERGY (P10-R12 KAOLINITE; 1500 LB LEVEL)

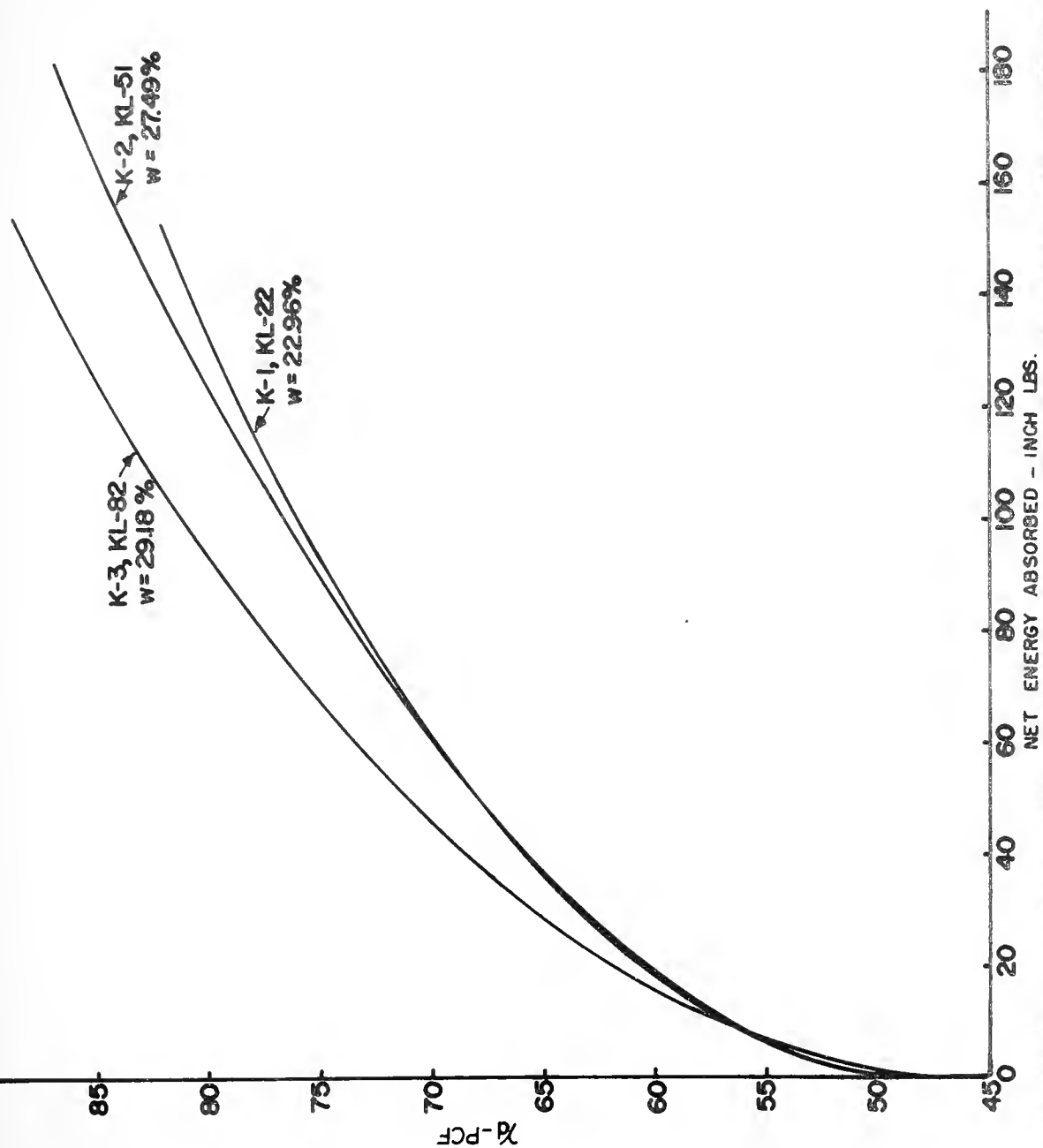


FIGURE D8. EFFECT OF MOISTURE CONTENT ON χ_d vs. ENERGY (P12-R20 KAOLINITE; 1500 LB LEVEL)

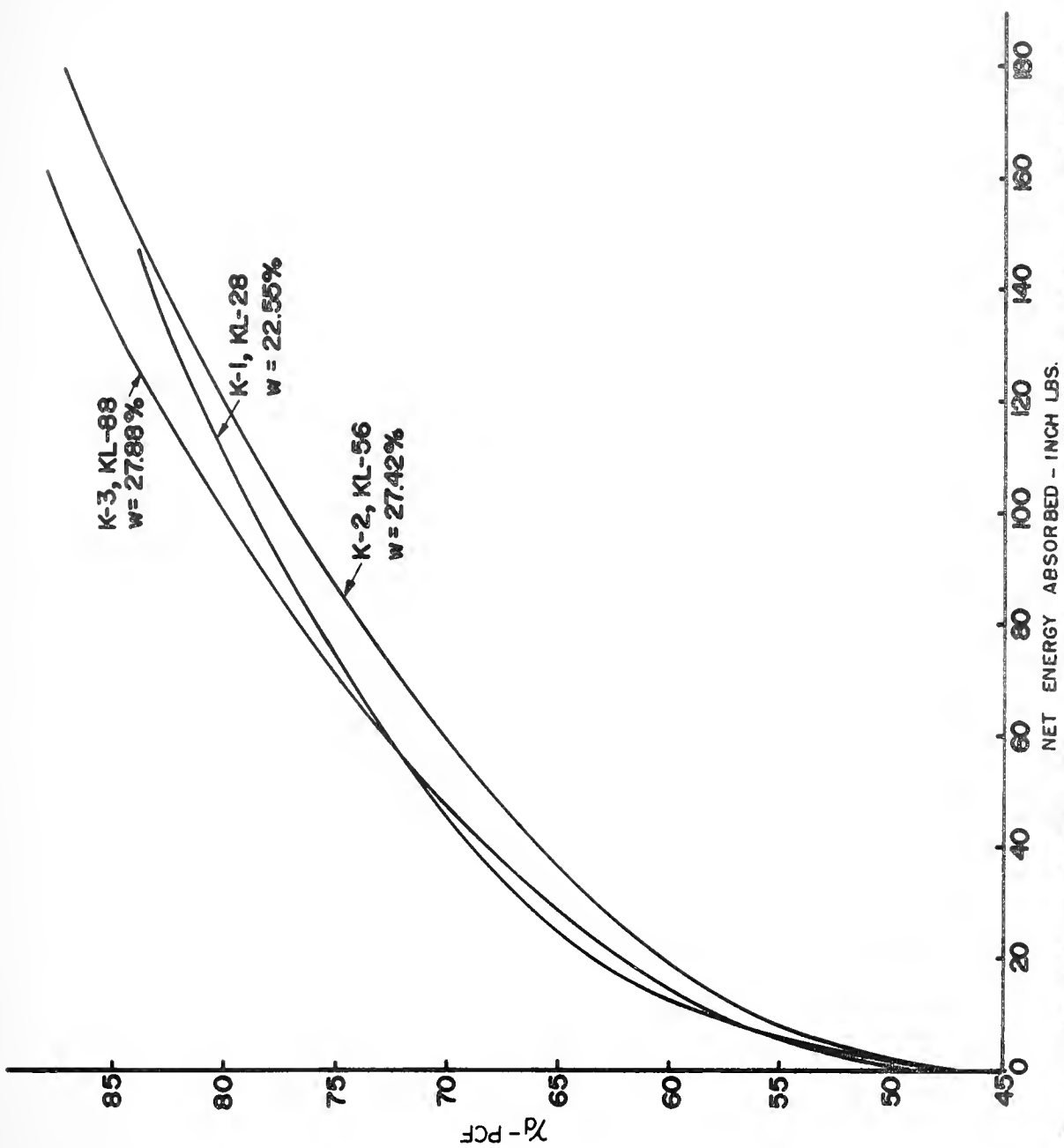


FIGURE D9 EFFECT OF MOISTURE CONTENT ON γ_d vs. ENERGY (P20-R40 KAOLINITE; 1500 LB LEVEL)

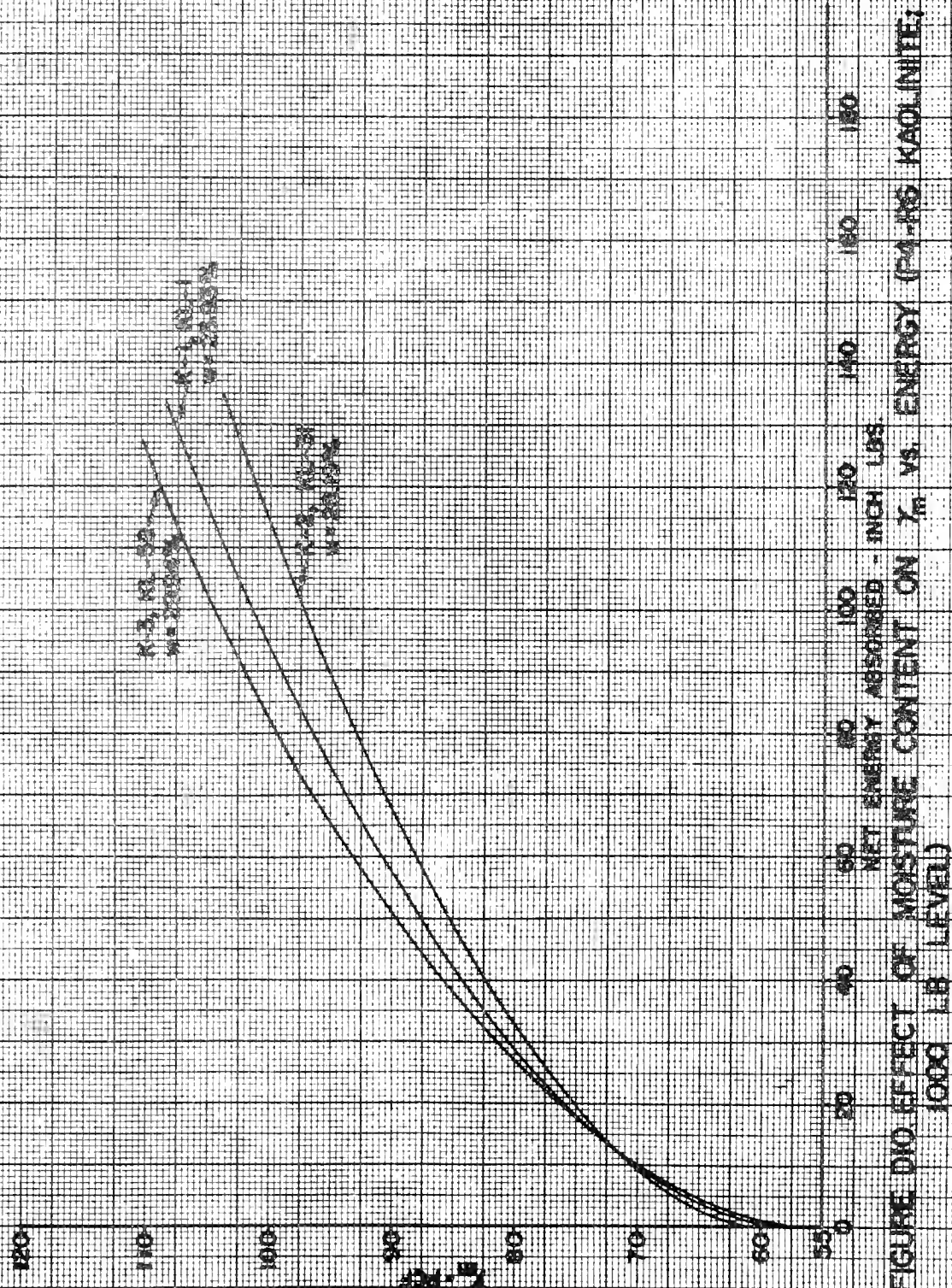


FIGURE D10 EFFECT OF MOISTURE CONTENT ON χ_m VS. ENERGY (P4-R6 KAOLINITE; 1000 LB LEVEL)

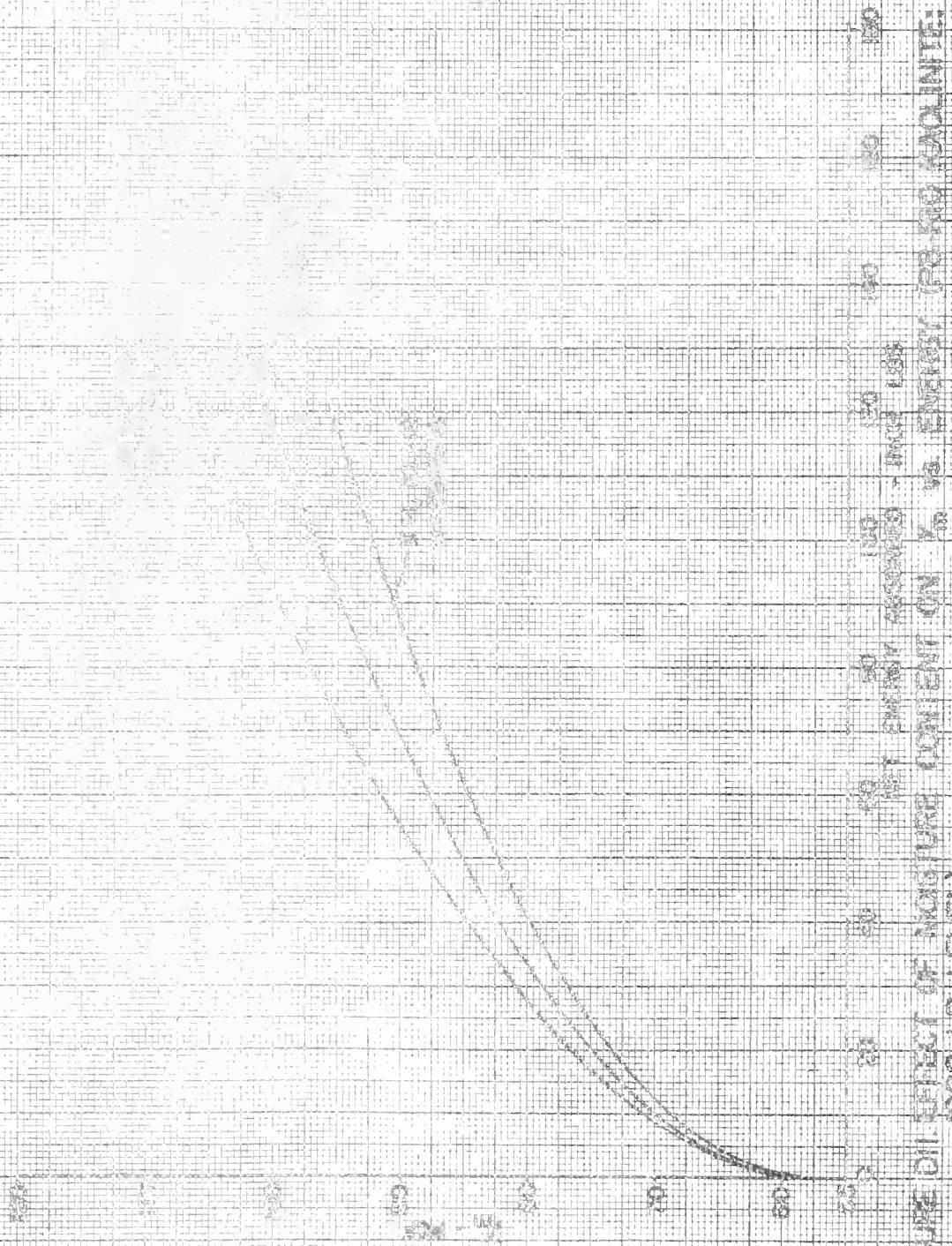


FIGURE DII EFFECT OF MOISTURE CONTENT ON Y_m vs. ENERGY (PB-800 MOISTURE, 1000 LB LEVEL)

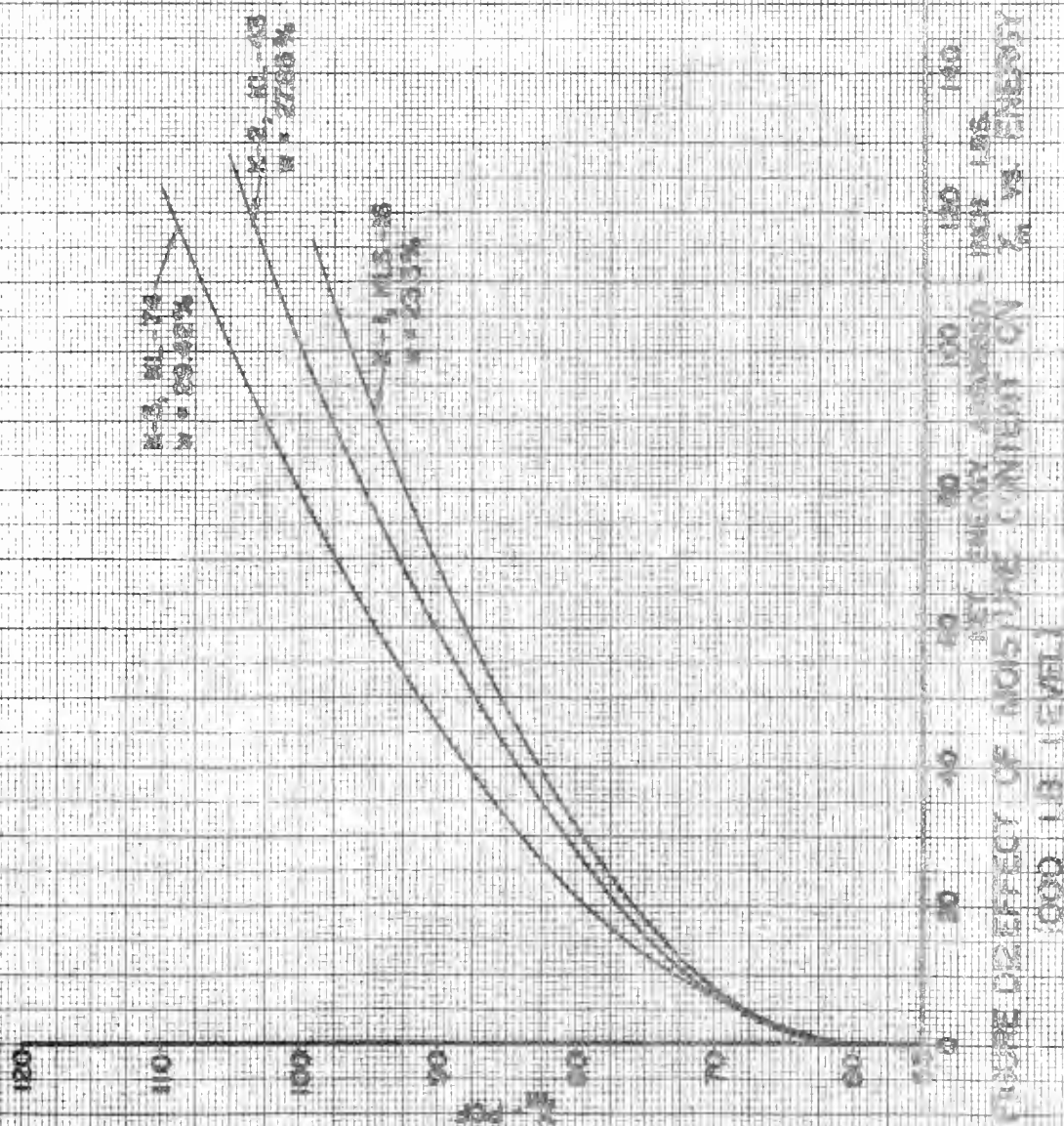


FIGURE 12. EFFECT OF MOISTURE CONTENT ON E_m VS. ENERGY (P.D. 12.2) (WELL)

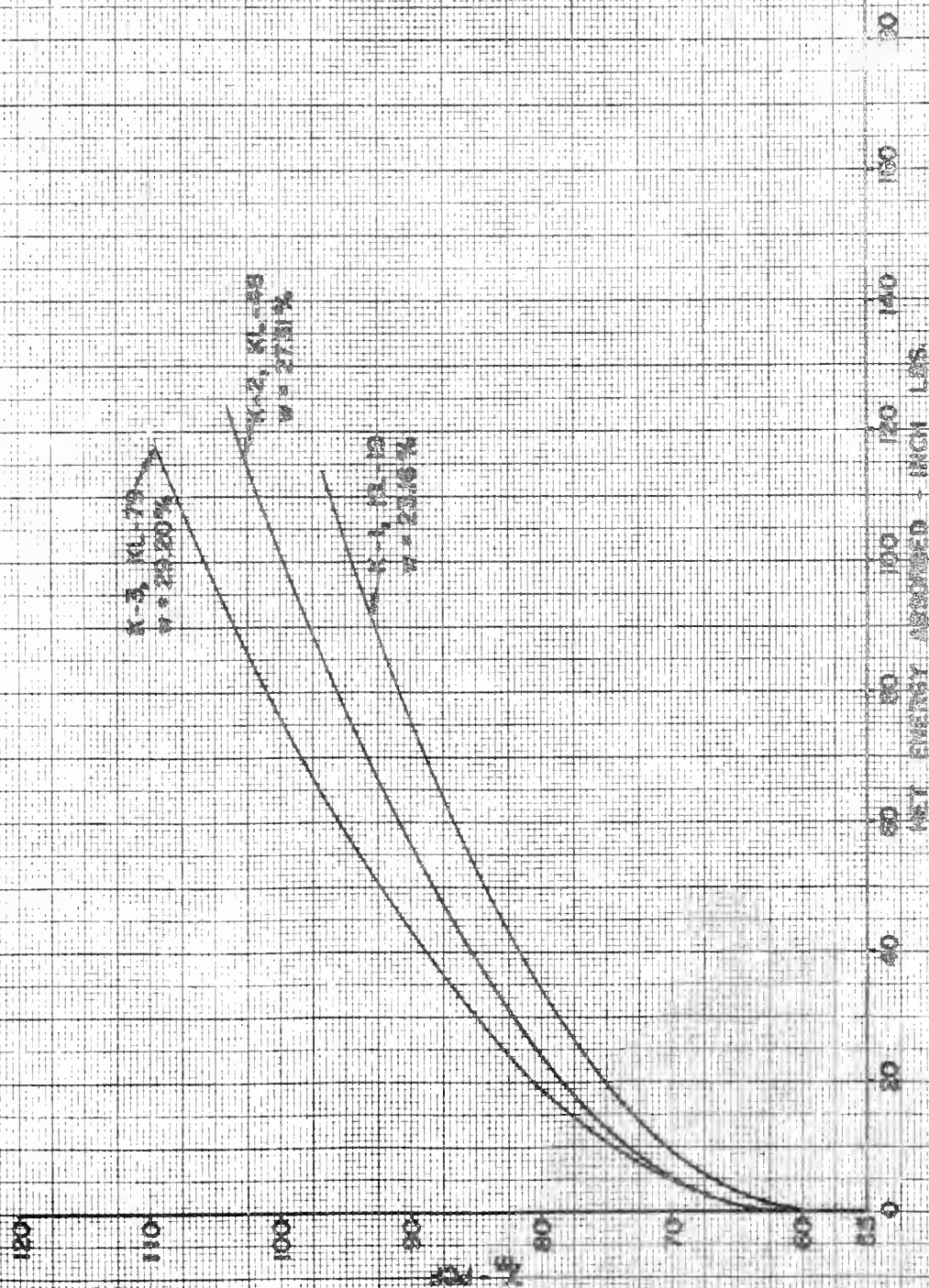


FIGURE D3 EFFECT OF MOISTURE CONTENT ON X_0 VS. ENERGY (P12-R20 KAOLINITE)
1000 LB. LEVEL)

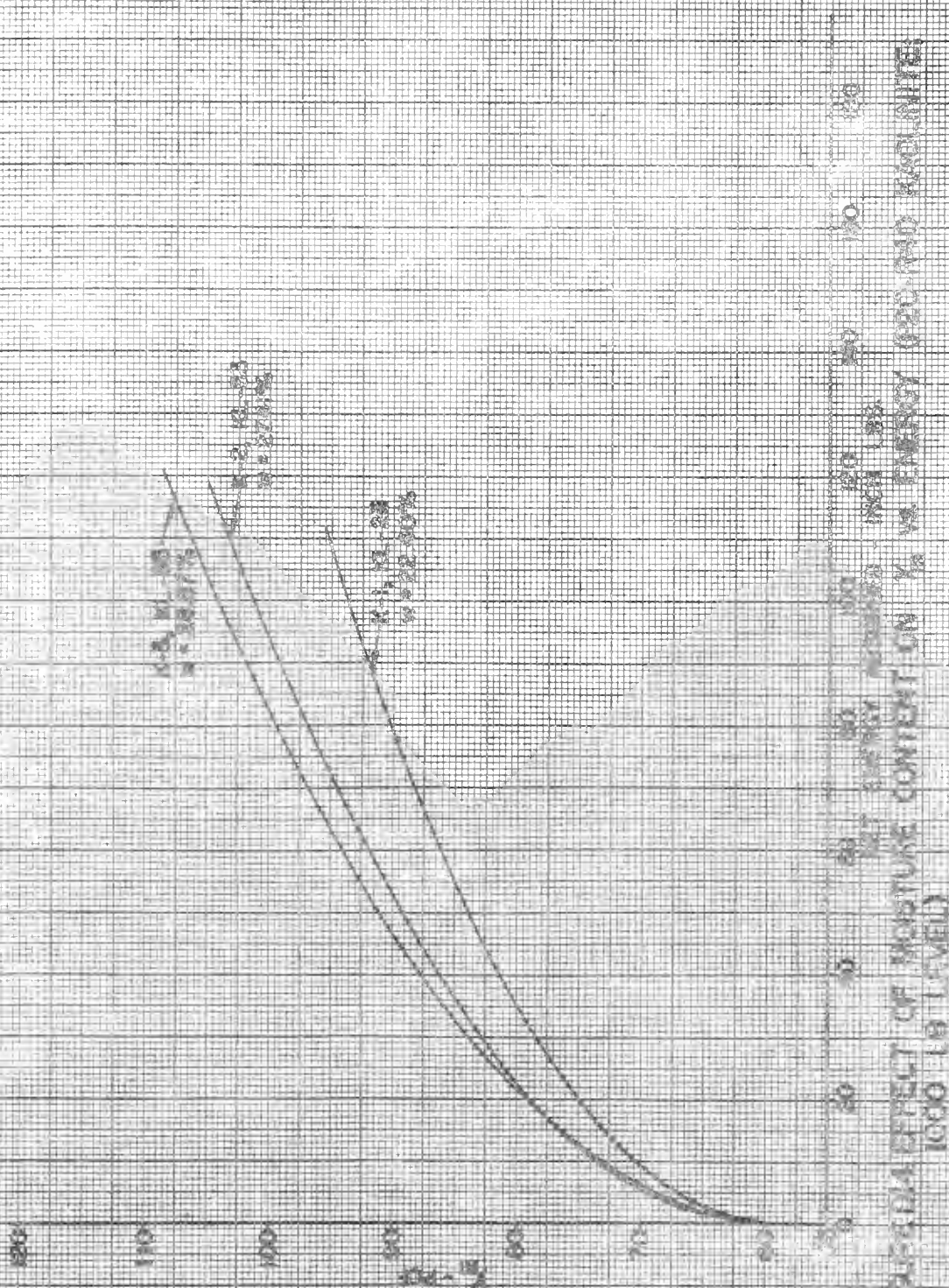


FIGURE 11. EFFECT OF MOISTURE CONTENT ON PERCENT ENERGY ABSORBED FOR DIFFERENT MOISTURE RATIOS

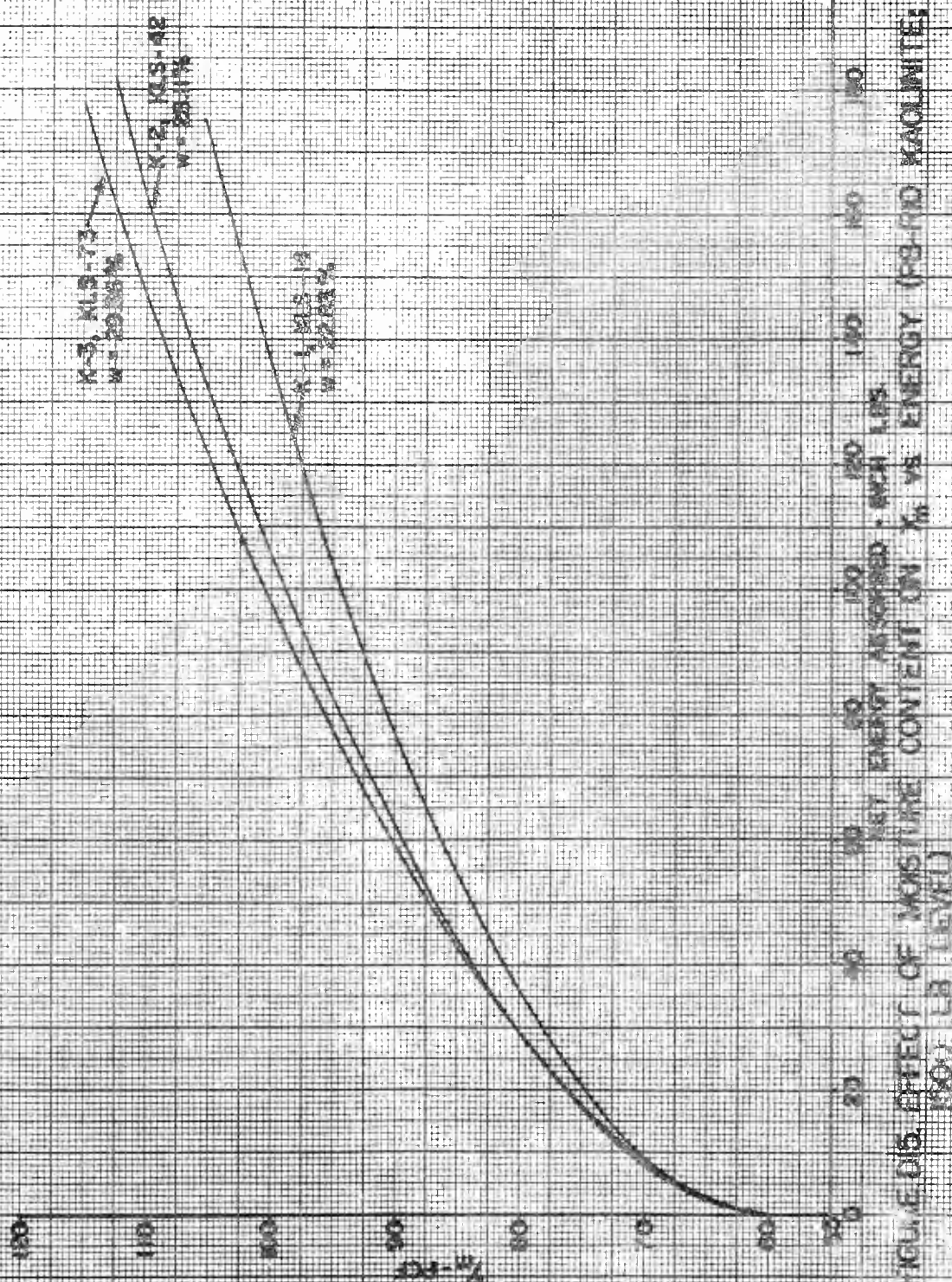


FIGURE 115. EFFECT OF MOISTURE CONTENT ON X_m VS ENERGY (PS-RD KAOLINITE); (PS-RD) LB LEVEL

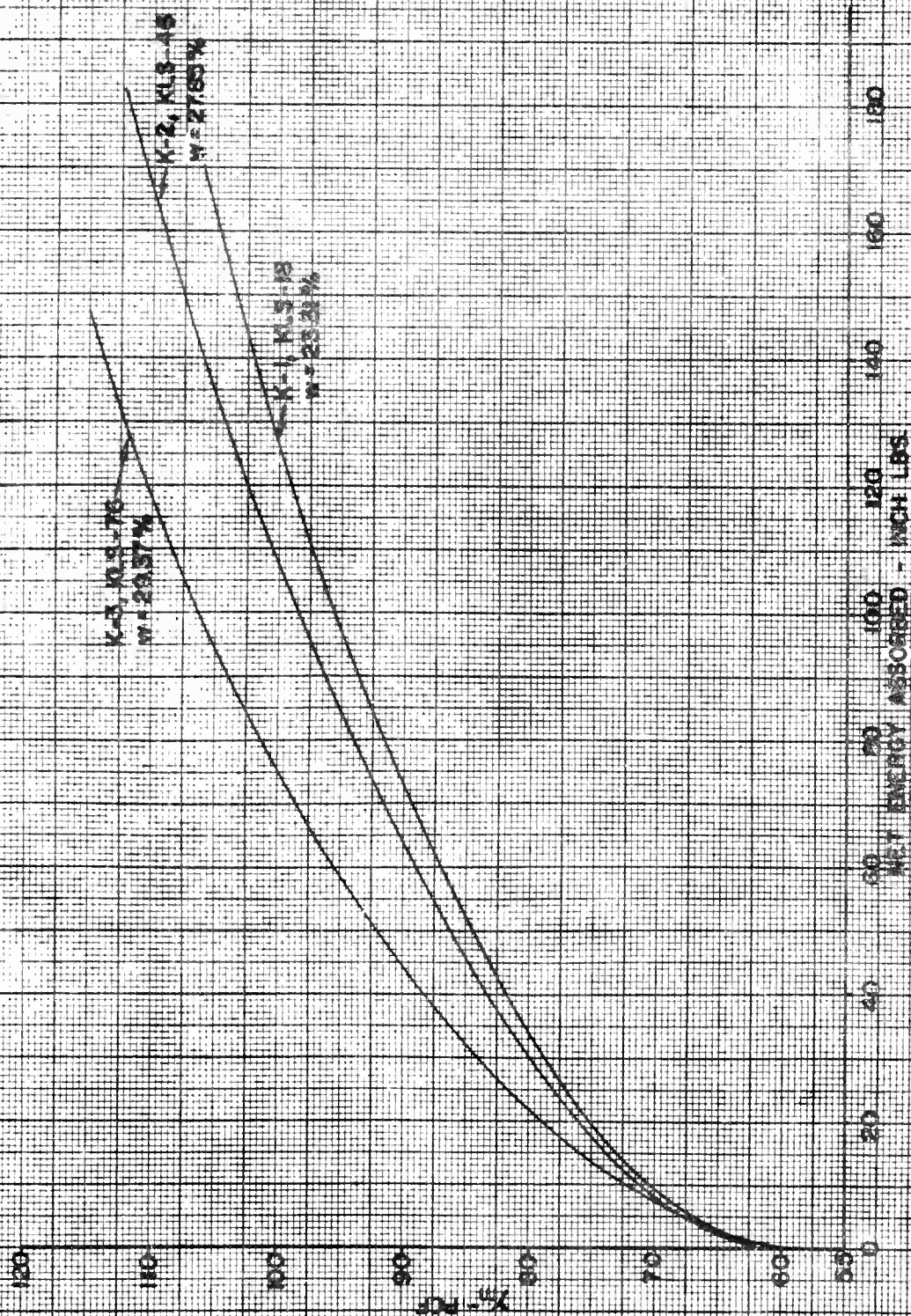
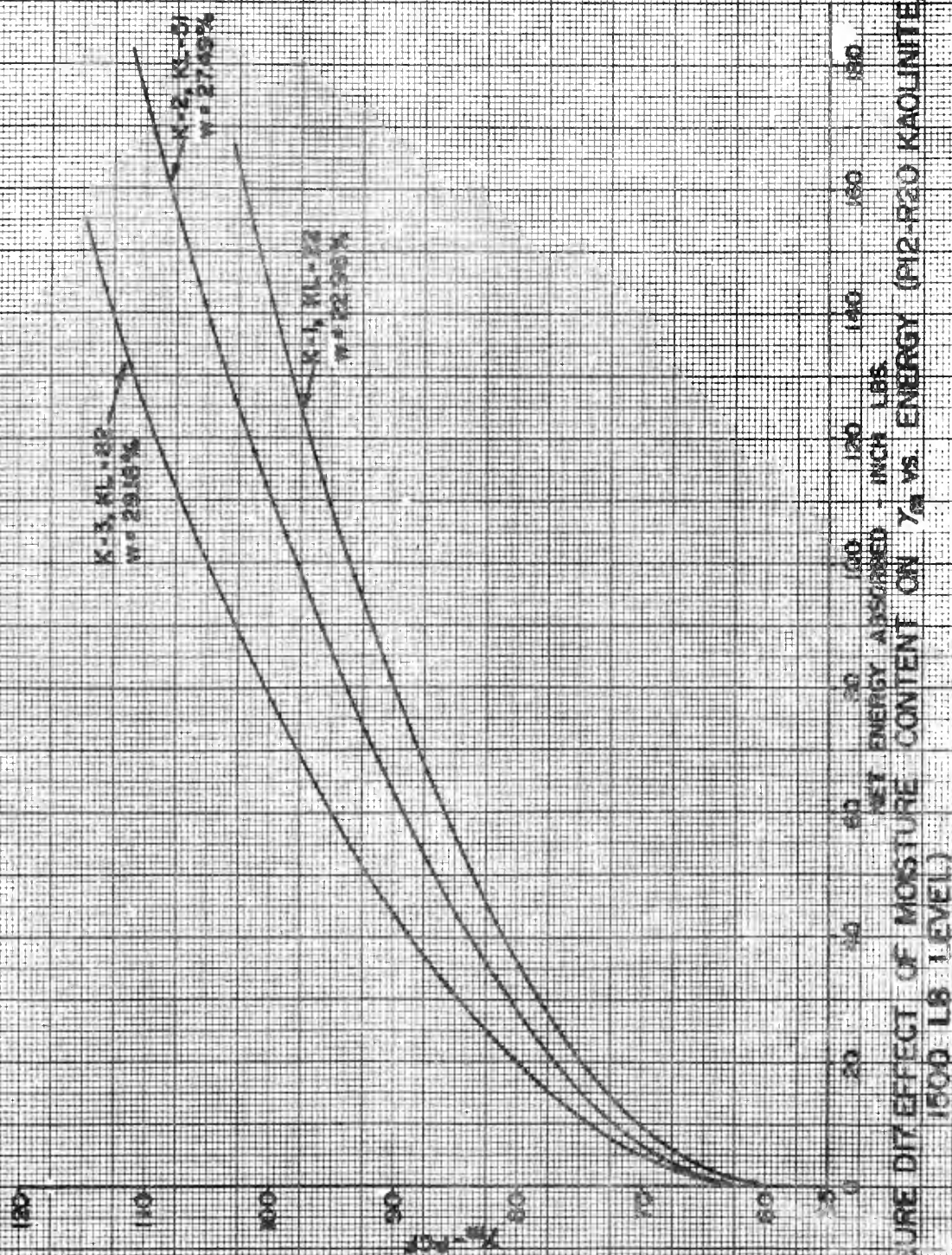


FIGURE D16. EFFECT OF MOISTURE CONTENT ON γ_m VS. ENERGY (PIO-R12 KAOLINITE; 1500 LB LEVEL)



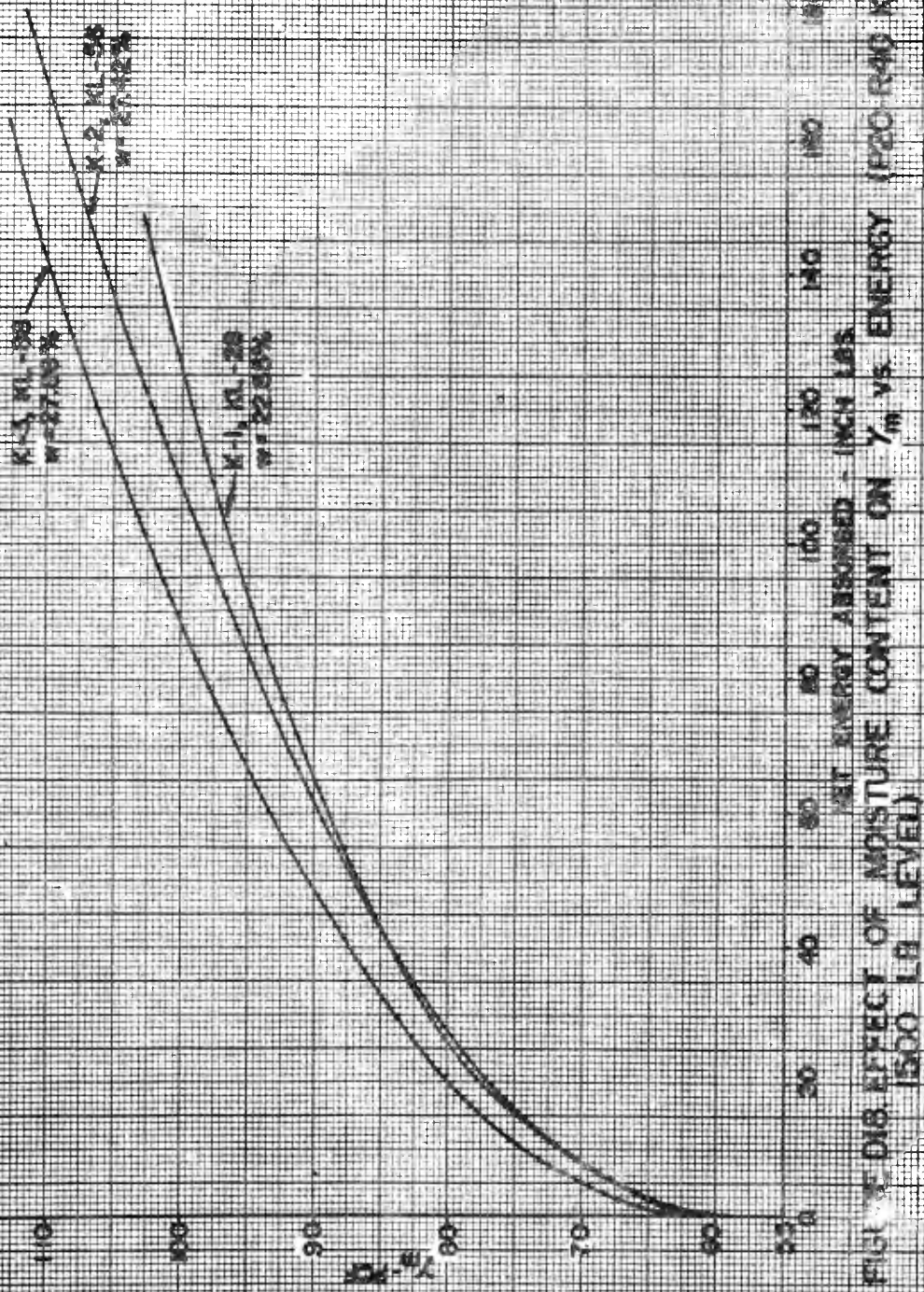


FIGURE D18. EFFECT OF MOISTURE CONTENT ON γ_m VS. ENERGY (F20 R-40 KAOLINITE) 1500 LB. LEVEL

Appendix E

Explanation of Wald-Wolfowitz Run Test

Two samples, X_1, \dots, X_{n_1} and X'_1, \dots, X'_{n_2} , from two populations with continuous cumulative distribution functions $F_1(X)$ and $F_2(X)$, respectively, are tested against the hypothesis that $F_1(X) = F_2(X)$. To test the hypothesis the samples are pooled and arranged in an ascending (or descending) order of magnitude. This arrangement is then coded by assigning a descriptor, 1 or 2, 2 or 3, etc., according to whether we encounter an X or X' . The sequence might look like

1112122211222

A cluster of one or more ones or one or more twos is designated as u and is called a run. The example above exhibits six runs.

The mean of u is defined as

$$E(u) = \frac{2n_1n_2}{n_1+n_2} + 1$$

and the variance of u is defined as

$$\text{Var}(u) = \frac{2n_1n_2(2n_1n_2 - n_1 - n_2)}{(n_1+n_2)^2(n_1+n_2-1)}$$

where n_1 and n_2 are the number of observations from populations $F_1(X) = F_2(X)$ respectively.

The hypothesis ($F_1(X) = F_2(X)$) is rejected when

$$\left| u - E(u) \right| \geq (\text{Var}(u))^{1/2} (2.576) \quad *$$

* Rejection at the 1% level of significance.

In the analysis reported here only two combinations of n_1 and n_2 occurred, namely 18 and 18, and 18 and 16.

$$\begin{aligned} \text{when } n_1 = 18 \text{ and } n_2 = 18 \quad & E(u) = 19.00 \\ & \text{Var}(u) = 8.74 \\ & \sqrt{\text{Var}(u)} = 2.95 \end{aligned}$$

Therefore, reject the hypothesis that $F_1(X) = F_2(X)$ at the 1% level if

$$|u - 19.00| \geq 7.60$$

$$\begin{aligned} \text{when } n_1 = 18 \text{ and } n_2 = 16 \quad & E(u) = 17.94 \\ & \text{Var}(u) = 8.18 \\ & \sqrt{\text{Var}(u)} = 2.86 \end{aligned}$$

Therefore, reject at the 1% level if

$$|u - 17.94| \geq 7.37$$

Occasionally ties will occur when the samples are pooled and rearranged. That is, the same numerical value will appear in both samples. The usual way to reconcile this problem is by flipping a coin. This method with the following convention was used in this analysis.

X_i and X'_i have the same numerical value.

flip a coin: heads $\longrightarrow X_i, X'_i$

 tails $\longrightarrow X'_i, X_i$

The detailed results of the run test are given below in Table E1. For brevity the "code" identifies population pairs from Table 9.

Table E1. Detailed Results of Wald-Wolfowitz Run Test

<u>Code</u>	<u>n₁</u>	<u>n₂</u>	<u>u, runs</u>	<u>u - E(u)</u>	<u>Result</u>
1	18	18	6	13	Reject
2	18	18	14	5	Cannot Reject
3	18	18	4	15	Reject
4	18	18	2	17	Reject
5	18	18	4	15	Reject
6	18	18	2	17	Reject
7	18	18	6	13	Reject
8	18	18	19	0	Cannot Reject
9	18	18	6	13	Reject
10	18	18	12	7	Cannot Reject
11	18	18	16	3	Cannot Reject
12	18	18	15	4	Cannot Reject
13	16	18	14	3.94	Cannot Reject
14	18	18	10	9	Reject
15	16	18	2	17	Reject
16	18	18	10	9	Reject
17	18	18	2	17	Reject
18	18	18	2	17	Reject
19	18	18	2	17	Reject
20	18	18	14	5	Cannot Reject
21	18	18	14	5	Cannot Reject
22	18	16	4	13.94	Reject
23	18	18	15	4	Cannot Reject
24	18	18	26	7	Cannot Reject
25	18	18	12	7	Cannot Reject
26	18	18	14	5	Cannot Reject
27	18	18	4	15	Reject
28	18	18	10	9	Reject
29	18	18	8	11	Reject
30	18	18	2	17	Reject
31	18	18	7	12	Reject
32	18	18	6	13	Reject
33	18	18	4	15	Reject
34	18	18	6	11	Reject
35	18	18	14	5	Cannot Reject
36	18	18	10	9	Reject

Table El. (continued)

37	18	16	8	9.94	Reject
38	16	18	10	7.94	Reject
39	18	18	2	17	Reject
40	18	18	2	17	Reject
41	18	18	8	11	Reject
42	18	18	2	17	Reject
43	18	18	2	17	Reject
44	18	18	4	15	Reject
45	18	18	2	17	Reject

Appendix FAdditional Moisture Content-Unit Weight Relations

The figures in Appendix F show the conventional and equal net input moisture-unit weight relations at the 1000 lb level.

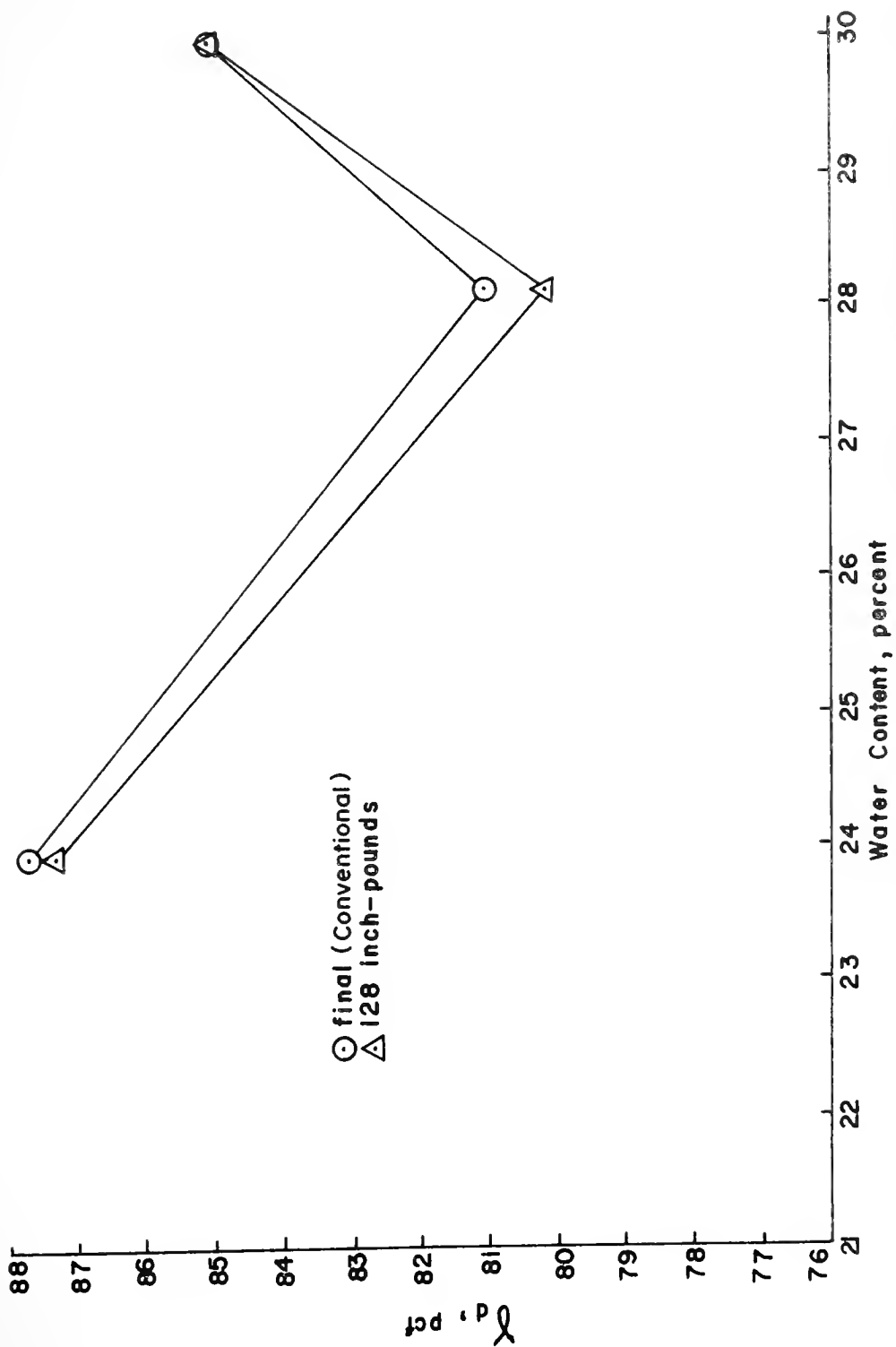


FIGURE F1. CONVENTIONAL AND EQUAL NET INPUT MOISTURE-UNIT WEIGHT RELATIONS (P4-R6;1000 LB LEVEL)

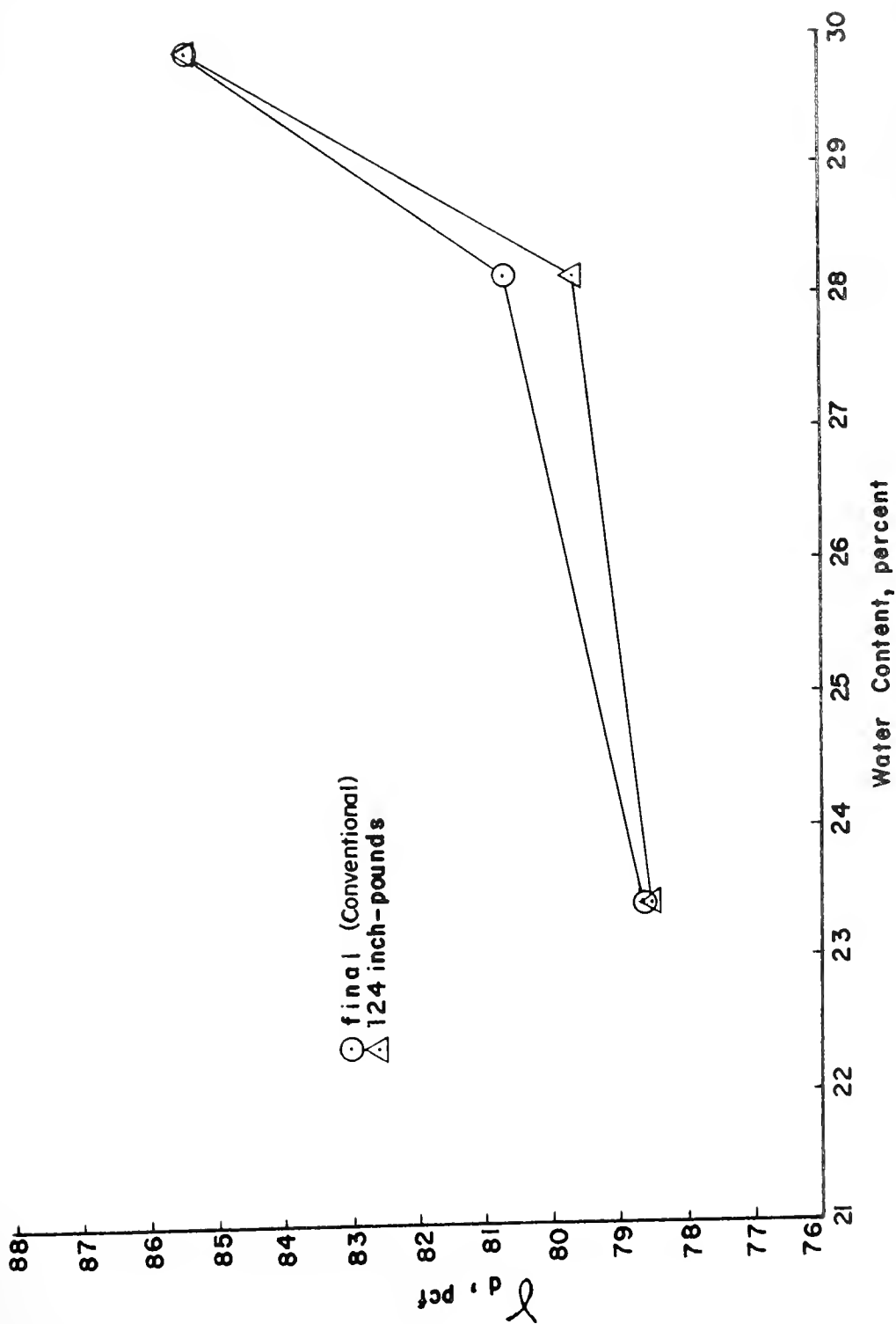


FIGURE F2. CONVENTIONAL AND EQUAL NET INPUT MOISTURE-UNIT WEIGHT RELATIONS (P6-R8; 1000 LB LEVEL)

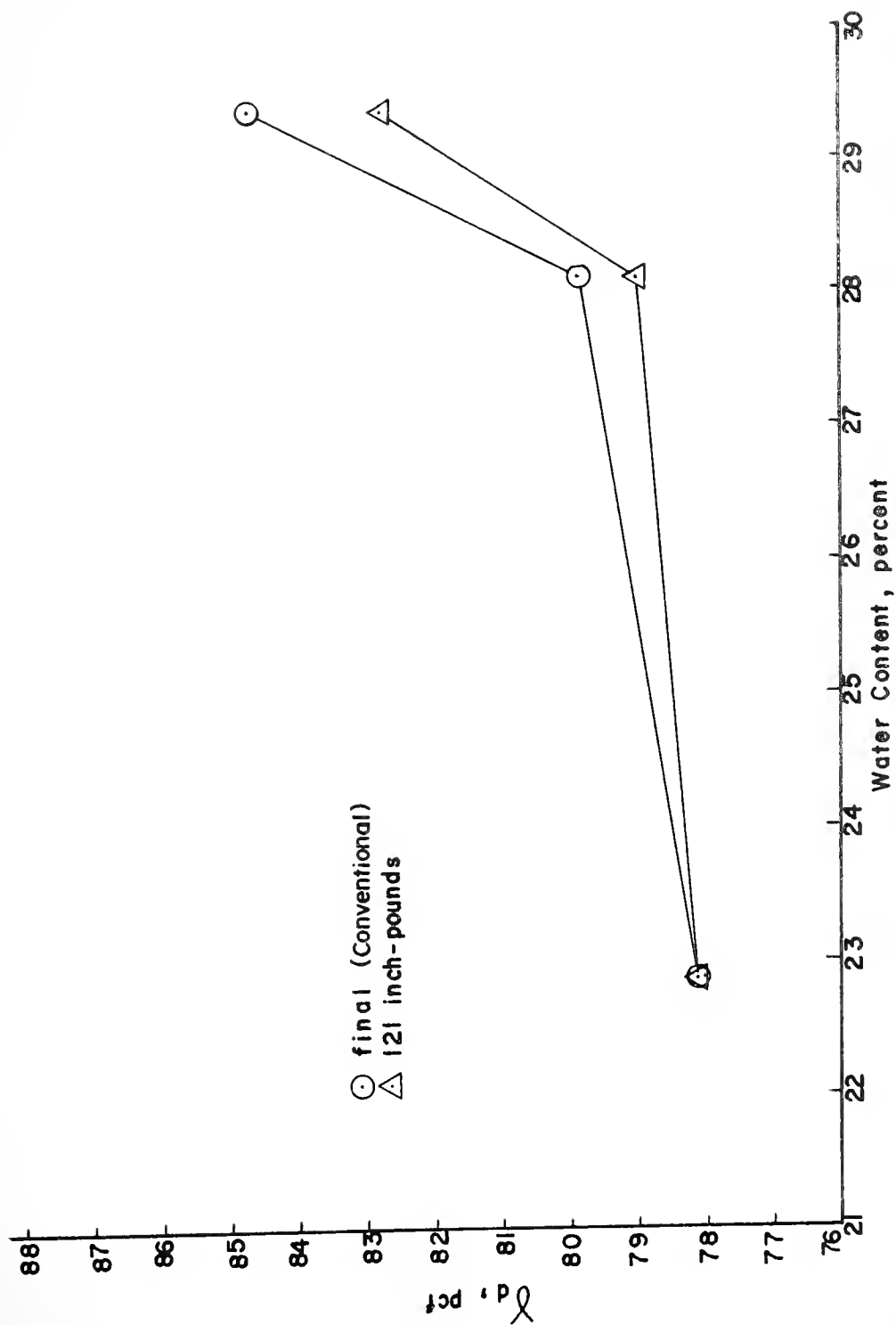


FIGURE F3. CONVENTIONAL AND EQUAL NET INPUT MOISTURE-UNIT WEIGHT RELATIONS (P8-RIO; 1000 LB LEVEL)

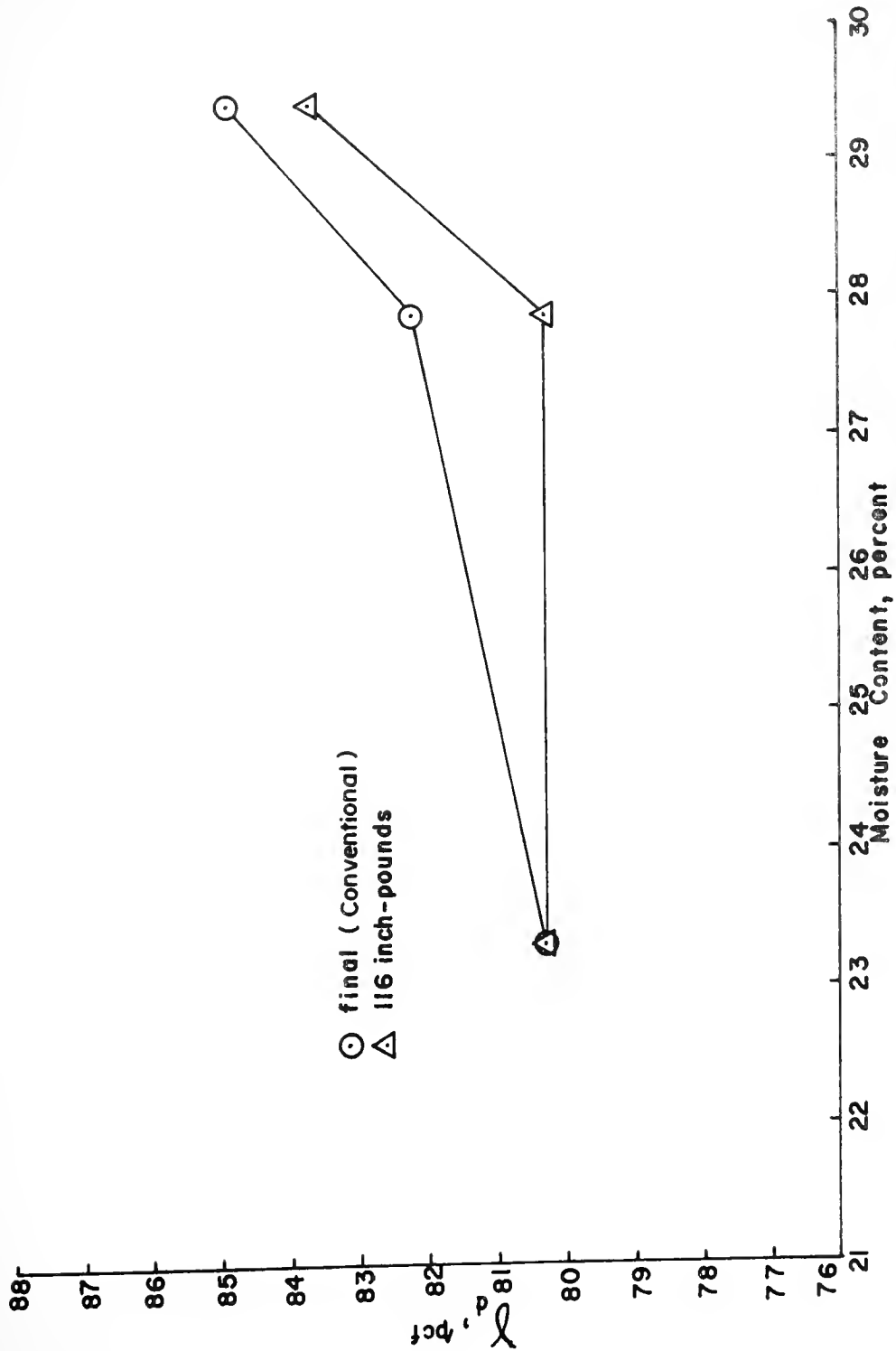


FIGURE F4. CONVENTIONAL AND EQUAL NET INPUT MOISTURE-UNIT WEIGHT RELATIONS (PIO-R12; 1000 LB LEVEL)

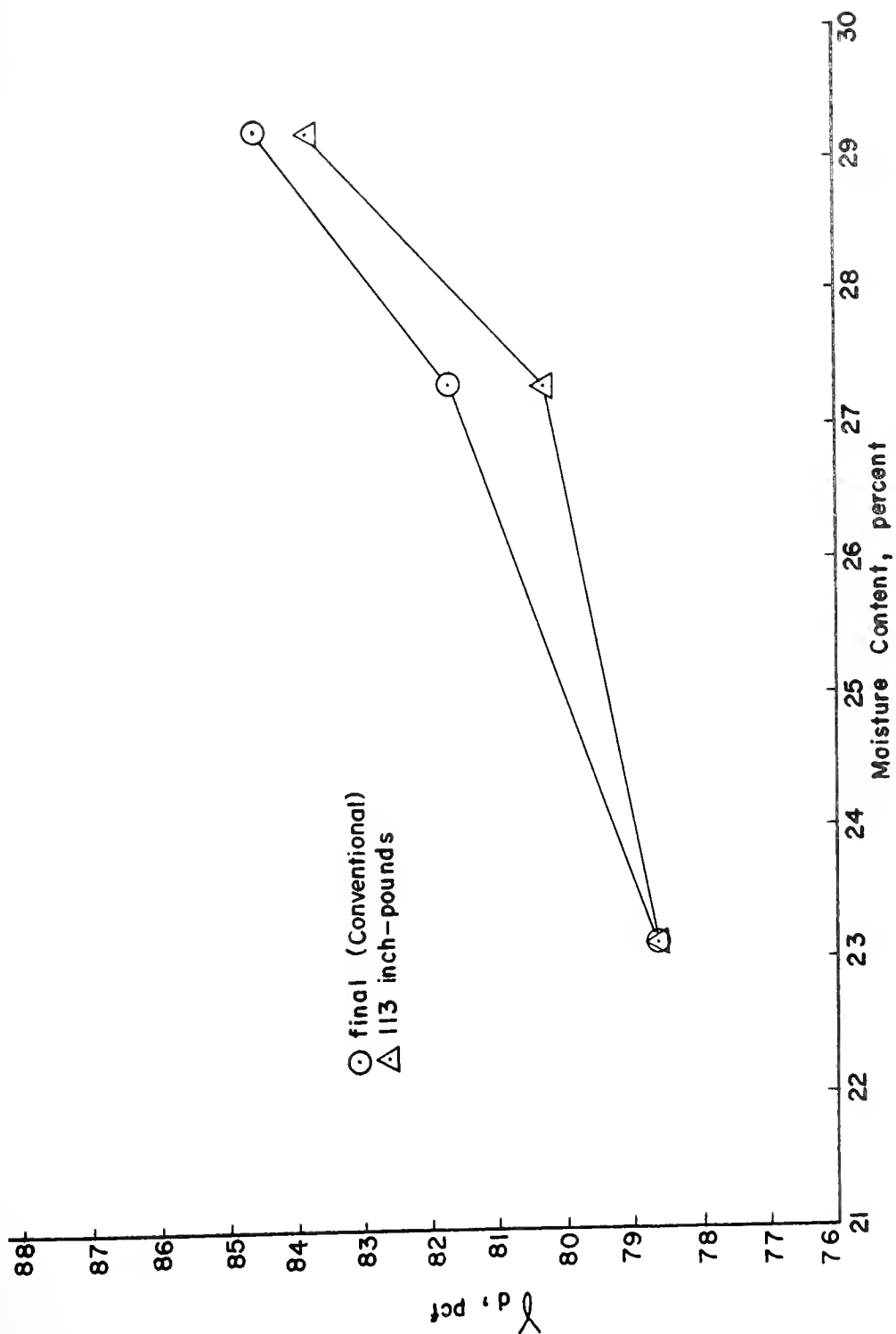


FIGURE F5 CONVENTIONAL AND EQUAL NET INPUT MOISTURE-UNIT WEIGHT RELATIONS (PI2-R20; 1000 LB LEVEL)

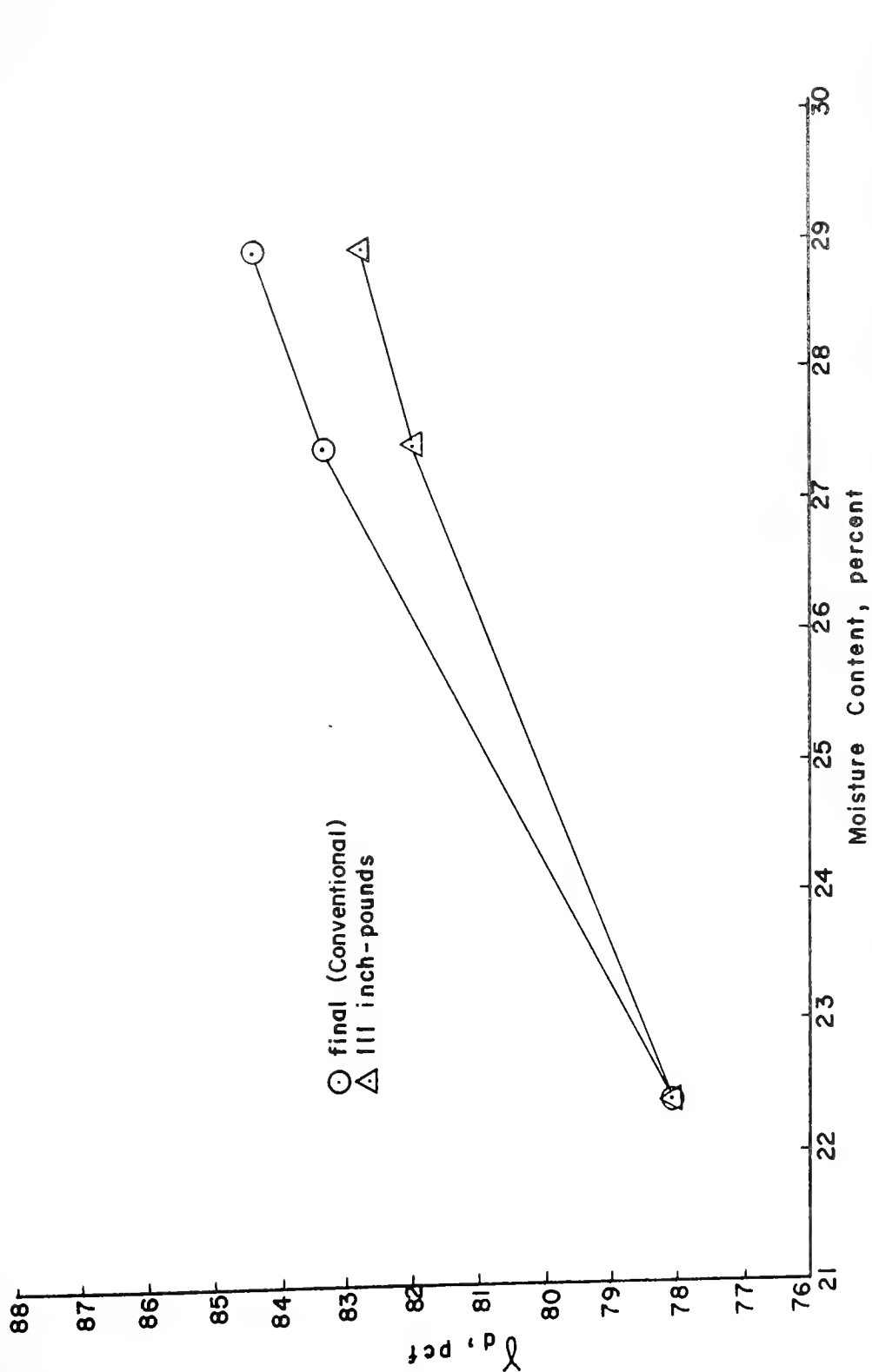


FIGURE F6. CONVENTIONAL AND EQUAL NET INPUT MOISTURE-UNIT WEIGHT RELATIONS (P20-R40; 1000 LB LEVEL)

Appendix G

Equations for Achievement of Compacted Unit Weight

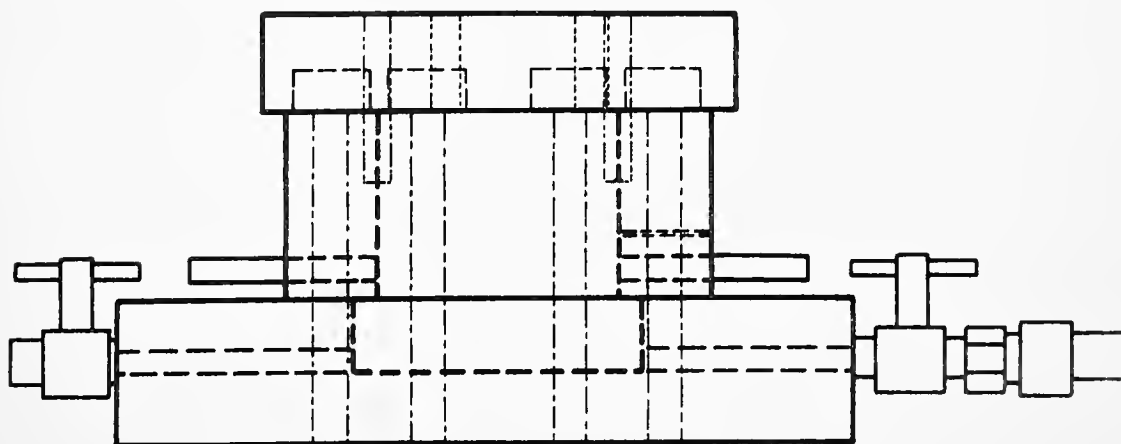
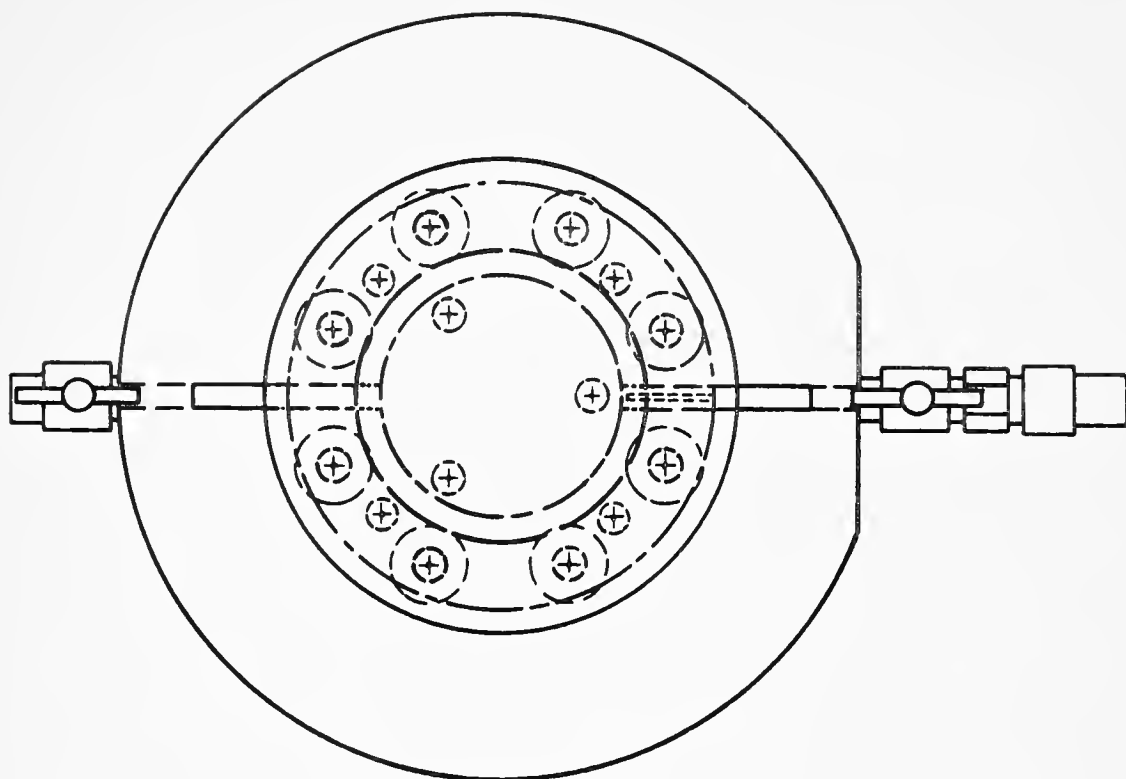
Table G1. Equations of γ_m - E net Relationship for Samples
Compacted at the 1,500 lb. Level

(γ_m is in lb./ft.³ and E is in inch-lb.)

KL-8, K-1, P6-R8	$\gamma_m = 64.68703 + 0.41086 E - 0.00112E^2$
KL-37, K-2, P6-R8	$\gamma_m = 64.45871 + 0.42488 E - 0.00102E^2$
KL-67, K-3, P6-R8	$\gamma_m = 62.45325 + 0.62912 E - 0.00186E^2$
KLS-14, K-1, P8-R10	$\gamma_m = 64.71348 + 0.41566 E - 0.00111E^2$
KLS-42, K-2, P8-R10	$\gamma_m = 64.71090 + 0.46312 E - 0.00114E^2$
KLS-73, K-3, P8-R10	$\gamma_m = 63.97688 + 0.49482 E - 0.00121E^2$
KLS-18, K-1, P10-R12	$\gamma_m = 64.40123 + 0.44353 E - 0.00122E^2$
KLS-46, K-2, P10-R12	$\gamma_m = 65.08487 + 0.45281 E - 0.00110E^2$
KL-76, K-3, P10-R12	$\gamma_m = 64.30318 + 0.64268 E - 0.00209E^2$
KL-22, K-1, P12-R20	$\gamma_m = 64.19255 + 0.42652 E - 0.00123E^2$
KL-51, K-2, P12-R20	$\gamma_m = 66.33944 + 0.42501 E - 0.00103E^2$
KL-82, K-3, P12-R20	$\gamma_m = 66.17992 + 0.58045 E - 0.00178E^2$
KL-28, K-1, P20-R40	$\gamma_m = 64.72833 + 0.51943 E - 0.00188E^2$
KL-56, K-2, P20-R40	$\gamma_m = 65.32454 + 0.46175 E - 0.00119E^2$
KL-88, K-3, P20-R40	$\gamma_m = 67.16945 + 0.51736 E - 0.00151E^2$

Appendix H:

Dimensions and Details of Compaction Mold



Scale: $\frac{1}{2}'' = 1''$

FIGURE HI. PLAN AND SIDE VIEW OF COMPACTION MOLD

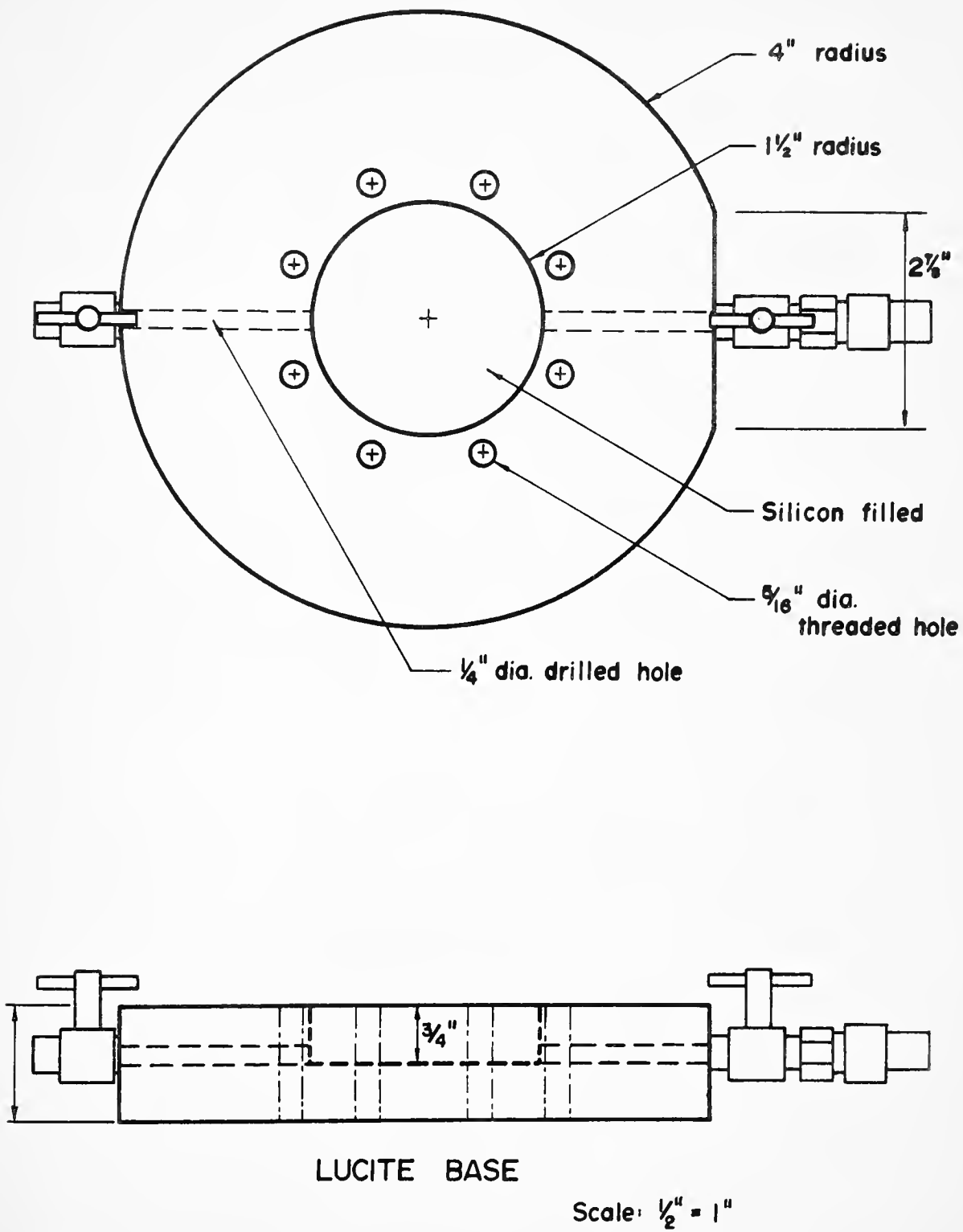
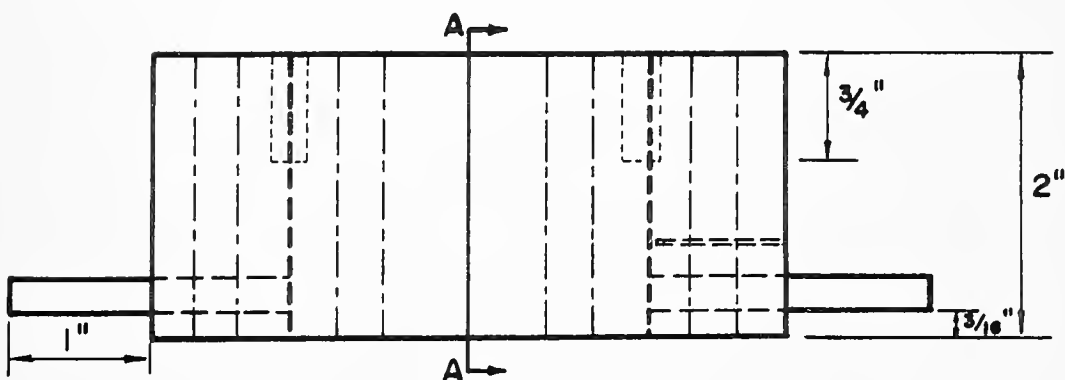
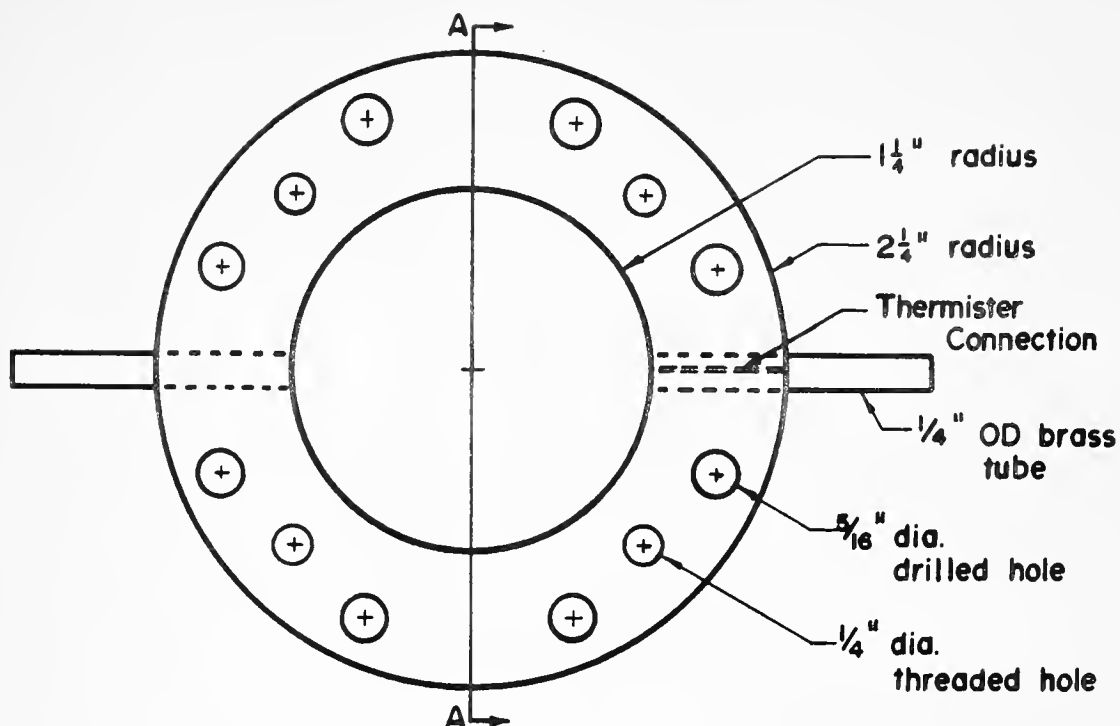


FIGURE H2. PLAN AND SIDE VIEW OF LUCITE BASE



BRASS RING

Scale: $\frac{3}{4}" = 1"$

FIGURE H3. PLAN AND SIDE VIEW OF SAMPLE CONFINING RING

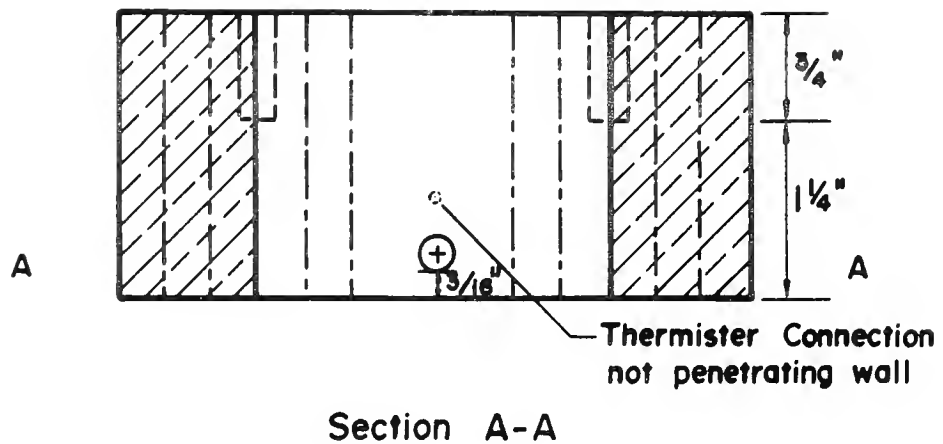
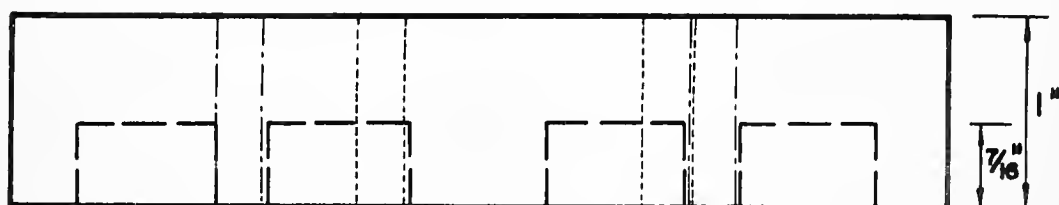
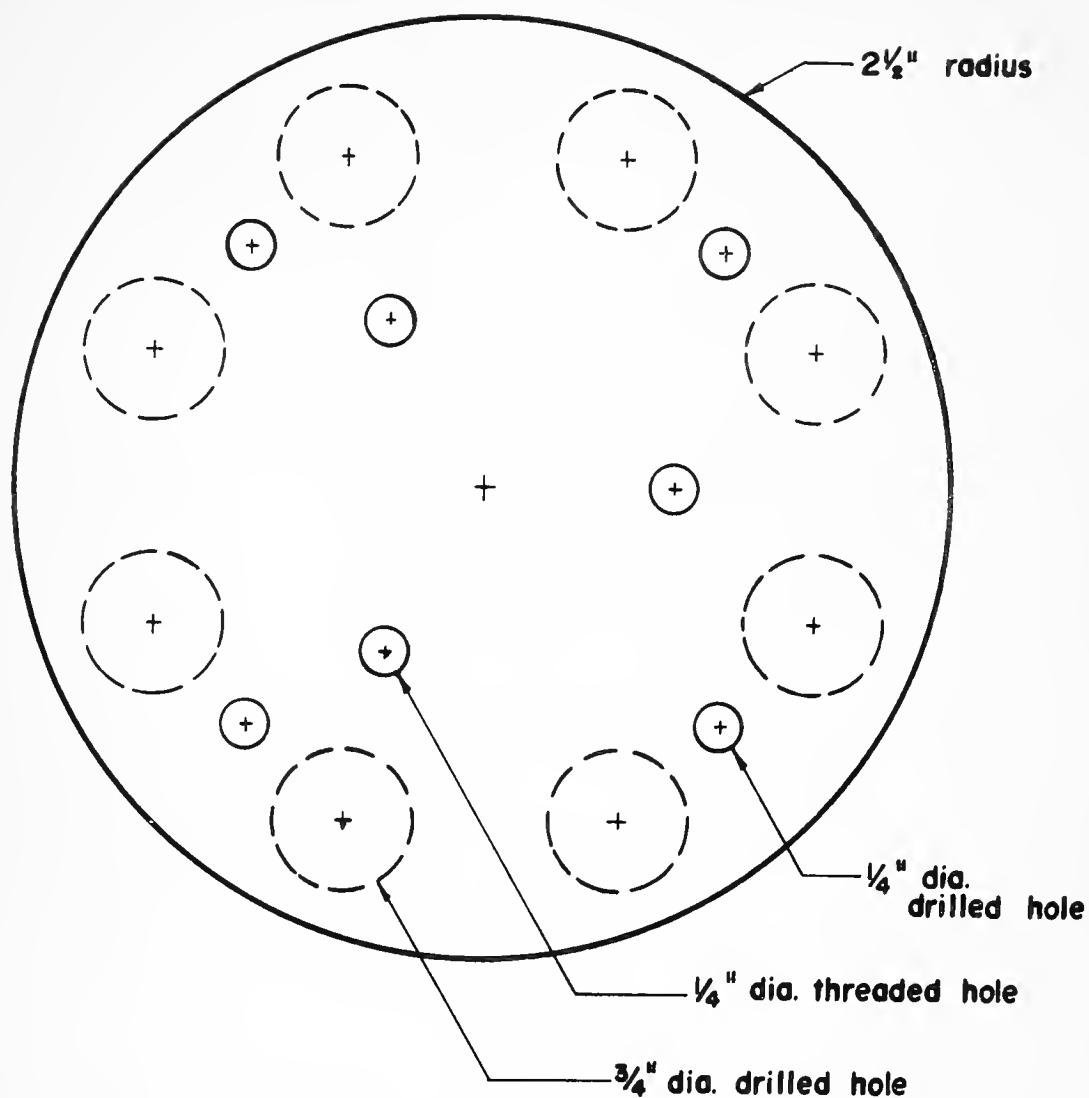


FIGURE H4. VIEW OF SECTION THROUGH SAMPLE
CONFINING RING



LUCITE TOP

Scale: 1" = 1"

FIGURE H5. PLAN AND SIDE VIEW OF LUCITE TOP CAP

VITA

VITA

Ralph J. Hodek was born June 10, 1941 at Chicago, Illinois. His primary and secondary education was obtained at Berwyn and Cicero, Illinois.

He was awarded a BSCE in 1963 and an MSCE in 1965, both from Michigan Technological University. From 1965 to 1969 he was a student in residence at Purdue University. Since 1969 he has been a member of the faculty at Michigan Technological University.

The writer is an Associate Member of the American Society of Civil Engineers. He is a member of the Board of Public Works of Houghton County, Michigan and is a registered professional engineer in the State of Michigan.

